Functional supramolecular nanofibers and their applications in nanoparticle immobilization and catalysis

DISSERTATION

zur Erlangung des akademischen Grades

eines Doktors der Naturwissenschaften (Dr. rer. nat.)

in der Bayreuther Graduiertenschule für Mathematik

und Naturwissenschaften (BayNAT)

der Universität Bayreuth

vorgelegt von

Markus Drummer

geboren in Bad Kissingen

Bayreuth, 2022

Der experimentelle Teil der vorliegenden Arbeit wurde in der Zeit von Januar 2017 bis März 2021 am Lehrstuhl Makromolekular Chemie I der Universität Bayreuth unter der Betreuung von Herrn Prof. Dr. Hans-Werner Schmidt angefertigt.

Vollständiger Abdruck der von der Bayreuther Graduiertenschule für Mathematik und Naturwissenschaften (BayNAT) der Universität Bayreuth genehmigten Dissertation zur Erlangung des akademischen Grades eines Doktors der Naturwissenschaften (Dr. rer. nat.).

Dissertation eingereicht am: 13.05.2022

Zulassung durch das Leitungsgremium: 02.06.2022

Wissenschaftliches Kolloquium: 21.11.2022

Amtierender Direktor: Prof. Dr. Hans Keppler

Prüfungsausschuss:

Prof. Dr. Hans-Werner Schmidt (Gutachter)

Prof. Dr. Andreas Greiner (Gutachter)

Prof. Dr. Markus Retsch (Vorsitz)

Prof. Dr. Birgit Weber

Die vorliegende Arbeit ist als Monographie verfasst.

Teile der Arbeit sind bereits in der folgenden Publikation erschienen:

Diese Publikation ist in der vorliegenden Arbeit mit der Literaturstelle [138] zitiert.

List of abbreviations

^{1}H-NMR	Nuclear magnetic resonance spectroscopy
AE	Adsorption efficiency
ATR	Attenuated total reflection
Au	Gold
AuNPs	Gold nanoparticles
a. u.	Arbitrary unit
BTA	1,3,5-benzenetrisamide
$CDCl_3$	Deuterated chloroform
DCM	Dichlormethane
DMF	*N,N*-dimethylformamide
DMSO	Dimethyl sulfoxide
DSC	Differential scanning calorimetry
e. g.	For example
EDX	Energy-dispersive X-ray spectroscopy
EI	Spray ionization
EtOH	Ethanol
et al.	et alli (and others)
FT-IR	Fourier-transform infrared spectroscopy
H_2	Hydrogen
H_2O	Deionized water
$HAuCl_4 \cdot 3H_2O$	Tetrachloroauric (III) acid trihydrate
ICP-OES	Inductively coupled plasma-optical emission spectrometry
IPA	Isopropanol
KOH	Potassium hydroxide

LSPR	Localized surface plasmon resonance
MeOH	Methanol
MS	Mass spectrometry
NaBH$_4$	Sodium borohydride
NH$_3$	Ammonia
NMR	Nuclear magnetic resonance
NP	Nanoparticle
p. a.	Pro analysis
PAN	Polyacrylonitrile
PS	Polystyrene
PTFE	Polytetrafluorethylene
SAXS	Small-angle x-ray scattering
SEM	Scanning electron microscopy
TEM	Transmission electron microscopy
TGA	Thermal gravimetric analysis
THF	Tetrahydrofuran
UV	Ultraviolet
wt	Weight

List of symbols

λ	Wavelength
$\tilde{v}$	Wavenumber
δ	Chemical shift
ε	Strain
σ	Stress
°C	Degree Celsius
A	Area
Å	Angstrom
c	Concentration
cm	Centimeter
d	Distance
D	Diameter
F	Force
g	Gram
h	Hour
k_{app}	Apparent reaction rate constant
K	Kelvin
kV	Kilovolt
L	Liter
l	Length
m	Mass
M	Molecular weight
M	Molar
mbar	Millibar

mg	Milligram
MHz	Megahertz
min	Minute
mL	Milliliter
μm	Micrometer
mM	Millimolar
mol	Mol
$\bar{M}_n$	Number average molar weight
m/z	Mass-to-charge ratio
M^+	Molecular ion peak
nm	Nanometer
ρ	Density
Pa	Pascal
ppm	Part per million
rpm	Revolutions per minute
RT	Room temperature
s	Second
T	Temperature
T_c	Crystallization temperature
T_m	Melting temperature
U	Voltage
wt%	Weight percent

Table of contents

Summary

Functional nanofibers hold great potential for the efficient and controlled filtration and immobilization of metal nanoparticles and their use in catalytic applications. However, to maintain high catalytic activity, nanoparticle agglomeration has to be avoided and leaching to be prevented. To overcome these issues, efficient and stable deposition of metal nanoparticles on support materials has to be realized. Homogeneous distribution without agglomeration is the overall goal.

In this context, supramolecular nanofibers based on 1,3,5-benzenetrisamides (BTAs) are promising candidates due to their large and well-defined surface area. In focus of this thesis, functionality is achieved using BTAs with pyridine and terpyridine peripheral substituents, which are tailored to form supramolecular nanofibers and firmly connect nanoparticles to the fiber surface. Surprisingly, little is known so far about such BTAs, their self-assembly behavior to supramolecular nanofibers and their function and use. Therefore, this thesis deals with *pyridine- and terpyridine-containing functional supramolecular BTA nanofibers and their application in nanoparticle immobilization and catalysis*.

The first part addresses the *synthesis, characterization and self-assembly behavior of functional BTAs with pyridine or terpyridine substituents*. Besides the number of pyridine substituents in the BTA building block, the length and type of a spacer between the BTA core and the periphery were varied to investigate structure-property relations. The molecular BTA structure has a significant influence on the self-assembly behavior and final morphology of the supramolecular objects. For example, BTAs with a mixture of pyridine and aliphatic substituents from ethyl acetate or 2-butanone tend to form ribbon-like structures with typical widths in the range of 1-10 μm or supramolecular fibers with diameters in the range of 100-500 nm from 2-butanone or alcohol/water mixtures. Especially BTAs with three pyridine or terpyridine substituents form nanofibers from alcohol/water mixtures with fiber diameters in the range of 80-300 nm. A BTA with three pyridine substituents and no spacer and a BTA with three terpyridine substituents and ethoxy spacer were identified as best candidates for further experiments since they rapidly form functional nanofibers with a small diameter by self-assembly upon cooling or cooling and simultaneous evaporation of the solvent.

The second part deals with the *preparation of mechanically stable fiber composites*. These composites were prepared from polymer microfibers in combination with functional supramolecular BTA fibers. Two different processing techniques, the *in situ formation* of functional supramolecular nanofibers in a polymer support fabric and the *wet-laid process* using short electrospun polyacrylonitrile (PAN) microfibers and terpyridine-containing BTA nanofibers, were used. In particular, the wet-laid technique turned out to have great potential. This technique allowed the reproducible preparation of stable and compact composite nonwoven sheets scaled up to composites with a diameter of 20 cm. The composites feature a homogeneous fiber distribution. Interestingly, the mechanical stability is significantly improved with an increasing amount of the BTA fibers due to the formation of an

interpenetrating network of BTA nanofibers and PAN microfibers. The functional composite nonwoven sheets are stable in water, shape-persistent and exhibit good wetting behavior, which is a prerequisite for catalytic applications in aqueous media.

The third part discusses the functionality of the surface of the supramolecular BTA nanofibers with respect to *the immobilization of gold nanoparticles* (AuNPs). Immobilization experiments of AuNPs were carried out in different ways on single supramolecular nanofibers and composite nonwoven sheets prepared by wet-laid technique. For example, *simple mixing* of different pyridine-containing BTAs with a AuNP dispersion showed that the adsorption efficiency is significantly increased with an increasing number of pyridine substituents in the BTA. Especially one BTA with three terpyridine substituents showed after mixing for 5 min with a AuNP dispersion a very high adsorption efficiency with 140 µg Au per mg BTA fiber. The composites were successfully loaded by *immersion* into AuNP dispersions or *filtration* of AuNP dispersions through the composite. The immersion method leads to a homogeneous distribution of AuNPs, whereas filtration allows a faster immobilization. The most promising approach is the *in situ formation* of AuNPs in the composite nonwoven sheet since extremely small and homogeneously distributed AuNPs can be generated directly on top of the terpyridine groups of the BTA nanofibers. Beneficially, the AuNPs are firmly deposited in all composites without agglomeration and no or very minimal leaching of AuNPs was determined.

In the last part, the Au-loaded composite nonwoven sheets were used to demonstrate their *catalytic potential* exemplarily by the reduction of 4-nitrophenol to 4-aminophenol as model reaction. The composites showed high catalytic activity with apparent reaction rate constants comparable to those reported in literature and could be reused several times without loss of catalytic activity. No or only minimal leaching of AuNPs was observed during catalysis. Besides typical discontinuous lab scale experiments, a continuous process was also developed and evaluated. Both processes showed high catalytic activity. A promising result is that the technically more relevant continuous process is much faster in achieving full conversion of the model reaction.

Zusammenfassung

Funktionelle Nanofasern bieten ein großes Potenzial für die effiziente und kontrollierte Filtration und Immobilisierung von Metallnanopartikeln und deren Einsatz in katalytischen Anwendungen. Um eine hohe katalytische Aktivität aufrechtzuerhalten, muss jedoch die Agglomeration von Nanopartikeln vermieden und ein Auslaugen verhindert werden. Um diese Probleme zu überwinden, muss eine effiziente und stabile Abscheidung von Metallnanopartikeln auf Trägermaterialien erreicht werden. Dabei ist eine homogene Verteilung ohne Agglomeration das übergeordnete Ziel.

In diesem Zusammenhang sind supramolekulare Nanofasern auf Basis von 1,3,5-Benzoltrisamiden (BTAs) aufgrund ihrer großen und gut definierten Oberfläche vielversprechende Kandidaten. Im Fokus dieser Arbeit steht die Funktionalität von BTAs mit peripheren Pyridin- und Terpyridin-Substituenten, die so zugeschnitten sind, dass sie supramolekulare Nanofasern bilden und Nanopartikel fest mit der Faseroberfläche verbinden. Überraschenderweise ist bisher wenig über solche BTAs, ihr Selbstassemblierungsverhalten zu supramolekularen Nanofasern und ihre Funktion und Verwendung bekannt. Aus diesem Grund beschäftigt sich diese Arbeit mit *pyridin- und terpyridinhaltigen funktionellen supramolekularen BTA-Nanofasern und deren Anwendung in der Nanopartikel-Immobilisierung und Katalyse*.

Der erste Teil befasst sich mit der *Synthese, Charakterisierung und dem Selbstassemblierungsverhalten von funktionellen BTAs mit Pyridin- oder Terpyridin-Substituenten*. Neben der Anzahl der Pyridin-Substituenten im BTA-Baustein wurden auch die Länge und die Art des Spacers zwischen dem BTA-Kern und der Peripherie variiert, um Struktur-Eigenschafts-Beziehungen zu untersuchen. Die molekulare BTA-Struktur hat einen erheblichen Einfluss auf das Selbstassemblierungsverhalten und die endgültige Morphologie der supramolekularen Objekte. So neigen BTAs mit einer Mischung aus Pyridin und aliphatischen Substituenten aus Ethylacetat oder 2-Butanon dazu, bandartige Strukturen mit typischen Breiten im Bereich von 1-10 µm oder aus 2-Butanon oder Alkohol/Wasser-Mischungen supramolekulare Fasern mit Durchmessern im Bereich von 100-500 nm zu bilden. Insbesondere BTAs mit drei Pyridin- oder Terpyridin-Substituenten bilden aus Alkohol/Wasser-Gemischen Nanofasern mit Durchmessern im Bereich von 80-300 nm. Ein direkt mit drei Pyridin-Substituenten verknüpftes BTA und ein BTA mit drei Terpyridin-Substituenten, die über einen Ethoxy-Spacer verknüpft sind, wurden als geeignetste Kandidaten für weitere Experimente identifiziert, da sie durch Selbstassemblierung beim Abkühlen oder Abkühlen und gleichzeitigem Verdampfen des Lösungsmittels schnell funktionelle Nanofasern mit einem kleinen Durchmesser bilden.

Der zweite Teil befasst sich mit der *Herstellung von mechanisch stabilen Faserkompositen*. Diese wurden aus Polymermikrofasern in Kombination mit funktionellen supramolekularen BTA-Fasern hergestellt. Dabei kamen zwei unterschiedliche Verarbeitungstechniken zum Einsatz, die *in situ*-Bildung von funktionellen supramolekularen Nanofasern in einem polymeren Trägergewebe und das

Nassablageverfahren unter Verwendung von kurzen elektrogesponnenen Polyacrylnitril (PAN)-Mikrofasern und terpyridinhaltigen BTA-Nanofasern. Insbesondere das Nassablageverfahren erwies sich als sehr vielversprechend. Diese Technik ermöglichte die reproduzierbare Herstellung von stabilen und kompakten Kompositen, die bis zu einem Durchmesser von 20 cm skaliert werden konnten. Die Komposite weisen eine homogene Verteilung der supramolekularen Fasern auf. Interessanterweise wird die mechanische Stabilität mit zunehmendem Anteil der BTA-Fasern deutlich verbessert, da sich ein interpenetrierendes Netzwerk aus BTA-Nanofasern und PAN-Mikrofasern bildet. Die funktionalen Komposite sind stabil in Wasser, formbeständig und weisen ein gutes Benetzungsverhalten auf, was eine Voraussetzung für katalytische Anwendungen in wässrigen Medien ist.

Im dritten Teil wird die Funktionalität der Oberfläche der supramolekularen BTA-Nanofasern im Hinblick auf die *Immobilisierung von Goldnanopartikeln* (AuNPs) diskutiert. Experimente zur Immobilisierung von AuNPs wurden auf unterschiedliche Weise an einzelnen supramolekularen Nanofasern und an Kompositen, die mittels Nassablageverfahren hergestellt wurden, durchgeführt. So zeigte beispielsweise das *einfache Mischen* verschiedener pyridinhaltiger BTAs mit einer AuNP-Dispersion, dass die Adsorptionseffizienz mit zunehmender Anzahl von Pyridin-Substituenten im BTA deutlich zunimmt. Insbesondere ein BTA mit drei Terpyridin-Substituenten zeigte nach 5-minütigem Mischen mit einer AuNP-Dispersion eine sehr hohe Adsorptionseffizienz mit 140 µg Au pro mg BTA-Faser. Die Komposite wurden erfolgreich durch *Eintauchen* in AuNP-Dispersionen oder durch *Filtration* von AuNP-Dispersionen durch das Komposit beladen. Dabei führt die Eintauchmethode zu einer homogenen Verteilung der AuNPs, während die Filtration eine schnelle Immobilisierung ermöglicht. Der vielversprechendste Ansatz ist die *in situ*-Bildung von AuNPs im Komposite, da extrem kleine und homogen verteilte AuNPs direkt auf den Terpyridin-Gruppen der BTA-Nanofasern gebildet werden können. Vorteilhafterweise sind die AuNPs in allen Kompositen ohne Agglomeration fest fixiert und es wurde kein oder nur ein sehr geringes Auslaugen von AuNPs festgestellt.

Im letzten Teil wurde das *katalytische Potential* der goldbeladenen Komposite exemplarisch anhand der katalytischen Modellreaktion von 4-Nitrophenol zu 4-Aminophenol gezeigt. Die Komposite zeigten eine hohe katalytische Aktivität mit Reaktionsgeschwindigkeitskonstanten, welche vergleichbar sind mit denen aus der Literatur, und konnten mehrfach ohne katalytischen Aktivitätsverlust wiederverwendet werden. Während der Katalyse wurde kein oder nur ein minimales Auslaugen von AuNP beobachtet. Neben den typischen diskontinuierlichen Experimenten im Labormaßstab wurde auch ein kontinuierlicher Prozess entwickelt und evaluiert. Beide Verfahren zeigten im Allgemeinen eine hohe katalytische Aktivität. Ein vielversprechendes Ergebnis ist, dass mit dem technisch relevanteren kontinuierlichen System die vollständige Umsetzung der Modellreaktion wesentlich schneller erreicht wird.

1 Introduction

Fabrics and nonwovens have become increasingly important in various applications, in particular as filter media. In the last two years, during the COVID-19 pandemic, this has become apparent in daily life, demonstrating the beneficial role of nonwoven-based face masks. Apart from the use in air filtration and human protection equipment, nonwovens are well established in hygiene, medical, automotive, wipes, water filtration or catalysis. Notably, there is still a large room for improvement for fibrous materials with respect to efficiency and for opening new fields of applications. Therefore, research is dedicated to the development of new fiber morphologies, composites or processes. Here, the specific control of the size and morphology, as well as the chemical and physical properties of the fibers, plays a decisive role in their application. [1,2] By combining different materials and processing technologies, there is an infinite number of possibilities to create novel composite nonwovens with unique properties. [3,4] The introduction will give an overview of different methods and materials for nano- and microfiber production. Research identified that, in particular, progress with respect to efficiency could be made by using micro- and nanofiber technologies. A distinction will be made between the common "top-down" approaches, which are commonly used in industry and a "bottom-up" approach, which allows for the preparation of supramolecular nanofibers. Based on this, different types and manufacturing methods of functional composite fabrics or nonwovens and their application are presented. Since functional composites for the application in immobilization of nanoparticles (NPs) and in catalysis are investigated in this thesis, the basics of the immobilization of NPs on different support materials as well as catalysis with precious metals are also discussed.

1.1 Preparation of micro- and nanofibers

As mentioned above, the fabrication of micro- or nanofibers has been a major field of academic and industrial research for years. [5–8] The preparation techniques of fibers can be divided into two conceptually different approaches shown in **Figure 1**.
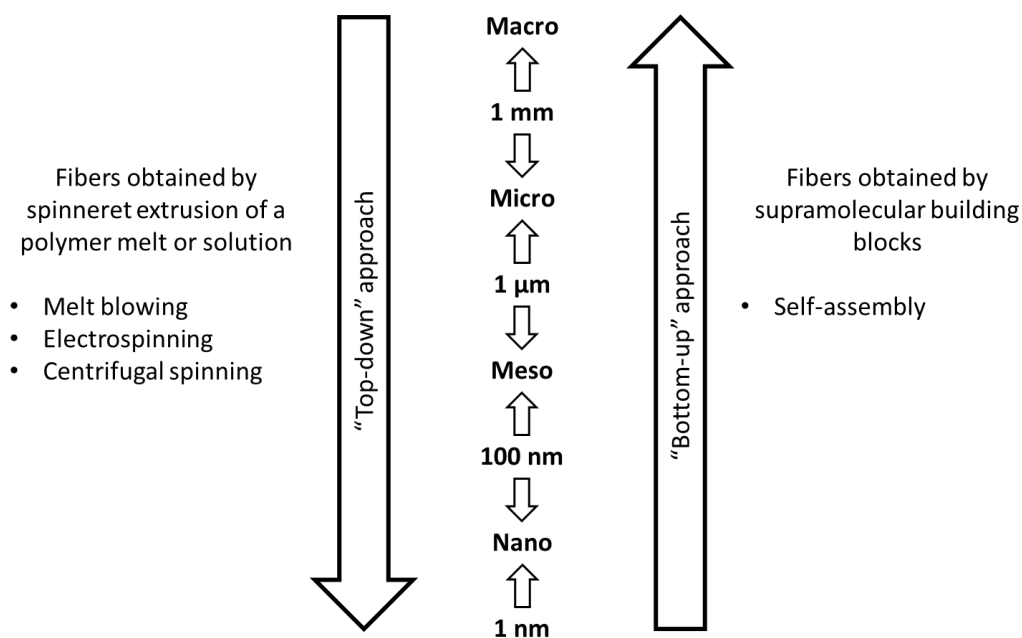

Figure 1: Schematic representation of the "top-down "and "bottom-up "approaches for the fabrication of micro, meso- or nanofibers. Source: University of Bayreuth; Macromolecular Chemistry I.

"Top-down" approaches involve mechanical deformation processes of macroscopic bulk material to create from large to small micro- or nanofibers. For fiber production typically spinning methods are employed. The common spinning processes, such as melt blowing, electrospinning or centrifugal spinning, are based on spinneret extrusion of a polymer melt or solution. [1,2]

In contrast, in "bottom-up" approaches, molecules themselves serve as building blocks to produce from small to large micro- or nanofibers. In this context, supramolecular chemistry can be beneficially used, where molecular building blocks self-assemble into fibrous objects due to the formation of non-covalent intermolecular interactions, such as hydrogen bonds or π-π interactions. [9] Besides self-assembly, template synthesis is known for the preparation of polymeric fibers. [1,8]

In the following, different methods of fiber preparation are briefly presented and their advantages and disadvantages are discussed.

Melt blowing

Melt blowing is one of the most important fiber extrusion processes, in which a polymer melt is extruded from several parallel nozzles and a hot air stream after the nozzle reduces the fiber thickness or splits the fibers to produce fibers in a large amount (**Figure 2**). Due to the hot air flow, randomly

oriented fibers with a broad diameter distribution between several nano- and millimeters are prepared. The average fiber diameter depends on several parameters such as the melt viscosity, melt and air temperature, air velocity and throughput rate. A disadvantage is the "limitation" of useable polymers due to their high melting temperatures in combination with their rheological behavior, which eventually leads to possible thermal degradation during processing.[1,10,11]
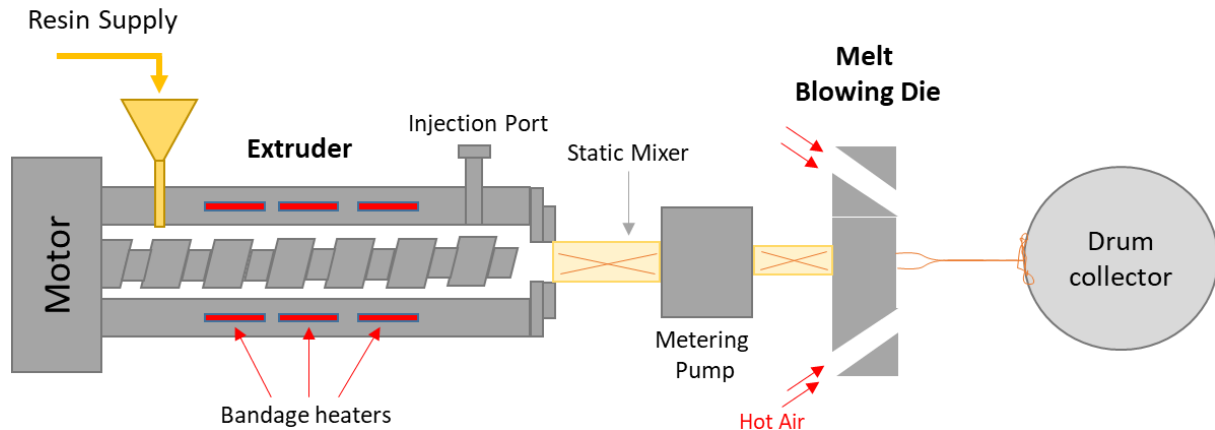
Figure 2: Schematic of the melt blowing process setup. Adapted from [11].

Solution blowing

The production of fibers using solution blowing is based on the acceleration of a polymer solution via a concentric nozzle to a collector using a high-velocity gas flow. On the way to the collector, the formed polymer jet is stretched due to the high gas flow and solvent evaporation. Randomly oriented fibers are deposited on the collector. Fiber morphology and diameter are influenced by several parameters such as the polymer solution flow rate, gas flow pressure, solution concentration or distance between nozzle and collector. Solution blowing is characterized by high productivity. A major disadvantage is the use of solvents, which limits the number of processable polymers if environmentally friendly and non-harmful solvents should be used. [12,13]

Centrifugal spinning

Centrifugal spinning is an extrusion-based process in which a polymer melt or solution is ejected from the nozzles of a rotating spinning head due to centrifugal forces (**Figure 3**). During this process, the jet is stretched, the solvent evaporates or the melt solidifies and subsequently fibers are deposited on a collector. The morphology and fiber diameter are mainly influenced by the rotation speed of the spinning head, the nozzle configuration, the temperature and the collector distance. Due to the flexible application of melt or solution, a large number of materials can be applied for centrifugal spinning. A further advantage is the high production rate with increasing rotating speed and a higher safety compared to electrospinning since no voltage is required. The main disadvantages are the quality of the fabricated fibers and the productivity, which strongly depends on the rotating speed and material properties. [2,5]
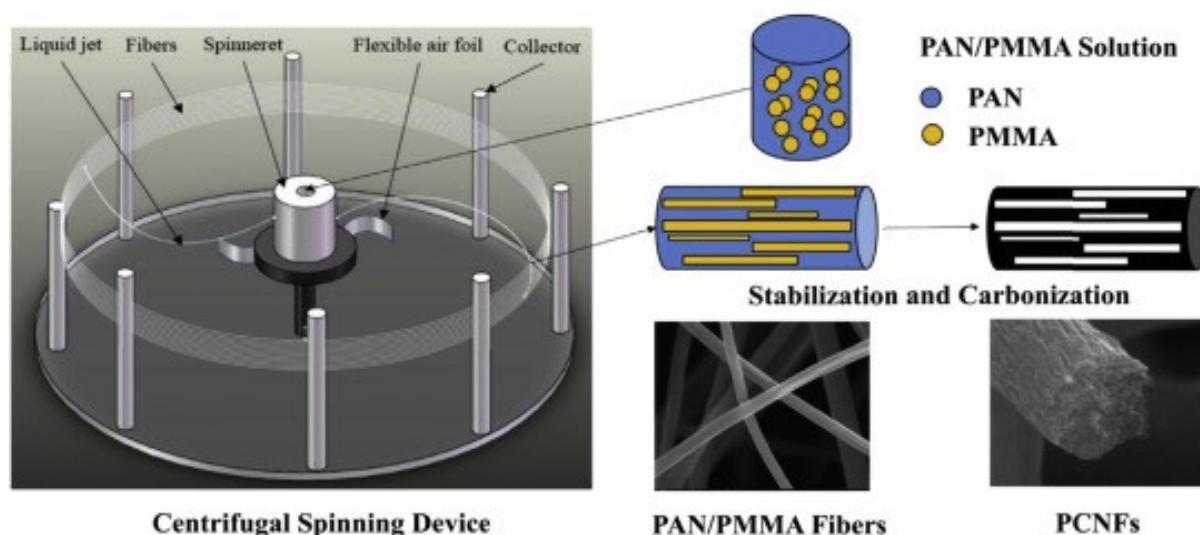
Figure 3: Schematic representation of the centrifugal spinning device and the fabrication of precursor polyacrylonitrile (PAN)/poly(methyl methacrylate) (PMMA) fibers and porous carbon nanofibers (PCNFs). Reprinted with permission from [14] © 2015 Elsevier.

Electrospinning

The most commonly used and well-established process on a lab scale today for the production of micro- or nanofibers is electrospinning. With this method, infinite fibers on the nano- and micrometer scale can be produced from solution, suspension or melt by applying a strong electric field. **Figure 4** shows the schematic electrospinning setup. With the aid of a syringe pump (1), the polymer solution or melt (2) is conveyed to the tip of a metal needle (3), where a polymer drop is formed. By applying a high voltage (4) between the metal needle and the collector (5), which acts as a counter electrode, the polymer drop is electrostatically charged and the surface tension of the drop is overcome. The polymer drop deforms into a so-called Taylor cone and a charged fiber jet (6) is formed, stretched due to the evaporation of the solvent and accelerated to the counter electrode. The fiber jet initially runs in a straight line and is then bent, curled or looped in a complex path due to different instabilities (Plateau-Rayleigh and whipping instability).[15,16] Finally, the fibers (7) are deposited on a collector. The orientation of the fibers can be controlled by choice of the collector. Randomly oriented fibers (nonwovens) are obtained using a static collector, whereas aligned fibers can be produced with rotating collectors at high speeds.[1,2,5,13,15]
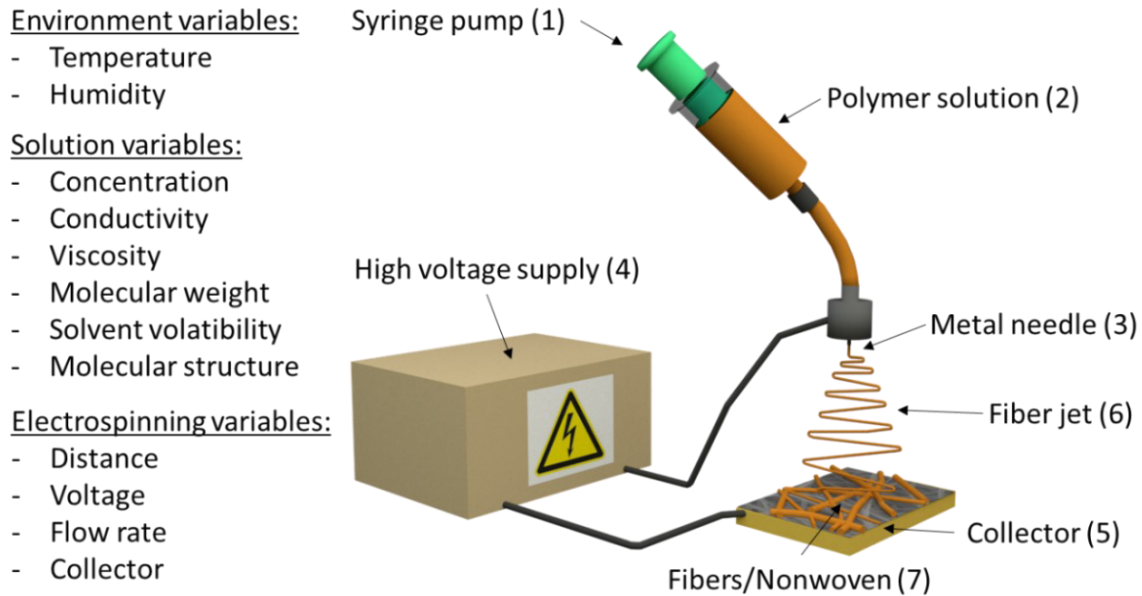
Figure 4: Schematic setup of electrospinning. The polymer solution is delivered to the metal needle via a syringe pump. By applying a high voltage between the needle and the collector, a spinning jet is accelerated to the collector, where the fibers are deposited.

The morphology and fiber diameter of electrospun fibers are influenced by a variety of parameters. In order to obtain homogeneous and defect-free fibers, a high polymer concentration or molecular weight is required. To form a continuous fiber jet, the electrostatic force must overcome the surface tension. In the case of low molecular weight compounds or too low polymer concentrations, the critical entanglement concentration is not reached and only polymer particles or short fibers are formed due to the liquid's attempt to reduce the surface tension. This process is often referred to as electrospraying. The formation of droplets can be prevented by forming a sufficient number of entanglements of the free polymer chains during stretching. [2,13] Increasing the voltage or conductivity of the spinning solution also has a positive effect on homogeneous fiber formation. [13] Increasing the viscosity of the polymer solution (higher polymer concentration or higher molecular weight) leads to an increase in fiber diameter. In addition, if the viscosity is too high, there is a risk that the jet will break off and thus, no continuous fibers will be formed. [13,17] A reduction of the fiber diameter can be achieved by a lower flow rate, smaller cannula diameters or by increasing the electric field. [5] The choice of solvent also has a significant influence on the fiber diameter and morphology. The properties depend on the conductivity, vapor pressure and dielectric properties of the solvent. Thinner fibers can be obtained, for example, by using solvents with a high dielectric constant. [18] In addition to the parameters mentioned above, there are many other influencing factors such as the thermal properties of the polymer, the distance between needle and collector as well as the temperature and humidity. [5] Electrospinning has several advantages compared to the previously mentioned fiber fabrication methods, such as a larger choice of materials, a high throughput of continuous fibers, the production of larger nonwoven areas and the possibility to adjust the fiber morphology selectively (e.g., cylindrical,

ribbon or porous structures) and thickness by a variety of parameters. The main disadvantages of electrospinning are the upscaling problem for the industry, low cost-benefit efficiencies and the use of (harmful) solvents.

Template synthesis

The fabrication of nanofibers via template synthesis is based on filling the pores of a previously produced submicron- or nanoporous structure with a (polymer) melt or solution. Subsequently, the template can be removed to obtain the pure fibers (**Figure 5**). The fiber diameter is determined by the pore size. Due to the uniform structure of the template, fiber structures with a limited length but defined morphology are obtained. The length of the fibers is typically in the range of a few micrometers and the template is destroyed or has to be removed after fiber production limiting the use of this approach for large scale processing. [1,8,19]

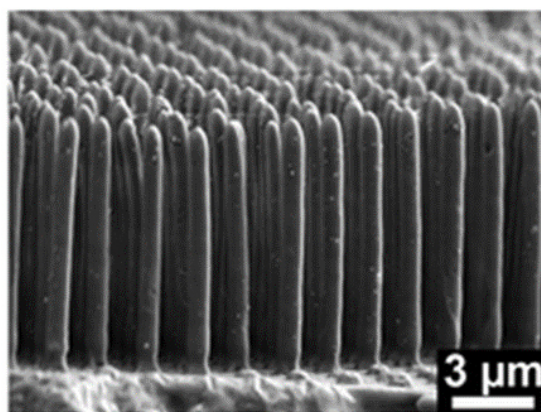**Figure 5**: SEM micrograph of polyacrylate nanofibers fabricated by template synthesis. Reprinted with permission from [20] © 2008 American Chemical Society.

In addition to the methods mentioned above, nanofibers can also be produced by self-assembly of molecular building blocks by forming non-covalent interactions. This "bottom-up" method is based on supramolecular chemistry and will be discussed in the next section.

1.2 Supramolecular class of 1,3,5-benzenetrisamides

Supramolecular chemistry is a well-established research field and topic of current interest for a large number of research groups. In 1978, Jean-Marie Lehn defined supramolecular chemistry as "*the chemistry of molecular assemblies and intermolecular bonds.*" [9,21] Since then, supramolecular chemistry has developed into a broad interdisciplinary field of biology, chemistry, physics and materials science. Supramolecular chemistry is a "bottom-up" approach in which individual molecular building blocks organize and arrange into defined nanostructures by forming non-covalent intermolecular interactions. These secondary interactions differ in their binding energies and orientations (directional, slightly directional or non-directional). The most common non-covalent interactions are ion-ion, dipole-dipole, ion-dipole, van-der-Waals, π-π-interactions, cation-π and anion-π interactions, coordination bonds and hydrogen bonds (**Table 1**). [9,21]

Table 1: Common supramolecular interactions, their directionality, binding energies and a corresponding example. Adapted from [9].

Supramolecular interaction	Directionality	Binding energies (kJ mol^{-1})	Examples
Ion-ion	Nondirectional	100-350	NaCl
Dipole-dipole	Slightly directional	5-50	-CN groups
Ion-dipole	Slightly directional	50-200	Na$^+$ crown ether complex
van der Waals	Nondirectional	<5	Inclusion compounds
π-π-interactions	Directional	2-50	Benzene (edge-to-face)
cation-π and anion-π interactions	Directional	5-80	$^+$N(CH$_3$)$_4$·(toluene)
coordination bonds	Directional	100-300	M-pyridine
hydrogen bonds	Directional	4-120	Carboxylic acid dimer

Self-assembly can be described as "*the spontaneous and reversible association of molecules or ions to form larger, more complex supramolecular entities according to the intrinsic information contained in the molecules themselves*." [9] Self-assembly behavior depends on the molecular structure and physical properties of the building blocks, the strength and orientation of the inter- and intramolecular interactions and several processing parameters such as the solvent, concentration, pH value or temperature. [21] Since self-assembly is a dynamic and reversible process, undesired, ill-defined or damaged structures can be easily repaired. In addition, thermodynamic and kinetic considerations play an important role since the self-assembly process must result in lower free Gibbs energy and thermodynamically more stable structures than the individual building blocks or subunits of those. As a result, mostly highly ordered structures are obtained, reaching the most energetically favored structure. In general, the duration of the self-assembly processes can vary from extremely short to very long. Furthermore, different self-assembly mechanisms can be distinguished, such as isodesmic, cooperative or anti-cooperative self-assembly, varying in their kinetics. Due to this multitude of possibilities for the self-assembly process, there are a plethora of supramolecular motifs capable of forming one-dimensional architectures, including amphiphilic molecules, proteins, peptides or rod-like molecules. [21,22] One of the best known and most studied building blocks are 1,3,5-benzenetrisamides

(BTAs). [23] These compounds generally require considering three major and decisive parts with respect to their molecular design (**Figure 6**): i) the 1,3,5-substituted central benzene core unit is responsible for the C_3 symmetry and planarity, ii) the amide moieties forming directed hydrogen bonds and ensuring one-dimensional crystal growth and iii) peripheral substituents enabling manipulation of crystallographic order and dissolution in different solvents and may also provide the objects' functionality.
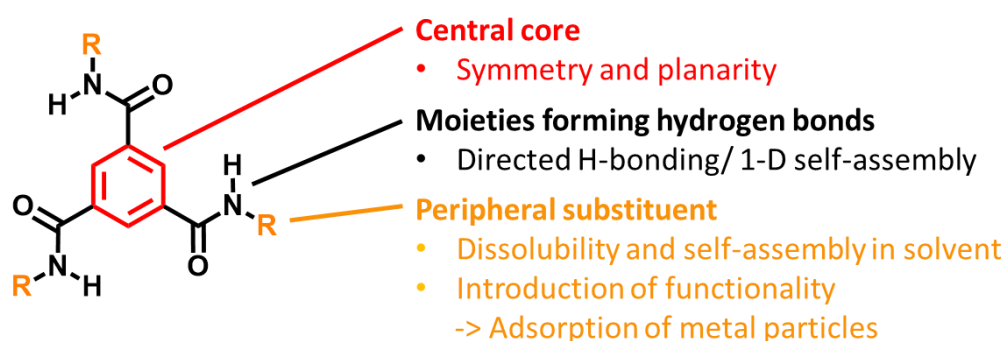

Figure 6: Structural elements of 1,3,5-benzenetrisamides, including a central core unit, moieties forming hydrogen bonds, optional spacers and the peripheral substituents. Source: University of Bayreuth; Macromolecular Chemistry I.

Over the last decades, a large number of BTAs with different peripheral substituents have been synthesized and characterized in detail. Liquid crystalline behavior was observed over a broad temperature range for several linear alkyl-substituted BTAs by Matsunaga et al. in the 1980s. [24] Further studies on the phase behavior of linear and branched alkyl-substituted 1,3,5-benzene- and cyclohexanetrisamides, respectively, were carried out by Timme et al. using DSC, XRD and IR measurements. The thermal properties were strongly influenced by small changes in molecular structure. [25] Studies on the influence of the amide connectivity and bulky aryl substituents on the self-assembly behavior were carried out by the group of Meijer. [26,27] Among others, BTAs with acid groups, pyridine units or crown ethers have been investigated in further studies showing good compatibility of the BTAs with water. [23,28]

Crystal structures of BTA derivatives

Depending on the peripheral substituents, different crystal structures are formed. The crystal structures of several BTAs in bulk or solution were determined by X-ray powder diffraction and solid-state NMR spectroscopy. In 1999, Lightfoot et al. reported the crystal structure of a BTA derivative with helical columnar structures, which result from the triple formation of hydrogen bonds between the amide units of adjacent molecules. Partial tilting of the amide units was observed, with all amide groups of one BTA molecule oriented in the same direction. The benzene rings of adjacent molecules are stacked parallel to each other but rotated by 60° (**Figure 7**). [23,29] Further BTAs comprising bulky side chains (e.g., *tert*-butyl substituent) showed a similar columnar aggregation. [23,30]
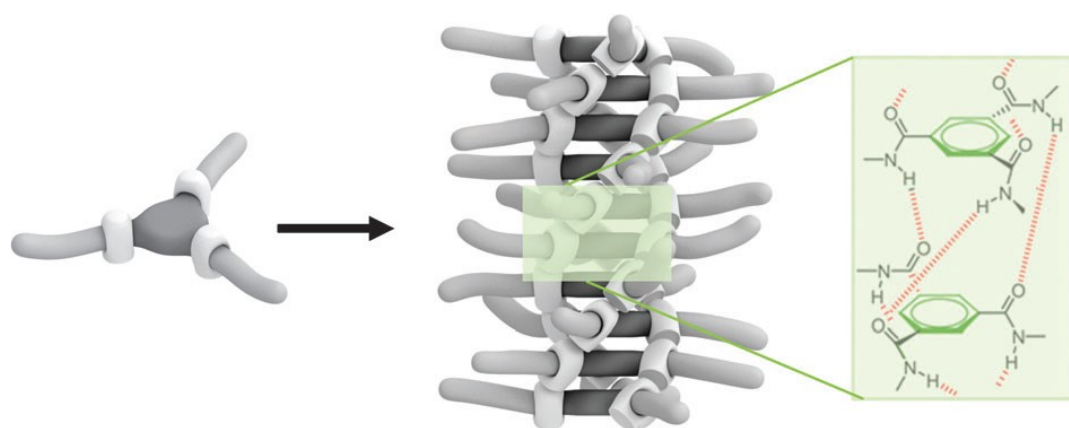
Figure 7: Schematic representation of BTA self-assembly into helical columnar structures by the formation of three-folded intermolecular hydrogen bonds. Reprinted with permission from [23] © 2012 Royal Society of Chemistry.

Besides the formation of supramolecular columnar structures, other crystal structures were also observed.[23,30] BTAs with very short linear alkyl chains (methyl or ethyl) form supramolecular sheets. In contrast, a three-dimensional network based on hydrogen bonding is observed for BTA with a propyl side chain. [31,32] In the case of *N,N',N''*-trimethyl-1,3,5-benzenetricarboxamide, one hydrogen bond is formed between the molecules within one column, whereas the other two hydrogen bonds are formed with adjacent columns. The crystal structure of a pyridine-substituted BTA derivate reveals the formation of an infinite two-dimensional honeycomb grid. [32]

Theoretical investigations of some BTA derivatives were carried out by Albuquerque et al. to investigate the influence of the molecular structure on the columnar arrangement and the associated formation of macrodipoles. Due to numerous localized dipole moments, which occur due to the same orientation of the amide groups of the BTAs, macrodipoles are formed within a supramolecular column. Small changes in molecular structure result in strong variations of the macrodipole formation and strength. Compared to BTAs, trisamides with cyclohexane core form columnar aggregates with significantly stronger macrodipoles since the amide groups exhibit free rotation and can therefore point in the direction of the macrodipole axis. [33]

Formation of BTA nanofibers from solution

Due to the formation of strong triple hydrogen bonds, robust one-dimensional supramolecular structures on the nanoscale can be obtained by self-assembly of BTAs from solution under certain conditions. [23] For this purpose, the BTA has to be molecularly dissolved in a solvent. Then, the self-assembly process has to be induced by an external parameter such as the temperature, concentration or pH value of the BTA solution or the addition of a non-solvent to the solution. **Figure 8** schematically shows the self-assembly process.
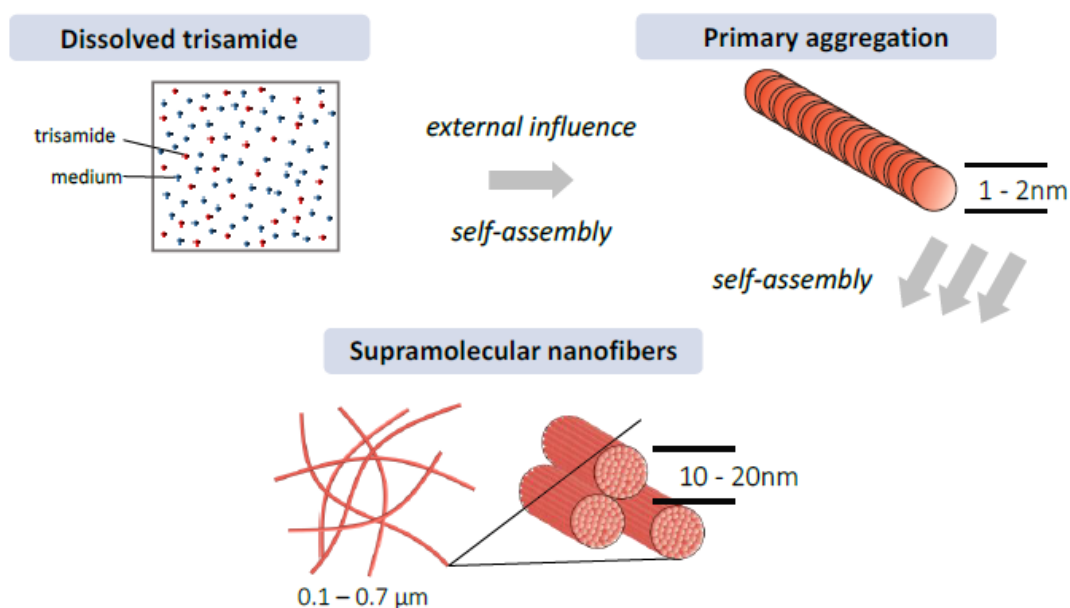
Figure 8: General schematic representation of the self-assembly process of BTAs from solution. Self-assembly of the dissolved BTA molecules is initiated by external parameters resulting in the formation of single BTA molecules into supramolecular columns. Further self-assembly results in the formation of supramolecular nanofibers in the nanometer range. Source: University of Bayreuth; Macromolecular Chemistry I.

The chemical structure of the supramolecular building blocks plays a decisive role in the structure formation since, in particular, the kind of secondary interactions is responsible for this. Moreover, the size and shape of these building blocks, as well as the type and position of functional groups within these components, decide what kind of structures are formed. Thus, structure formation is primarily encoded in the molecular structure. C_3 symmetrical molecules tend to organize in defined fibrous structures. [23]

Apart from the molecular structure, the solvent also plays an important role and determines the solubility and self-assembly behavior at a certain BTA concentration and temperature. Therefore, the knowledge of their phase behavior in solution in terms of a phase diagram is essential. **Figure 9** shows the self-assembly process of a solvent and BTA system upon cooling of the solvent.
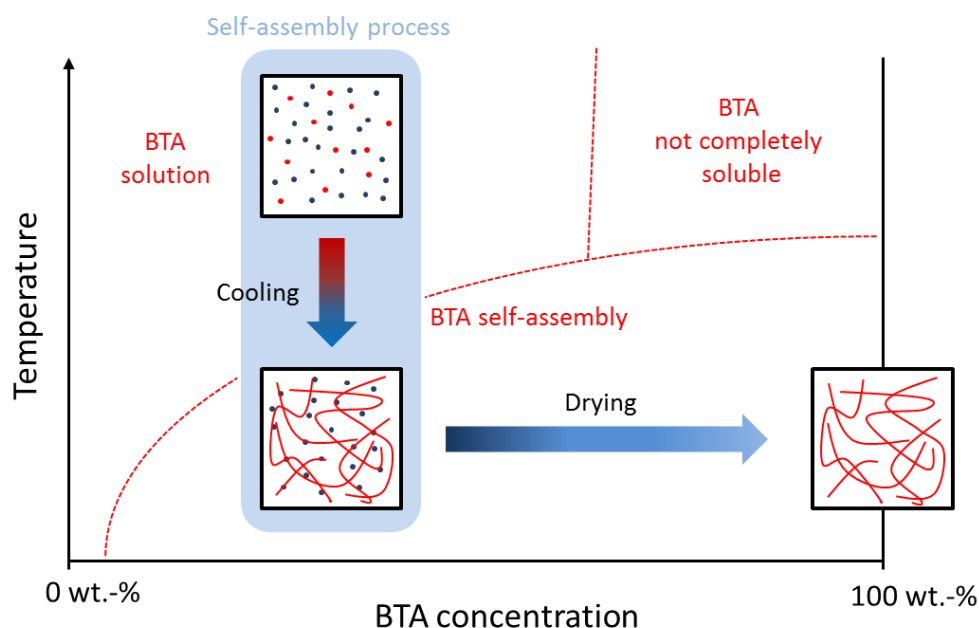
Figure 9: Schematic representation of the self-assembly process from solution upon cooling. Above a certain temperature, the BTA (red dots) is completely dissolved in the solvent (blue dots). By cooling, the formation of supramolecular nanofibers (red lines) is induced in the solution and a fiber dispersion is obtained. Isolated nanofibers can be obtained by subsequent filtration. Source: University of Bayreuth; Macromolecular Chemistry I.

The BTA compound is completely dissolved in a solvent at elevated temperatures. Upon cooling, supramolecular nanofibers begin to form after a certain time, which can be in the range of a few minutes to several days due to a strong temperature-dependent solubility of the BTA in the selected solvent. The nanofibers can be isolated from the solution after the cooling process via filtration.

Technically much more relevant but even more complex is the self-assembly of a BTA from solution upon cooling and simultaneous evaporation of the solvent, which is shown in **Figure 10**. After dissolving the BTA compound at elevated temperatures, a certain volume is removed from the batch and dripped onto a silicon wafer or glass slide. Cooling and simultaneous evaporation of the solvent lead to supersaturation of the dropped solution, resulting in the formation of supramolecular fibers. Thus, self-assembly is induced by cooling the solution or increasing the BTA concentration. The addition of a non-solvent is another possibility to initiate the self-assembly process.
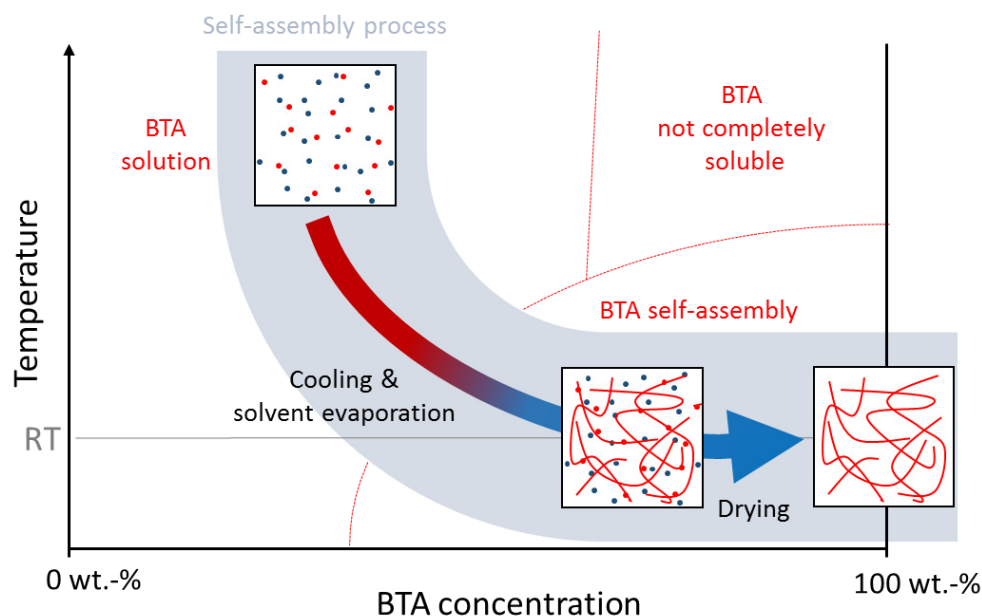
Figure 10: Schematic representation of the self-assembly process from solution upon cooling and simultaneous evaporation of the solvent. Above a certain temperature, the BTA (red dots) is completely dissolved in the solvent (blue dots). After placing a droplet of a hot BTA solution on a substrate, supramolecular nanofibers (red lines) are induced upon cooling and evaporating of the solvent. Complete evaporation of the solvent results in dried supramolecular fibers. Source: University of Bayreuth; Macromolecular Chemistry I.

Different studies were carried out to investigate the complexity of fiber formation. For example, Weiss et al. systematically studied the influence of the stirring velocity and the cooling temperature on the fiber diameter and morphology during self-assembly upon cooling of an alkoxy-substituted BTA derivative. By applying a given stirring velocity and an external cooling bath, the cooling rate (in a non-linear manner) can be controlled. Consequently, with increasing stirring velocity, larger cooling rates and, in turn, thinner fibers are obtained. [34]

A polar BTA derivative with *p*-carboxylphenyl substituents was investigated by Bernet et al.. Here, the carboxylic acid groups allow for selective protonation or ion formation, thus changing the solubility behavior via pH change. Thus, forming a supramolecular hydrogel upon changing the pH value or temperature was demonstrated. [35] The group of Liu showed the formation of a thermo-reversible gel upon the addition of water to a BTA solution in DMF. Nanofibrous structures of the BTA derivative with ethyl cinnamate substituent were observed by scanning electron microscopy. [36]

Application of BTAs

Due to the large variety of substituents, BTAs can find applications in numerous fields. As mentioned before, BTAs can form hydro- or organogels, which could be used as an insulating material or in tissue engineering. [23,35] Mohmeyer et al. showed that BTAs as additive materials could improve the electret properties of isotactic polypropylene (i-PP). At very low concentrations, the BTA molecules form nano-aggregates that can act as efficient charge traps. [37] In addition, certain BTA derivatives act as efficient

nucleating or even clarifying agents for i-PP. The crystallization temperature can be reduced and optical properties can significantly be improved even with a small BTA concentration. [38,39] Besides polypropylene, other polymers such as polyvinylidene fluoride or polybutylene terephthalate can also be nucleated by BTA derivatives. [40,41] By using BTAs as nucleating agents, the insulating and mechanical properties of polystyrene foams can be significantly improved. [42,43] BTA nanofibers are also ideally suited for air filtration applications. [44–46] BTA nanofibers were prepared *in situ* in a polymer fabric acting as support material by self-assembly from solution. These nanofiber-microfiber composites show high filtration efficiencies in removing particles from the air. [45,46]

Benzentrisamides with different amid connectivity or different substituents

Most BTAs have three identical substituents and therefore exhibit a high degree of symmetry within their structure. However, there are also some examples of BTAs where not all three substituents are identical or where the linkage of the amide moiety is completely or partially inverted. This means the C=O group is linked to the benzene core in the case of one or two amide groups (C-centered) and the N-H group is directly linked to the cores at the correspondingly different position (N-centered). **Figure 11** shows an overview of the different possibilities of asymmetric BTAs.
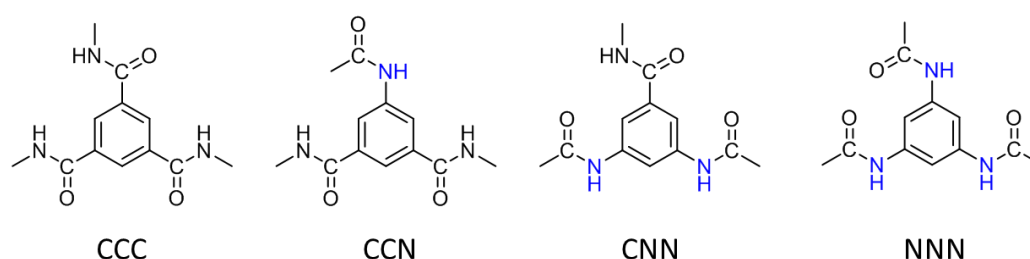

| CCC | CCN | CNN | NNN |

Figure 11: Different possibilities of amide linkage between the central benzene core and the peripheral substituents. On the left side, all amide units are C-centered and on the right side N-centered.

Abraham et al. synthesized several BTA derivates, which were systematically varied in the amide linkages between the benzene core and the peripheral substituents as well as in their aliphatic substituents. The main focus was the investigation of structure-property relationships in relation to the nucleation and clarification of isotactic polypropylene (i-PP). It was demonstrated that the change of the amide connectivity partly brings along significant differences in the thermal properties and in the nucleation efficiency of i-PP. The melting temperature is generally highest with the completely C-centered BTA and decreases from left to right, according to **Figure 11**, so that the lowest melting temperature usually shows the fully N-centered BTA. Only a few of the examined BTAs showed very good nucleation or clarification ability. No general trend regarding the chemical structure could be detected. [39] In a further study, BTAs were investigated, acting as nucleating agents for poly(vinylidene fluoride). In addition to several symmetrical BTAs (completely C- or N-centered), two BTAs based on 5-aminoiophthalic acid (CCN, one amide bond inverted) and 3,5-diaminobenzoic acid (CNN, two amide bonds inverted) were investigated, respectively. As substituents, *tert*-butyl and cyclohexyl were used.

Due to the different amide linkages, significant differences in the solubility of the additives in the polymer melt were found for the same substituent (*tert*-butyl). [41]

A more obvious asymmetry is present if different peripheral substituents are chosen instead of the different amide linkages. For example, Meijer's group has synthesized and characterized asymmetric BTAs with two n-octyl and one chiral methyl alkyl side chain. It could be shown that also asymmetric BTAs in solid-state exhibit columnar structures by the formation of threefold α-helical intermolecular hydrogen bonds. [27] In another work of the Meijer group, carboxylic acid functionalized water-soluble BTAs were reported, which self-assemble in water into one-dimensional fibers, nonwovens or hollow nanotubes (**Figure 12**). [47]
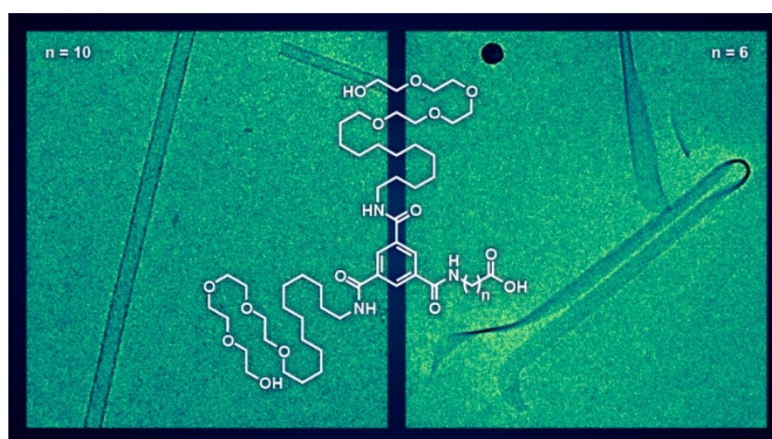

Figure 12: Cryo-TEM micrographs of supramolecular structures resulting from the self-assembly of the shown BTA with n = 10 (left) and n = 6 (right) in water. Reprinted with permission from [47] © 2018 American Chemical Society.

1.3 Functional composite materials

Composite fabrics or nonwovens can be found everywhere in our everyday life. However, the terms "composite", "fabric" and "nonwoven" are not used uniformly and there are numerous definitions depending on the corresponding industry sectors. In 1990, Holliday defined a composite as "*a material comprising two or more different parts or elements in which each material has its own unique characteristics. These materials may include fiber, fabric, plastics, superabsorbents or other materials that effect and become a homogenous part of and are non-separable from, the total structure*". [3]

The difference between a fabric and a nonwoven is the manufacturing process. According to ISO 9092 and CEN EN 29092, a nonwoven is defined as "*a manufactured sheet, web or batt of directionally or randomly oriented fibers, bonded by friction and/or cohesion and/or adhesion, excluding paper and products which are woven, knitted, tufted, stitch-bonded incorporating binding yarns or filaments or felted by wet-milling, whether or not additionally needled, the fibers may be of natural or man-made origin. They may be staple or continuous filaments or be formed in situ.*" [3] In contrast, a fabric is mainly made by weaving or knitting yarns. Woven fabrics are prepared by interlacing two or more yarns at 90° angles to another, whereas knit fabrics are fabricated by interloping one or more yarns. [48] The advantages of nonwovens over fabrics are the far simpler manufacturing process, a wider choice of filaments or fibers and the possibility to adjust the properties of the nonwovens more specifically, resulting in a broader application range. [4]

In the following, the focus will be given on composite nonwovens, which can be classified according to the type of raw materials (fibers, filaments, particulate or hybrid materials) or the method of production, which takes place in three steps. In the first step, the nonwoven is formed, then it is bonded using mechanical, thermal or chemical techniques and finally finished. The major methods of nonwoven fabrication include polymer-laid, dry-laid and wet-laid techniques. [3,49,50]

Polymer-laid process

Polymer-laid nonwovens are prepared by polymer extrusion spinning processes such as melt-blowing (**chapter 1.1**) or spun-bonding. The principle of both techniques is quite similar. However, polymers with lower molecular weights are used for melt-blowing compared to spun-bonding. [49,50]

Dry-laid process

Dry-laid nonwovens are formed by conventional carding processes. In the first step, fiber bundles are separated mechanically and then the individual fibers are deposited on a support to form nonwovens. The orientation of the fibers can be controlled during the bonding step. In contrast, air-laid nonwovens are produced by suspending short fibers in the air and then depositing them on a permeable support by applying a vacuum. [49,50]

Wet-laid process

Wet-laid nonwovens are based on the papermaking process in which fibers are dispersed in water in a first step. The homogeneous fiber dispersion is then placed on a screen conveyor belt, allowing the water to run off and form a uniform web. Finally, the nonwoven is dried. [49,50] The wet-laid process on a lab scale is shown schematically in **Figure 13**.
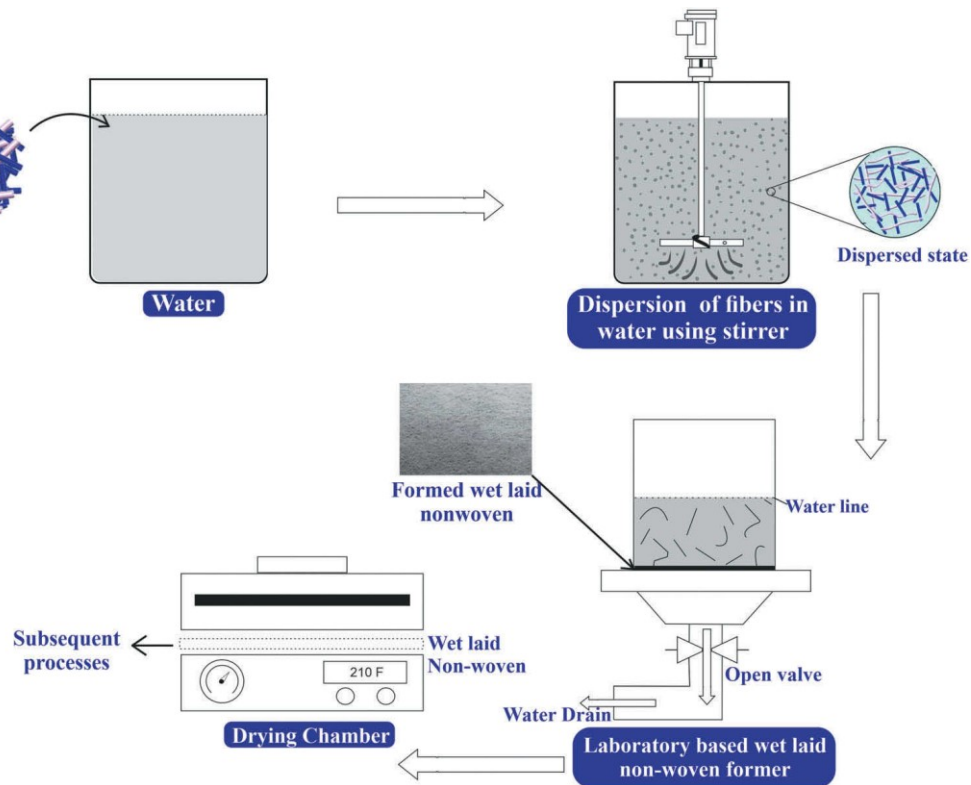

Figure 13: Schematic representation of the wet-laid process for the production of nonwovens. Reprinted with permission from [49] © 2019 Taylor & Francis.

In comparison to other manufacturing methods, the wet-laid technique is particularly characterized by the fact that a wide variety of fiber types can be combined with each other as well as with other materials (additives) and no harmful solvents have to be used. However, a large amount of water or solvent is required and the homogeneity of the nonwovens depends on several parameters such as fiber length, fiber concentration and different machine parameters.

Mechanical bonding of the nonwoven can be achieved by needle-punching, where a needle with barbs is used to create fiber entanglements. Another approach uses a high-speed water jet to entangle the fibers, which is referred to as hydroentanglement. By heating thermoplastic material, the nonwovens can be thermally bonded and a compact structure can be formed. The chemical bonding is achieved by adding adhesives or binding materials, e.g., adding materials with lower melting points. Finally, the functionality or appearance of the nonwovens can be specifically adjusted by wet (dyeing, coating, chemical treatment) or dry finishing (calendering, emerizing or embossing).

There are innumerable examples of composite nonwovens used for various applications. In the following, three selected examples of fiber-fiber composites are described in more detail. The combination of carboxymethyl cellulose (CMC) fibers and PP/PE core/shell fibers significantly improved the wet strength of CMC nonwovens prepared by wet-laid technology. CMC fibers are frequently used in the medical field as a product for wound dressings or adhesion prevention barriers due to their high water absorption properties, gelation behavior, biocompatibility and biodegradability. These properties have not been changed by blending the CMC nonwoven with PP/PE fibers. The wet-laid process was carried out using different ratios of CMC and PP/PE fibers dispersed in EtOH/H_2O solution. After filtration of the fibers, the nonwoven was dried and calendered at 120 °C. The PP/PE fibers act as binding fibers for CMC fibers by melting the PE shell of the core-shell PP/PE fibers, which remain stable in their shape but become slightly thicker (**Figure 14**). [49,51]
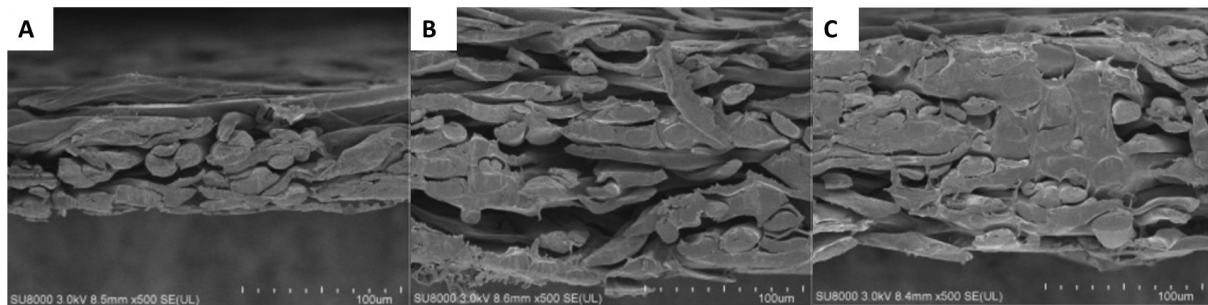

Figure 14: A-C: SEM micrographs showing the cross-sections of composite CMC nonwovens with different ratios of CMC and PP/PE. **A**: neat CMC nonwoven, **B**: CMC: PP/PE = 8:2 and **C:** CMC: PP/PE = 6:4. Adapted and reprinted with permission from [51] © 2013 Springer Nature.

Liu et al. demonstrated the preparation of PAN nanofiber/net air filters by a novel humidity-induced electrospinning/netting method (**Figure 15**). [52]
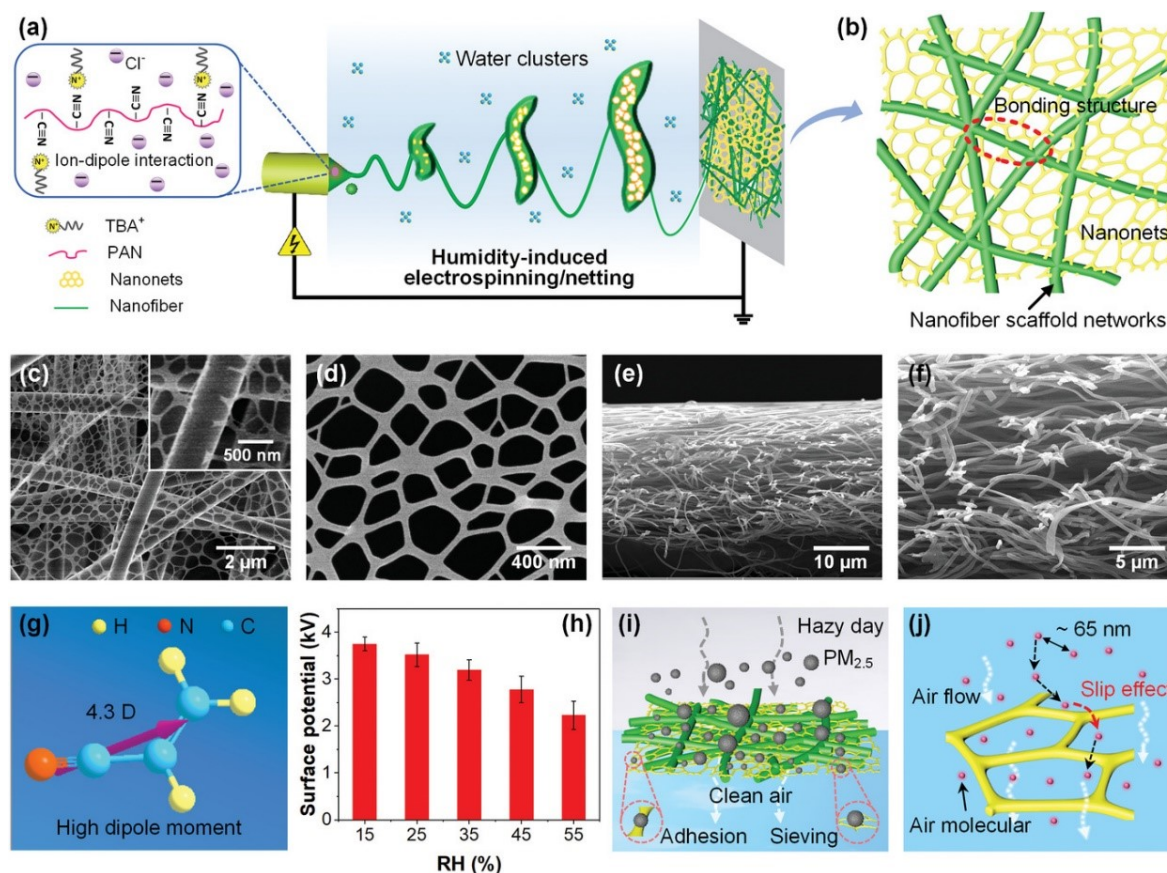
Figure 15: Schematic representation of (**a**) the production of nanofiber/net structures by humidity-induced electrospinning/netting technique of PAN solution with surfactant TBAC and (**b**) the PAN nanofiber/net dual-network structure. SEM micrographs of nanofiber/net nonwoven (**c-f**) showing the dual-network structure. High adhesion of particulate matter is observed due to high dipole moment (**g**) and enhanced surface potential, which depends on the relative humidity (**h**). Schematics of (**i**) the filtration process, including adhesion and sieving and (**j**) the mechanism of slip effect of airflow using the dual-network structure. Reprinted with permission from [52] © 2019 Wiley-VCH.

The charged droplets formed during electrospinning are deformed and phase-separated during jet formation due to ion-dipole interactions between the cationic surfactant tetrabutylammonium chloride (TBAC) and PAN. The nanonets are tightly bonded to the PAN nanofiber scaffold to form a dual-network structure. Due to the small pore size and high porosity, the system is an excellent air filter with efficiencies up to 99.99 % for particles smaller than 300 nm and with low-pressure drop. [52] There are numerous other examples where functional composite nonwovens have been produced by top-down approaches. [53–55]

Langner et al. were able to show that the wet-laid technique can be used to prepare filtration nonwovens as efficiently as those produced by electrospinning of polymer solutions. [56] However, the advantage of the wet-laid method is that different components (such as supramolecular fibers or additives) can be combined more easily. Reich et al., for example, fabricated electrically conductive composite nonwovens by adding silver nanowires (**Figure 16**). [57]
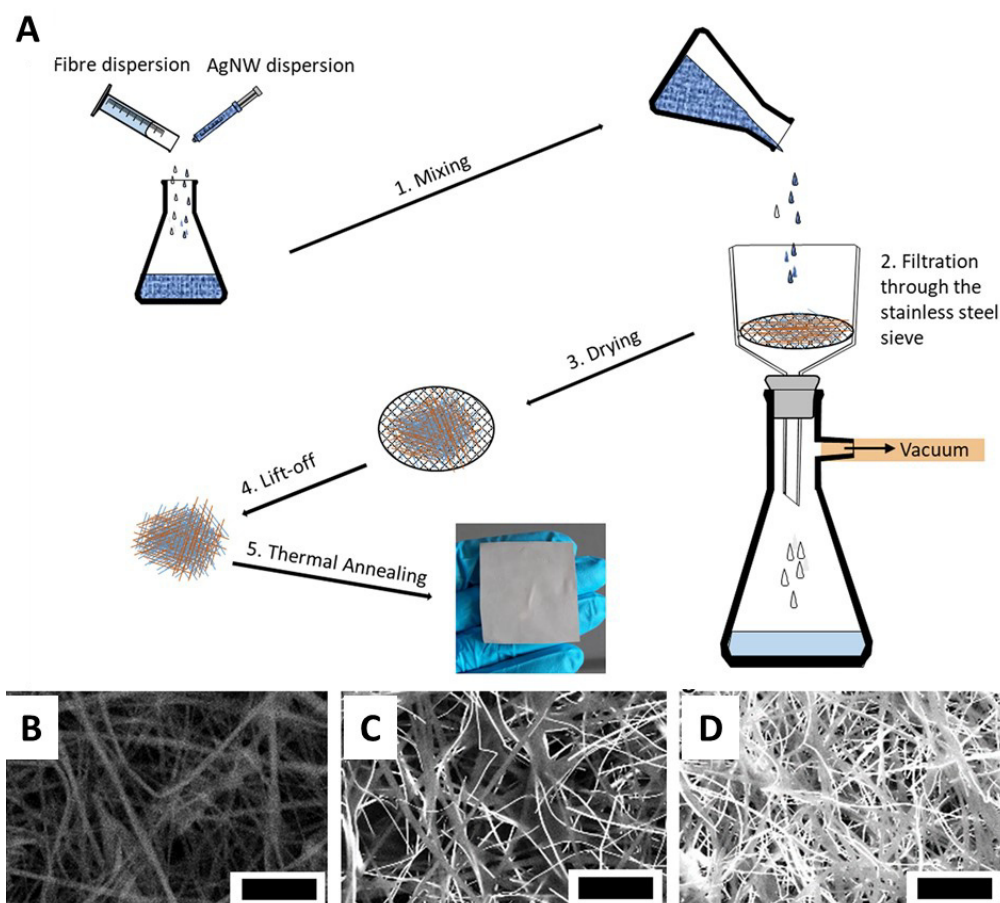
Figure 16: (**A**) Schematic illustration of the production of a functional composite nonwoven consisting of a PAN/PCL short fiber dispersion and silver nanowires (AgNW) by wet-laid technique; (**B-D**) SEM micrographs of composite nonwovens with increasing AgNW content (from left to right). The scale bar is 5 µm. [57]

In general, there are only a small number of composite nonwovens where fibrous structures are created using a bottom-up approach. Supramolecular chemistry enables the generation of supramolecular fibers by self-assembly of small molecules. In 2011, Krieg et al. reported, for example, the fabrication of a supramolecular nonwoven for the size-selective separation of AuNPs from solution. A homogenous supramolecular layer was formed on the cellulose acetate support inside a commercial syringe filter by filtration of a PP2b solution. PP2b forms a three-dimensional network in a THF/H$_2$O mixture enabling efficient and size-selective filtration of AuNPs from aqueous solution (**Figure 17**).[58]
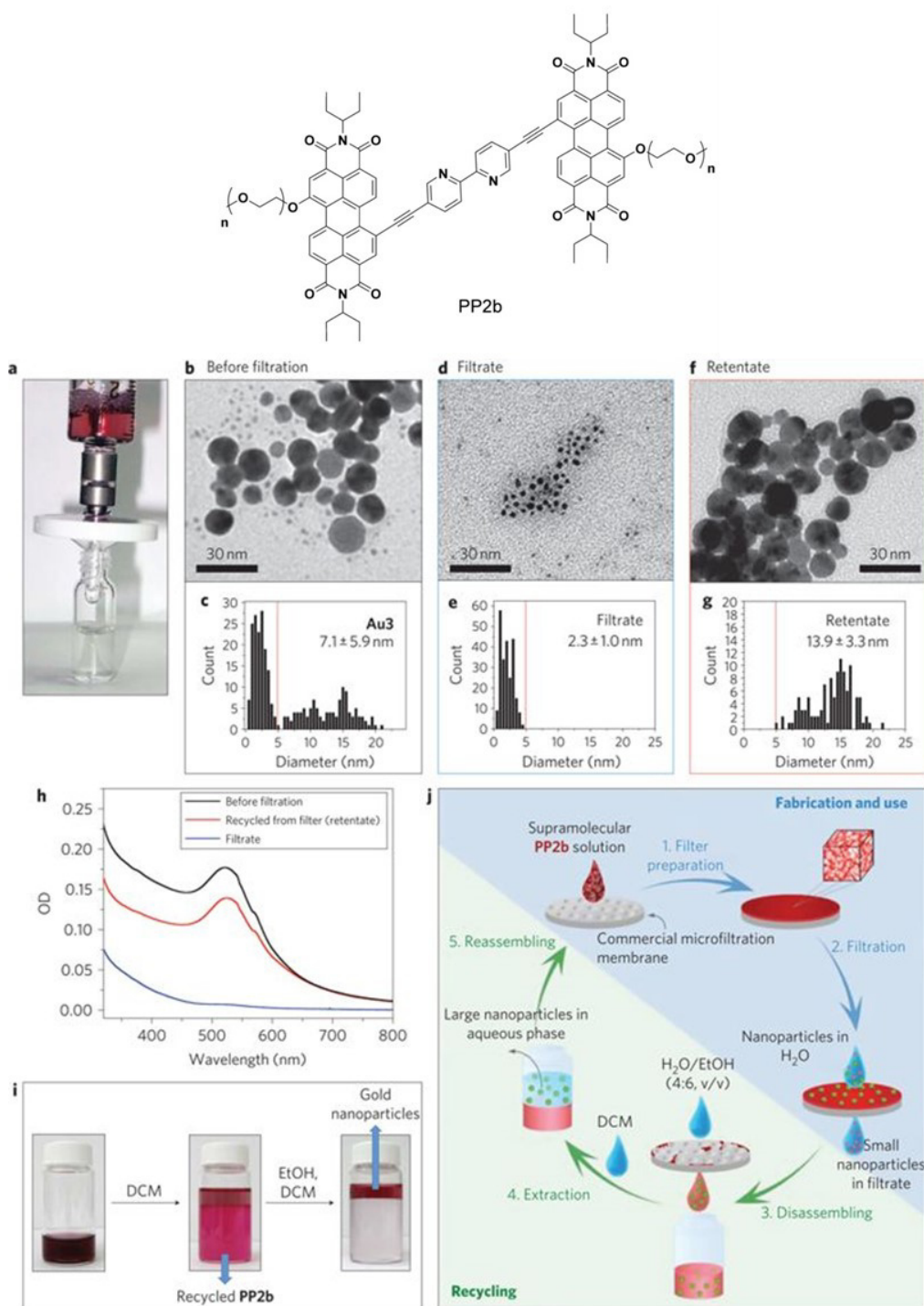
Figure 17: Filtration of AuNPs using a supramolecular nonwoven of PP2b. (**a**) Photograph of the filtration experiment using a commercial syringe filter containing a supramolecular layer of PP2b. (**b**) TEM micrograph of Au3 before filtration and (**c**) the corresponding particle size histogram. (**d**) TEM micrograph of the filtrate and (**e**) corresponding histogram. (**f**) TEM micrograph of the retentate and (**g**) corresponding histogram. Red lines in the histograms show the cutoff of the filter. (**h**) UV/Vis spectra of the Au3 solution before filtration (black), retentate (red) and filtrate (blue). (**i**) Photographs showing the recovery of PP2b and AuNPs by extraction. (**j**) Schematic of the fabrication, use and recycling of the supramolecular nonwoven. Reprinted with permission from [58] © 2011 Springer Nature.

Another example is the development of an ureido-cytosine-functionalized supramolecular polymer, which shows thermoreversible behavior, rapid film formation and a fiber-like self-assembled microstructure. By spin-coating the polymer solution onto a cellulose acetate nonwoven, an efficient filter for the fluorescent dye rhodamine 6G could be produced. [59]

These different examples demonstrate that by combining a wide variety of materials and technologies, composite nonwovens enable both a technical and an economical solution by creating multifunctional products in smaller production steps.

1.4 Metal nanoparticles

In recent decades, the research field of metal NPs has become increasingly important due to its potential in many different applications. [60–63] Here, metal NPs are particularly characterized by their unique optical, electrochemical and catalytic properties. NPs, in general, are defined as objects with all dimensions having a size below 100 nm. Consequently, they exhibit a very high surface-to-volume ratio due to their small size. Metal NPs, in addition, offer a large number of available active sites per area and therefore are of particular interest to be used in catalysis. Gold in its bulk form, for example, shows no catalytic activity. Another special feature of metal NPs is the so-called localized surface plasmon resonance (LSPR) at a specific wavelength depending on the size, shape and local refractive index. LSPR refers to the collective oscillation of electrons in metal NPs caused by the electromagnetic interaction of the metal NP with the incident light of a specific wavelength. The model for describing the plasmon resonance is based on the assumption that positively charged metal atoms are locally fixed and that free valence electrons can move around these metal atoms. If the wavelength of the incident light is larger than the size of the metal NPs, there is an interaction between the electromagnetic field caused by the incident light and the free valence electrons. [64] The effect of LSPR of NPs is mainly used in optoelectronics or sensors. [60,61] Depending on the metal, the LSPR features an absorption maximum at different wavelengths. AuNPs exhibit a LSPR in the range of 500-700 nm, which is why AuNP dispersions show a red to purple color.

Since metal NPs tend to aggregate or agglomerate due to their high specific surface energy, the metal NPs have to be stabilized by capping agents during synthesis or be immobilized on supporting materials. [65,66] The stabilizing ligands adsorb to the NP surface by strong coordination, chemisorption or electrostatic interactions. Subsequently, the stabilization of NPs is achieved either by steric or electrostatic repulsion or a combination of both. Steric stabilization is realized using bulky ligands such as polymers or surfactants, whereas electrostatic stabilization can be generated by charged ligands and the formation of an electrical double layer around the NP. [67] Different physical (e.g., ultrasonication, photo-irradiation), chemical (e.g., sol-gel process, chemical reduction, electrochemical synthesis, chemical vapor deposition) or biological (e.g., via bacteria, enzymes or proteins) methods can be used to prepare metallic NPs of different size and morphology. [61] Since this work focuses on AuNPs, the most common synthetic routes for the synthesis of colloidal AuNPs are described in more detail below.

Synthesis and stabilization of gold nanoparticles

One of the best-known methods to prepare colloidal AuNPs is the reduction with sodium citrate. This method was already introduced by Turkevich in the 1950s. [68] It involves reducing tetrachloroauric acid trihydrate ($HAuCl_4 \cdot 3H_2O$) in boiling water with a sodium citrate solution. A color change from light yellow to wine red indicates the successful reduction and synthesis of spherical AuNP. Sodium citrate acts not only as a reducing agent but also as stabilizing ligand. Over the years, the Turkevich method has been further developed or modified by using different temperatures, reaction times, pH values, reducing agents or concentrations of metal precursors or reducing agents. [66,69,70] For example, Bastús et al. have developed a kinetically seeded-growth approach in which highly monodisperse AuNPs with a controllable diameter of 10-200 nm can be obtained by reducing $HAuCl_4$ with sodium citrate (**Figure 18**). [71]

ratio = [Au³⁺] / [Au seeds]   **Size Focusing**   **Ostwald Ripening**
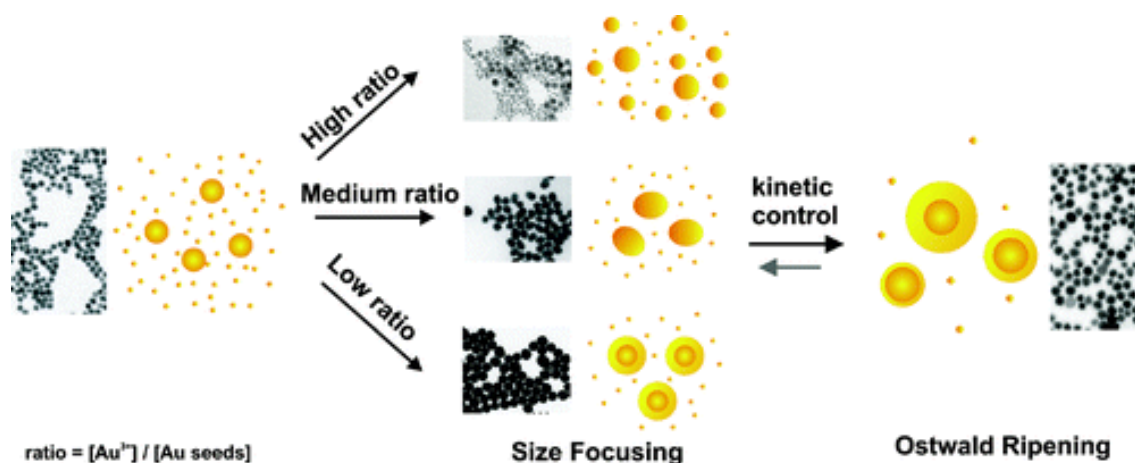
Figure 18: Schematic of the different growth pathways of kinetically controlled seeded growth of AuNPs. Temperature control of the solution and regulation of the Au precursor to seed ratio enable controlled size focusing. A higher amount of the Au precursor leads to the formation of oval-shaped particles or new nucleation of smaller AuNPs. Reprinted with permission from [71] © 2011 American Chemical Society.

A lower temperature reduces the reaction rate and thus prevents secondary nucleation. The reactivity of the Au species is controlled by adjusting the pH value, which allows a higher monodispersity of the NPs. A narrow AuNP distribution can be achieved by regulating the number of Au atoms injected during the growth step. [71] In further studies, the preparation of AuNPs with a diameter below 10 nm was shown by using strong reducing agents such as sodium borohydride ($NaBH_4$) or tannic acid. The combination of tannic acid as a reducing agent and a large excess of sodium citrate as stabilizing agent leads to the formation of AuNPs with a diameter of 3.5 nm and a very narrow distribution. [72]

To receive stable AuNPs and avoid agglomeration over time, AuNPs can also be stabilized with thiol derivatives. The first thiol-stabilized AuNPs were produced in the 1990s. [73] Brust and Schiffrin applied the principle of two-phase ligand exchange of a Au^{3+} complex from water to toluene phase with tetraoctylammonium bromide (TOAB) as a phase transfer agent. *In situ* synthesized AuNPs with a water-insoluble long-chain thiol were prepared by the two-phase reduction of $HAuCl_4$ by $NaBH_4$ in the

presence of an alkanethiol, which prevents aggregation in an organic medium.[66] This method has also been further developed and modified until today. [69,70]

Besides sodium citrate or alkanethiols, alkylammonium salts are often used as stabilizing agents and phase transfer reagents, allowing dispersion in an organic or aqueous medium. Tetraalkylammonium ligands can prevent aggregation of NPs by forming an electrical bilayer through the polar head group and can ensure steric repulsion due to the presence of a lipophilic side chain. The group of Roucoux used *N,N*-dimethyl-*N*-alkyl-*N*-(hydroxyalkyl)ammonium salts as capping agents to prepare size- and shape-controlled AuNPs. [74]

Poly(*N*-vinyl-2-pyrrolidone) (PVP) as a linear polymer is also often used as a capping agent due to its commercial availability, relatively low cost and good solubility in several solvents. Due to the hydrophobic carbon chains of PVP, which interact with each other in the solvent, the NPs are stabilized by repulsive steric effects. The advantage of polyvinyl alcohol (PVA), which can be chemically bonded to the NPs by the hydroxyl group, is based on the water solubility, biocompatibility and biodegradability of PVA. The synthesis of NPs is based on the Brust-Schiffrin method (mentioned before) or a ligand-exchange reaction. The size of the NPs can be adjusted by varying the polymer concentration. The higher the polymer concentration, the better the stabilization and the smaller the NPs. [67] The group of Greiner reported the preparation of long-term stable and redispersible AuNP powder produced by spray-drying. After the preparation of AuNPs according to the Turkevich method, PVA or PVP was added as a stabilizing agent, and the aqueous AuNP dispersion was spray dried into hollow capsules. The AuNPs are located in the polymer shell of these capsules and showed no aggregation in the dry state. The AuNP powder is redispersible in water. Starting from PVP@AuNPs, the AuNPs can be incorporated into other stabilizing polymers in organic solvents by ligand exchange reactions (**Figure 19**). [75]

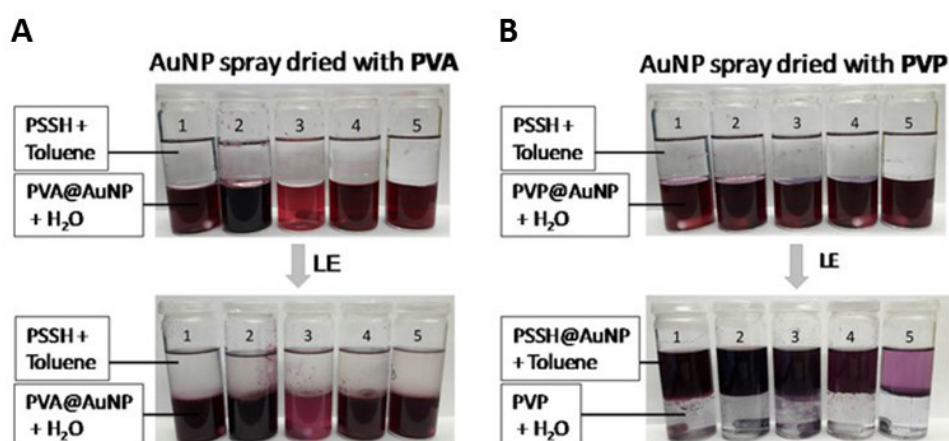**Figure 19:** Two-phase ligand exchange reaction of spray-dried AuNPs with thiol-functionalized PS (PSSH) in toluene. (**A**) Using PVA@AuNPs, the ligand exchange is not successful because PVA is a too strong stabilizing ligand for AuNPs. (**B**) With PVP@AuNPs, a ligand exchange reaction takes place because PVP is a weaker ligand than PVA and can be replaced by PSSH. Reprinted with permission from [75] © 2019 Wiley-VCH.

In addition, many other ligands can be used to stabilize metal NPs due to their functional groups. These include i.a. polyols [76], amines [77], or phosphorous ligands [78].

As shown before, the choice of ligand plays an important role in controlling the NP size or shape as well as the NP properties and prevents not only agglomeration through steric or electrostatic stabilization but also the unlimited growth of NPs. Removal of capping agents is difficult and can lead to NP aggregation. [66,69]

Immobilization of metal nanoparticles on support materials

Another possibility to stabilize metallic NPs is the immobilization of NPs on support materials such as silica, alumina, MOFs, graphene or other forms of carbon, as well as different types and architectures of polymers using various techniques. [61,65,66,69] Especially polymeric supports offer several advantages over monomeric ligands, such as better long-term stability of NPs or better solubility adjustment. The often-used amphiphilic character of the polymers also provides better compatibility and processability. The synthesis of polymer-stabilized AuNPs can be performed by the so-called "grafting to" or "grafting from" technique. The "grafting from" technique is a kind of functionalization, as the polymerization takes place on the Au surface in the presence of an initiator. In contrast, with the "grafting to" method, the previously synthesized polymers are attached to the surface of the NPs via heteroatoms within the polymer structure or the polymers are used as a template to stabilize AuNPs as core/shell NPs. [69]

A frequently used method for the immobilization of NPs on a support material is the so-called deposition method. For this purpose, the NPs are already synthesized in a previous step and then immobilized by deposition on a support. The colloidal deposition is based on the simple immersion of the support in an aqueous or organic NP dispersion, followed by different purification steps such as centrifugation, filtration or multiple washing. [79] The immobilization depends on electrostatic interactions and the possibility of forming chemical bonds between the ligands at the NP surface and the functional groups of the support material. For this reason, the surface of the support materials is often functionalized. [65] The main advantage of the deposition method is a high control of particle size, morphology and composition of the NPs independent of the support material. Additionally, a homogeneous distribution of the NPs in the support material and no change in NP size or shape due to the mild conditions are observed generally. However, the diffusion of the NP dispersion into the pores can take a very long time, depends on the wetting behavior of the support material and the stabilizing ligands often remain bound on the NP surface, which can negatively influence the immobilization efficiency and catalytic performance. [66,67,79] These issues can often be avoided with polymer supports.

Schöbel et al. showed the immobilization of AuNPs within functional patches of patchy nonwovens prepared by a combination of coaxial electrospinning and crystallization-driven self-assembly (**Figure 20**).
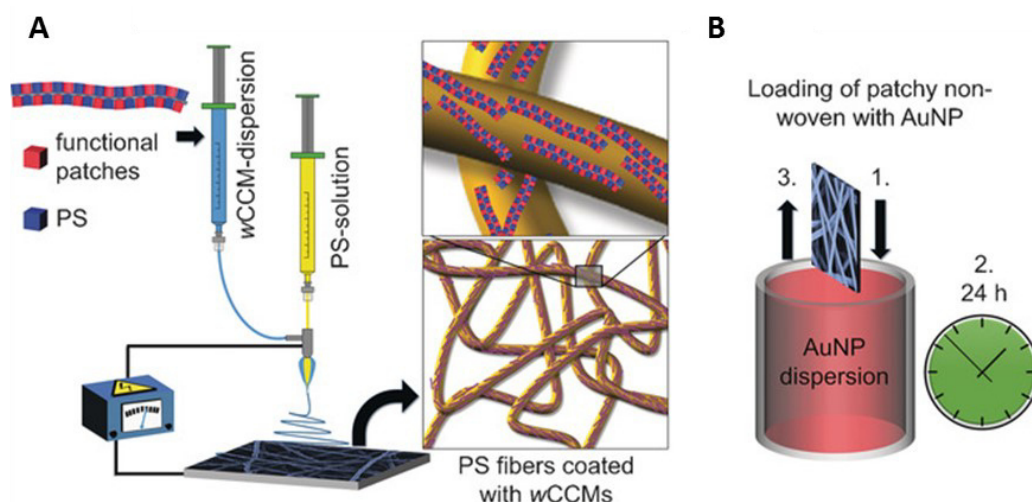
Figure 20: (**A**) Preparation of catalytically active patchy nonwovens by coaxial electrospinning of a PS solution and patchy worm-like crystalline-core micelle (wCCM) dispersion and (**B**) subsequent loading with AuNPs by simple dipping method. Reprinted with permission from [80] © 2017 Wiley-VCH.

PS-*b*-PE-*b*-PMMA triblock terpolymers were used to form patchy worm-like crystalline-core micelles (wCCMs) obtained by crystallization-driven self-assembly. After polymerization, the PMMA block was functionalized with diisopropylamino groups, which enabled an efficient binding of AuNPs. Coaxial electrospinning of a PS solution and the functionalized wCCMs dispersion leads to patchy nonwovens. AuNPs were immobilized in the functionalized patches by dipping the nonwovens in preformed citrate stabilized AuNP dispersion. These nonwovens could be used as a catalyst system for organic reactions according to the tea bag principle. [80] There are numerous other examples where AuNPs have been immobilized on surface-modified electrospun fibers by simply immersing the nonwovens in a AuNP dispersion. [81,82]

The second approach of NP immobilization is the *in situ* NP formation on support materials. Therefore, the support material is mixed with a salt precursor solution and subsequently reduced *in situ* using different components such as UV irradiation, ultrasonication, reducing agents or bacteria. [82,83] First, the metal ions coordinate with the functional groups of the support material before the ions are reduced to NPs on the surface of the support material. In contrast to the principle of deposition, hybrid materials can be produced with less time and effort by *in situ* NP formation on a support material. The most significant advantage is that no additional stabilizing ligands are needed and bonded to the NP surface, which could influence the catalytic activity. The disadvantages of this method are a more difficult control of NP formation and a strong influence of different support materials on the type of NP formation since this is a heterogeneous nucleation process. [79]

Different kinds of polymeric architectures can be used as support for the *in situ* synthesis of AuNPs. Aubrit et al. reported, for example, the immobilization of non-functionalized AuNPs on cylindrical phases of PS-*b*-PVP block copolymers perpendicular and parallel to the substrate (**Figure 21**). [84]
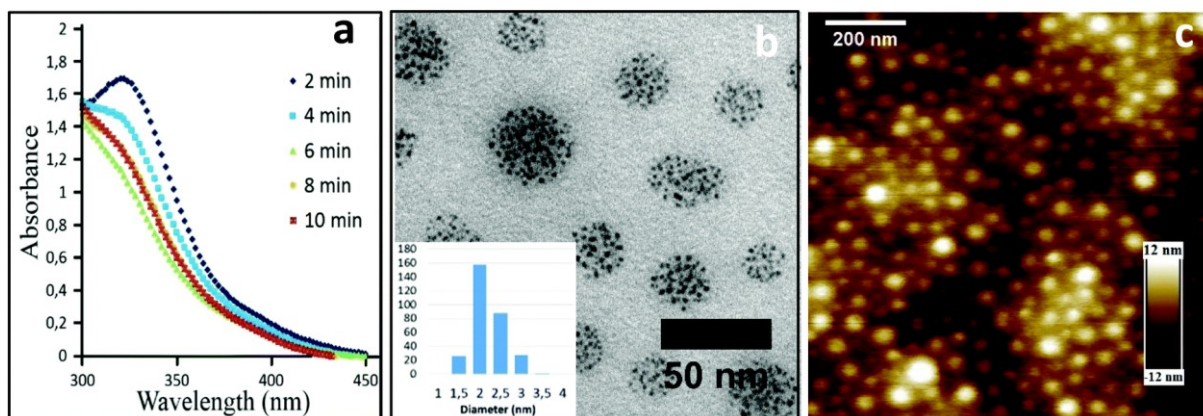
Figure 21: (**a**) UV-Vis spectra demonstrating the formation of AuNPs due to a decrease of the Au(III) peak at 325 nm; (**b**) TEM micrograph of the AuNPs confined in the PVP domains and inset showing the corresponding size distribution of the AuNPs; (**c**) AFM height image is showing the cylinder organization on the surface of the spin-casted film. Reprinted with permission from [84] © 2018 Royal Society of Chemistry.

AuNPs were formed by sonication or irradiation of a Au salt in the PS-*b*-PVP copolymer solution, followed by the preparation of anisotropic films by spin-casting or coating of the block copolymer solutions. The AuNPs in a size range of 2-4 nm are only located within the PVP cylindrical domains due to the interactions between the Au and pyridine groups of PVP. [84]

The group of Ballauf showed the formation of AuNPs in spherical polyelectrolyte brushes consisting of a PS core and long cationic polyelectrolyte chains. As shown in **Figure 22**, the generation of AuNPs takes place only in the polyelectrolyte layer of the carrier particle due to strong attractions between the AuNPs and the polyelectrolyte chains caused by a negative surface charge of the AuNPs. NPs immobilized in these spherical polyelectrolyte brushes showed high catalytic activity and reusability in an aqueous medium. [85]

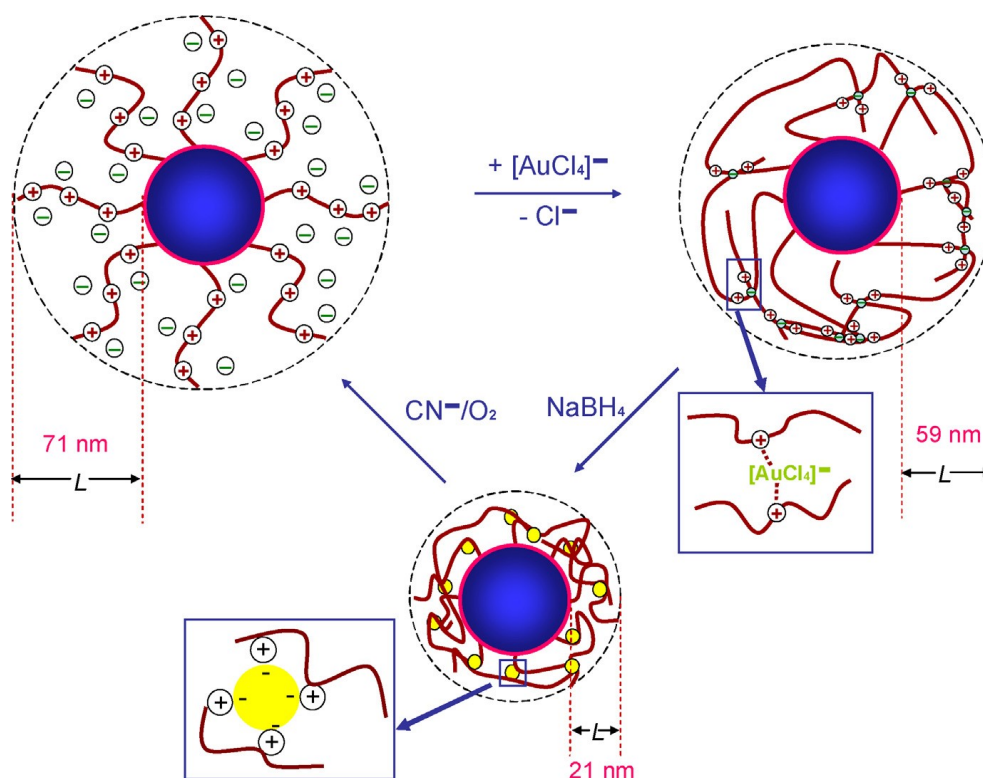**Figure 22:** Schematic for the generation of AuNPs and their dissolution with CN^-/O_2. In the first step, the Cl^- ions, which serve as counterions in the electrolyte layer, are exchanged by adding a $HAuCl_4$ solution. Excess of $AuCl_4^-$ ions are removed by ultrafiltration since only the immobilized $AuCl_4^-$ ions lead to well-dispersed NPs. These are generated by reduction with $NaBH_4$ accompanied by a strong decrease of the layer thickness. In the last step, AuNPs are dissolved by complexation with CN^-/O_2. Reprinted with permission from [85] © 2016 Elsevier.

Besides block copolymers and polyelectrolyte brushes, dendrimers or microgels are also suitable as polymer support for the immobilization of NPs. [86]

The group of Shi reported a method to immobilize AuNPs within electrospun PVA/PEI (polyethyleneimine) nanofibers by *in situ* reduction. Crosslinked PVA/PEI fiber mats were immersed into a $HAuCl_4$ solution to adsorb the $AuCl_4^-$ ions via binding to the free amine groups of the PEI. AuNPs with a diameter of 11.8 nm were obtained by further reduction with $NaBH_4$. The fiber morphology did not change with AuNPs, but the mechanical properties of the fibers were improved compared to the fibers without AuNPs. [87] The preparation of a AuNP-loaded PAN nanofibrous nonwoven by a combination of electrospinning, amidation and electroless plating technique was reported by Liu et al. in 2015. Amination of the PAN fibers creates amine and imide moieties on the fiber surface as anchor groups for the immobilization of AuNPs. The *in situ* formation of AuNPs was achieved by first immersing the nonwoven in a $HAuCl_4$ solution to adsorb the Au ions before subsequent reduction by light or UV irradiation (**Figure 23**). [88]
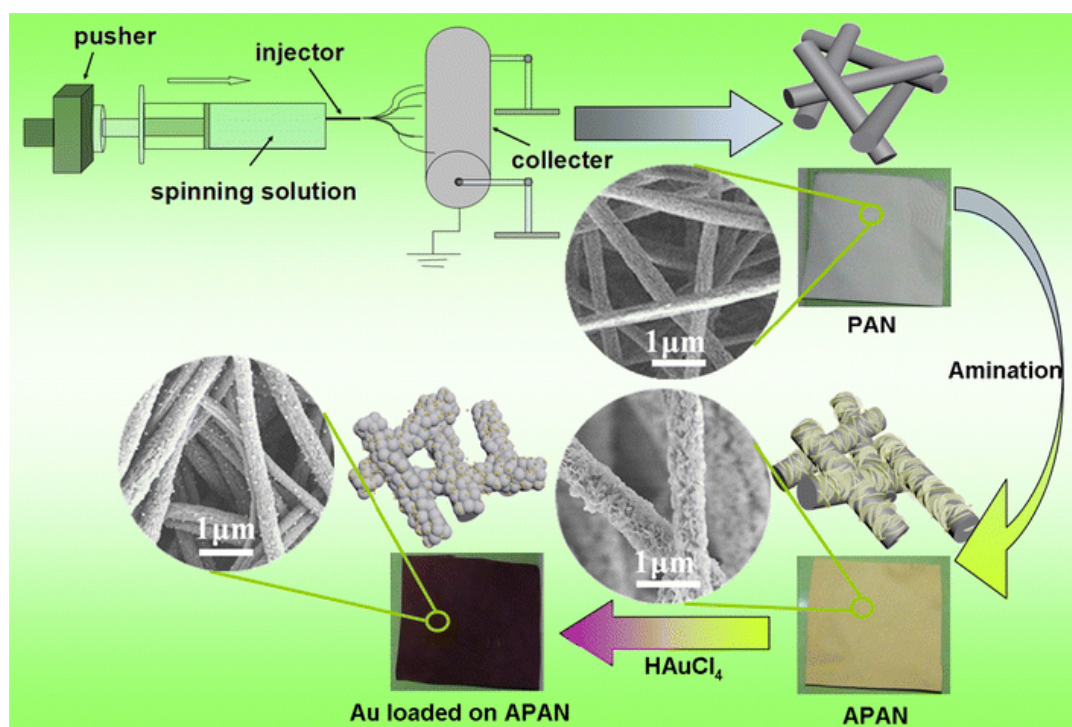
Figure 23: Schematic representation of the preparation of Au-loaded PAN fiber nonwovens. In the first step, electrospinning was used to produce PAN fiber nonwovens. The surface of the nonwovens was aminated in the second step by immersion in diethylenetriamine solution in the presence of sodium carbonate as a catalyst at 90 °C. The immobilization of AuNPs was achieved by immersing the aminated nonwoven in a $HAuCl_4$ solution followed by reduction by irradiation. Reprinted with permission from [88] © 2015 Springer Nature.

Depending on the irradiation type, AuNPs with a size in the range of 6-12 nm were generated within 2-12 h. The smallest AuNPs were formed without light irradiation. In this case, however, the formation of AuNPs took about 12 h. The prepared Au-loaded nonwovens showed good catalytic activity, stability and recycling, but no detailed information is given about the leaching of AuNPs during catalysis. [88]

1.5 Catalytic reactions with metal nanoparticles

As already mentioned in the previous chapter, metal NPs are excellent catalysts for organic reactions due to their high surface-to-volume ratio. Especially AuNPs have high catalytic activity and are therefore used in numerous reactions such as CO oxidation, alcohol oxidation or nitroarene reduction. [89,90] Among the gold-catalyzed reactions, the reduction of nitrophenol compounds is one of the best known and studied Au-catalyzed reactions since nitro compounds are toxic and carcinogenic and the resulting amino products are important precursors for the production of analgesic and antipyretic drugs such as paracetamol. [86,91] Different methods for the degradation of nitrophenols have been investigated, such as photocatalytic degradation, electrochemical methods, microbial degradation, adsorption or oxidation processes. However, these methods each have different drawbacks, whereas the chemical reduction of nitrophenols in aminophenols in the presence of a catalyst is the most promising method. The main advantages of catalytic reduction are low costs and fast and complete conversion to less toxic aminophenols. For that reason, many different catalytic systems were prepared and studied for the reduction of especially 4-NP to 4-AP. Additionally, the reduction of 4-NP in the presence of $NaBH_4$ is an excellent model reaction for testing the catalytic activity of catalyst systems due to the simple reaction control by *in situ* UV/Vis measurements. The reaction can be carried out in an aqueous medium at RT, takes place only in the presence of a catalyst and no further side products are obtained (**Figure 24**).
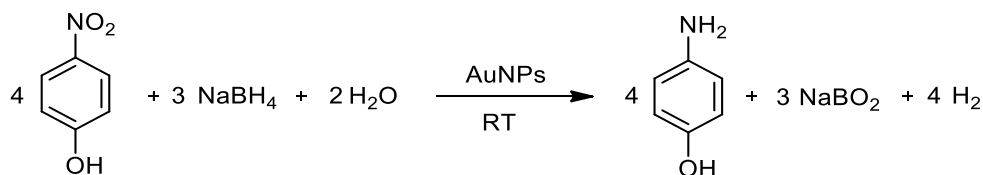
Figure 24: Reaction of 4-NP to 4-AP in the presence of $NaBH_4$ and a AuNP catalyst in an aqueous medium.

By adding $NaBH_4$ to 4-NP, the 4-nitrophenolate ion is formed, which gives the reaction solution a strong yellowish color. The maximum of the absorption band of 4-nitrophenolate appears at a wavelength of 400 nm and decreases over time after the addition of a catalyst. On the other hand, the absorption band of 4-aminophenolate appears at a wavelength of about 300 nm and the absorption increases during successful reduction. The end of the reaction is indicated by the complete disappearance of the absorption peak of 4-nitrophenolate and by a color change from a strongly yellowish to a colorless solution. [91,92] **Figure 25** shows exemplarily a typical time-dependent progress of UV/Vis absorption spectra of 4-NP during reduction to 4-AP.
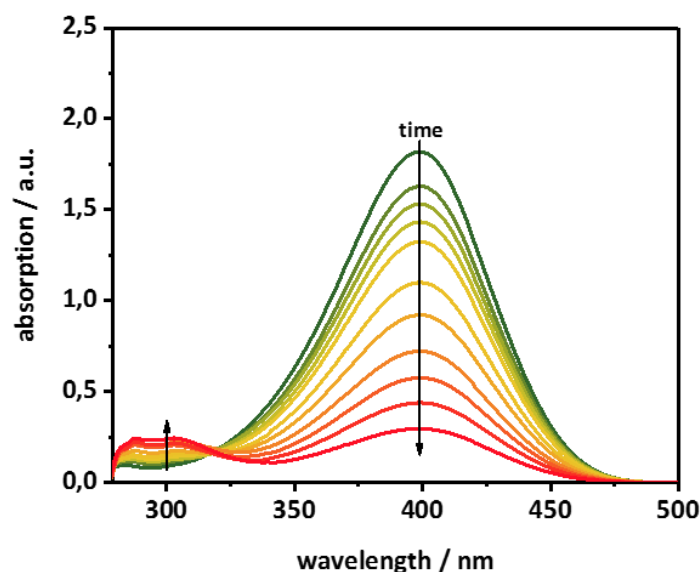
Figure 25: Typical UV/Vis spectra of the reduction of 4-NP (peak at 400 nm) to 4-AP (peak at 300 nm) in the presence of a catalyst and NaBH₄.

In the presence of a large excess of NaBH₄ compared to the concentration of 4-NP and the catalyst, the reduction of 4-NP follows pseudo-first-order kinetics. The following **equations 1-3** describe the progress of the reaction:

$$r = \frac{\partial C_t}{\partial t} = ln\left(\frac{C_t}{C_0}\right) = -k_{app}t \qquad\qquad 1$$

$$r = ln\left(\frac{A_t}{A_0}\right) = -k_{app}t \qquad\qquad 2$$

$$r = ln\left(\frac{A_t}{A_0}\right) = ln\left(\frac{C_t}{C_0}\right) = -k_{app}t \qquad\qquad 3$$

Where r is the rate of reduction, C_t is the concentration of 4-NP at a certain time t, C_0 is the initial concentration at t=0, A_t is the absorption of 4-NP at the time t and A_0 is the initial absorption at t=0. According to **equation 2**, the apparent rate constant k_{app} can be determined directly from the plot $-ln(A_t/A_0)$ against the time t, since the slope of this plot corresponds to k_{app}. Here, the absorption ratio of 4-NP equals the concentration ratio of 4-NP in the reaction medium from the time t to the initial time t=0 (**equation 3**).

Despite numerous investigations and studies, the exact reaction mechanism of 4-NP reduction cannot be fully explained to date. However, most research groups refer to the Langmuir-Hinshelwood adsorption model to explain the reaction mechanism of 4-NP reduction (**Figure 26**). [86,91,93] At the beginning of the reaction, both reactants, 4-NP and NaBH₄, are adsorbed fast to the surface of the AuNPs. Here, the 4-NP molecule is adsorbed as it is, whereas NaBH₄ is converted to the corresponding ion BH₄⁻, which reacts further to B(OH)₄⁻ in the aqueous medium. The adsorption of both reactants is based on an equilibrium process described by the classical Langmuir isotherm. Besides the adsorption

of 4-NP and BH4$^-$ active hydrogen is formed, which is also adsorbed on the AuNP surface and ensures the removal of oxide layers or impurities on the surface of the AuNPs. Due to the formation of gas bubbles during the reaction, the absorption measurements can be hindered, leading to partially incorrect absorption curves. BH_4^{-1} acts as an electron donor transferring an electron to 4-NP via the catalyst surface, where 4-NP acts as an electron acceptor. In the end, 4-NP is converted to 4-AP, which is desorbed from the AuNP surface. However, so far, no report can be found describing the different stages in the conversion of 4-NP to 4-AP. Various studies have shown that the rate constant is increased with a smaller AuNP size and is proportional to the total AuNP surface area. [91,94] Furthermore, functional groups on the NP surface influence the catalytic activity due to a reduction of the active surface area of the AuNPs. [95]
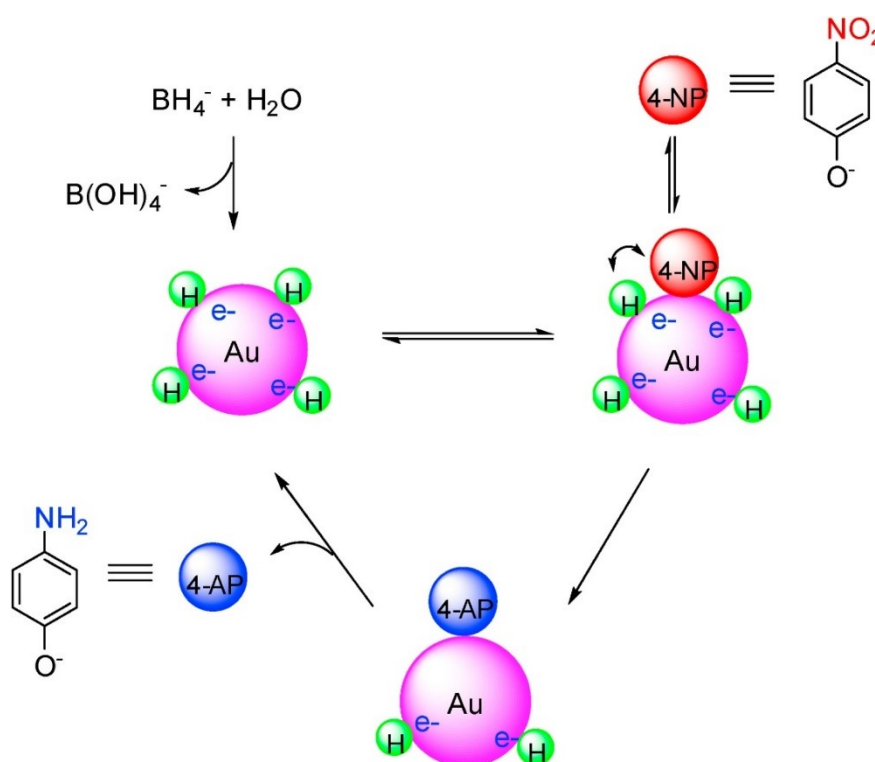
Figure 26: Schematic mechanism of the Langmuir-Hinshelwood model for the reduction of 4-NP to 4-AP catalyzed by AuNPs in the presence of NaBH$_4$ in an aqueous medium. Reprinted with permission from [91] © 2015 Elsevier.

The most important factors in the preparation of an efficient catalyst system are a high catalytic activity, high specific surface area, low amounts of catalyst, easy reusability and recyclability and high stability during reaction or recycling. Catalyst production is therefore very complex and is influenced by a wide range of parameters. To ensure high reaction rates, the specific surface area should be as large as possible. However, aggregation of small AuNPs into larger particles leads to a reduction of the specific surface area due to insufficient stabilization and consequently to a loss of catalytic activity. For that reason, AuNPs are stabilized by different capping agents or are immobilized on various support materials (**chapter 1.4**).

The group of Kitchens compared the catalytic activity of colloidal AuNPs to supported AuNPs for the reduction of 4-NP (**Figure 27**). Citrate-stabilized AuNPs with a diameter of around 6 nm were synthesized using NaBH₄ as a reducing agent. The supported AuNP catalyst was prepared by mixing the prepared colloidal AuNPs with titania at certain pH values.
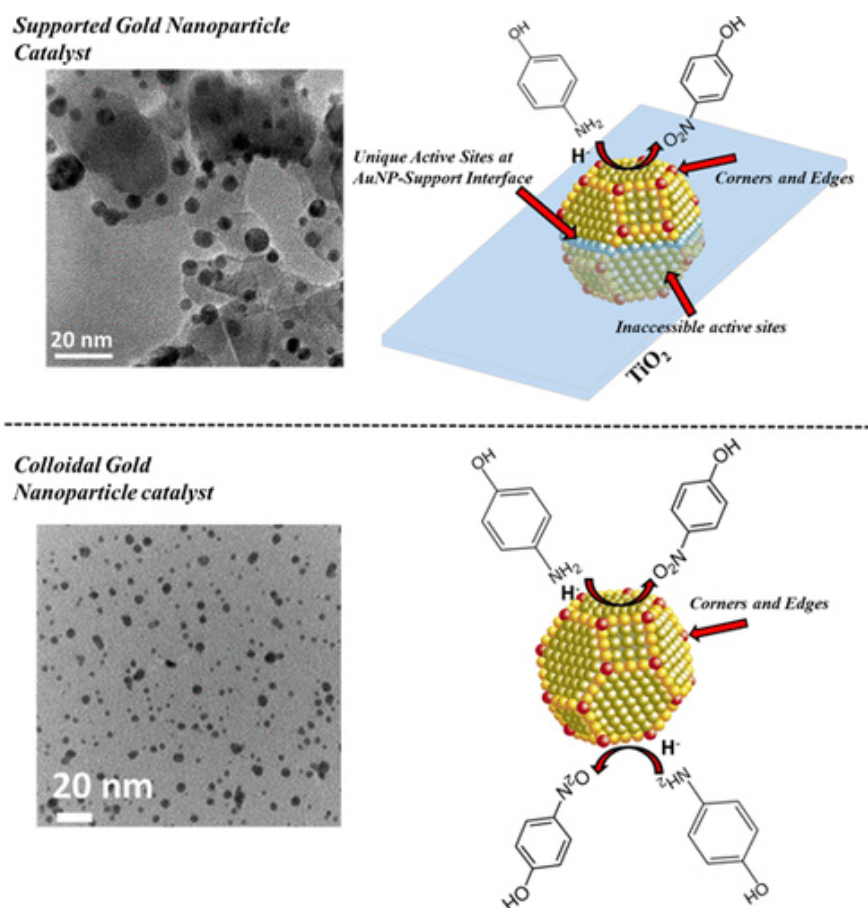
Figure 27: Supported AuNP catalyst in comparison with colloidal AuNP catalyst. Reprinted with permission from [90] © 2018 American Chemical Society.

Using a UV/Vis spectroscopy-based mercaptobenzimidazole (2-MBI) adsorption method, the available surface area of colloidal and supported AuNPs could be quantified. The catalytic activity was determined by turnover frequency (TOF) measurements based on the Au mass and available surface area. Compared to colloidal AuNPs, significantly lower reaction rates for supported AuNPs normalized to Au mass were observed. The available surface area of the AuNPs is reduced by 60 % due to the immobilization on the support material. Annealing the AuNPs, which can be used to remove the stabilizing ligands, leads to even lower reaction rates. During annealing, NPs on the support material grow, reducing the active surface area. Interestingly, in comparison to the colloidal AuNPs, higher TOF values normalized to the surface area were determined for the supported AuNPs. It is assumed that the titania support increases the catalytic activity by active sites at the AuNP-support interface, which is more active than face, corner or edge sites. [90]

Recently, the group of Greiner reported that, contrary to common understanding, the reactivity of smaller AuNPs is not necessarily higher than that of larger AuNPs. Catalytic reduction of 4-NP was carried out with Citrate@AuNPs and PVP@AuNPs of different sizes and under the same conditions keeping the total surface area constant. Interestingly, the reactivity increased with larger AuNP diameters, which could be explained by an increased formation of defects on the surface of larger AuNPs resulting in more active sites. [96] Despite the higher catalytic activity and better selectivity of colloidal NPs, industrially supported NPs are mainly used as catalysts for catalytic reactions since recovery by mechanical processes, such as filtration or centrifugation and reusability, is much easier than with colloidal NP. [90] A support material also provides better catalyst stability and tends to avoid leaching of AuNPs. [86]

Rossi et al. investigated the role of stabilizing ligands of colloidal AuNPs on the catalytic properties. The capping agents can strongly influence the catalytic activity of NPs, which is why the ligands must be specifically selected for catalysis or should be avoided as far as possible. Basically, ligands adsorbed on a metal surface reduce the catalytic activity due to electrostatic or steric shielding effects. The reactants are less able to be adsorbed and converted at the catalytically active sites. [66] Various studies have shown that strong binding ligands, such as thiol ligands, stabilize the NPs better but reduce the catalytic activity more than weak ligands, such as sodium citrates, amines or alkylammonium salts. [97,98] However, there are also examples where capped NPs are catalytically more active than naked NPs or are less active at the beginning but remain active for a longer time. [99–101] Often, stabilizing ligands partially remain on the NP surface after immobilization on support resulting in a loss of activity. [102,103] However, through the formation of a passivation layer, stabilizing ligands can also improve the catalytic performance through steric and electronic effects and influence the selectivity (**Figure 28**). [66,100] Various studies have shown that capping agents also play a significant role in the selectivity of catalysis. [100] The stabilizing ligands can act as a bridge between the reactants and the active sites of the NPs.
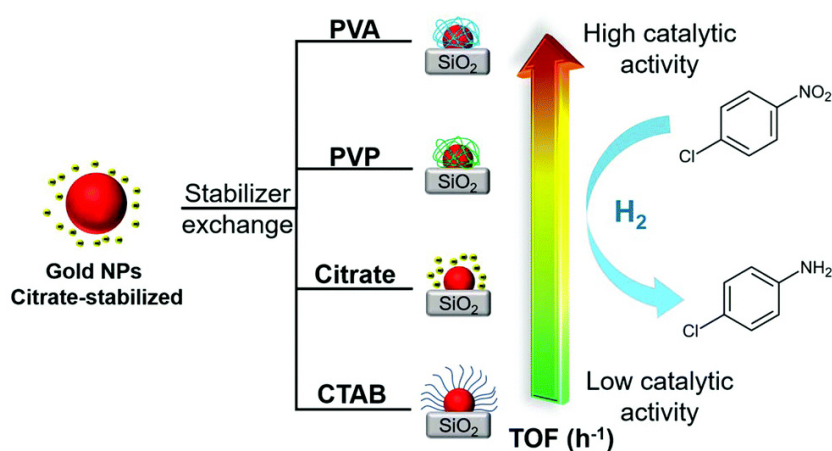

Figure 28: Substitution of stabilizing ligands and their influence on the catalytic activity of the AuNPs supported on SiO$_2$. Reprinted with permission from [66] © 2018 Royal Society of Chemistry.

Zhong et al. investigated the exchange of citrate-stabilized AuNPs by PVA, PVP and cetyltrimethylammonium bromide (CTAB) and the influence on the catalytic performance of the hydrogenation of *p*-chloronitrobenzene and cinnamaldehyde. [104] Citrate-stabilized AuNPs can be substituted by PVP, PVA or CTAB rapidly since the citrate anion is a weak stabilizing ligand for AuNPs. In contrast to the ligand exchange with PVP or PVA, the AuNP diameter was increased during the exchange with CTAB, indicating a relatively weak stabilization of AuNPs by CTAB. After immobilization of AuNPs on SiO_2, the catalytic activity of the supported AuNPs was investigated. For the reduction of *p*-chloronitrobenzene, the highest activity of AuNPs was observed with polymer capping ligands (PVA or PVP). However, for the hydrogenation of cinnamaldehyde, the highest catalytic activity of AuNPs with citrate ligands was achieved. This shows that the influence of the ligands on the catalytic activity of each reaction can be different. Steric hindrance or modification of the electronic structure of the catalytically active AuNP sites ensures the different catalytic activities. [104]

When immobilizing colloidal AuNPs on a support with functional groups, the stabilizing ligand can be replaced by the functional groups on the support surface stabilizing the AuNPs. However, it cannot be determined exactly to what extent the stabilizing ligand is replaced. [66,105] Instead of colloidal AuNPs, *in situ* AuNPs can be formed on the support surface, which are stabilized by the functional groups of the support material. This avoids using additional stabilizing ligands during the synthesis of colloidal AuNPs. [88] To conclude, there are many different possibilities to prepare catalyst systems. However, there still exist some challenges regarding fast and complete conversion of 4-NP to 4-AP, recovery and reusability of the catalyst and the prevention of leaching of AuNPs from the support during catalysis.

2 Aim and Motivation

Supramolecular chemistry provides the opportunity to create defined self-assembled nanofibers via a bottom-up approach. In particular, 1,3,5-benzenetrisamides (BTAs) are a well-known class to achieve supramolecular nanofibers by self-assembly into columnar structures driven by three directed hydrogen bond strands. Functionality of the BTAs can be achieved via the surface of the supramolecular nanofiber by selecting appropriate peripheral substituents. Thus, BTAs with tailored functional substituents are promising candidates, for example, for the immobilization of metal nanoparticles (NPs). Pyridine and terpyridine derivatives are well-known ligands to allow for the complexation of metal NPs. However, less is known about pyridine- and terpyridine-substituted BTAs and their self-assembly behavior to supramolecular nanofibers, particularly in view of the immobilization of NPs and their use in catalytic applications.

Therefore, the objectives of this thesis, as illustrated in **Figure 29**, are the syntheses and characterization, to the most part novel functional BTAs carrying pyridine or terpyridine moieties and the investigation of their self-assembly into supramolecular nanofibers. Structure-property relations with respect to their self-assembly behavior should be explored. In particular, emphasis is given on the preparation of stable and shape-persistent structures based on functional microfiber-nanofiber composites. Their use to immobilize metal NPs on the functional BTA nanofibers surface for catalytic applications will be explored.

From molecular design to supramolecular nanofibers to functional composites to applications

I. Synthesis, characterization and self-assembly of BTAs with pyridine and terpyridine substituents

II. Functional microfiber-nanofiber composites

III. Immobilization of AuNPs on functional supramolecular nanofibers and

IV. Use in catalytic applications
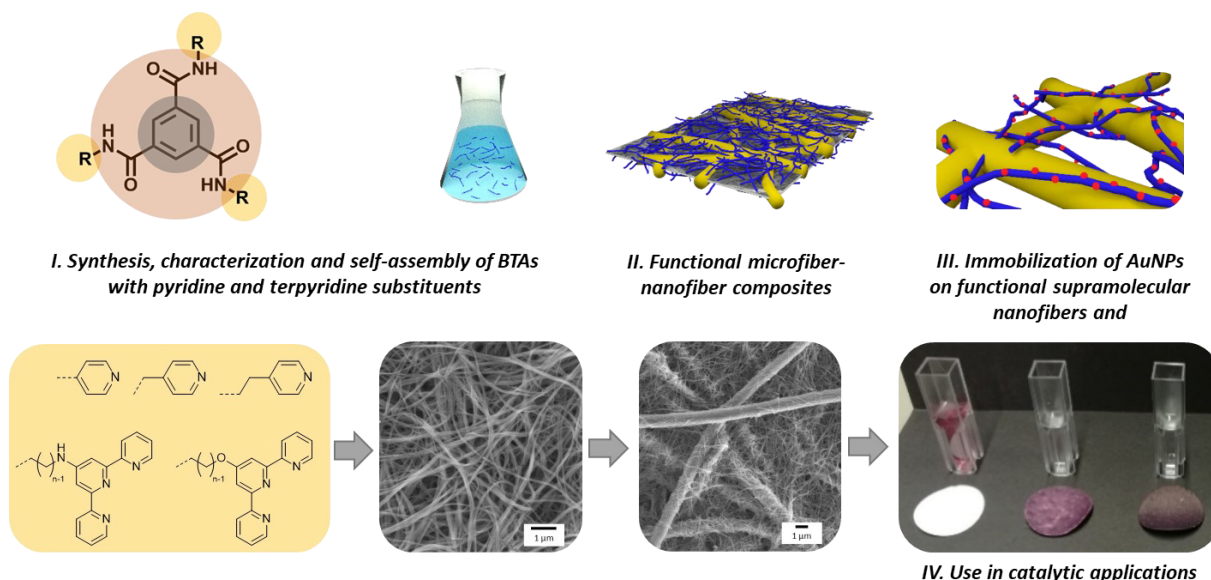
Figure 29: This thesis is divided into four objectives dealing with (**I**) the synthesis and characterization as well as self-assembly studies of pyridine- and terpyridine-substituted 1,3,5-benzenetrisamides to supramolecular nanofibers, (**II**) the preparation of stable, functional microfiber-nanofiber composites and (**III**) the immobilization of metal NPs and ions on the BTA nanofibers and (**IV**) their use in catalytic applications.

Synthesis, characterization and self-assembly of 1,3,5-benzenetrisamides with pyridine and terpyridine substituents

In the first part, a series of BTAs with pyridine or terpyridine moieties will be synthesized and characterized to study the influence of molecular design on thermal properties, solution and self-assembly behavior. This approach includes the variation of the number of pyridine and terpyridine substituents in the BTA molecule and the length and type of the spacers between the core unit and the peripheral pyridine or terpyridine substituents. In particular, the aim is to understand how solubility and self-assembly are influenced by the different numbers and types of peripheral substituents and spacers. Suitable BTAs will be investigated in view of varying the processing conditions for self-assembly from solution, which are expected to be applied as functional supramolecular BTA nanofibers featuring a high chemical and thermal stability under different applications conditions to be used for the immobilization of metal NPs and in catalytic reactions. Especially, small nanofiber diameters are desirable to generate a large surface area with a high density of functional groups. Therefore, the fundamental question is how pyridine- and terpyridine-containing BTAs should be designed to generate supramolecular nanofibers with small diameters by self-assembly from solution.

Functional microfiber-nanofiber composites

The second part deals with the preparation of functional fiber composites based on support polymer microfibers and functional supramolecular BTA nanofibers with pyridine and terpyridine substituents. Such a combination shall allow for the preparation of composite materials with sufficient mechanical stability for different applications. For that reason, it should be investigated how mechanically stable and shape-persistent functional microfiber-nanofiber composites can be prepared. Two different approaches, the *in situ* formation of functional BTA nanofibers within polymer fabrics as well as the preparation of compact composite nonwoven sheets by the wet-laid technique, will be investigated. The first approach was applied in previous works with non-functionalized BTA nanofibers and shall be transferred to functional BTAs. In particular, emphasis is given to a wet-laid process combining electrospun short polymer fibers and functional supramolecular BTA nanofibers. In this context, this process will be carried out for the first time. Here, the influence of various parameters such as the BTA concentration, ratios of polymer and BTA fibers, as well as the process conditions on the morphology and stability of the compact fiber composites will be investigated and characterized by several methods such as scanning electron microscopy or tensile tests. Particular attention will be paid to the extent to which the supramolecular BTA nanofibers influence the mechanical properties of the prepared polymer microfiber/supramolecular nanofiber composites.

Immobilization of metal nanoparticles and ions on functional supramolecular nanofibers

An application of these composite materials shall be investigated and discussed in the third part of the thesis. For this, gold nanoparticles (AuNPs) or ions will be immobilized on the surface of the supramolecular BTA nanofibers. So far, only very few systems based on supramolecular nanofibers are known that can efficiently immobilize metal NPs. The main question is how effective and stable functional supramolecular BTA nanofibers can act as AuNP carrier. Various influences on the immobilization of AuNPs on the fiber surface have not yet been fundamentally investigated. Three different techniques (immersion, filtration and *in situ* formation) to fix AuNPs or Au ions on the surface of the functional supramolecular nanofibers will be explored and compared with each other. Besides the spatial distribution of the AuNPs on the fiber surface, the maximum loading capacity on the nanofibers and the NP leaching behavior shall be investigated using various characterization methods such as scanning electron microscopy (SEM), energy-dispersive X-ray spectroscopy (EDX), transmission electron microscopy (TEM) or inductively coupled plasma optical emission spectrometry (ICP-OES). By varying the parameters, the aim is to determine which parameters and to what extent the immobilization of AuNPs on the surface of the functional BTA nanofibers is influenced.

Functional supramolecular nanofibers and their use in catalytic applications

The functionality of the Au-loaded composite nonwovens shall be demonstrated as an example for the catalytic reduction of 4-nitrophenol as a model reaction. Fundamental experiments shall help to answer whether Au-loaded supramolecular BTA nanofibers can be used as a catalytically active system and how the corresponding Au-loaded composite nonwovens perform in 4-nitrophenol reduction compared to other Au-loaded fiber-based catalytic systems. Therefore, the composites shall be tested and compared both in a discontinuous but also in a technically more relevant continuous manner. The catalytic performance will be investigated mainly with respect to the influence of the composite components as well as the different NP systems. In particular, the question of whether the composites can be reused several times without losing catalytic activity plays a decisive role. Therefore, the reusability of the composites will be verified by several catalysis cycles. In addition, ICP-OES measurements will be used to check the leaching behavior of the AuNP during catalysis.

3 Synthesis, characterization and self-assembly of 1,3,5-benzenetrisamides with pyridine and terpyridine substituents

BTAs are a well-known class of small molecules, which are highly suited for the preparation of supramolecular nanofibers by a fast and straightforward bottom-up process, i.e., the self-assembly from solution. By selecting tailored peripheral substituents of the BTAs, different properties and specific functionalities can be generated, enabling the use of BTAs in various areas, such as the immobilization of metal NPs. Numerous suitable chemical groups with heteroatoms such as nitrogen or sulfur for the immobilization of metal particles can be found in literature. In particular, peripheral substituents with specific anchor groups such as pyridines or terpyridines shown in **Figure 30** allow for the complexation of metal particles or ions quickly and easily since pyridines and terpyridines are well-known coordination or chelating ligands for metals.
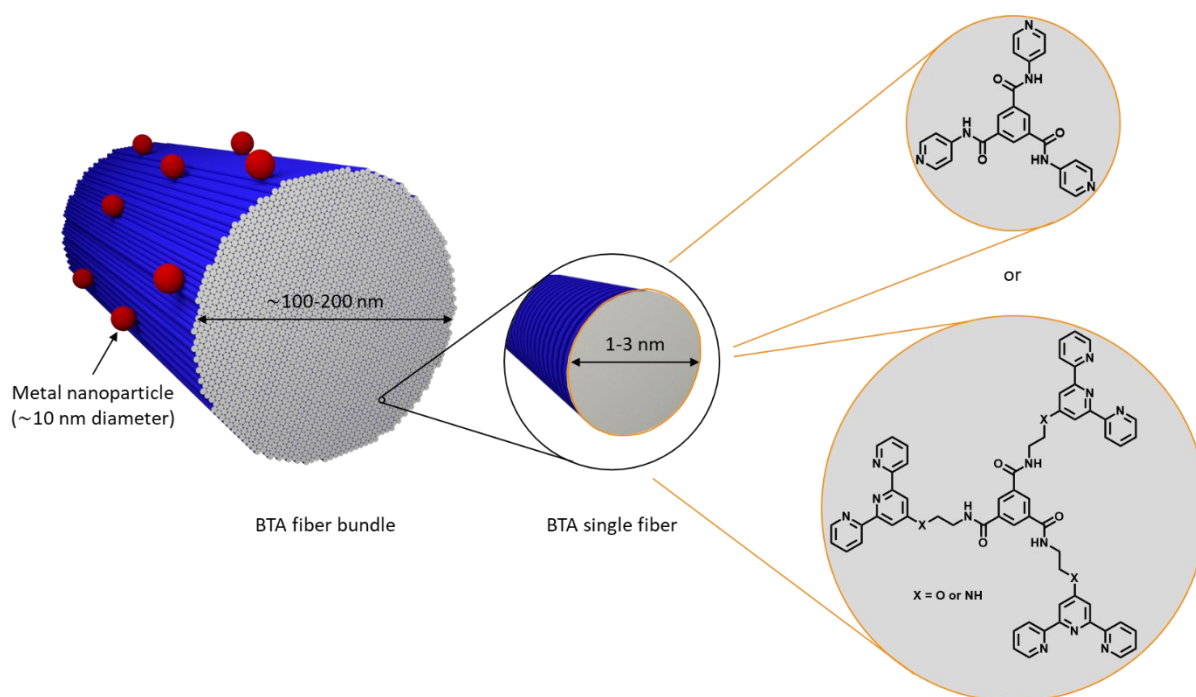
Figure 30: Schematic representation of a BTA fiber bundle (blue) with adsorbed metal nanoparticles (red). The BTA fiber bundle has a diameter of about 100-200 nm and consists of numerous BTA single fibers, which in turn are formed from single pyridine-containing BTA or terpyridine-containing BTA molecules with a diameter of about 1-3 nm. Both BTAs have a central benzene core and three amide units, which allow the formation of hydrogen bonds with adjacent BTA molecules. The peripheral functional substituents such as pyridine or terpyridine can interact with metal NPs.

Over the last 25 years, a couple of BTAs with pyridine or terpyridine substituents were published. [28,106-112] However, no comprehensive and comparative studies have been carried out so far regarding the thermal properties as well as the self-assembly behavior of different pyridine- or terpyridine-containing BTAs, which will be discussed in more detail in this chapter. The following pyridine- or terpyridine-containing BTA can be found in literature.

45

1,3,5-Benzenetrisamides with pyridine substituents in literature

The first pyridine-functionalized BTA *N,N',N''*-tris(4-pyridylmethyl)benzene-1,3,5-tricarboxamide shown in **Figure 31** was reported in 1996. [113] This BTA exhibits a methylene group inserted as a spacer between the amide group and the peripheral pyridine substituent. So far, this BTA has been used, among others, as a ligand for the preparation of octahedral nanocages [114–116] and in combination with differently substituted isophthalic acids for the preparation of Cd[II] coordination polymers, which can form either a 3D network or a 1D chain structure. [117]
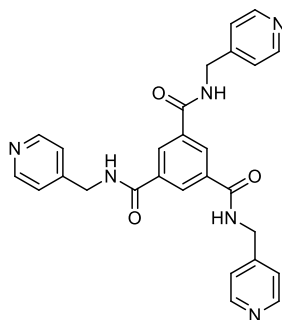
Figure 31: Chemical structure of the first published pyridine-containing BTA *N,N',N''*-tris(4-pyridyl-methyl)benzene-1,3,5-tricarboxamide.

N,N',N''-tri(pyridine-3-yl)benzene-1,3,5-tricarboxamide and *N,N',N''*-tri(pyridine-4-yl)-benzene-1,3,5-tricarboxamide shown in **Figure 32** are two further literature-known pyridine-containing BTAs, which only differ in the position of the nitrogen atom within the pyridine ring. The latter of the two BTAs is the most-published BTA with pyridine substituents so far. Both BTAs are insoluble in water but can be dissolved in mixtures of H_2O and organic solvents such as DMSO, DMF or MeOH, act as efficient hydrogelator and self-assemble into fibrous structures. [28]

Figure 32: SEM micrographs of xerogels obtained from a MeOH/H$_2$O mixture for (**A**) *N,N',N''*-tri(pyridine-4-yl)benzene-1,3,5-tricarboxamide (0.2 wt%) and (**B**) *N,N',N''*-tri(pyridine-3-yl)benzene-1,3,5-tricarboxamide (0.1 wt%). Adapted and reprinted with permission from [28] © 2004 American Chemical Society.

A further study reported that the single-crystal structure of *N,N',N''*-tri(pyridine-4-yl)-benzene-1,3,5-tricarboxamide depends strongly on the solvent in which the BTA was recrystallized. This BTA has the tendency to include solvent molecules, p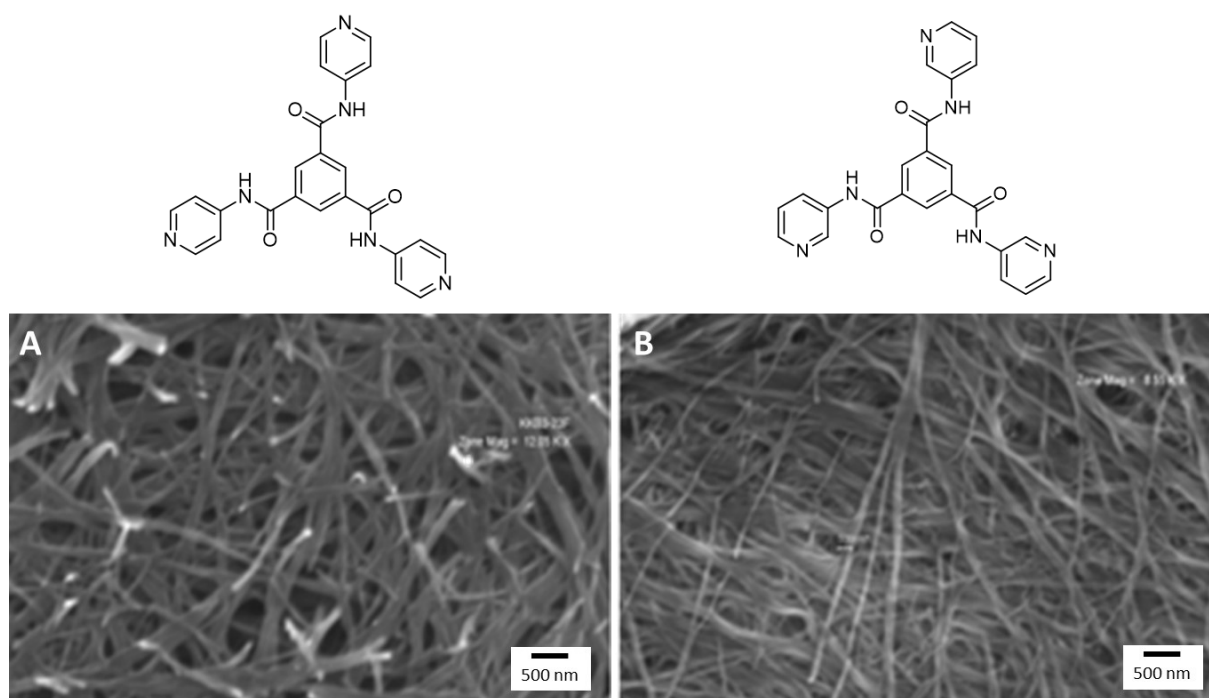referably water, into the crystal lattice. [112] Different groups reported about this BTA as a tridentate bridging ligand in MOFs [118] or hydrogen-bonded organic frameworks (HOFs). [107,108,119] The group of Zhong, for example, reported a very stable HOF based on this BTA, which can be used for the selective adsorption of gases (CO$_2$) and liquids (benzene). Here, one molecule of the BTA forms hydrogen bonds to three adjacent molecules via the amide bonds and the pyridine substituents, thus forming a 2D supramolecular honeycomb-like structure. The adjacent layers were held together by additional π-π interactions so that a 3D microporous structure with a pore size of 6.8 Å x 4.5 Å is obtained. [119] Further application of *N,N',N''*-tri(pyridine-4-yl)-benzene-1,3,5-tricarboxamide is as a fluorescence color-tunable photoluminescence material in combination with rare earth metal ions [109], as detector and adsorber of aldehydes [120] as well as a multi-functional stimulus-responsive fluorescent hydrogel in combination with naphthalimide derivatives. [110,121]

1,3,5-Benzenetrisamides with terpyridine substituents in literature

In contrast to the pyridine substituents, terpyridine ligands exhibit three electron-poor pyridine heterocycles, which are linked to each other via freely rotatable σ-bonds in the respective 2 or 2 and 5 positions of the pyridine groups. Due to the electron deficit of the pyridine rings, metal centers with high electron density form particularly strong complexes with terpyridine ligands.

So far, only two terpyridine-containing BTAs, which differ by the utilized C3 and C8 spacer between the amide moieties and the peripheral terpyridine substituent, were reported in literature, as shown in **Figure 33**.
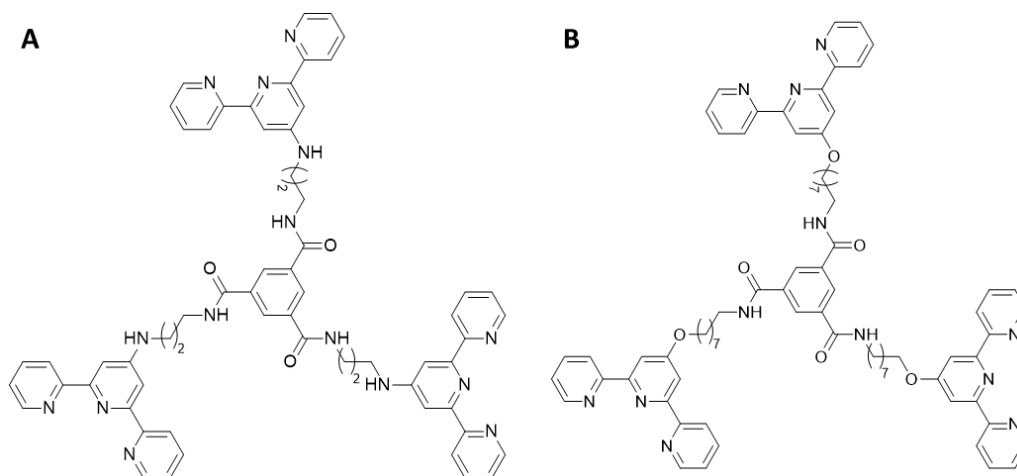
Figure 33: Chemical structure of (**A**) N^1,N^3,N^5-tris(2-([2,2':6',2''-terpyridin]-4'-ylamino)propyl)benzene-1,3,5-tricarboxamide and (**B**) N^1,N^3,N^5-tris(8-([2,2':6',2''-terpyridin]-4'-yloctyl)-benzene-1,3,5-tricarboxamide.

One of these terpyridine-containing BTAs is N^1,N^3,N^5-tris(2-([2,2':6',2''-terpyridin]-4'-ylamino)-propyl)benzene-1,3,5-tricarboxamide, which exhibits a C$_3$-symmetrical central core unit and can self-assemble into helices due to the formation of threefold hydrogen bonds between the amide moieties of adjacent BTA molecules. In 2012, this BTA was reported first acting as a tripodal ligand. Using a 7:3 mixture of H$_2$O/MeOH, gel formation of this BTA was observed. Dried samples of the gel showed a fibrous structure of the BTA with intertwining bundles of strings. A fiber diameter of around 20 nm was determined from TEM micrographs. In the presence of EuCl$_3$, this BTA forms luminescent supramolecular gels, where Eu^{III} ions coordinate to the terpyridine unit, as shown in **Figure 34**. [122]
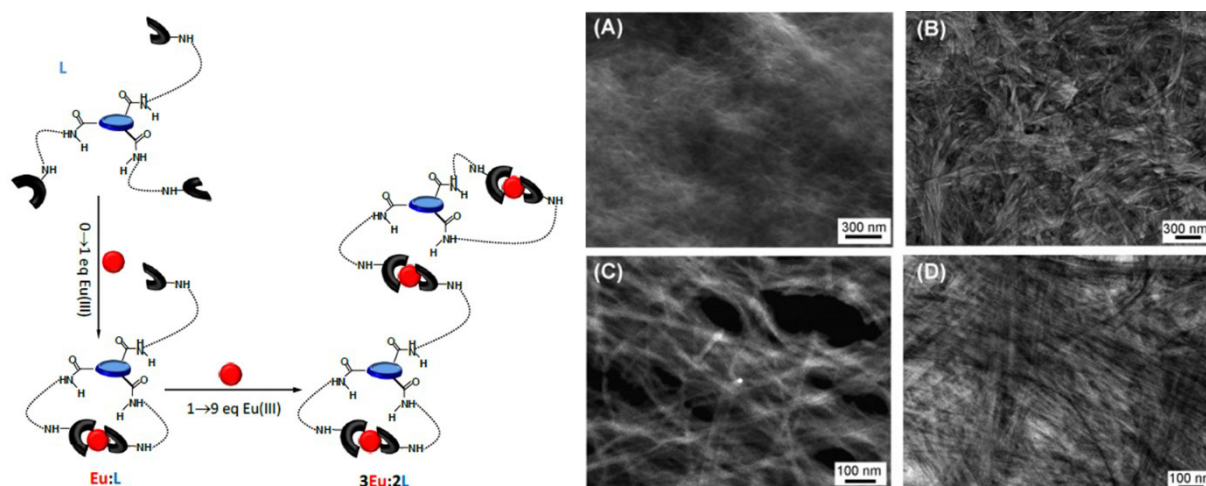
Figure 34: Schematic representation of the formation of a supramolecular 1:1 and 3:2 EuCl$_3$-N^1,N^3,N^5-tris(2-([2,2':6',2''-terpyridin]-4'-ylamino)-propyl)benzene-1,3,5-tricarboxamide (**BTA**) species in solution depending on the equivalents of Eu^{III} (left) and SEM micrographs of (**A**) **BTA** and (**B**) a gel of EuCl$_3$ and **BTA** as well as HAADF STEM micrographs of (**C**) **BTA** and (**D**) a gel of EuCl$_3$ and **BTA**. Adapted and reprinted with permission from [122] © 2012 Wiley-VCH.

For this, different molar ratios of the BTA and EuCl$_3$·6H$_2$O were mixed in MeOH/H$_2$O (95:5) mixtures resulting in a stable and highly transparent gel upon evaporation of the solvents. Even higher-structured fibrous areas were found in the case of a gel consisting of EuCl$_3$ and the BTA. The higher stability of the gel with EuCl$_3$ was observed since Eu^{III} ions act as a supramolecular "glue", and single supramolecular strands are connected together due to the coordination to Eu^{III}. [122]

In further studies, it was shown that N^1,N^3,N^5-tris(2-([2,2':6',2''-terpyridin]-4'-ylamino)-propyl)benzene-1,3,5-tricarboxamide can form 3D supramolecular metallogels with different metals like Fe(II), Cu(II) or Zn(II) [123], can be used as a template for the growth of salt nanowires [124] or achiral AuNPs with different sizes and helical order on supramolecular nanofibers [125]. **Figure 35** shows the formation of a supramolecular gel based on this BTA and a chiral compound (trimesoyltri D-alanine or trimesoyltri L-alanine). After the addition of Au(I) ions to the preformed gel of the BTA and the chiral compound, AuNPs were obtained by UV reduction of the Au(I) ions via UV irradiation. Here the anionic carboxylate groups of the chiral compound serve as templates for Au(I) ions. The formation of helical nanofibers and thus the possibility to get the spatial arrangement of the AuNPs on the helical nanofiber surface is achieved due to the presence of the chiral compound. The helical structure is driven by the formation of strong interlayer hydrogen bonds between the carbonyl and amine groups.
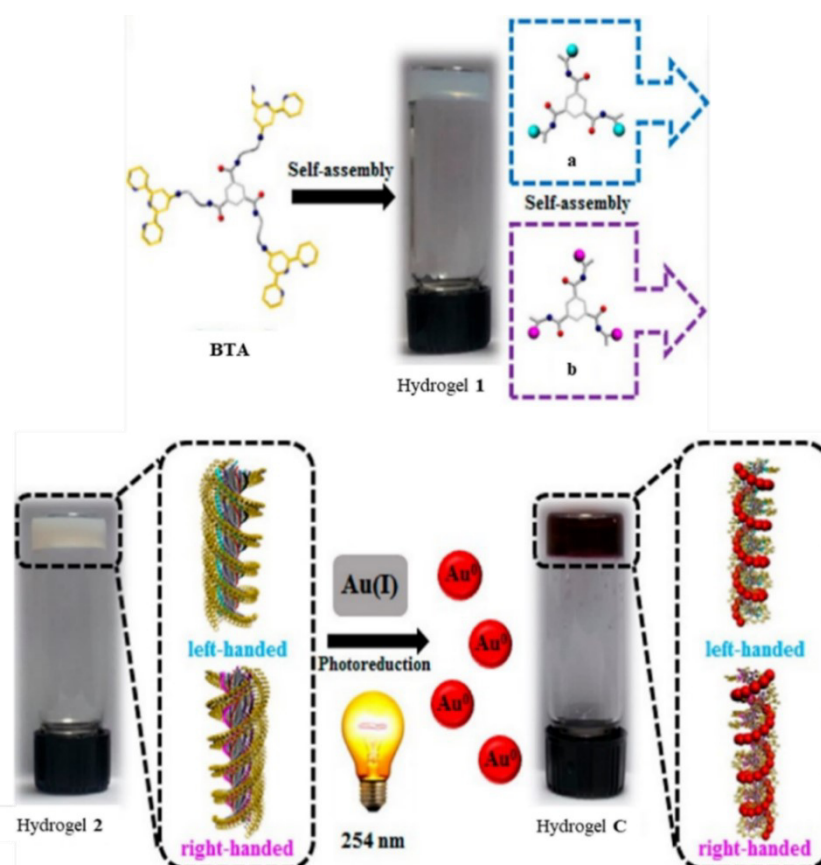
Figure 35: Hydrogel formation obtained by controlled self-assembly of nanofibers with tunable helicity by addition of a chiral compound (**a** or **b**) to N^1,N^3,N^5-tris(2-([2,2':6',2''-terpyridin]-4'-ylamino)-propyl)benzene-1,3,5-tricarboxamide (**BTA**) and further addition of Au(I) followed by UV photo-irradiation to generate helical AuNP superstructures. Adapted and reprinted with permission from [125] © American Chemical Society.

Additionally, the BTA shows interesting fluorogenic and sensing properties and can be used as a chemoprobe for metal ions. Depending on the choice of the solvent or metal ions, the emission of the BTA can be tuned in solution due to different aggregation behaviors of the BTA molecules. [126]

The other terpyridine-containing BTA found in literature, the N^1,N^3,N^5-tris(8-([2,2':6',2''-terpyridin]-4'-yloctyl)benzene-1,3,5-tricarboxamide (**Figure 33B**) was shown to form a lanthanide coordination polymer. [127] Here, the terpyridine unit acts as a lanthanide sensitizer for Eu^{3+} and Tb^{3+} and as blue-emitting material. The emission color of the lanthanide coordination polymer can be tuned by varying the molar ratios of Eu^{3+}/Tb^{3+} and by changing the excitation wavelength. This system can also be used as a highly selective luminescent anion senor for $H_2PO_4^-$. [128]

The current literature survey demonstrated that there is some information about a few pyridine- and only two terpyridine-containing BTAs, which can be used for different applications. A comprehensive and comparative study on the class of pyridine- or terpyridine-containing BTAs to evaluate the use of this class, in general, is not performed so far. This includes, in particular, a straightforward study with respect to the molecular design covering the variation of the number of pyridine substituents in the BTA molecule and of different spacer lengths and types. Apart from the

structural variation, especially the self-assembly behavior from solution should be investigated. For this purpose, a library of BTAs with pyridine and terpyridine substituents shown in **Figure 36** was created by synthesizing and subsequently characterizing them.

The synthesized BTAs were divided into four groups, which particular differ by the number of pyridine substituents used (Group I-III), and the number of terpyridine substituents, i.e., the three times use of terpyridine substituents instead of pyridine ones (Group IV). In detail, the BTAs in the first group (**3a-c**) based on benzene-1,3,5-tricarbonyl acid all have three pyridine substituents each and differ only in the length of the alkyl spacer between the amide and pyridine moieties. The second group shows BTAs (**9a-c**) based on 5-nitroisophthalic acid with two pyridine substituents and one aliphatic substituent compared to group III with BTAs (**16a-c**) based on 3,5-dinitrobenzoyl acid carrying one pyridine and two aliphatic substituents. Group IV includes BTAs based on benzene-1,3,5-tricarbonyl acid with terpyridine substituents, which have different lengths through an alkylamine (**21a-c**) or alkoxy spacer (**24a-e**).

I. BTAs with **three pyridine** substituents
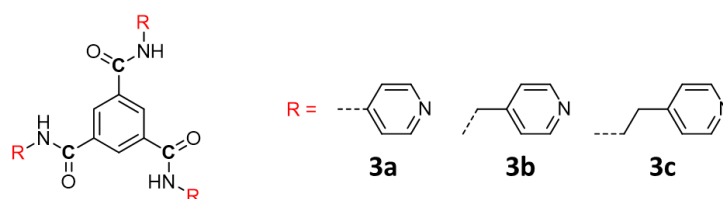
II. BTAs with **two pyridine** substituents
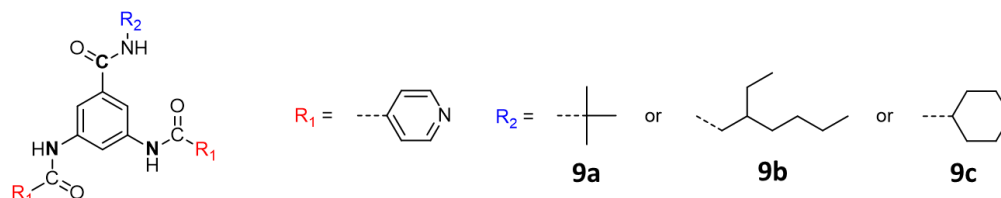
III. BTAs with **one pyridine** substituent

IV. BTAs with three **terpyridine** substituents

Figure 36: Overview of all pyridine- and terpyridine-substituted BTAs studied in this work.

3.1 Benzenetrisamides with pyridine substituents

3.1.1 Benzenetrisamides with three pyridine substituents

The first group investigated here comprises three different BTAs **3a-c** with three pyridine substituents and alkyl spacers of different lengths between the amide and pyridine unit. **3a** is al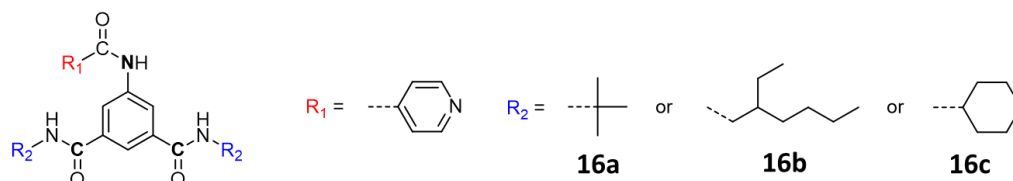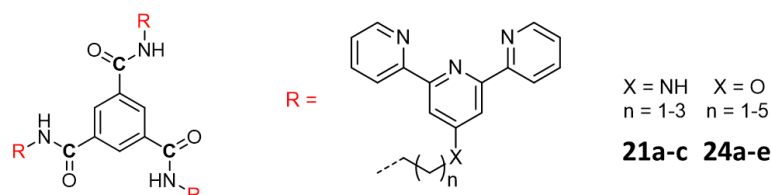ready described in literature. It was also fundamentally characterized and investigated with respect to self-assembly behavior from solution as part of the doctoral thesis of Hannes Welz (Macromolecular Chemistry I, University of Bayreuth). The synthesis of **3b** has also been described in literature, whereas **3c** was synthesized for the first time in this work. For both **3b** and **3c**, there is no information about the self-assembly behavior from solution. The aim of the investigations is to find out what influence the systematically varied molecular structure of **3a-c** has on the thermal properties, solubility and self-assembly behavior. Can the incorporation of an alkyl chain spacer between the amide moiety and the peripheral pyridine substituent cause the BTA to form columnar structures? To answer these questions, two BTAs (**3b** and **3c**) with one and two methyl groups between the amide and pyridine units are investigated, in addition to the BTA without an alkyl spacer (**3a**).

3.1.1.1 Synthesis and characterization

For a comparative investigation, **3a-c** had to be synthesized first. Therefore, we have synthesized new compounds and revisited the literature-known syntheses. The syntheses of **3a-c** were carried out by Jutta Failner and Sandra Ganzleben (Macromolecular Chemistry I, University of Bayreuth) under my supervision. **3a** and **3b** were synthesized in an analogous manner as described in literature, whereas **3c** was synthesized for the first time. The characterization of **3a-c** was performed by myself.

3a-c can be prepared in a general synthetic approach that is the amidation reaction according to standard literature procedures. In detail, the BTAs (**3a-c**) were obtained by the reaction of 1,3,5-benzenetricarboxylic acid chloride (**1**) with the corresponding amine derivative (**2a-c**). The amine was used in slight excess to ensure a complete substitution of the core unit. THF was used as solvent and triethylamine was used as acid scavenger. The general synthetic route is shown in **Scheme 1**.
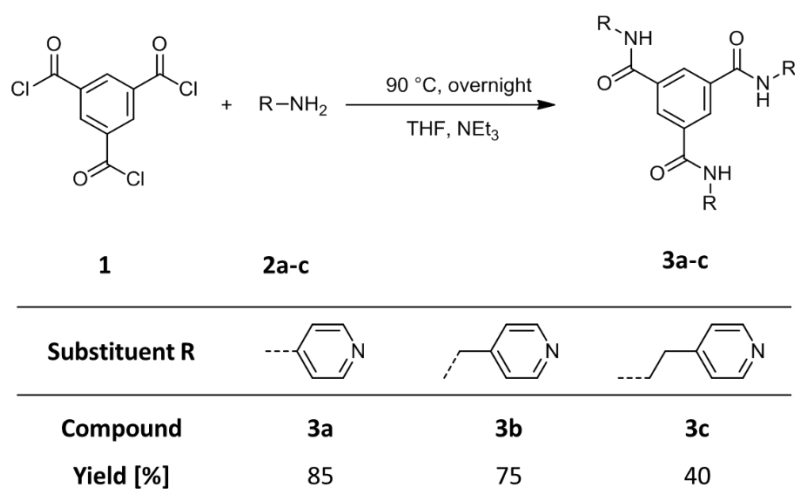
Scheme 1: Synthetic route to **3a-c** by conversion of 1,3,5-benzenetricarboxylic acid chloride **1** with the respective amine derivative **2a-c** in THF and triethylamine.

Purification of **3a-c** was performed by recrystallization or boiling in different solvents. Detailed information on synthesis and purification is described in the experimental part (**chapter 7**). The yields after purification of **3a** and **3b** were significantly higher at 85 % and 70 %, respectively, in contrast to the yield of **3c** at 40 %, which is probably attributed to more extensive purification steps of the compound. The BTAs were structurally characterized and clearly identified by ^{1}H-NMR spectroscopy, mass spectrometry and FT-IR spectroscopy. Thermal characterization was performed by DSC and TGA measurements.

Molecular characterization

Figure 37 shows exemplarily the ^{1}H-NMR spectrum of **3c** measured in DMSO. The N-H protons of the amide groups can be found at 8.82 ppm as a triplet (**2**). A sharp singlet at 8.47 ppm corresponds to the three protons of the central benzene core (**1**). The protons of the aromatic pyridine substituent can be assigned to the signals at 7.28 ppm (**5,5'**) and 8.34 ppm (**6,6'**). The two protons next to the nitrogen of the pyridine substituent (**6**) are low field-shifted compared to the other two protons of the pyridine substituent (**5**) due to the -I effect of the nitrogen atom. For the same reason, the methylene protons next to the amide moiety at 3.56 ppm (**3**) are also low field-shifted compared to both protons next to the pyridine substituent (signal **4,** 2.89 ppm). Full substitution of the trimesic acid trichloride was confirmed by the integration ratio of signals **1** and **3**. The clear assignment and absence of other signals allow for unambiguous identification of compound **3c** in high purity. **3a** and **3b** were evaluated and identified in the same manner. Their spectra are shown in **Figure 134** and **Figure 135**.
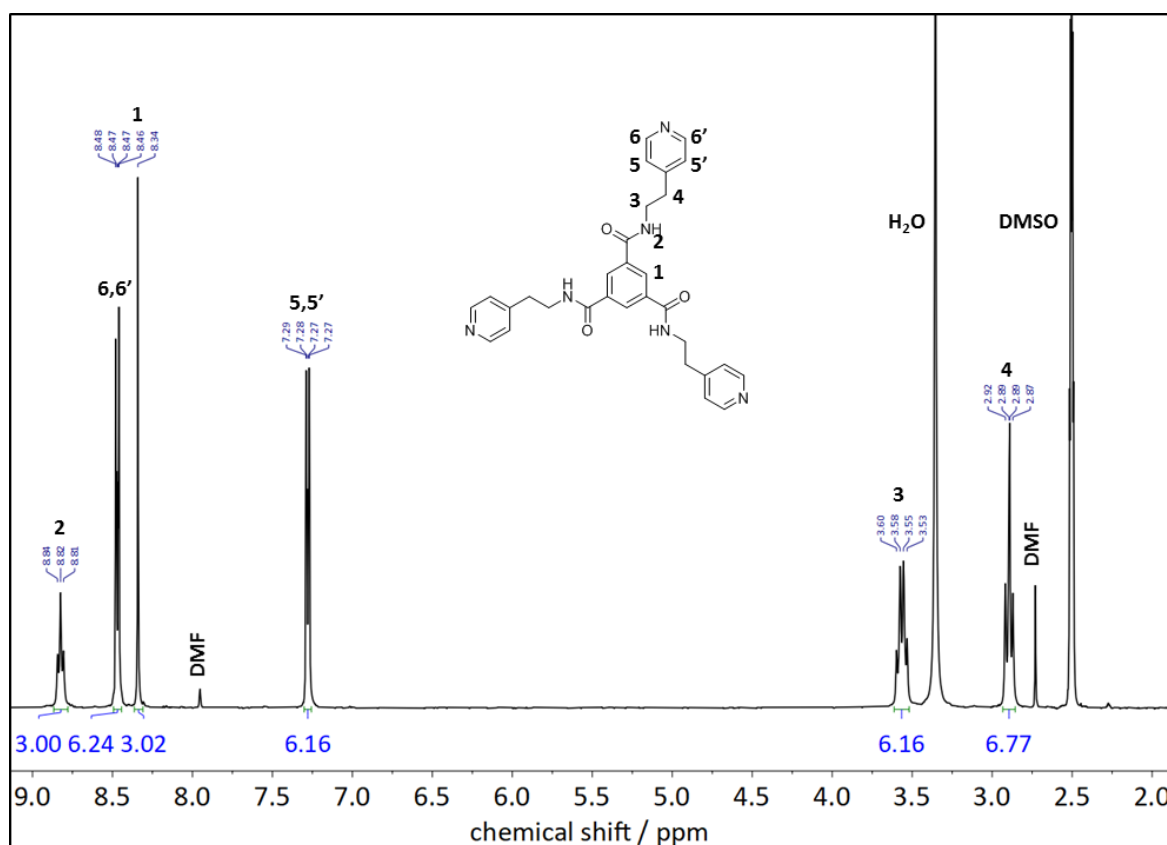
Figure 37: ^{1}H-NMR spectra of **3c** measured in deuterated DMSO. The signals were assigned to the corresponding hydrogen atoms according to the chemical structure of **3c**.

Investigation of hydrogen bonding interactions by FT-IR spectroscopy

In general, BTAs are well-known to form highly defined and directed hydrogen bonds due to the three amides into a columnar arrangement of the molecules with a threefold hydrogen bond pattern. Therefore, FT-IR spectroscopy is a simple but efficient method to study the formation of hydrogen bonds due to distinct shifts in IR absorption bands. According to Stals et al., defined FT-IR vibrations indicate the formation of hydrogen bonds resulting in a columnar structure of BTA compounds.[27] The N-H stretching vibration at a wavenumber of ~3240 cm^{-1} (amide A) and N-H bending and C-N stretching vibration at ~1560 cm^{-1} (amide II) give information about the crystallographic order, whereas the C=O stretching vibration at ~1640 cm^{-1} (amide I) is indicative for an amide compound. Non-bonded systems or structures with significantly weaker hydrogen bonds, which also include a non-columnar structure like, e.g., layered structures, often show a shift of the N-H stretching vibration to higher wavenumbers or multiple occurrences of this vibration. In contrast, a shift of the amide II vibration (N-H bending & C-N stretching) to lower wavenumbers (~1530 cm^{-1}) is indicative of a non-columnar structure. [23,27]
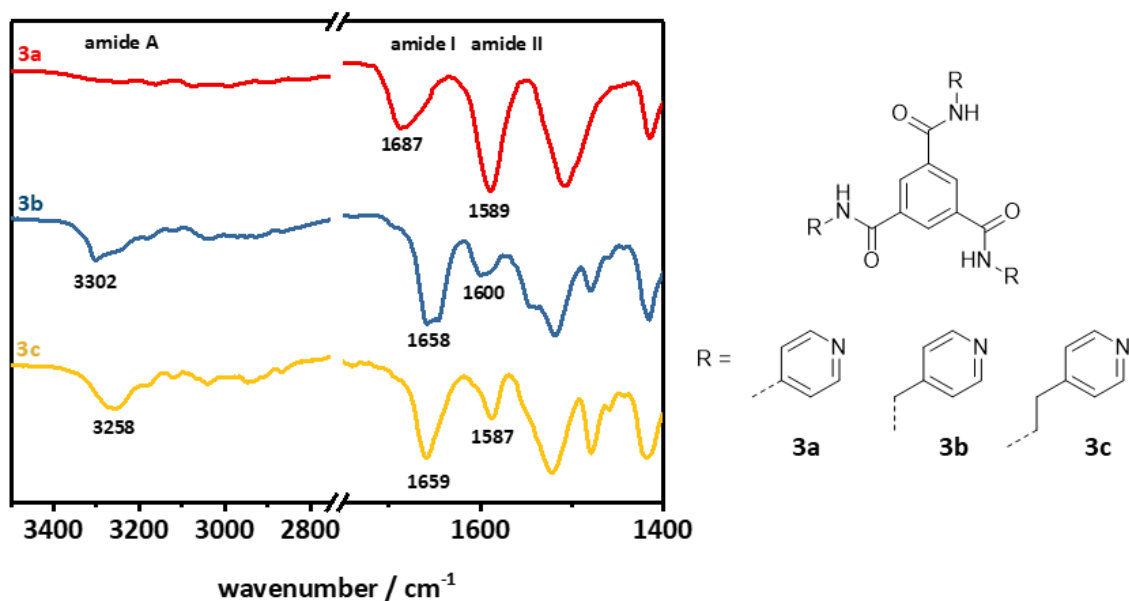
Figure 38: Normalized IR spectra of **3a-c** in the relevant wavenumber range of 3500-2800 cm^{-1} and 1750-1400 cm^{-1}.

It is known from literature that **3a** does not form columnar structures. This is confirmed by the FT-IR spectrum of **3a** shown in **Figure 38** since no amide A vibration is observed in the region of about 3240 cm^{-1} and the amide I and II vibrations are not in the characteristic wavenumber ranges, which are indicative of columnar arrangements. In the case of **3b** and **3c**, all three characteristic amide vibrations are present, as shown in **Figure 38**. These vibrations are shifted compared to the characteristic wavenumber ranges in both cases, which is why non-columnar structures are assumed for **3b** and **3c** as well.

Thermal characterization

In addition to the molecular characterization, the synthesized BTAs were also examined in view of their thermal properties to reveal the thermal behavior, which is required for further processing steps. Moreover, the thermal behavior of the BTAs is often indicative of their solubility behavior. The higher the melting point or the decomposition/sublimation temperature of a compound, the more likely it is to have low solubility, often due to strongly bonded hydrogen bonds.

Thermal behavior was investigated by means of TGA and DSC. The thermal stability and degradation of the BTAs were analyzed by TGA. For a better comparison of the synthesized BTAs, the temperature at 5 % weight loss was determined. The TGA measurements were carried out in a temperature range of 30-700 °C. In addition, the thermal transitions (melting temperature and crystallization temperature) of the BTAs were investigated by means of DSC measurements. For this purpose, the compounds were measured in two cycles in a temperature range of 50-300 °C.

Figure 39 shows the TGA curves of **3a-c**. Due to the three amide linkages in the BTA molecule and the formation of hydrogen bonds between the amide units, **3a-c** exhibit high thermal stability.
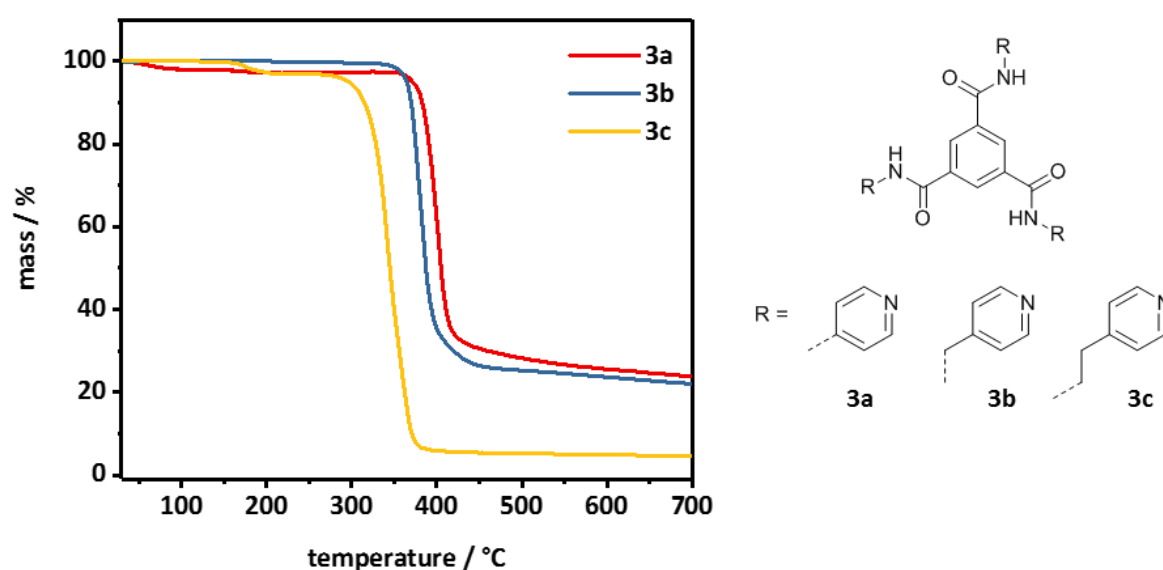
Figure 39: Thermogravimetric analysis of **3a-c** in a temperature range of 30-700 °C under nitrogen atmosphere and a heating rate of 10 K/min.

The temperature at 5 % weight loss for **3a** is 371 °C. However, there is a significant weight loss of around 3 % at the beginning of the TGA measurement. This is due to methanol, which is trapped in the crystal structure. The value is approximately in agreement with the molecular weight of one methanol per BTA molecule. The solvent was included in the crystal structure during the purification and escaped within a temperature range of 30-150 °C. Due to the incorporation of the alkyl spacer between the amide unit and the pyridine substituent, the thermal stability decreases with increasing spacer length. However, the difference between **3a** and **3b** is not significant. Presumably, the longer alkyl spacer

prevents intramolecular interactions, resulting in lower thermal stability. The TGA curve of **3c** also shows a slight weight loss in the range of 150-200 °C, which is the temperature range where **3c** melts. The entrapped DMF used for purification can escape after melting of **3c**. The temperature at 5 % weight loss for **3c** is 297 °C. Despite repeated drying under high vacuum, the solvent could not be removed entirely. The TGA curves also show that for **3a** and **3b**, a hardly soluble black residue of 20 % remains in the crucibles even at high temperatures. In contrast, an almost 100 % weight loss can be observed for **3c**.

The melting temperatures of **3a-c** were determined by individual DSC measurements. **Figure 40** shows the DSC curves of **3a-c**. In all DSC curves, a melting peak can be observed in the first heating curve. However, no crystallization can be observed during cooling. For this reason, no melting peaks were found in the second heating curve. The melting temperature of **3a** is determined at a temperature of about 320 °C according to DSC measurements. In the first DSC heating curve, a recrystallization peak can also be seen at a temperature of about 175 °C. **3b** exhibits a melting temperature of 264 °C according to DSC measurements. The lowest melting temperature has **3c** with about 200 °C. Interestingly, the DSC diagram shows two peaks at 193 °C and 200 °C. When comparing the melting points of **3a-c**, it is noticeable that the melting temperatures decrease with longer spacer length between the amide moiety and peripheral substituent. This is due to the contribution of the aliphatic chain to the entropy, which increases with the incorporation of the aliphatic spacer. Moreover, the secondary interactions between the amide units and pyridine substituents also play an important role and affect the thermal properties.
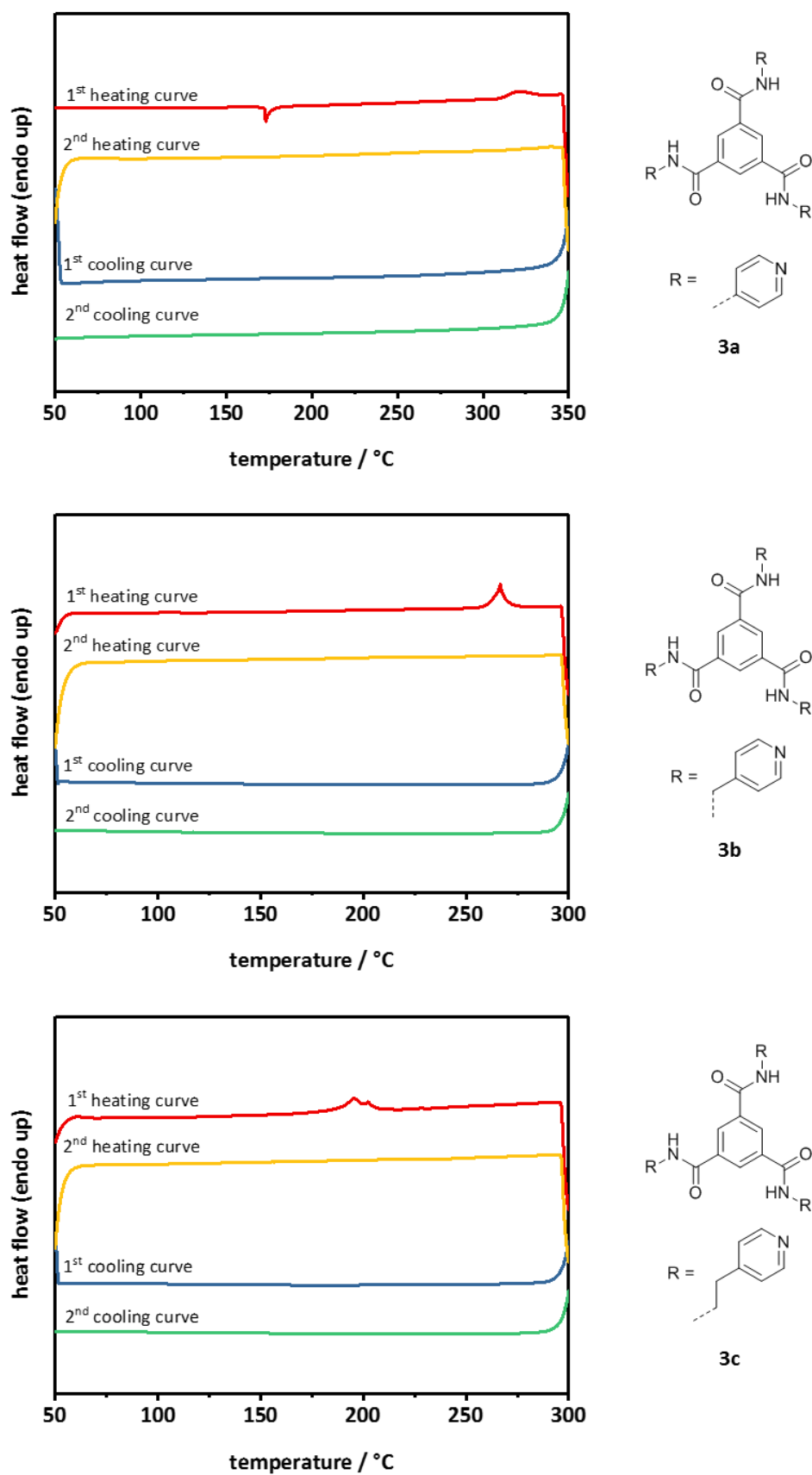
Figure 40: DSC heating and cooling scans of **3a-c**. The DSC curves were recorded in a temperature range of 50-300 °C (350 °C in the case of **3a**) with a scanning rate of 10 K/min.

3.1.1.2 Self-assembly studies

It is known from literature that **3a** can form thermo-reversible gels when cooling a warm BTA solution consisting of a solvent mixture of water and a protic solvent such as MeOH, DMSO or DMF. [28,129] In his doctoral thesis Hannes Welz has already performed basic solubility and self-assembly investigations of **3a** in pure solvents and in solvent mixtures. **3a** is soluble in some pure solvents such as MeOH or EtOH at low concentrations (<0.1 wt%) and elevated temperatures and forms fibers by self-assembly from solution. For **3b** and **3c**, no information about self-assembly can be found in literature.

Investigations of the self-assembly behavior are essential for a fundamental understanding of nanoobject formation and evaluation but also in view of the preparation of polymer microfiber-supramolecular nanofiber composites, where the compounds must be able to form fibers by self-assembly upon cooling and evaporation. Therefore, the solubility and self-assembly behavior of **3a-c** from solution upon cooling and simultaneous evaporation of the solvent was investigated.

Solubility experiments showed that **3a** is completely insoluble in water. The combination of organic solvents such as acetone, isopropanol (IPA), EtOH or THF with water as co-solvent in a ratio of 8:2 (w/w) leads to self-assembly and formation of supramolecular fibers. The formation of fibers takes place within a very short time. **3a** can be dissolved at elevated temperatures up to a maximum concentration of 0.5 wt%. The formation of supramolecular fibers from the two exemplary solvent mixtures EtOH/H_2O and THF/H_2O, both at a ratio of 8:2 (w/w) and at a BTA concentration of 0.5 wt%, is shown in **Figure 41**.
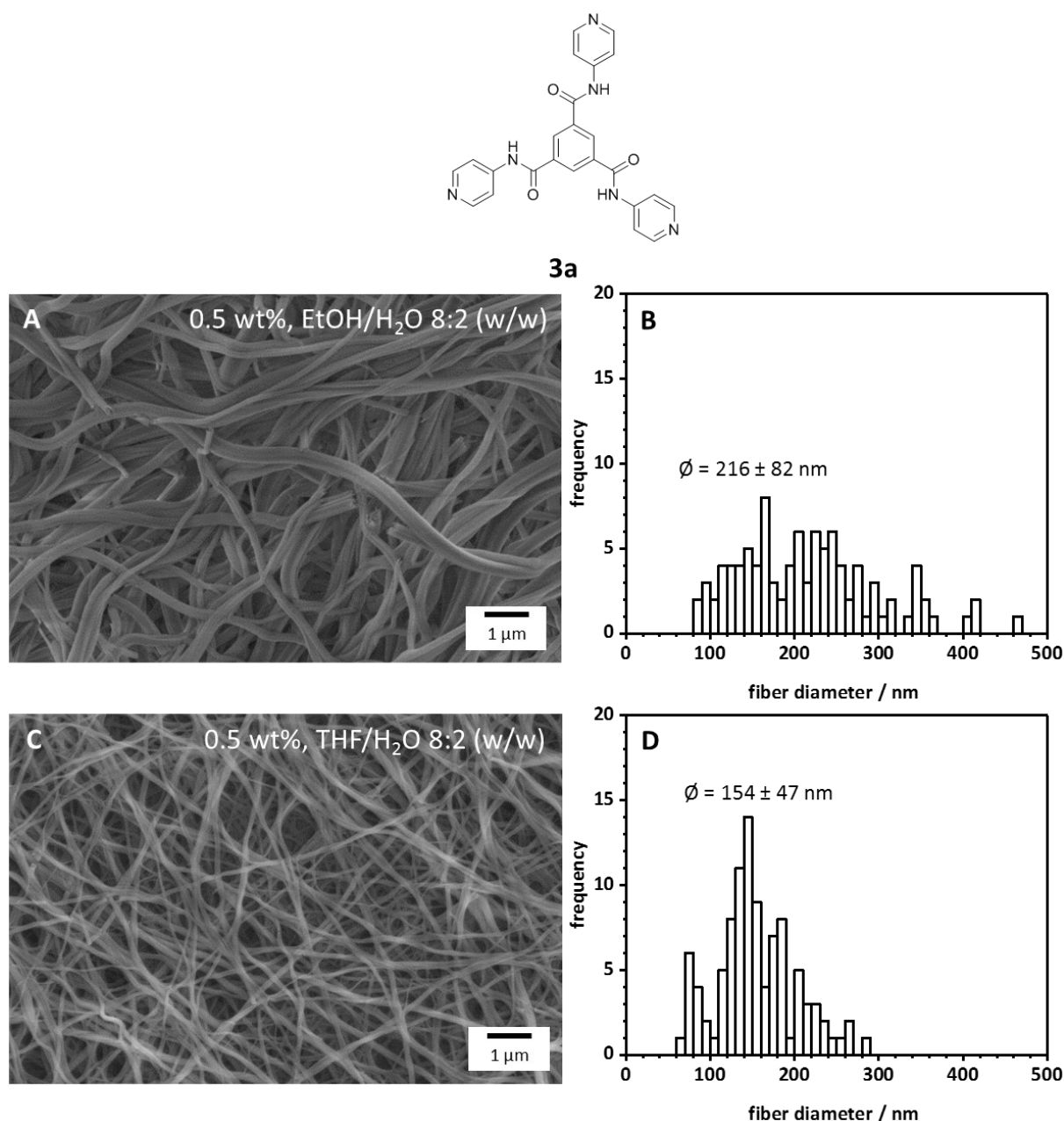
Figure 41: SEM micrographs (**A, C**) of supramolecular nanofibers of **3a** and the corresponding fiber histograms (**B, D**). The supramolecular fibers were prepared by self-assembly upon cooling and evaporation from an 8:2 (w/w) EtOH/H$_2$O (**A**) or THF/H$_2$O (**C**) mixture (0.5 wt% of **3a**). The histograms of the fiber diameters are based on the evaluation of at least 100 fibers.

As shown in **Figure 41,** supramolecular fibers with different fiber diameters and fiber diameter distributions were observed depending on the choice of the solvent system, demonstrating the impact of the solvent system on the object formation. Fibers with an average diameter of 154 ± 47 nm are generated from an EtOH/H$_2$O (8:2, w/w) mixture, whereas thinner fibers from a THF/H$_2$O (8:2, w/w) mixture were achieved. Fibers are formed, although it is evident from literature or the FT-IR spectrum of **3a** shown before that **3a** does not form columnar structures.

In contrast to **3a**, **3b** and **3c** have significantly better solubility. Both BTAs are completely dissolved at RT, for example, at a concentration of 1.0 wt% in EtOH. Presumably, the solubility is significantly improved by the insertion of the CH_2 group (in the case of **3b**) or the two CH_2 groups (in the case of **3c**) between the amide unit and peripheral pyridine substituent. This trend is in agreement as described with DSC. However, both compounds did not form fibers by self-assembly from pure solvents. Hollow tubes with an average diameter of 1.7 ± 0.5 µm were formed by cooling and evaporation of a BTA solution with 0.5 wt% of **3b** in EtOH/H_2O (8:2, w/w) solvent mixture. In contrast, significantly thicker tubes or ribbon-like structures with an average diameter of 5.5 ± 2.3 µm were obtained during the evaporation of a THF/H_2O (8:2, w/w) solvent mixture, as shown in **Figure 42**. The formation of the supramolecular structures for **3b** took several minutes, which is significantly longer compared to **3a**.
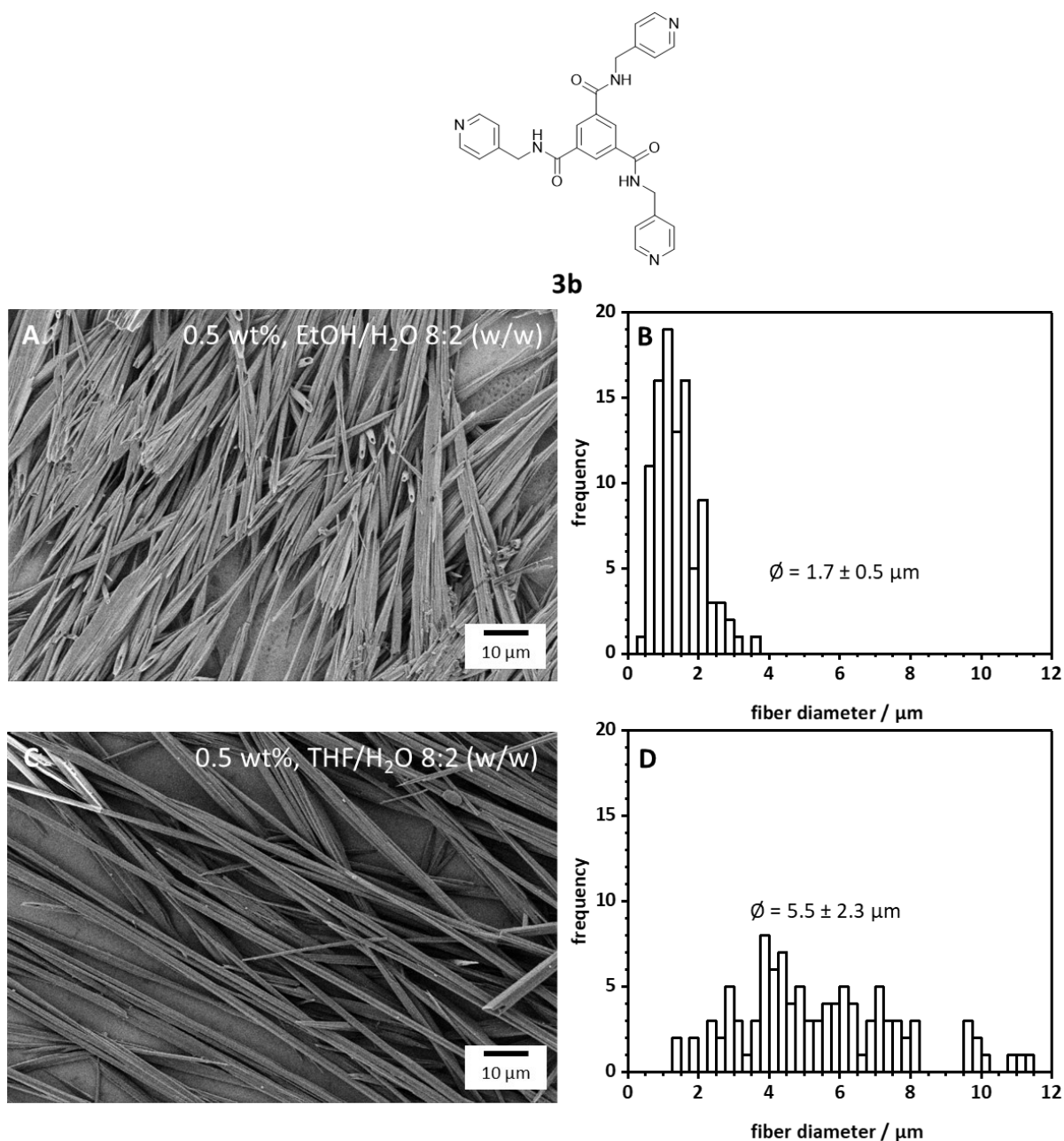
Figure 42: SEM micrographs (**A, C**) of supramolecular hollow tubes or ribbon-like structures of **3b** and the corresponding fiber histograms (**B, D**). The supramolecular fibers were prepared by self-assembly upon evaporation from an 8:2 (w/w) EtOH/H$_2$O (**A**) or THF/H$_2$O (**C**) mixture (0.5 wt% of **3b**). The histograms of the fiber diameters are based on the evaluation of at least 100 fibers.

In the case of **3c**, no defined structures could be observed by applying these self-assembly protocols from pure solvents or solvent mixtures at different BTA concentrations.

3.1.2 Benzenetrisamides with two pyridine substituents

The triple pyridine-substituted BTA **3a** is well-known from literature and forms very thin nanofibers in selected solvent systems. However, as shown before by FT-IR measurements and known from literature [28], **3a** forms no columnar structures and thus, the fibers are expected to feature an intrinsic poorer mechanical stability. In contrast, the supramolecular fibers of aliphatic BTAs showed excellent mechanical stability intrinsically as well as in fabrics. [45,46,130] The reason for this is most probably the formation of columnar structures. Since BTAs comprising a complete substitution pattern with three pyridine substituents are not necessarily required in view of the immobilization of NPs, the idea came up to synthesize BTAs with two or only one pyridine substituent. The aim is to synthesize pyridine-containing BTAs, which show columnar stacking, can form supramolecular fibers and are mechanically stable in a support structure in aqueous media.

3.1.2.1 Synthesis and characterization

In general, different approaches can be considered to realize BTAs with two different substituents. As shown in **Scheme 2**, for the targeted compounds **9a-c**, a straightforward synthetic route was selected based on dinitrobenzoic acid as core unit. This approach allows for a three-step synthesis starting from 3,5-dinitrobenzoyl chloride, which is commercially available, to the final CNN-centered BTA carrying two pyridine and one aliphatic substituent without affecting the formerly introduced side groups by the other steps. In previous works, CNN-centered BTAs with three *tert*-butyl or cyclohexyl substituents were already synthesized and investigated at our department. [41] In both cases, the BTAs showed a columnar stacking and supramolecular fibers were formed using the triple *tert*-butyl-substituted CNN-centered BTA. For that reason and additionally due to their bulkiness enforcing a macrodipole reduction, *tert*-butyl, ethylhexyl and cyclohexyl were selected as substituents besides the pyridine substituent in the syntheses of **9a-c**. The syntheses of the new compounds **9a-c** were carried out by Jutta Failner and Sandra Ganzleben (Macromolecular Chemistry I, University of Bayreuth) under my supervision. Here, the first conversion steps to obtain **9a-c** were performed in an analogous manner as carried out in previous works. The characterization of **9a-c** was performed by myself.

Substituent R	---⊣— (tert-butyl)	(ethylhexyl)	(cyclohexyl)
Compound	9a	9b	9c
Yield [%]	71	60	81
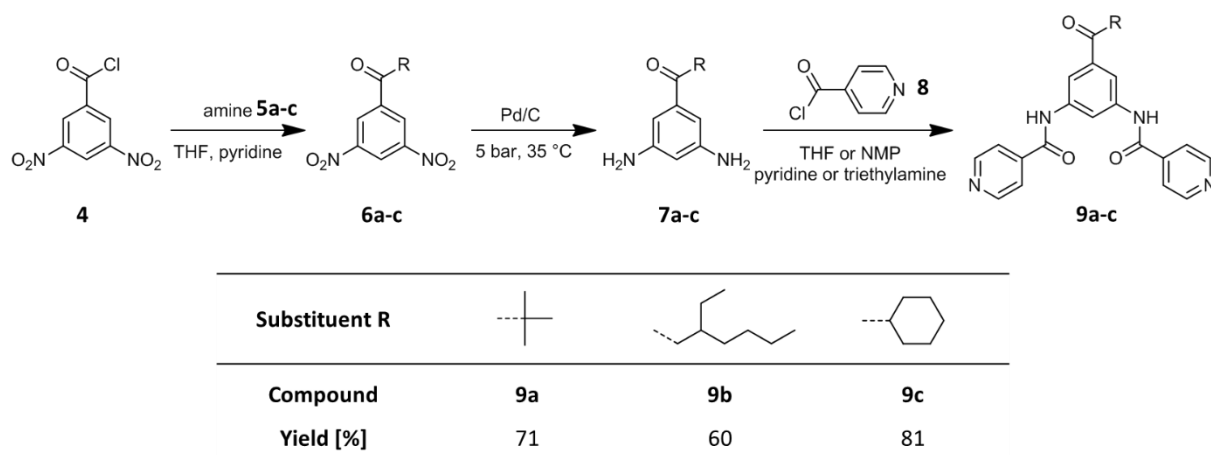
Scheme 2: Multi-step synthesis of BTAs **9a-c** with two pyridine substituents and one aliphatic substituent (*tert*-butyl, ethylhexyl or cyclohexyl).

In the first step, 3,5-dinitrobenzoyl chloride (**4**) reacts with the corresponding aliphatic amine (**5a-c**) in the presence of THF as solvent and pyridine as acid scavenger to form the corresponding 3,5-dinitrobenzamide (**6a-c**). Their nitro groups are reduced to the corresponding amine derivative in a hydrogenation reactor using palladium on activated carbon at a pressure of 5 bar and elevated temperature. Before the pyridine substituent is introduced into the molecule in the final step, isonicotinoyl chloride (**8**) had to be synthesized by the reaction of isonicotinic acid with oxalyl chloride in the presence of DCM and DMF as a catalyst. Finally, the respective 3,5-diaminobenzamide (**7a-c**) reacts with isonicotinoyl chloride (**8**) in THF or NMP as solvent and pyridine or triethylamine as a base to form two amide bonds to the final BTA (**9a-c**).

Purification of **9a-c** was performed by recrystallization or boiling in different solvents. Detailed information on synthesis and purification is described in the experimental part (**chapter 7**). The yields after purification of **9a-c** are in the range of 60-80 %, whereby the differences can be explained by the different purification conditions. The BTAs were structurally characterized and clearly identified by ^{1}H-NMR spectroscopy, mass spectrometry and FT-IR spectroscopy. Thermal characterization was performed by DSC and TGA measurements.

Molecular characterization

Figure 43 shows exemplarily the ^{1}H-NMR spectrum of **9a,** which has two pyridine substituents and one *tert*-butyl substituent.
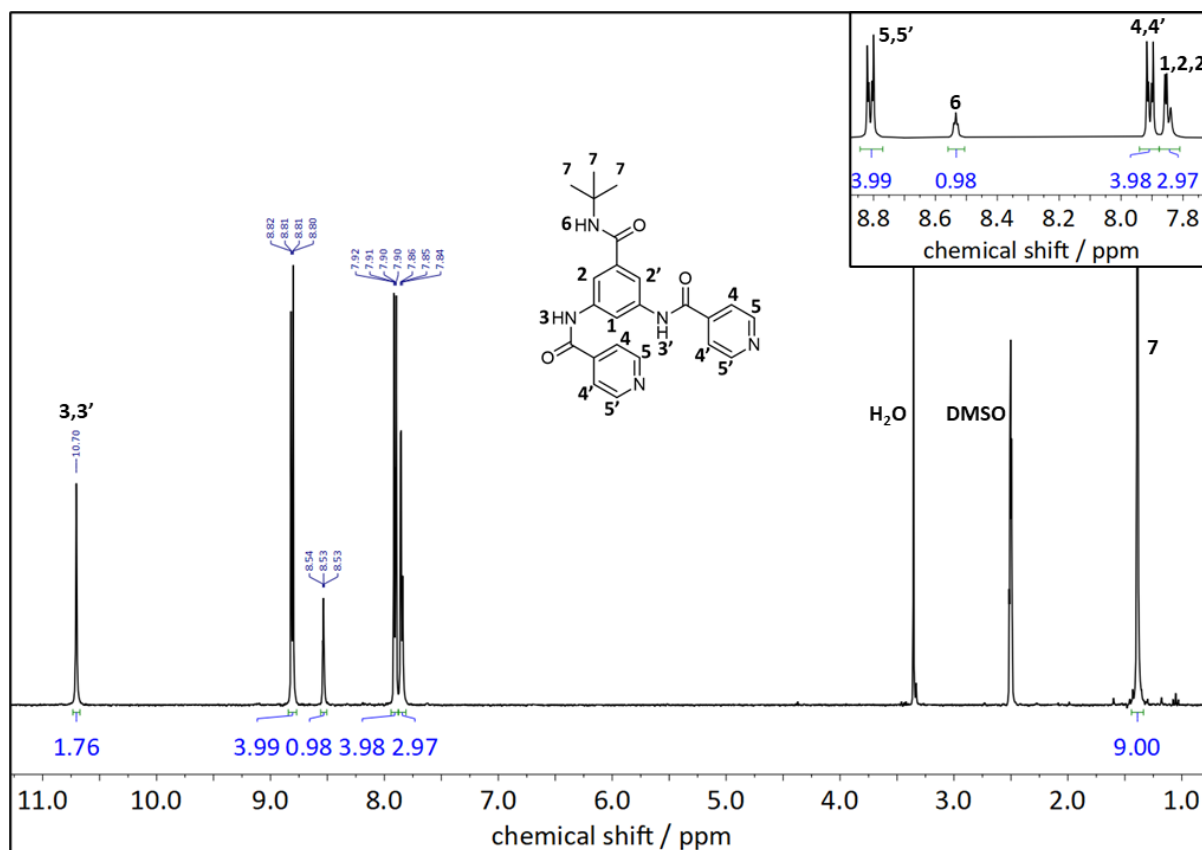
Figure 43: ^{1}H-NMR spectra of **9a** measured in deuterated DMSO. The signals were assigned to the corresponding hydrogen atoms according to the chemical structure of **9a**.

Due to the different amide linkages at the central benzene core, the N-H protons of the three amide groups and the protons of the benzene core are not identical. A sharp singlet at 10.70 ppm (**3**) corresponds to the N-H protons of the amide groups, which are N-centered. A distinct triplet at 8.53 ppm (**6**) belongs to the N-H proton of the C-centered amide group. The three protons of the benzene core are, despite their different spatial environment, closely together at a chemical shift of 7.85 ppm (**1,2,2'**). The protons of the methyl groups are assigned to the multiplet at 1.38 ppm (**7**). Finally, the four protons of the pyridine ring can be assigned to the doublet at 8.81 ppm (**5,5'**) and the doublet at 7.91 ppm (**4,4'**). The clear assignment and absence of other signals allow for unambiguous identification of compound **9a** in high purity. **9b** (with ethylhexyl substituents) and **9c** (with cyclohexyl substituents) were evaluated and identified in the same manner. Their spectra are shown in **Figure 136** and **Figure 137**.

Investigation of hydrogen bonding interactions by FT-IR spectroscopy

FT-IR measurements were performed as already described in **chapter 3.1.1** to investigate the formation of columnar structures due to the formation of three directed hydrogen bonds. The corresponding IR spectra of **9a-c** are shown in **Figure 44**.
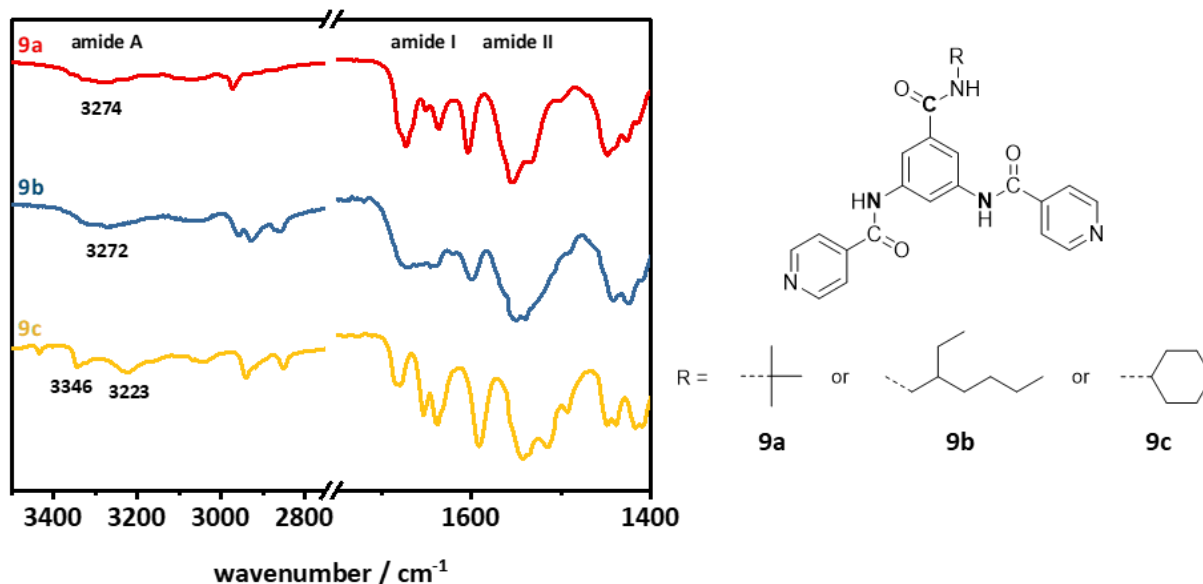
Figure 44: Normalized IR spectra of **9a-c** with two pyridine substituents and one aliphatic substituent. Only the relevant wave number range of 3500-2750 cm^{-1} and 1750-1400 cm^{-1} is shown.

Due to the lower symmetry and arrangement of the functional groups in contrast to **3a-c**, the IR spectra are expectedly more complicated. Depending on the connectivity of the amide group to the central benzene core, the characteristic amide vibrations are at different wavenumbers and two separate vibrations can be expected in the case of **9a-c**, respectively. This can be explained well by the IR spectra of two reference BTAs, which are CCC- and NNN-centered and carry both three *tert*-butyl substituents. The characteristic amide vibrations of both reference BTAs differ significantly in their wavenumber, but both BTAs form a columnar stacking. The vibrations indicating the presence of amide groups (amide A, amide I and II) can be seen in all three compounds **9a-c**. In the case of **9a** and **9b**, only one N-H stretching vibration can be found at around 3270 cm^{-1}, whereas **9c** shows two N-H stretching vibrations at about 3223 and 3346 cm^{-1}. Thus, the N-H stretch vibration of **9a** and **9b** is in between the wavenumbers of the N-H stretch vibration of the NNN-centered reference BTA (3295 cm^{-1}) and the CCC-centered reference BTA (3226 cm^{-1}), indicating the presence of strong hydrogen bonds. Two C=O vibrations are present for **9a** and **9c**, each of which can be attributed to the characteristic C=O vibration of the reference BTAs. For **9b**, two C=O vibrations are not clearly visible. The same observations can be made for the N-H bending and C-N stretching vibration. More precise statements about the formation of columnar stackings are only possible with crystal structure analyses.

Thermal characterization

Analogous to the previous **chapter 3.1.1**, the thermal stability was determined by means of TGA. These curves of **9a-c** are shown in **Figure 45**. It was found that all three BTAs exhibit high thermal stability. Due to the smallest substituent (*tert*-butyl), the thermal stability of **9a** is lowest with a temperature of 347 °C at 5 % weight loss. The difference in thermal stability between **9b** and **9c** is not very significant. For **9a** and **9b**, a slight weight loss can be observed at the beginning up to a temperature of approx. 100 °C. This is similar to the findings described in **chapter 3.1.1** and is most probably attributed to trapped solvent, which can evaporate under these conditions during the measurement. The TGA curves show that for **9a-c**, a hardly soluble black residue of 20-30 % remains in the crucibles even at high temperatures similar to **3a-c**.
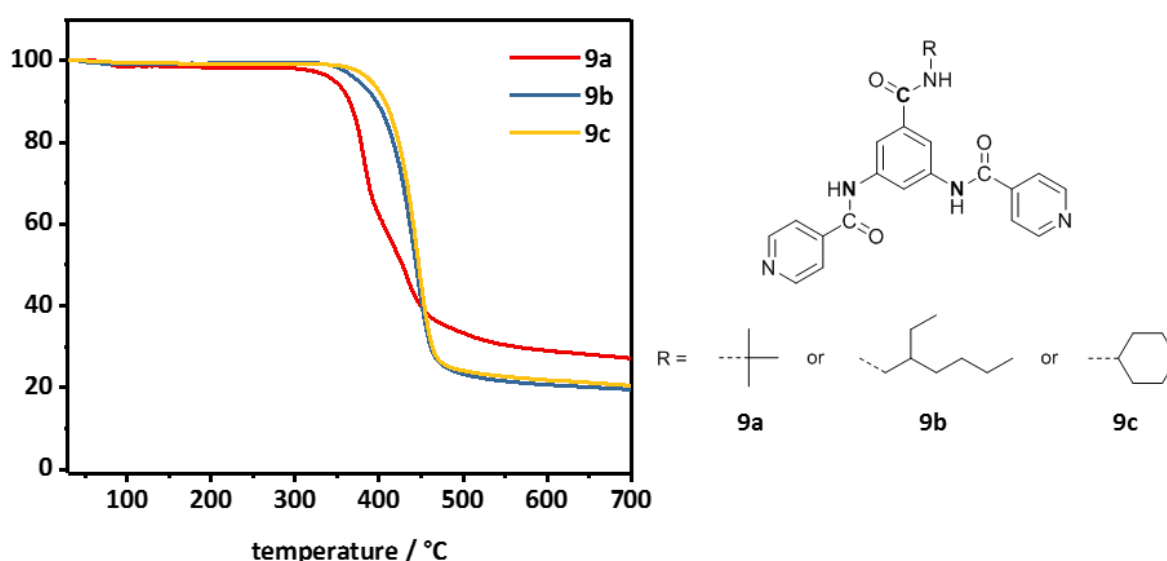
Figure 45: Thermogravimetric analysis of **9a-c** in a temperature range of 30-700 °C under nitrogen atmosphere and a heating rate of 10 K/min.

In the same manner, as described in the previous chapter **3.1.1**, the melting temperatures of **9a-c** were determined by DSC measurements (**Figure 46**).

In both the first and second heating DSC curves, an endothermic melting peak can be seen in the case of **9a-c**. In the following, the melting peaks from the second heating curve are compared in each case. The highest melting point is 257 °C for **9a**, which carries two pyridine substituents and a *tert*-butyl group. The melting point of **9c** is somewhat lower, whereas the melting point of **9b**, at about 200 °C, is considerably lower. In contrast to the *tert*-butyl substituent of **9a**, the ethylhexyl substituent is more flexible. The better flexibility leads to an increase in entropy and ultimately to a lower melting point. Since a cyclohexyl substituent is rather bulky, the melting temperature of **9c** is higher than for **9b** with an ethylhexyl substituent. A crystallization temperature could only be observed in the two cooling curves of **9a**. It is noticeable that, compared to the first cooling curve, the crystallization temperature drops by 18 °C in the second cooling curve due to the degradation of **9a**. This is also evident from a

67

lower enthalpy of the crystallization peak in the second cooling curve compared to the first cooling curve. In the case of **9b** and **9c**, no exothermic peak could be determined for the crystallization.
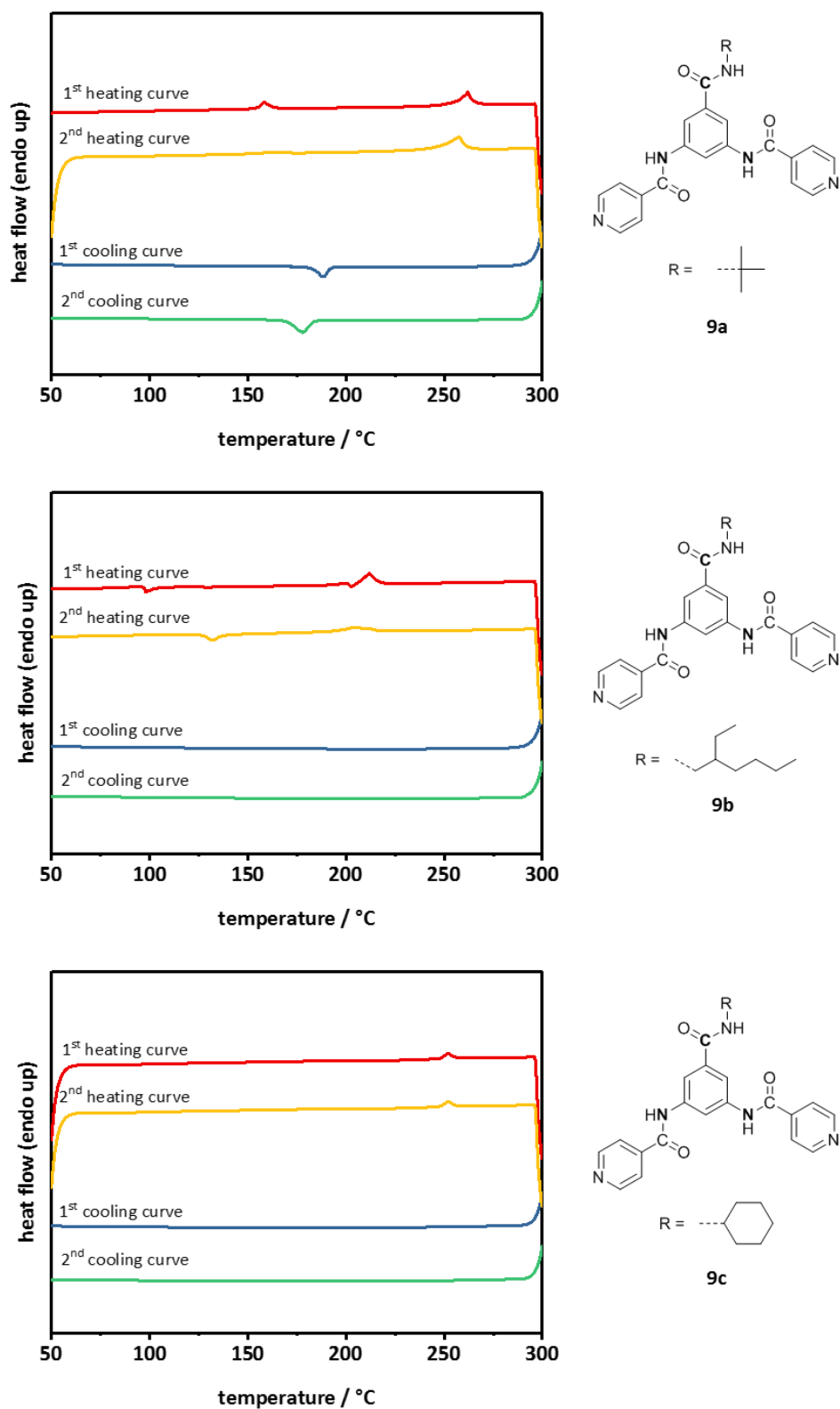
Figure 46: DSC heating and cooling scans of **9a-c**. The DSC curves were recorded in a temperature range of 50-300 °C with a scanning rate of 10 K/min.

3.1.2.2 Self-assembly studies

No information on the self-assembly behavior of BTAs carrying pyridine and aliphatic substituents can be found in literature so far. To obtain a fundamental understanding of the formation of nanoobjects based on such BTAs, the solubility and self-assembly behavior of **9a-c** were investigated. Of particular interest is whether supramolecular fibers can be generated despite two different substituents. Since the self-assembly behavior depends on various parameters such as the solvent, the BTA structure or the process conditions, a screening experiment with **9a-c** was carried out.

For this purpose, the solubility of **9a-c** was investigated in numerous solvents with a wide range of polarity at different temperatures. Additionally, different alcohol/water mixtures in certain proportions (1:9 to 9:1 (w/w)) were used for the screening experiment. Solutions with a concentration of 0.5 wt% of the corresponding BTA were prepared and heated to 75 °C while stirring. The solubility was verified optically and by the scattering of a laser pointer. Then it was checked whether the respective BTAs can form supramolecular nanofibers via self-assembly upon cooling or upon cooling and simultaneous solvent evaporation.

Self-assembly from solution upon cooling and evaporation

One droplet of the solution was taken from each hot BTA solution and placed on a silicon wafer to investigate the formation of supramolecular structures upon cooling and simultaneous evaporation of the solvent. Final drying was performed at ambient conditions. The samples were then sputtered with a 1.3 nm thick platinum layer and analyzed by SEM.

Self-assembly from solution upon cooling

The hot BTA solutions were cooled to RT and left to rest under ambient conditions. When no supramolecular structures were formed after a long period of time (more than one day), the BTA solution was stored at -18 °C to initiate self-assembly by cooling. After a certain period of time, the formation of supramolecular structures can be observed optically. The duration of this depends, among other things, on the solvent or BTA selected. To investigate the morphology of the supramolecular structures, a droplet of the BTA dispersion is placed on a silicon wafer. After complete drying of the sample under ambient conditions, the sample is sputtered with 1.3 nm platinum and analyzed by SEM.

9a-c are completely soluble at a concentration of 0.5 wt% in relatively many, mainly polar solvents such as several alcohols or ketones. However, **9a-c** are completely insoluble in water. The different aliphatic substituents of **9a-c** have no or very little effect on the solubility. In addition to pure solvents, alcohol/water mixtures in certain proportions (1:9 to 9:1) are also suitable for completely dissolving **9a-c**. Supramolecular structures were only formed with a few solvent systems. In most cases, the solubility is too good and the BTAs remain completely dissolved at RT (or at storing at -18 °C) even after

a few days. Interestingly, supramolecular structures were obtained only by self-assembly upon cooling. Self-assembly upon cooling and evaporation of the solvent resulted only in spherical particles.

Figure 47 shows exemplarily SEM micrographs of supramolecular structures obtained after self-assembly upon cooling of **9a** and **9b**.
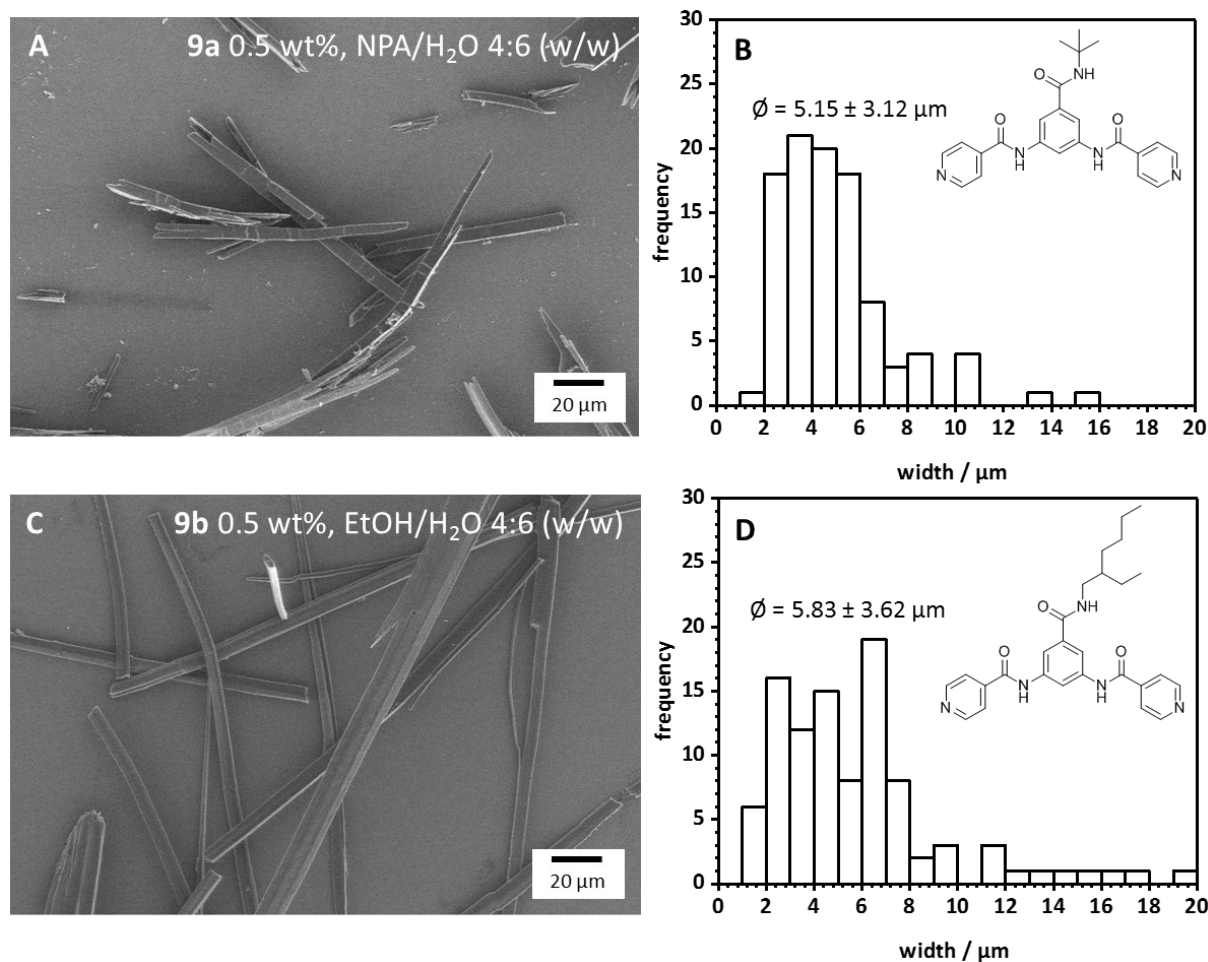
Figure 47: SEM micrographs of supramolecular structures of **9a-b** prepared by self-assembly upon cooling at a concentration of 0.5 wt% in different alcohol/water mixtures 4:6 (w/w) (**A, C**). The corresponding histograms (**B**, **D**) are based on the evaluation of at least 100 fibers.

For example, in the case of **9a** and **9b**, ribbon-like structures of different sizes are formed by self-assembly upon cooling in solution. In both examples, the solvent used was an alcohol/water mixture with a ratio of 4:6 (w/w). No supramolecular structures were observed in pure solvents. It can be assumed that the high proportion of water as a non-solvent is necessary for self-assembly. The average width of the structures is in the range of 5-6 μm. However, a very broad distribution can be seen from the histograms in each case. It can also be assumed that the very thick ribbon structures consist of several thinner ribbons. An indication of this is that a splitting of the ribbons into several small ones can be observed, especially at the ends of the structures. In the case of **9c**, no ribbon-like or fibrous structures were formed within several days.

3.1.3 Benzenetrisamides with one pyridine substituent

Finally, the number of pyridine substituents in the BTA structure is further reduced. Therefore, the corresponding BTAs have only one pyridine and two aliphatic substituents. As shown before, the substitution of one pyridine moiety already provides more promising features in view of columnar packing of the BTAs, as demonstrated by FT-IR. Thus, the aim is to synthesize pyridine-containing BTAs, which show a more pronounced columnar packing and, as a result, form well-defined supramolecular nanofibers from solution. This also provides a comprehensive study of the extent to which the number of pyridine substituents, as well as the different aliphatic substituents, affect the self-assembly behavior.

3.1.3.1 Synthesis and characterization

As described in the previous section **3.1.2**, there are different approaches to realizing BTAs with two different substituents. As shown in **Scheme 3**, a straightforward synthetic route based on 5-nitroisophthalic acid as core unit was selected for the desired compounds **16a-c**. This approach allows for a four-step synthesis starting from 5-nitroisophthalic acid to the final CCN-centered BTA carrying one pyridine and two aliphatic substituents without affecting the formerly introduced side groups by the other steps. CCN-centered BTAs with three *tert*-butyl or cyclohexyl substituents were already synthesized in previous works. [41] Due to this and so that the influence on the type and number of different aliphatic substituents on the self-assembly behavior can be studied, the same three aliphatic substituents (*tert*-butyl, ethylhexyl and cyclohexyl) were selected besides the pyridine substituent for the synthesis of **16a-c**, analogous to the previous section **3.1.2**. The syntheses of the new compounds **16a-c** were carried out by Jutta Failner and Sandra Ganzleben (Macromolecular Chemistry I, University of Bayreuth) under my supervision. Here, all conversion steps to obtain **16a-c** except for the last step were carried out in an analogous manner as in previous work. The characterization of **16a-c** was performed by myself.
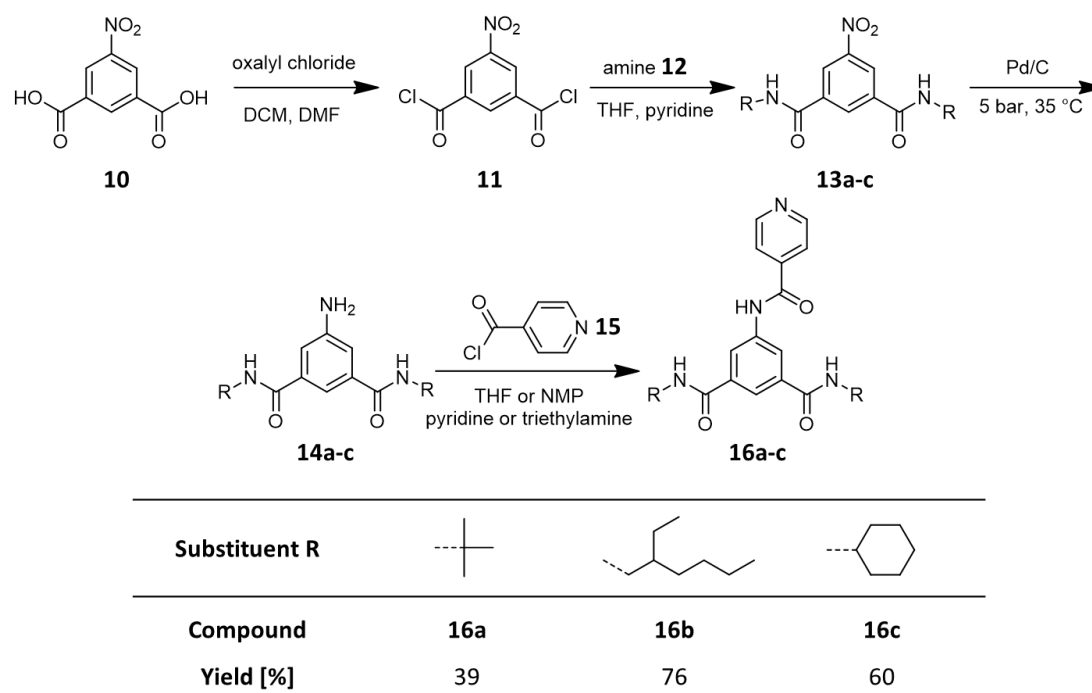
Scheme 3: Multi-step synthesis of BTAs **16a-c** with two pyridine substituents and one aliphatic substituent (*tert*-butyl, ethylhexyl or cyclohexyl).

In the first step, 5-nitroisophtaloyl dichloride (**11**) is synthesized by the reaction of 5-nitroisophthalic acid (**10**) and oxalyl chloride in the presence of DCM as solvent and DMF as the catalyst. Afterwards, the respective aliphatic amine (**12**) reacts with 5-nitroisophthaloyl dichloride (**11**) in THF to form *N′,N″*-di-alkyl-5-nitroisophthalamide (**13**). Here, pyridine serves as an acid scavenger for the HCl leaving group. In a further step, the nitro groups of *N′,N″*-di-alkyl-5-nitroisophthalamide (**13**) are reduced to the corresponding amine derivative in a hydrogenation reactor using palladium on activated carbon at 5 bar and elevated temperature. Before the pyridine substituent is introduced into the molecule in the final step, isonicotinoyl chloride (**15**) is synthesized by the reaction of isonicotinic acid with oxalyl chloride in the presence of DCM and DMF. Finally, 5-amino-*N′,N″*-alkyl-isophthalamide (**14**) reacts with isonicotinoyl chloride (**15**) in THF or NMP as solvent and pyridine or triethylamine as a base to form the corresponding BTAs (**16a-c**).

Purification of **16a-c** was performed by recrystallization or boiling in different solvents. Detailed information on synthesis and purification is described in the experimental part (**chapter 7**). The yields after purification of **16b** and **16c** were significantly higher at 76 % and 60 %, respectively, in contrast to the yield of **16a** at 39 %, which is probably attributed to more extensive purification steps of the compound. The BTAs were structurally characterized and clearly identified by ^{1}H-NMR spectroscopy, mass spectrometry and FT-IR spectroscopy. Thermal characterization was performed by DSC and TGA measurements.

Molecular characterization

Figure 48 shows exemplarily the ^{1}H-NMR spectrum of **16a**, which carries two *tert*-butyl and one pyridine substituent.
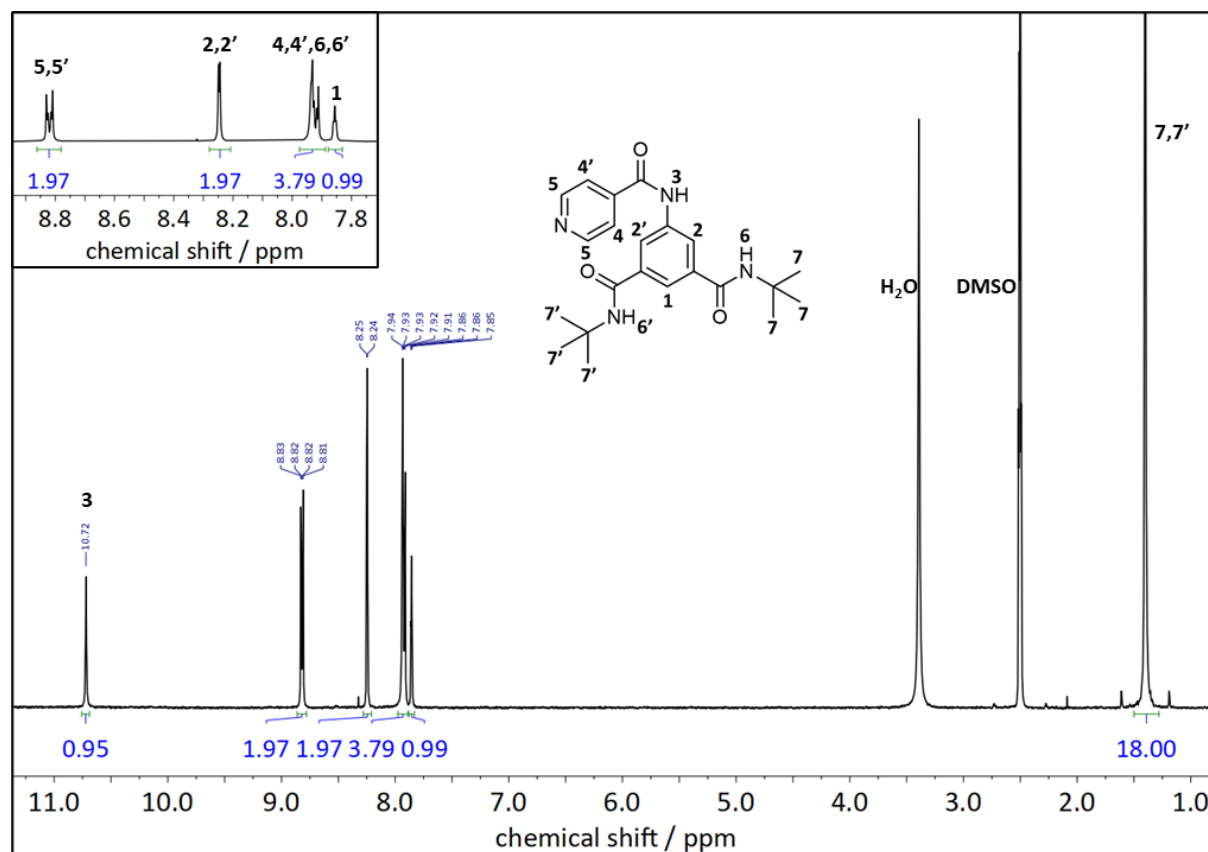
Figure 48: ^{1}H-NMR spectra of **16a** measured in deuterated DMSO. The signals were assigned to the corresponding hydrogen atoms according to the chemical structure of **16a**.

The NMR spectrum of **16a** looks comparably similar to the spectrum of **9a** because structurally, the same substituents are chosen and only the number of pyridine/*tert*-butyl substituents has been swapped. Due to the different amide linkages at the central benzene core, the N-H protons of the three amide groups and the protons of the benzene core are not identical. A sharp singlet at 10.72 ppm (**3**) corresponds to the N-H proton of the amide group, which is N-centered. The two protons of the C-centered amide groups are in the range of 7.96-7.90 ppm (**6,6'**). The doublet at 8.25 ppm (**2,2'**) can be assigned to the two protons at the benzene core, which are located next to the N-centered arm. The signal of the other proton at the benzene core is present as a triplet at 7.85 ppm (**1**). The four protons of the aromatic pyridine substituent can be assigned to the multiplet at 8.82 ppm (**5,5'**) and multiplet at 7.96-7.90 ppm (**4,4'**) and the signals of the strongly shielded protons of the methyl groups of the *tert*-butyl group are located at 1.40 ppm (**7**) as expected. The clear assignment and absence of other signals allow for unambiguous identification of compound **16a** in high purity. **16b** and **16c** were evaluated and identified in the same manner. Their spectra are shown in **Figure 138** and **Figure 139**.

Investigation of hydrogen bonding interactions by FT-IR spectroscopy

FT-IR measurements were performed as already described in the previous **chapters 3.1.1** and **3.2.1** to investigate the formation of columnar stacking due to the formation of three directed hydrogen bonds. The corresponding IR spectra of **16a-c** are shown in **Figure 49**.
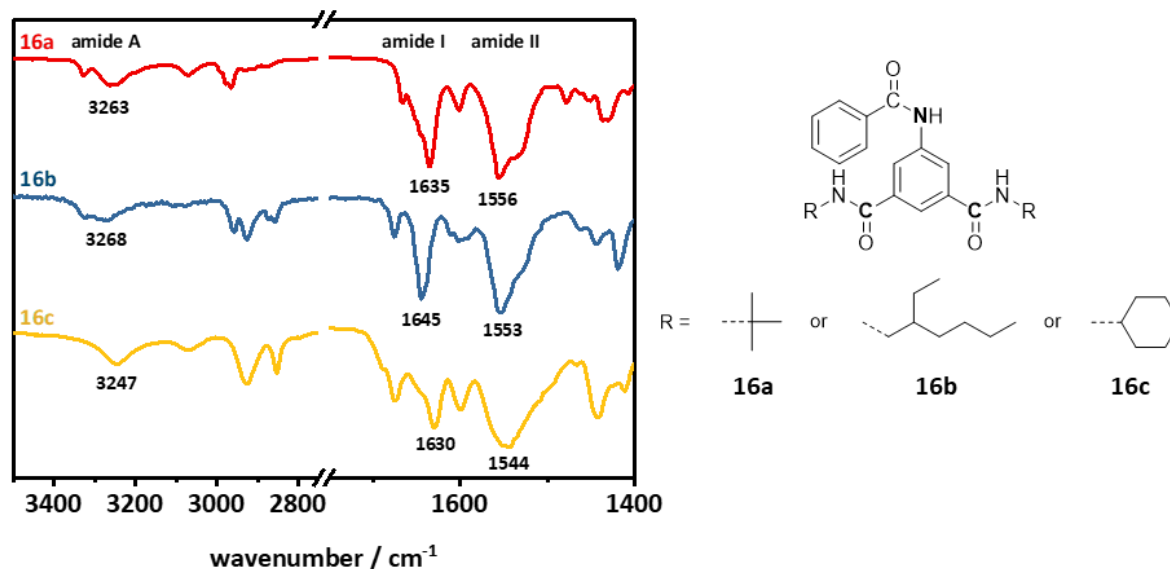
Figure 49: Normalized IR spectra of **16a-c** with two pyridine substituents and one aliphatic substituent. Only the relevant wave number range of 3500-2750 cm^{-1} and 1750-1400 cm^{-1} is shown.

The IR spectra of **16a-c** show similar complexity to the spectra of **9a-c** due to lower symmetry and arrangement of peripheral substituents compared to **3a-c**. The different linkage of the amide group to the central benzene core again leads to two vibrations each of the characteristic amide I and II bands at different wavenumbers, as exemplified for **16a** in **Figure 49**. The wavenumbers agree quite well with the wavenumbers of two reference BTAs, which are CCC- and NNN-centered and carry both three *tert*-butyl substituents. The N-H stretching vibration of **16a** is 3263 cm^{-1}, which is between the values of the two reference BTAs. Similar behavior is observed for **16b** and **16c**. Two characteristic C=O vibrations, but only one broad N-H bending and C-N stretching vibration, are observed for **16b** and **16c**, respectively. The values also agree relatively well with the values of both reference BTAs. From the IR spectra, it is not possible to make a more accurate statement about the presence of columnar structures due to the complexity. More precise statements are only possible with crystal structure analyses.

Thermal characterization

The thermal behavior was investigated by means of TGA and DSC measurements as described before in **chapter 3.1.1**. The corresponding TGA curves of **16a-c** are shown in **Figure 50**.
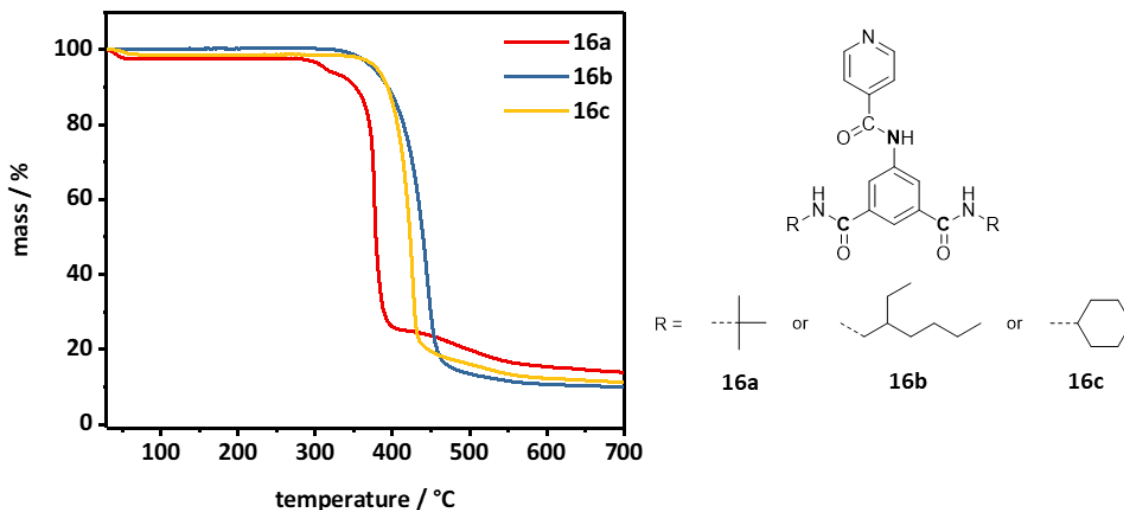
Figure 50: Thermogravimetric analysis of **16a-c** in a temperature range of 30-700 °C under nitrogen atmosphere and a heating rate of 10 K/min.

All three BTAs exhibit high thermal stability, which is attributed to the formation of hydrogen bonds. The lowest thermal stability exhibits **16a**, which carries two *tert*-butyl and one pyridine substituent. The temperature at 5 % weight loss is 313 °C. Due to the larger aliphatic substituents, the temperature at 5 % weight loss is about 60-70 °C higher for **16b** and **16c**. The difference between **16b** and **16c** is neglectable. Analogous to previous findings in **chapters 3.1.1** and **3.2.1**, a slight weight loss at the beginning of the TGA curves of **16a** and **16c** is attributed to trapped solvent, which can evaporate under these conditions during the measurement. The TGA curves also show that for **16a-c** a hardly soluble black residue of 10-20 % remains even at high temperatures in the crucibles.

The melting temperatures of **16a-c** were determined by individual DSC measurements. **Figure 51** shows the DSC curves of **16a-c**. In contrast to **16b-c**, **16a** does not show melting and crystallization peaks in the DSC curves. Accordingly, based on the TGA measurement, **16a** decomposes above a temperature of about 350 °C under incomplete sublimation. For the other two BTAs, phase transitions can be detected in the first and second heating/cooling curves. In each case, the melting and crystallization temperatures from the second heating/cooling curve are used for comparison. The melting temperature of **16b** (two ethylhexyl substituents) is 205 °C and the one of **16c** (two cyclohexyl substituents) is 293 °C. The higher melting point of **16c** compared to **16b** can be explained by the lower flexibility of the bulky cyclohexyl substituent, resulting in lower entropy than for **16b**. The crystallization peak of **16b** occurs at a temperature of 148 °C. Compared to the first cooling curve, the value is 8 °C lower, which indicates degradation of **16b**. The crystallization temperature of **16c** is significantly higher at 222 °C.
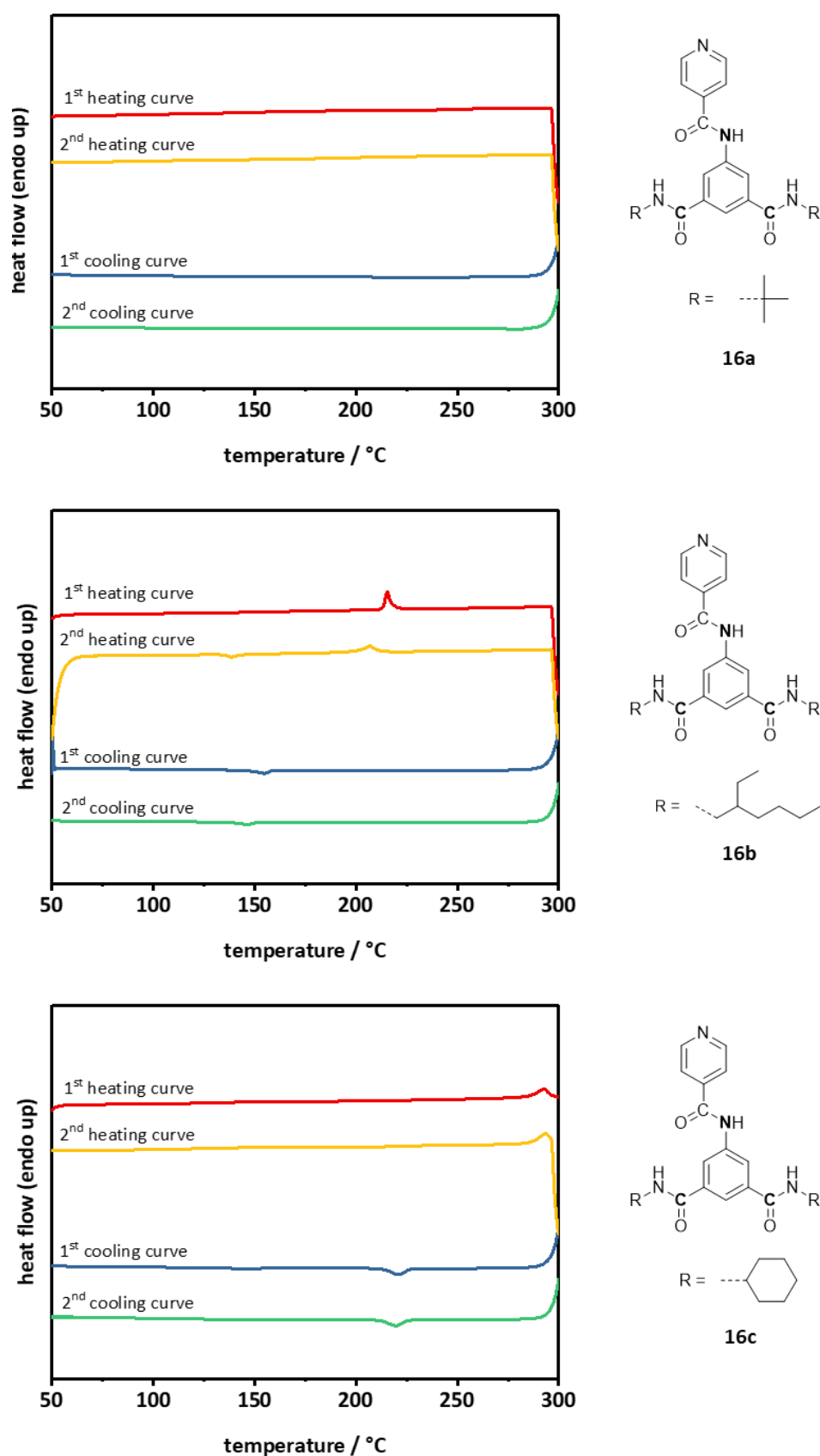
Figure 51: DSC heating and cooling scans of **16a-c**. The DSC curves were recorded in a temperature range of 50-300 °C with a scanning rate of 10 K/min.

3.1.3.2 Self-assembly studies

As already described for the CNN-centered BTAs **9a-c**, there is no information about the self-assembly behavior of CCN-centered BTAs **16a-c**. Therefore, analogous to **chapter 3.2.2**, investigations were carried out regarding the solubility and the formation of nanoobjects via self-assembly from solution. Numerous solvents of different polarities, as well as alcohol/water mixtures in certain proportions (1:9 to 9:1 (w/w)), were used for the screening experiments. As a standard concentration for the BTA solution, 0.5 wt% was selected.

16a-c are completely insoluble in water. **16a** can be completely dissolved at a concentration of 0.5 wt% in many solvents, especially in polar solvents such as alcohols or ketones. **16b** has good solubility in ketones such as acetone or 2-butanone at a concentration of 0.5 wt%, but not in any alcohol. The overall solubility of **16c** is only possible in very few solvents such as DMF or cyclohexanone. The decreasing solubility from **16a** to **16c** is due to the size, bulkiness and hydrophobicity of the aliphatic substituent. The cyclohexyl unit is the bulkiest and, like the ethylhexyl substituent, has a much higher hydrophobicity than the *tert*-butyl substituent. In addition to pure solvents, alcohol/water mixtures in certain proportions (1:9 to 9:1 (w/w)) are also suitable for completely dissolving **9a-c**. Screening experiments for self-assembly showed that supramolecular structures were only formed with a few solvent systems. In most cases, the solubility is too good and the BTAs remain completely dissolved at RT (or at storing at -18 °C) even after a few days. Interestingly, supramolecular structures were obtained only by self-assembly upon cooling. Self-assembly upon cooling and simultaneous evaporation of the solvent resulted surprisingly only in spherical particles.

Therefore, in the following **Figures 52-55**, exemplary SEM micrographs of supramolecular structures obtained after self-assembly upon cooling of **16a-c** are shown.

Figure 52: SEM micrographs (**A**, **B**) of supramolecular fibers of **16a** prepared by self-assembly upon cooling at a concentration of 0.5 wt% in 2-butanone. The corresponding fiber diameter histogram (**C**) is based on the evaluation of at least 100 fibers.

Supramolecular fibers were generated after cooling, e.g., from 2-butanone or an EtOH/H$_2$O mixture 4:6 (w/w) (**Figure 52** and **Figure 53**). Fibers were formed with 2-butanone only after several days and by additional storing at -18 °C. In contrast, BTA fibers were formed within one day at RT using an EtOH/H$_2$O 4:6 (w/w) solvent mixture. Nucleation is hindered or delayed in both cases. Possibly, due to the presence of water as a non-solvent, the formation of the supramolecular fibers in the alcohol/water takes place earlier. The fiber thickness varies depending on the solvent selected, as can be seen from the fiber histograms. Fibers of **16a** obtained from 2-butanone have an average fiber diameter of 327 ± 131 nm. In comparison, thinner fibers with a diameter of 172 ± 55 nm were generated from the EtOH/H$_2$O solvent mixture.

Figure 53: SEM micrographs (**A**, **B**) of supramolecular fibers of **16a** prepared by self-assembly upon cooling at a concentration of 0.5 wt% in EtOH/H$_2$O 4:6 (w/w). The corresponding fiber diameter histogram (**C**) is based on the evaluation of at least 100 fibers.

Compared to **16a**, after cooling a 0.5 wt% solution of **16b** in ethyl acetate or acetone ribbons with an average width of about 1.3 µm were obtained. The distribution of the ribbon width is significantly broader than that of the fibers of **16a**. The formation of the supramolecular structures took place at RT after a few days.

Figure 54: SEM micrographs of supramolecular ribbon-like structures of **16b** prepared by self-assembly upon cooling at a concentration of 0.5 wt% in ethyl acetate (**A**) and acetone (**C**). The corresponding histograms (**B**, **D**) are based on the evaluation of at least 100 ribbons.

Supramolecular ribbons were also observed for **16c** (**Figure 55**). However, the BTA concentration had to be reduced to 0.2 wt% because no complete dissolution was possible above this concentration. **2c** self-assembles in acetone after a few days at RT to form linear ribbons with a mean width of about 1.60 μm. If 2-butanone is chosen as a solvent instead of acetone, ribbons with very different widths in the range of about 200 nm up to 12 μm are obtained. This demonstrates the crucial role the choice of solvent plays in the formation of supramolecular structures. However, the thicker structures may consist of several thin structures, which cannot be detected on the SEM micrographs.
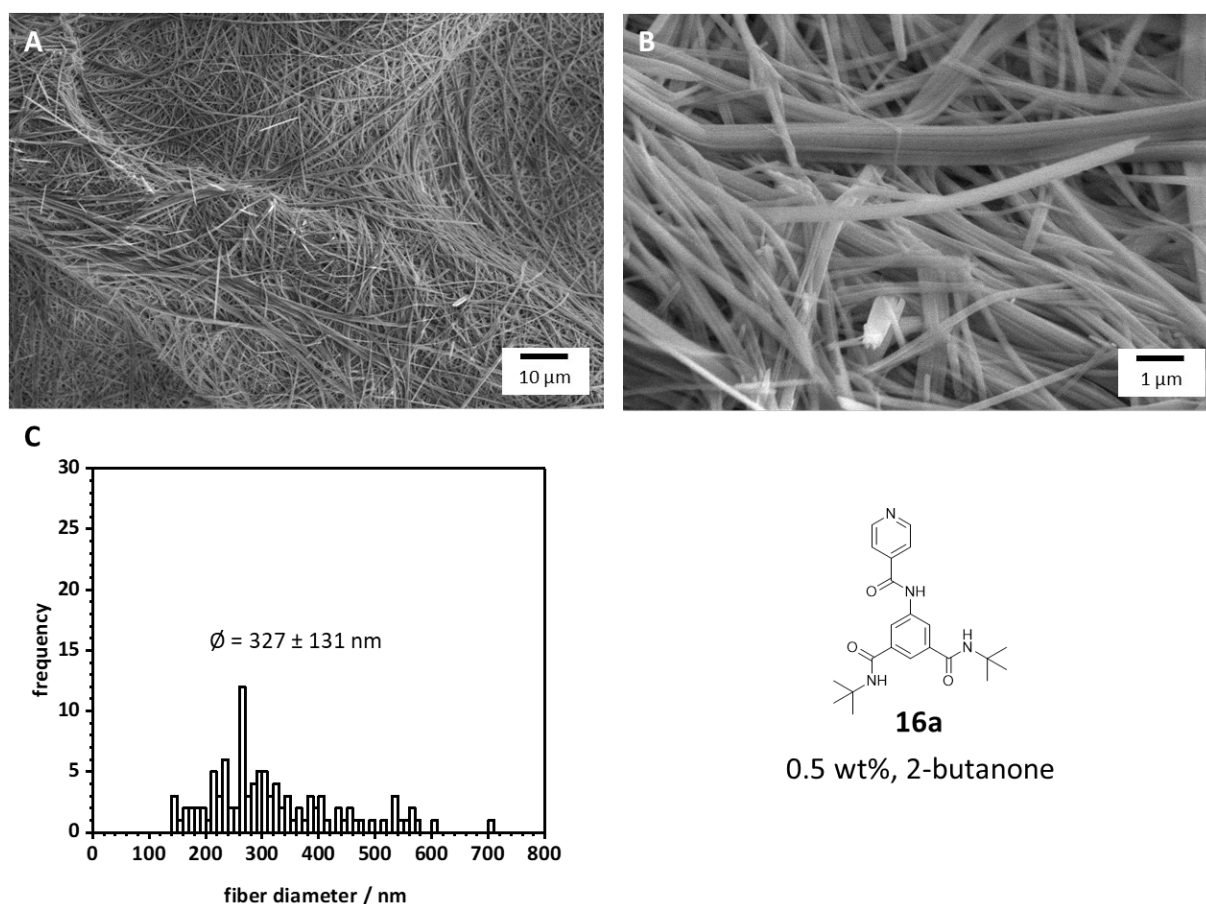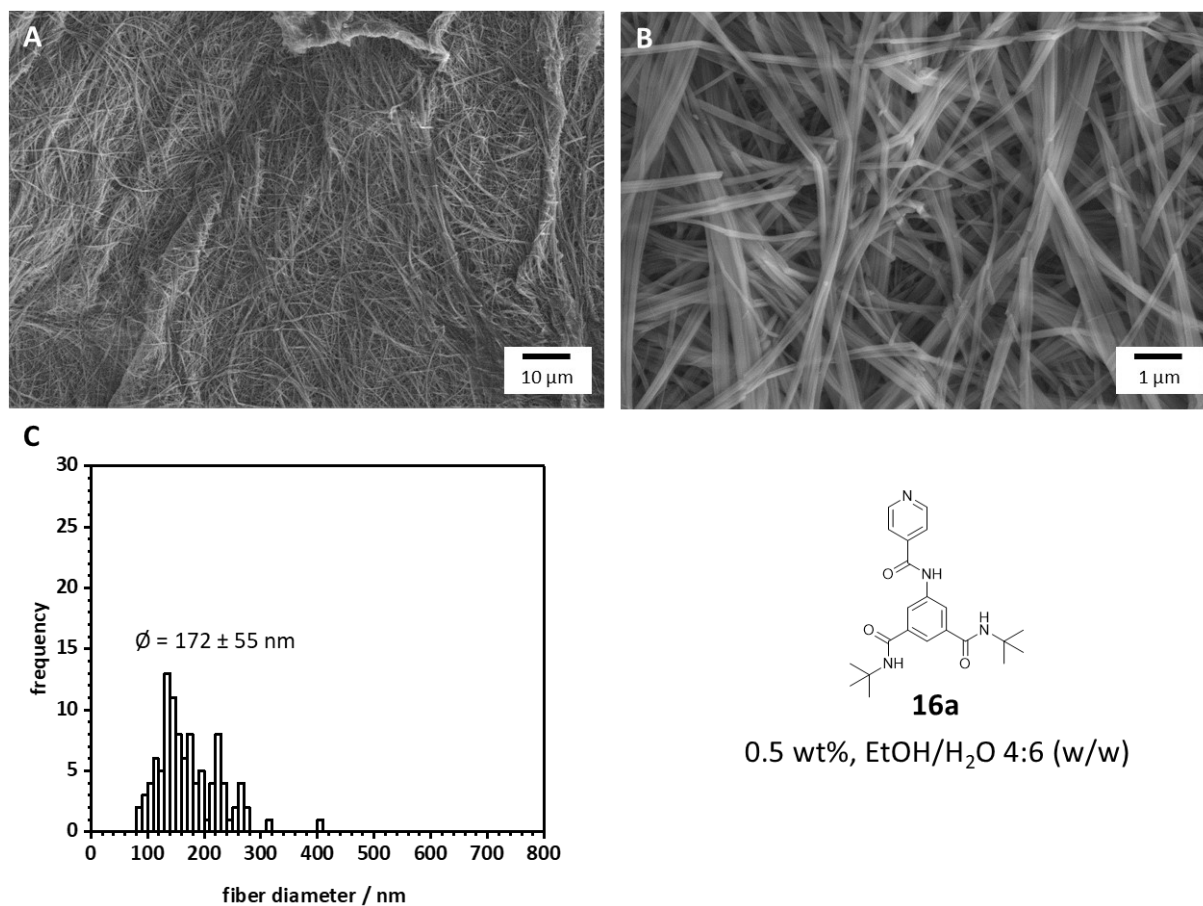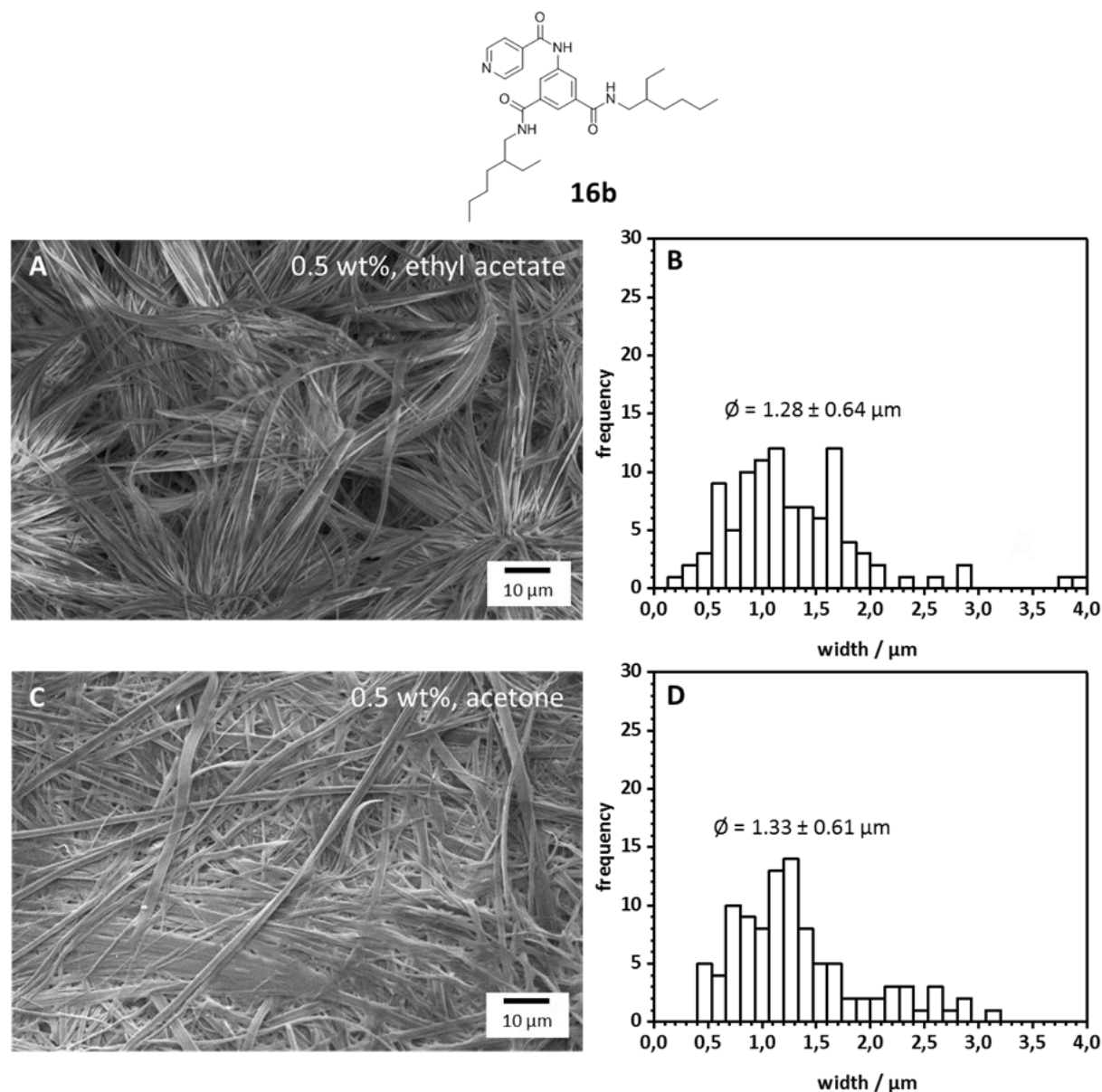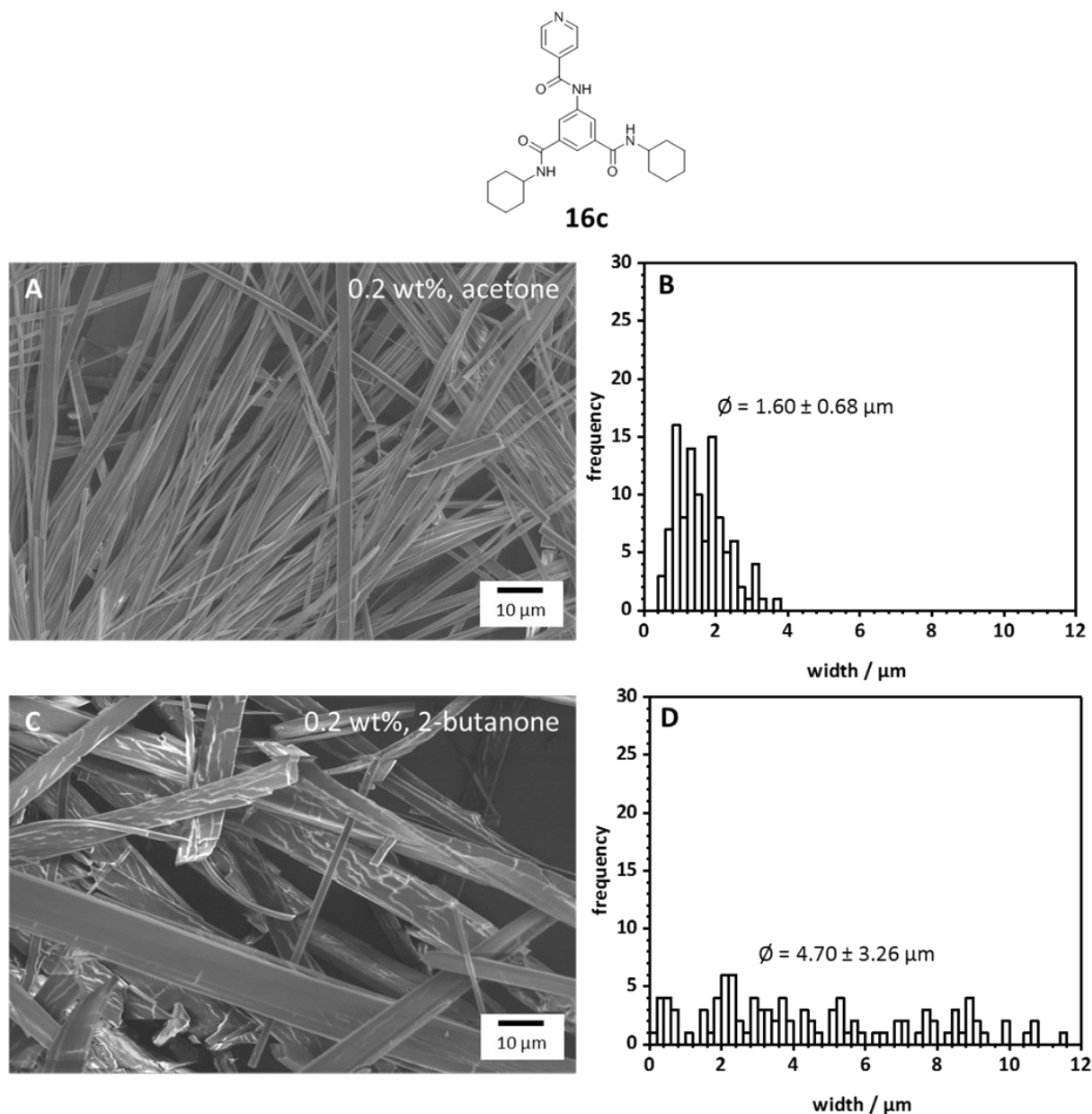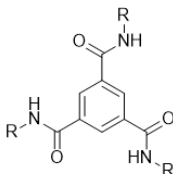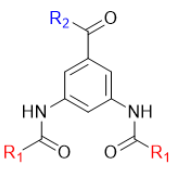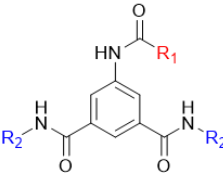

Figure 55: SEM micrographs of supramolecular ribbon-like structures of **16c** prepared by self-assembly upon cooling at a concentration of 0.2 wt% in acetone (**A**) and 2-butanone (**C**). The corresponding histograms (**B**, **D**) are based on the evaluation of at least 100 ribbons.

3.1.4 Conclusion of pyridine-containing benzenetrisamides

The syntheses of the BTAs with different numbers of pyridine substituents were all carried out successfully. This includes **3a-c**, which all exhibit three pyridine substituents and only differ in the length of the alkyl spacer between the amide and pyridine unit, **9a-c**, which are based on 3,5-dinitrobenzoic acid as core and carry two pyridine and one aliphatic substituent, and **16a-c**, which are based on 5-nitroisophthalic acid as core and carry one pyridine and two aliphatic substituents. All compounds were clearly identified by common analytic methods of organic chemistry, obtained in high purity and, with a few exceptions, in high yield. FT-IR indicates strongly bonded hydrogen bonds and the associated formation of a columnar structure via a threefold-directed hydrogen bond pattern. In the case of **3a-c**, it can be assumed that no columnar structures are formed. In particular for **3a**, this is in agreement with literature-known findings. For **9a-c** and **16a-c**, the evaluation of the IR spectra is more complicated due to the different connectivity of the amide groups with the central benzene core, which gives rise to a much larger number of vibrations. For more detailed information, crystal structure analyses would be necessary. All pyridine-containing BTAs **3a-c**, **9a-c** and **16a-c** exhibit high thermal stability. The thermal properties are summarized in **Table 2** for comparison.

Table 2: Overview of the thermal properties of BTAs **3a-c**, **9a-c** and **16a-c**, which differ in the number of pyridine substituents; n.d. = not determined.

Abbr.	Substituent R	T_m [°C]	T_c [°C]	$T_{5\% weight loss}$ [°C]
3a	pyridine	320	n.d.	371
3b	CH_2-pyridine	264	n.d.	369
3c	CH_2-CH_2-pyridine	193	n.d.	297

Abbr.	Substituent R1	Substituent R2	T_m [°C]	T_c [°C]	$T_{5\% weight loss}$ [°C]
9a	pyridine	tert-butyl	255	180	347
9b	pyridine	ethylhexyl	204	n.d.	375
9c	pyridine	cyclohexyl	250	n.d.	390

Abbr.	Substituent R1	Substituent R2	T_m [°C]	T_c [°C]	$T_{5\% weight loss}$ [°C]
16a	pyridine	tert-butyl	subl.	n.d.	313
16b	pyridine	ethylhexyl	205	148	375
16c	pyridine	cyclohexyl	293	222	379

The temperature at 5 % weight loss is at least 300 °C for all pyridine-containing BTAs. For the BTAs with three pyridine substituents, the thermal stability decreases with increasing alkyl spacer length since the contribution toward the entropy is increased by the incorporation of the alkyl chain. Strikingly, the different number of ethylhexyl substituents of **9b** and **16b** has no consequences on the thermal properties since both the temperature at 5 % weight loss and the melting temperature are identical. In contrast, the melting point of **16c** is almost 40 °C higher than that of **9c**, so the different number of cyclohexyl substituents plays a more important role. Surprisingly no crystallization peak can be observed for **9b-c**, as it is the case for **16b-c**. In contrast, a melting point is detectable for **9a** and **16a**, which may be due to the significantly smaller aliphatic substituent. Overall, it can be stated that crystallization does not occur for BTAs with three or two pyridine substituents, except for **9a.** The corresponding CNN or CCN-centered BTAs with three aliphatic substituents have significantly higher thermal stability or melting temperatures.

The solubility of **3a-c** increases with increasing spacer length so that **3c** is soluble in numerous solvents or solvent mixtures at concentrations of 1.0 wt%, whereas higher concentrations of **3a** are only soluble in solvent mixtures containing a small amount of water. Nanofibers by self-assembly upon cooling and simultaneous evaporation of the solvent were obtained only in the case of **3a**, whereas with **3b**, only hollow tubes or ribbons with significantly larger width were observed. This is the case, although the BTA molecules of **3a** and presumably also of **3b** cannot enter into columnar arrangements. Thus, despite the absence of characteristic IR vibrations indicating a columnar structure, nanostructures were generated by self-assembly processes from solution. This suggests that the secondary interactions between the amide units and the peripheral pyridine units have only a little or no negative effect on self-assembly from solution. Due to the overall good solubility of **9a-c** in numerous solvents, only very few solvent mixtures could be found from which supramolecular structures could be generated by self-assembly from solution. In contrast to **3a-c**, only ribbons with an average width of 5 µm and a broad distribution could be observed by self-assembly upon cooling, whereas self-assembly upon cooling and simultaneous evaporation of the solvent led surprisingly only to spherical particles. Furthermore, the choice of the aliphatic substituent of **9a-c** plays a crucial role since supramolecular structures were generated only with *tert*-butyl or ethylhexyl substituent. The solubility of **16a-c** in different solvents or solvent mixtures is somewhat poorer compared to **9a-c**, but this is advantageous for self-assembly. Some solvent systems could be found from which supramolecular fibers or ribbons were obtained. The choice of the aliphatic substituent within the BTA structure significantly influences the formation of supramolecular structures. Nanofibers can only be observed in the case of **16a**, which carries one pyridine and two *tert*-butyl substituents, whereas ribbons in the micrometer range were formed in the case of **16b** and **16c**, which carry the larger and more hydrophobic ethylhexyl and cyclohexyl substituents besides the pyridine substituent. These structures were formed by self-assembly upon cooling in solution after several hours/days or by storing at -18 °C.

To conclude, **3a** and **16a** are able to generate supramolecular nanofibers from solution. In the case of **16a**, fibers can be obtained by self-assembly upon cooling, i.e., the fibers are formed in the solvent. For further applications, such as the preparation of supramolecular microfiber-nanofiber composites, the fibers have to be filtered off from the solvent. Especially **3a** provides an interesting potential to be used as material for the preparation of polymer microfiber-/supramolecular nanofiber composites with *in situ* formation of fibers within the meshes of a polymer fabric due to the three pyridine substituents. Here, an important feature is also that the formation of supramolecular structures for **3a** takes place within a few minutes.

3.2 Benzenetrisamides with terpyridine substituents

In this chapter, eight BTAs **21a-c** and **24a-e**, each with three terpyridine substituents and alkyl spacers of different lengths between the amide and terpyridine unit, are described. In contrast to BTAs with simple pyridine moieties, the terpyridine side group provides the potential as an even more efficient ligand for the immobilization of metal NPs. Additionally, **21a-c** and **24a-e** differ in an amine or ether linkage between the alkyl chain and the terpyridine unit. **21b** is already described several times in literature, acting as a ligand for various metal ions. It was also investigated with respect to the self-assembly behavior from solution. **21a** and **21c**, as well as **24a-e**, were synthesized for the first time in this work. For that reason, no information about the self-assembly behavior from solution is available. Analogous to **3a-c**, the aim is to reveal what influence the systematically varied molecular structure of **21a-c** and **24a-e** has on the thermal properties, solubility and self-assembly behavior. In particular, emphasis is given on the influence of the different linkages between the alkyl chain and peripheral terpyridine substituent, as well as the different lengths of the alkyl chain spacer on the formation of columnar stackings of the BTA molecules. To address these questions, three BTAs (**21a-c**) with an amide group and five BTAs (**24a-e**) with an ether group between the alkyl chain and the terpyridine moiety are investigated. Additionally, the alkyl spacer length is varied from two (**a**) to six carbon atoms (**e**).

3.2.1 Synthesis and characterization

For a comparative investigation, **21a-c** and **24a-e** had to be synthesized first. Therefore, we revisited literature-known syntheses and synthesized new compounds. The syntheses of **21a-c** and **24a-e** were carried out by myself. Jutta Failner and Sandra Ganzleben (Macromolecular Chemistry I, University of Bayreuth) resynthesized some of these compounds under my supervision to have additional material for further investigations. The characterization of **21a-c** and **24a-e** was performed by myself.

21a-c and **24a-e** can be prepared in a two-step reaction. In a first step, a flexible linker to the terpyridine moiety was introduced by a nucleophilic substitution reaction of a chloroterpyridine with a diamine (**21a-c**) or by Williamson ether synthesis (**24a-e**) to obtain the amino-functionalized peripheral substituent. The subsequent conversion with trichloro trimesic acid to the corresponding BTA was performed according to standard literature procedures. More details on the synthesis steps are explained below.

*Synthesis of **21a-c** with alkylamine spacer between amide moiety and terpyridine unit*

In the first step, 4'-chloro-2,2':6',2''-terpyridine **17** was coupled with different diamines **18a-c** in a nucleophilic substitution reaction to obtain the amines **19a-c** according to **Scheme 4.** The reaction conditions were chosen according to literature procedures. [131,132]
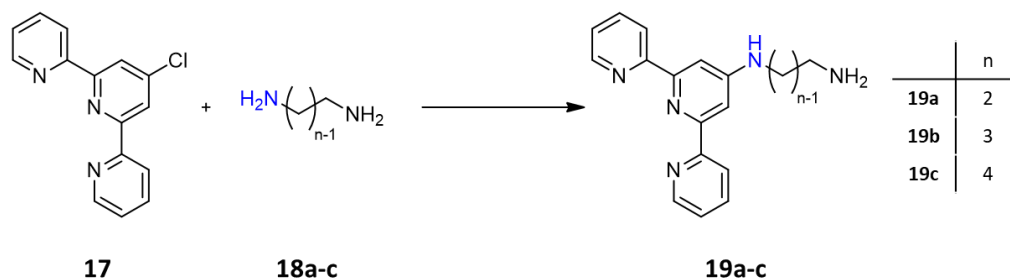
Scheme 4: Reaction of 4'-chloro-2,2':6',2''-terpyridine **17** with different diamines **18a-c** to amines **19a-c**.

In a second step, the corresponding BTAs **21a-c** were prepared by the reaction of 1,3,5-benzenetricarboxylic acid chloride **20** with previously prepared amine derivative **19a-c** in the presence of THF as solvent and triethylamine as acid scavenger (**Scheme 5**).
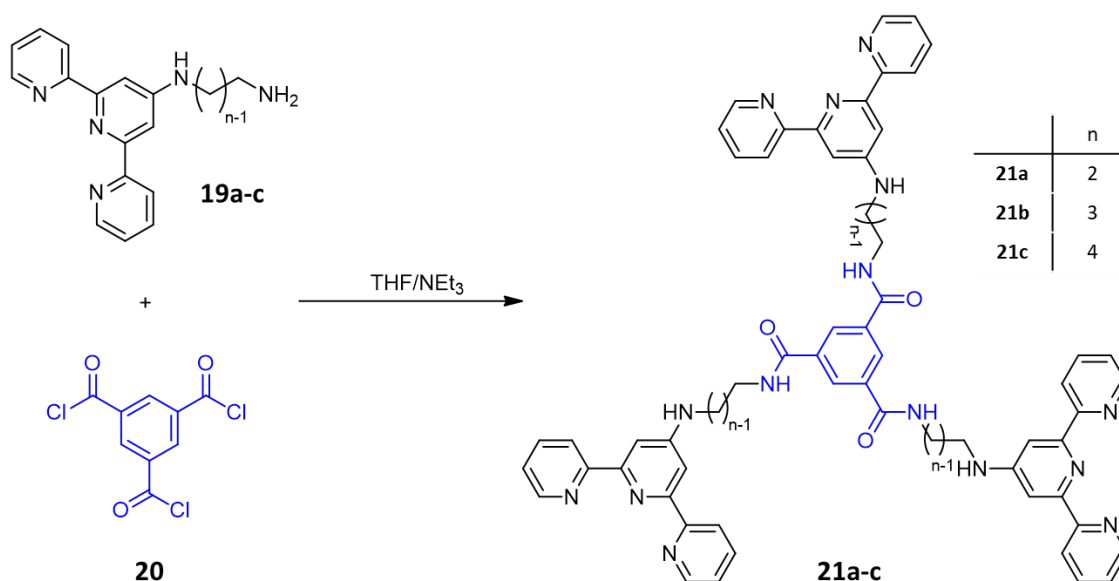
Scheme 5: Synthetic route to **21a-c** by conversion of 1,3,5-benzenetricarboxylic acid chloride **20** with the respective amine derivative **19a-c** in THF and triethylamine.

Purification of **21a-c** was performed by washing the solid with water and further recrystallization or boiling in different solvents. Detailed information on synthesis and purification is described in the experimental part (**chapter 7**). The yields after purification of **21a** and **21b** were higher at 63 % and 75 %, respectively, in contrast to the yield of **21c** at 47 %. This is attributed to the more extensive purification of **21c** by column chromatography.

Synthesis 24a-e with alkoxy alkyl spacer between amide moiety and terpyridine unit

First, 4-Chloro-2,2':6',2''-terpyridine **17** was coupled with various amino alcohols **22a-e** in a Williamson's ether synthesis to obtain the corresponding amines **23a-e** according to **Scheme 6**. The reaction conditions were chosen according to literature procedures. [133–137]
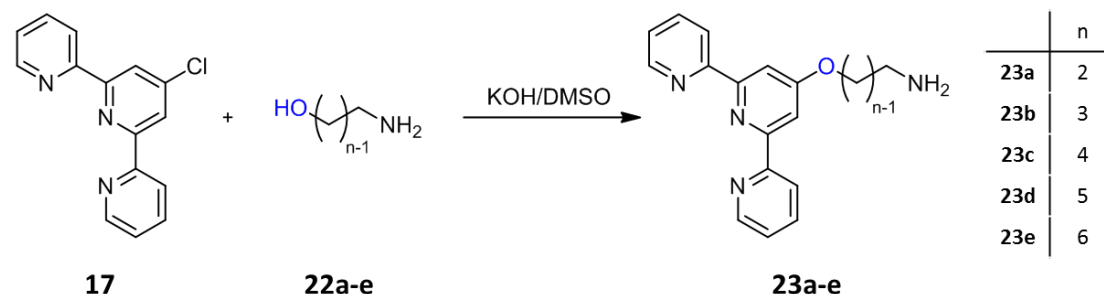
Scheme 6: Reaction of 4-Chloro-2,2':6',2''-terpyridine **17** with different amino alcohols **22a-e** to amines **23a-e**.

The synthesis of **24a-e** was performed analogously to **21a-c** according to **Scheme 7**.
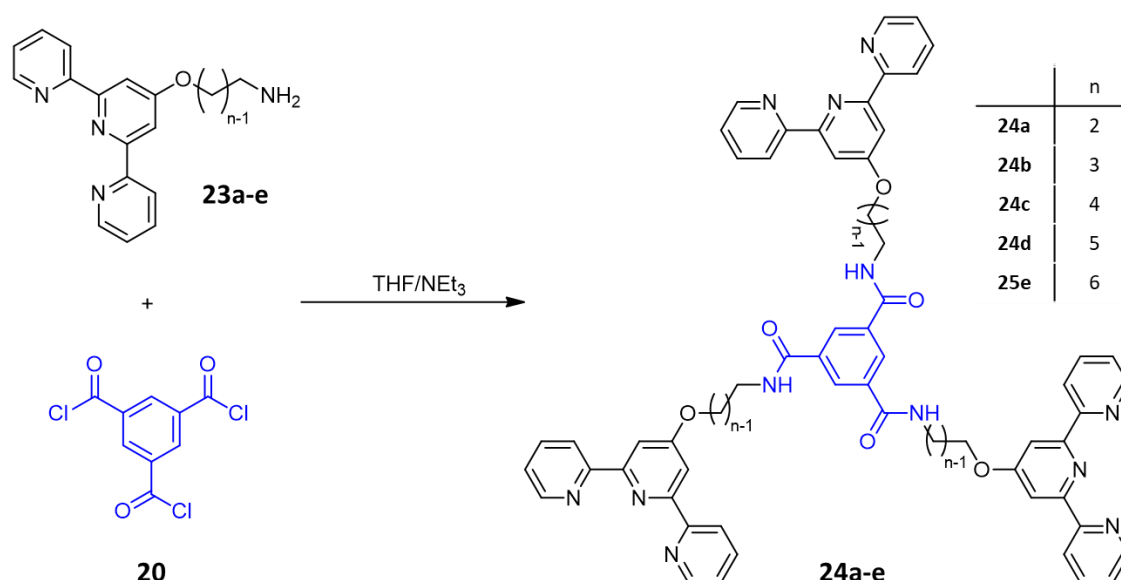
Scheme 7: Synthetic route to **24a-e** by conversion of 1,3,5-benzenetricarboxylic acid chloride **20** with the respective amine derivative **23a-e** in THF and triethylamine.

Purification of **24a-e** was performed by washing the solid with water and by further recrystallization or boiling in different solvents. Detailed information on synthesis and purification is described in the experimental part (**chapter 7**). Except for **24c**, the yield after purification was in the range of about 85 % in each case. **24c** was obtained with a somewhat low yield of 66 %. The BTAs **21a-c** and **24a-e** were structurally characterized and clearly identified by ^{1}H-NMR spectroscopy, mass spectrometry and FT-IR spectroscopy. Thermal characterization was performed by DSC and TGA measurements.

Molecular characterization

In the following, the ¹H-NMR spectra of **21a**, which has an ethylamine spacer and **24a**, which exhibits an ethoxy spacer, are presented exemplarily and discussed in more detail. **Figure 56** shows the ¹H-NMR spectrum of **21a** measured in DMSO.
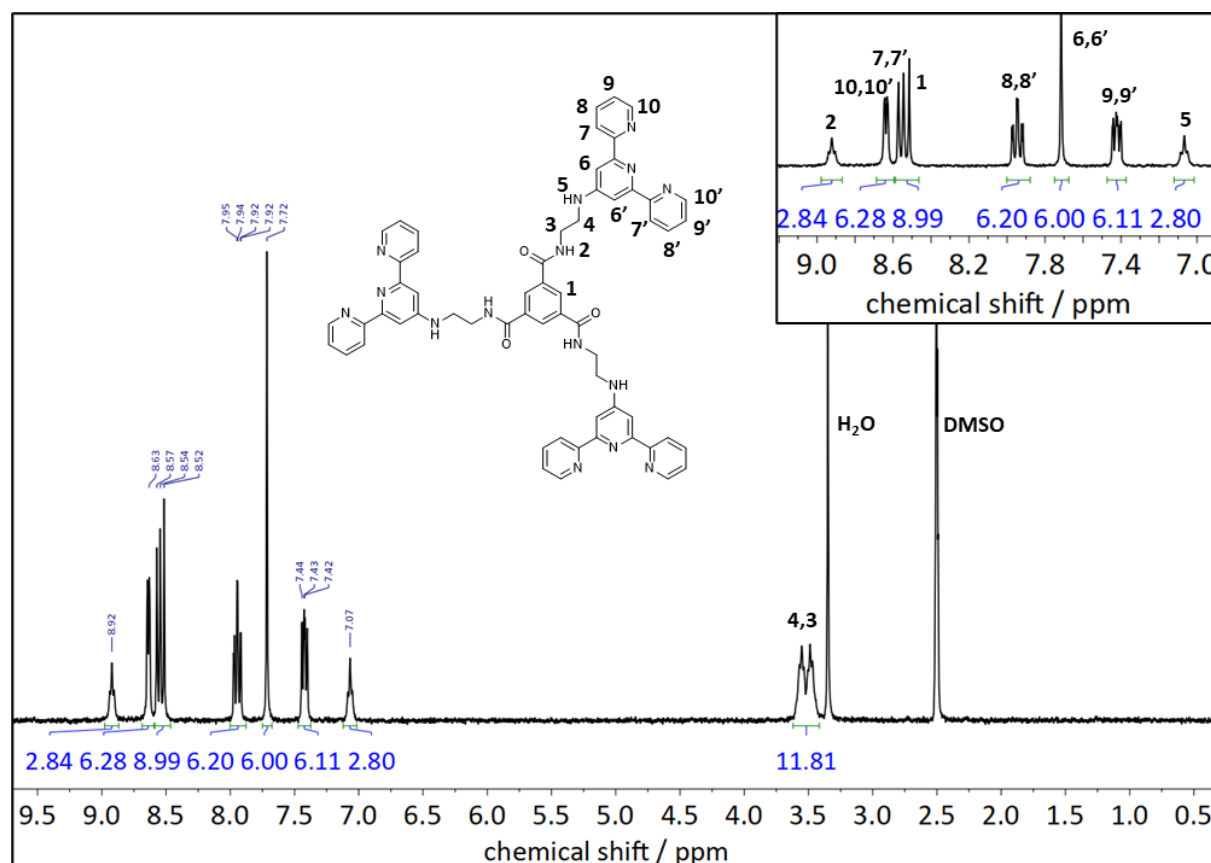
Figure 56: ¹H-NMR spectra of **21a** measured in deuterated DMSO. The signals were assigned to the corresponding hydrogen atoms according to the chemical structure of **21a**.

The N-H protons of the amide groups can be found at 8.92 ppm as a triplet (**2**). A sharp singlet at 8.50 ppm corresponds to the three protons of the central benzene core (**1**). The signals of both methylene groups can be found at 3.47 ppm (**3**) and 3.55 ppm (**4**). The protons of the aromatic terpyridine substituent can be assigned to the signals at 7.42, 7.71, 7.94, 8.55 and 8.63 ppm (**6-10**). Compound **21a** based on trimesic acid trichloride was attributed to the singlet of (**1**) representing a threefold symmetric substitution pattern and by the integration ratio of signals **1** and **3,4**. The clear assignment and absence of other signals allow for unambiguous identification of compound **21a** in high purity. **21b** and **21c** were evaluated and identified in the same manner. Their spectra are shown in **Figure 140** and **Figure 141**.

The NMR spectrum of **24a** shown in **Figure 57** looks very similar to **Figure 56** since both compounds differ only in the linkage of the alkyl chain and the terpyridine substituent.
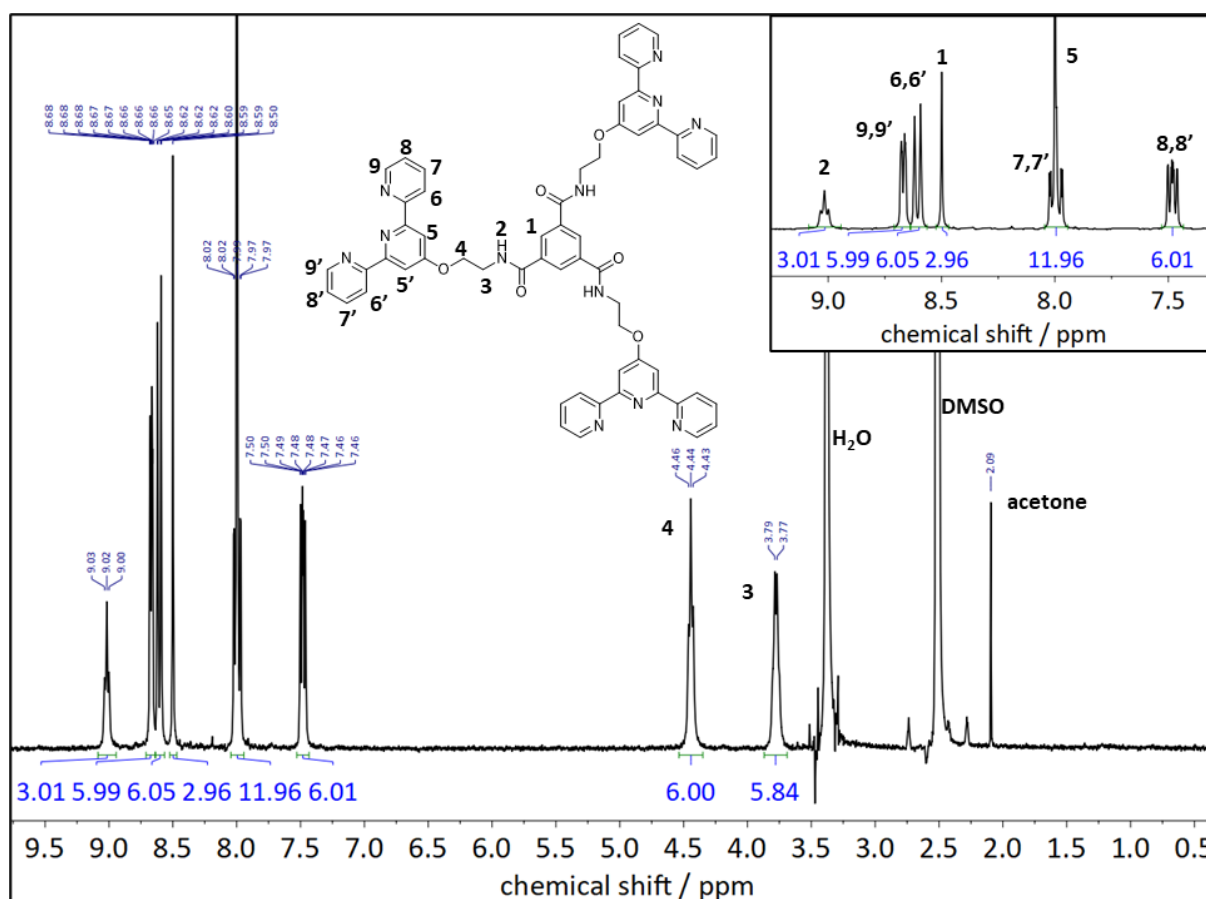
Figure 57: ^{1}H-NMR spectra of **24a** measured in deuterated DMSO. The signals were assigned to the corresponding hydrogen atoms according to the chemical structure of **24a**.

In a similar manner as outlined above, the N-H protons of the amide groups can be found at 9.00 ppm as a triplet (**2**). A sharp singlet at 8.49 ppm corresponds to the three protons of the central benzene core (**1**). The signal of the methylene group next to the ether group can be found at 4.43 ppm (**4**) and is shifted towards higher ppm values compared to the methylene group next to the amide group, which is observed at 3.77 ppm (**3**). Compared to the NMR spectrum of **21a**, the signals of both methylene groups are low field-shifted to higher ppm values due to a weaker -I effect of the ether group in contrast to the amine group. The protons of the aromatic terpyridine substituent can be assigned to the signals at 7.47, 7.95-8.01, 8.59 and 8.60 ppm (**5-9**). Signal **5** is shifted towards higher ppm values compared to the corresponding signal **6** in **Figure 56** due to the replacement of the amine group by an ether group. Compound **24a** based on trimesic acid trichloride was attributed to the singlet of (**1**) representing a threefold symmetric substitution pattern and by the integration ratio of signals **1** and **4**. The clear assignment and absence of other signals allow for unambiguous identification of compound **24a** in high purity. **24b-e** were evaluated and identified in the same manner. Their spectra are shown in **Figures 142-145**.

Investigation of hydrogen bonding interactions by FT-IR spectroscopy

FT-IR measurements were performed as described in the previous **chapter 3.1** to investigate the formation of columnar stacking due to the formation of three directed hydrogen bonds. The corresponding IR spectra of **21a-c** and **24a-e** are shown in **Figure 58** and **Figure 59**.
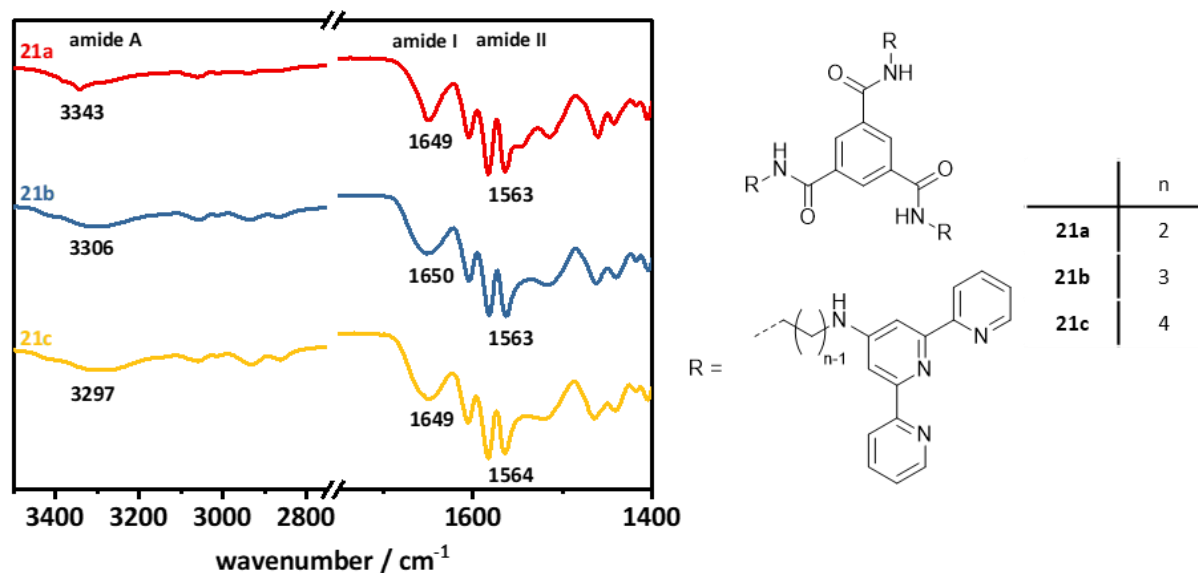
Figure 58: Normalized IR spectra of **21a-c** in the relevant wavenumber range of 3500-2800 cm^{-1} and 1750-1400 cm^{-1}.

The N-H stretching vibration (amide A) of **21a-c** shows a trend to higher wavenumbers compared to the characteristic amide A vibration at ~3240 cm^{-1}, which would indicate columnar stacking of the BTAs. The C=O stretching vibration (amide I) is located at a wavenumber of about 1650 cm^{-1} and the amide II vibration can be identified at a wavenumber of about 1560 cm^{-1}. Due to the shift of the amide A signal, self-aggregation into columnar structures is not assumed for **21a-c**. However, for **21b**, which is known from the literature, the amide A vibration at 3245 cm^{-1}, the amide I vibration at 1637 cm^{-1} and the amide II vibration at 1527 cm^{-1} have been reported. In this case, there is a shift of the amide II signal and not of the amide A signal. To date, no terpyridine-substituted BTA has undergone single-crystal structure analysis to be able to make clear statements about the crystal structure and formation of columnar structures.
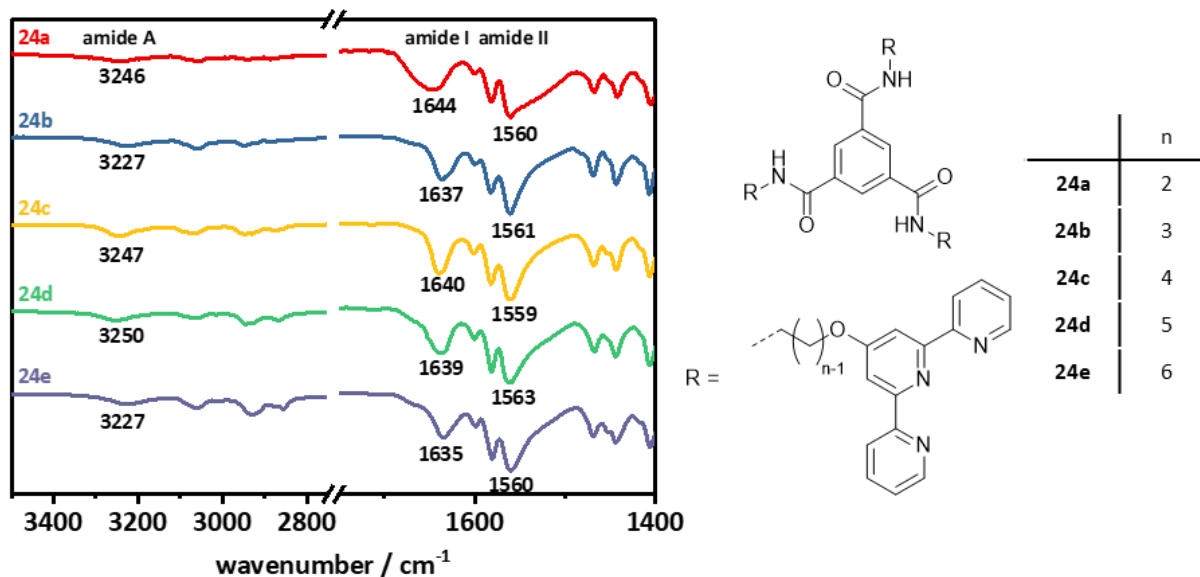
Figure 59: Normalized IR spectra of **24a-e** in the relevant wavenumber range of 3500-2800 cm^{-1} and 1750-1400 cm^{-1}.

In the case of **24a-e**, the typical amide A (3227-3267 cm^{-1}) and amide II vibration (1559-1563 cm^{-1}), which are indicative of columnar arrangements, can be recognized. Additionally, **24a-e** show a signal (C=O stretching vibration) at 1635-1646 cm^{-1}. Based on the identified signals, it can be assumed that **24a-e** form supramolecular columns by three-directional hydrogen bonds. The different length of the alkyl spacer, therefore, has no influence on this behavior since no significant difference can be observed in the respective IR spectra of **24a-e**.

Thermal characterization

The thermal behavior of terpyridine-containing BTAs was investigated by means of TGA and DSC measurements, as described in **chapter 3.1**. The corresponding TGA curves of **21a-c** and **24a-e** are shown in **Figure 60**.
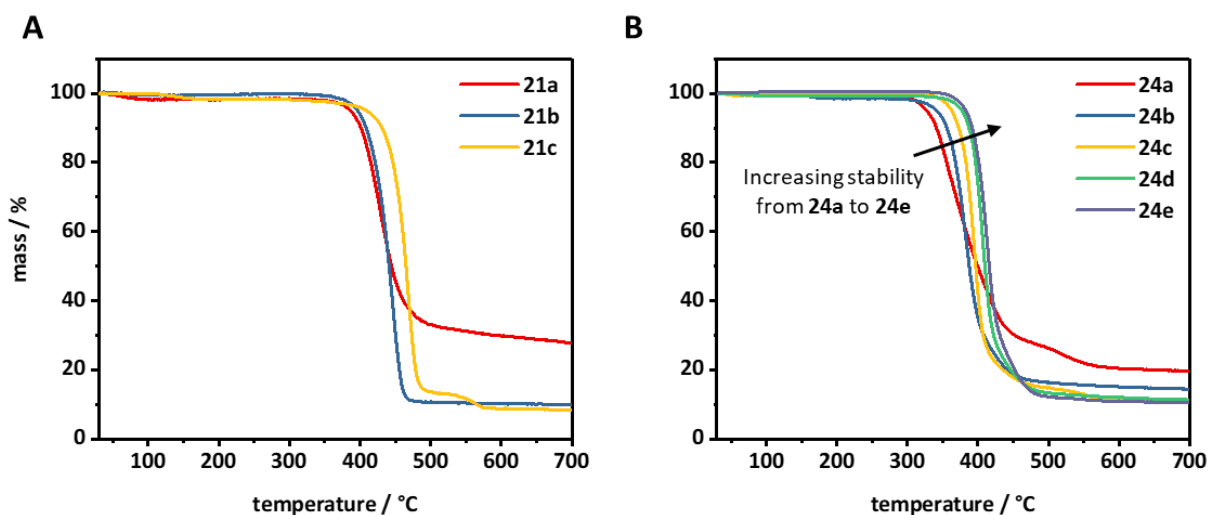
Figure 60: Thermogravimetric analysis of (**A**) **21a-c** and (**B**) **24a-e** in a temperature range of 30-700 °C under nitrogen atmosphere and a heating rate of 10 K/min.

All terpyridine-containing BTAs **21a-c** and **24a-e** exhibit high thermal stability, which is here also attributed to the formation of hydrogen bonds. The temperature at 5 % weight loss for **21a-c** is in the range between 387-408 °C. Compared to **21a-c**, **24a-e** show a slightly lower thermal stability with a temperature of 327-382 °C at 5 % weight loss. **Figure 60B** clearly shows that the thermal stability increases from **24a** to **24e**. The alkyl chain between the amide group and the terpyridine unit, which increases by one methylene group from **24a** to **24e**, decouples the peripheral terpyridine substituent from the amide unit. A slight weight loss of 1-2 % at the beginning of the TGA curves can be observed for most of the terpyridine-containing BTAs, which is attributed to trapped solvent, which can evaporate under these conditions during the measurement. The TGA curves also show that for **21a** a residue of 20 % and in the case of **21b** and **21c** of 10 % remains even at high temperatures. The same behavior can be observed for **24a-e**.

The DSC measurements, which were performed analogously to the previous DSC measurements in the range of 50-300 °C, are shown in the appendix (**chapter 8**). No phase transitions can be observed for **21a-c,** whereas only very weak and ambiguous melting transitions can be seen for **24a-e**. It is striking that if at all and except for **24e**, a phase transition can only be observed in the first heating curve. A clear trend with respect to the melting temperature is not evident due to the variation in alkyl chain length from **21a-c** or **24a-e**.

In summary, **21a-c** and **24a-e** have high thermal stability up to a minimum temperature of 300 °C and also the melting points (if any) are above 150 °C. For this reason, solubility tests or processing steps with temperatures up to 150 °C are no problem for the corresponding BTAs. The thermal properties - i.e., the melting temperature T_m, the crystallization temperature T_c and the temperature at 5 % weight loss $T_{5\% \text{ weight loss}}$ - are summarized in **Table 3**.

Table 3: Overview of the thermal properties of **21a-c** and **24a-e** with their corresponding melting temperatures T_m and crystallization temperatures T_c (determined by DSC) and the temperature at 5 % weight loss $T_{5\% \text{ weight loss}}$ (determined by TGA measurements under N_2 atmosphere and a heating rate of 10 K/min). For some compounds, no melting endotherm or crystallization exotherm up to 300 °C were determined (marked with n.d. = not determined), whereas the other compounds exhibit melting endotherms. The melting temperatures were determined from the first heating curve of the DSC measurement.

Abbr.	21a	21b	21c
Substituent			
T_m [°C]	n.d.	n.d.	n.d.
T_c [°C]	n.d.	n.d.	n.d.
$T_{5\% \text{ weight loss}}$ [°C]	387	396	408

Abbr.	24a	24b	24c	24d	24e
Substituent					
T_m [°C]	157	228	237	172	218
T_c [°C]	n.d.	n.d.	n.d.	n.d.	157
$T_{5\% \text{ weight loss}}$ [°C]	327	341	362	377	382

3.2.2 Self-assembly studies
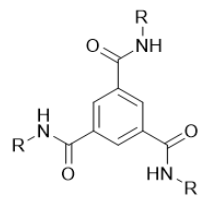
Only in the case of **21b** self-assembly studies are known. Here it was demonstrated that **21b** can form a supramolecular gel from a MeOH/H_2O (3:7 (w/w)) solvent mixture. Very thin nanofibers with intertwining bundles of strings were revealed for dried gels. [122] For all the other synthesized BTAs **21a**, **21c** and **24a-e**, no information about the self-assembly behavior can be found in literature.
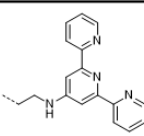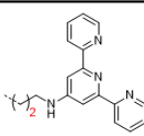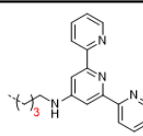
To get a comprehensive investigation of the formation of supramolecular nanoobjects based on terpyridine-containing BTAs, the solubility and self-assembly behavior of **21a-c** and **24a-e** were investigated. In this context, we particularly wanted to study the structure-property relations with respect to the self-assembly behavior of the terpyridine-containing BTAs **21a-c** and **24a-e**. The series allows one to investigate whether the different length of the alkyl spacer has an effect on the formation of supramolecular fibers. Additionally, we wanted to find out what effects the two different linkages between the alkyl chain and terpyridine substituent have on the solubility and self-assembly behavior. For this purpose, similar to what was described in **chapter 3.1.2.2**, investigations on the solubility of the BTAs as well as the formation of nanoobjects by self-assembly from solution were investigated. In a screening experiment, the solubility of **21a-c** and **24a-e** was evaluated in 15 common organic solvents as well as four solvent mixtures (EtOH/H_2O, IPA/H_2O, 1-propanol (NPA)/H_2O and THF/H_2O) in certain proportions (1:9 to 9:1 (w/w)) at elevated temperatures. Here, the water-based solvent mixtures are of particular interest from an environmental point of view. As a standard concentration for the BTA solution, 0.1 wt% was selected.
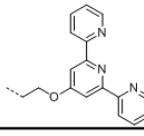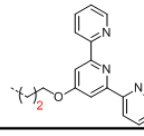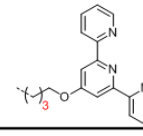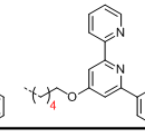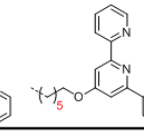
The solubility behavior of **21a-c** differs due to the different alkyl spacer lengths. All three compounds **21a-c** are completely insoluble in water. This is of great importance for further applications, such as the immobilization of NPs from aqueous media. A clear trend in solubility was that with increasing spacer length within the BTA structure, the solubility in polar solvents, especially short-chain alcohols such as EtOH, IPA and NPA, decreased. **21a-c** could be completely dissolved in selected solvents such as DMSO or DMF. However, no other trend was observed regarding the kind of solvent and molecular structure of **21a-c**. In the four selected mixtures of organic solvent and water, **21a** and **21b** are completely soluble up to a certain ratio, which is shown in **Table 4**, whereas **21c** is completely insoluble in all four solvent mixtures. In contrast to **21a-c** with different alkylamine spacers, **24a-e**, which exhibit an alkoxy spacer of different lengths, are not completely soluble in short-chain alcohols such as EtOH, IPA or NPA at a BTA concentration of 0.1 wt%. As expected, **24a-e** are completely insoluble in aqueous medium. In aprotic solvents such as DMSO, DMF or chloroform, **24a-e** are completely soluble. However, the four selected solvent mixtures, each containing a certain proportion of water, are the most promising candidates from an environmental point of view and since complete solubility was found independent of the length of the alkyl chain spacer for all compounds **24a-e** at certain solvent mixture ratios (see **Table 4**). Here, it was found that for complete solubility of **24a-e**, the organic solvent content must be larger than the water content. With increasing alkyl spacer length of **24a-e**,

the solubility in the four solvent mixtures decreased, i.e., **24a** is completely soluble in all four solvent mixtures, whereas **24d** or **24e** are only soluble in NPA/H_2O and THF/H_2O mixture at certain ratios. **Table 4** summarizes the solubility of **21a-c** and **24a-e** in the four solvent mixtures.

Table 4: Solubility of **21a-c** und **24a-e** in different solvent mixtures at a BTA concentration of 0.1 wt%. In each case, the solvent ratio at which the corresponding BTA is completely dissolved is indicated.

Abbr.	21a	21b	21c
Substituent			
EtOH / H_2O	≥6:4 ✓	≥4:6 ✓	✗
NPA / H_2O	≥6:4 ✓	≥3:7 ✓	✗
IPA / H_2O	≥6:4 ✓	≥4:6 ✓	✗
THF / H_2O	≥5:5 ✓	≥5:5 ✓	✗

Abbr.	24a	24b	24c	24d	24e
Substituent					
EtOH / H_2O	≥9:1 ✓	≥6:4 ✓	✗	✗	✗
NPA / H_2O	≥9:1 ✓	≥6:4 ✓	≥7:3 ✓	≥8:2 ✓	≥8:2 ✓
IPA / H_2O	≥9:1 ✓	≥9:1 ✓	≥9:1 ✓	✗	✗
THF / H_2O	≥5:5 ✓	≥5:5 ✓	≥8:2 ✓	≥5:5 ✓	≥8:2 ✓

Comparing **21a** with **24a** or **21b** with **24b**, which each have the same spacer length and differ only in the linkage between the alkyl chain and the terpyridine substituent (-O- or -NH-), it can be concluded that **21a** or **21b**, which have the -NH- linkage, show a better solubility.

Two different self-assembly processes from solution, shown schematically in **Figure 61**, were performed to check whether both processes are suitable for the preparation of supramolecular functional BTA nanofibers. Details about both self-assembly processes and the possibility to generate supramolecular fibers via these methods are essential for the later preparation of functional microfiber-nanofiber composites (see **chapter 4**). Here, the *in situ* formation of supramolecular BTA nanofibers in polymer fabrics or nonwovens is based on the self-assembly process upon cooling and simultaneous evaporation of the solvent, whereas for the preparation of composite nonwoven sheets via the wet-laid technique, self-assembly upon cooling is relevant.
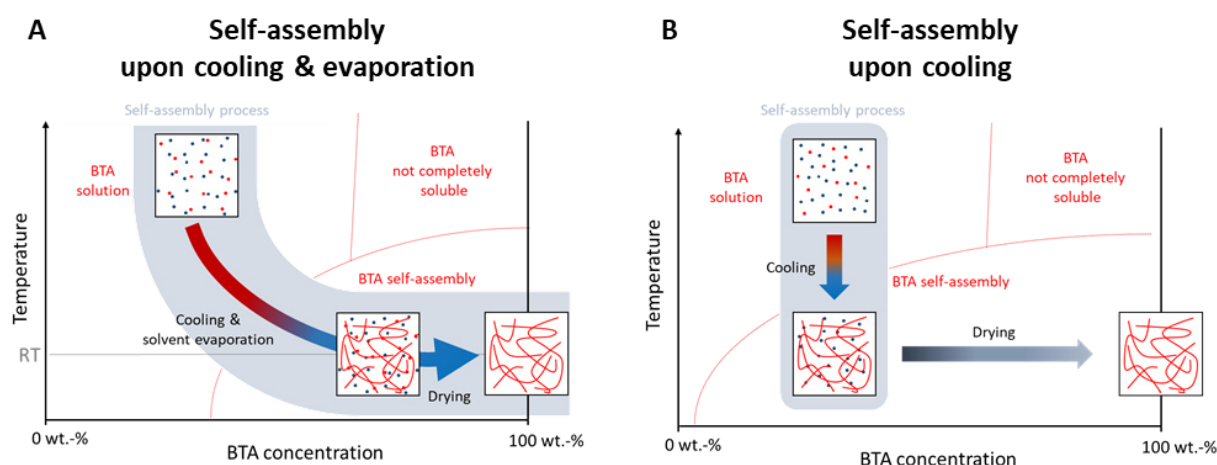
Figure 61: Schematic representation of the self-assembly process from solution (**A**) upon cooling and simultaneous evaporation of the solvent and (**B**) upon cooling of the BTA solution. In both cases, the BTA (red dots) is completely dissolved in the solvent (blue dots) at elevated temperatures. Upon cooling and simultaneous evaporation of the solvent (**A**) or by cooling the BTA solution (**B**), the formation of supramolecular nanofibers (red lines) is induced, resulting in supramolecular BTA nanofibers. Source: University of Bayreuth; Macromolecular Chemistry I.

To investigate what kind of morphology or especially if supramolecular BTA nanofibers are formed after self-assembly, a droplet of all completely dissolved BTA solutions was deposited on a silicon wafer in case of self-assembly upon cooling and evaporation. In the case of self-assembly upon cooling, a droplet was taken from all samples, in which the BTA self-assembled by cooling of the BTA solution and was also deposited on a silicon wafer. After complete evaporation of the solvent at RT, the samples were sputtered with platinum and examined by SEM.

In the following, selected examples of SEM micrographs after self-assembly of **21a-c** and **24a-e** from solution are shown and discussed.

*Supramolecular structures of **21a-c***

As shown in **Figure 62**, supramolecular fibers of **21a** can be generated by self-assembly from a 6:4 (w/w) EtOH/H_2O solvent mixture. After self-assembly upon cooling and evaporation, there are not only extremely thin nanofibers with a diameter of 38 ± 11 nm but also many spherical particles or vesicles. By self-assembly upon cooling, supramolecular fibers with a diameter of 135 ± 83 nm are formed within one day at RT. A few additional spherical particles/vesicles are most likely formed during the evaporation of the solvent. The fiber diameter is significantly larger and the distribution of the fiber diameter is much broader than by self-assembly upon cooling and evaporation. The same self-assembly behavior is observed with a 6:4 (w/w) IPA/H_2O or NPA/H_2O solvent mixture. Interestingly, only vesicles and no nanofibers are formed in the case of solvent mixtures with a higher alcohol proportion than described above. The solutions remain clear for weeks (even at storing at -18 °C) so that no self-assembly upon cooling takes place. Even if **21a** can be dissolved completely in a THF/H_2O solvent mixture above a ratio of 5:5, this system is not suitable for the fabrication of supramolecular fibers.

0.1 wt%, EtOH/H$_2$O 6:4 (w/w)

Self-assembly upon cooling & evaporation   **Self-assembly upon cooling**

Figure 62: SEM micrographs of spherical particles and supramolecular fibers of **21a** prepared by self-assembly upon cooling and evaporation (**A, B**) and self-assembly upon cooling (**D, E**) at a concentration of 0.1 wt% in a 6:4 (w/w) EtOH/H$_2$O solvent mixture. The corresponding fiber diameter histograms (**C, F**) are based on the evaluation of at least 100 fibers.

The two structurally similar **21b** and **21c** showed similar self-assembly behavior (not shown). However, **21c** could never be completely dissolved in the selected solvent systems. Self-assembly upon cooling and simultaneous solvent evaporation only leads to the formation of spherical particles/vesicles, whereas in the case of self-assembly upon cooling, supramolecular fibers were formed after a few hours. Again, some spherical particles/vesicles were detected, which are probably caused by the evaporation of the solvent and the associated self-assembly into vesicles.

Supramolecular structures of 24a-e

Figure 63 shows exemplarily the supramolecular structures of **24a**, which are obtained by self-assembly upon cooling and simultaneous solvent evaporation from DMF or DMSO solution.
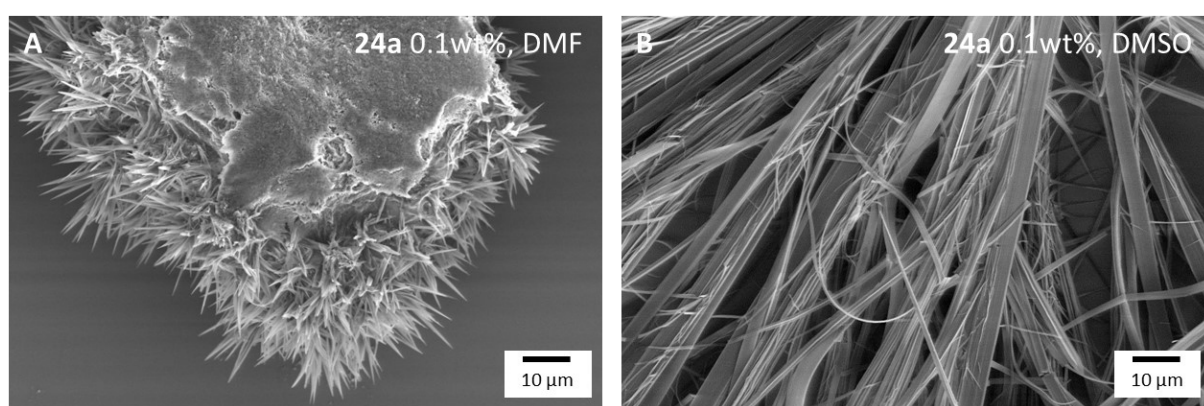
Figure 63: SEM micrographs of supramolecular structures of **24a** prepared by self-assembly upon cooling and evaporation at a concentration of 0.1 wt% in DMF and DMSO.

Fibrous structures are formed from both DMF and DMSO solutions. Using DMF as a solvent, not only sharp fibrous structures with a length of around 10-20 µm but also on top of these structures, significantly thinner and longer fibers are formed. In contrast, very long fibers (up to 400 µm) with a broad fiber diameter distribution are observed upon self-assembly from DMSO. **24b-e** can also be dissolved in the same pure solvents, but no supramolecular fibers are formed via self-assembly (not shown).

The formation of supramolecular fibers depends, as described previously, on various parameters such as the solvent system. This is illustrated by the following **Figure 64** and **Figure 65**, which show SEM micrographs of the supramolecular structures of **24a-e** formed by self-assembly upon cooling and simultaneous solvent evaporation from two different solvent mixtures (NPA/H_2O and THF/H_2O) at a BTA concentration of 0.1 wt%.

Prepared from a 9:1 (w/w) NPA/H$_2$O solvent mixture
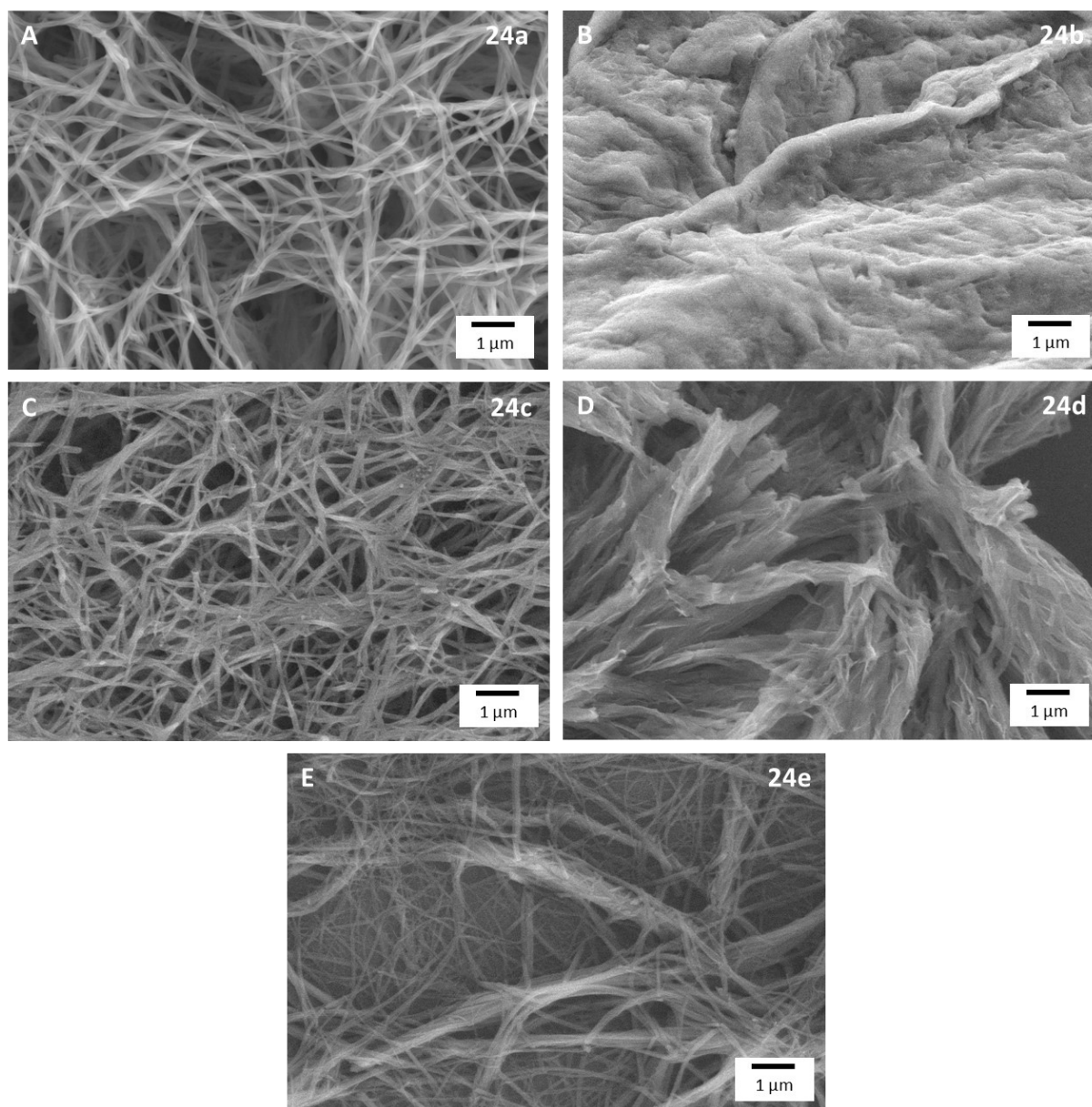
Figure 64: SEM micrographs of supramolecular structures of **24a-e** prepared by self-assembly upon cooling and evaporation at a concentration of 0.1 wt% in a 9:1 (w/w) NPA/H$_2$O solvent mixture.

In a 9:1 (w/w) NPA/H$_2$O solvent mixture, **24a-e** are completely soluble. Regardless of the molecular structure of **24a-e**, fibrous structures are observed by self-assembly upon cooling and evaporation. SEM micrographs of **24a, 24c** and **24e** show distinct supramolecular nanofibers, whereas fibrous structures can only be assumed in the case of **24b** and considerably thicker fibers or several fibers laid together are observed for **24d**.

Figure 65 shows the obtained morphologies after self-assembly upon cooling and evaporation from an 8:2 (w/w) THF/H$_2$O solvent mixture at a concentration of 0.1 wt% **24a-e**.

Prepared from a 8:2 (w/w) THF/H$_2$O solvent mixture
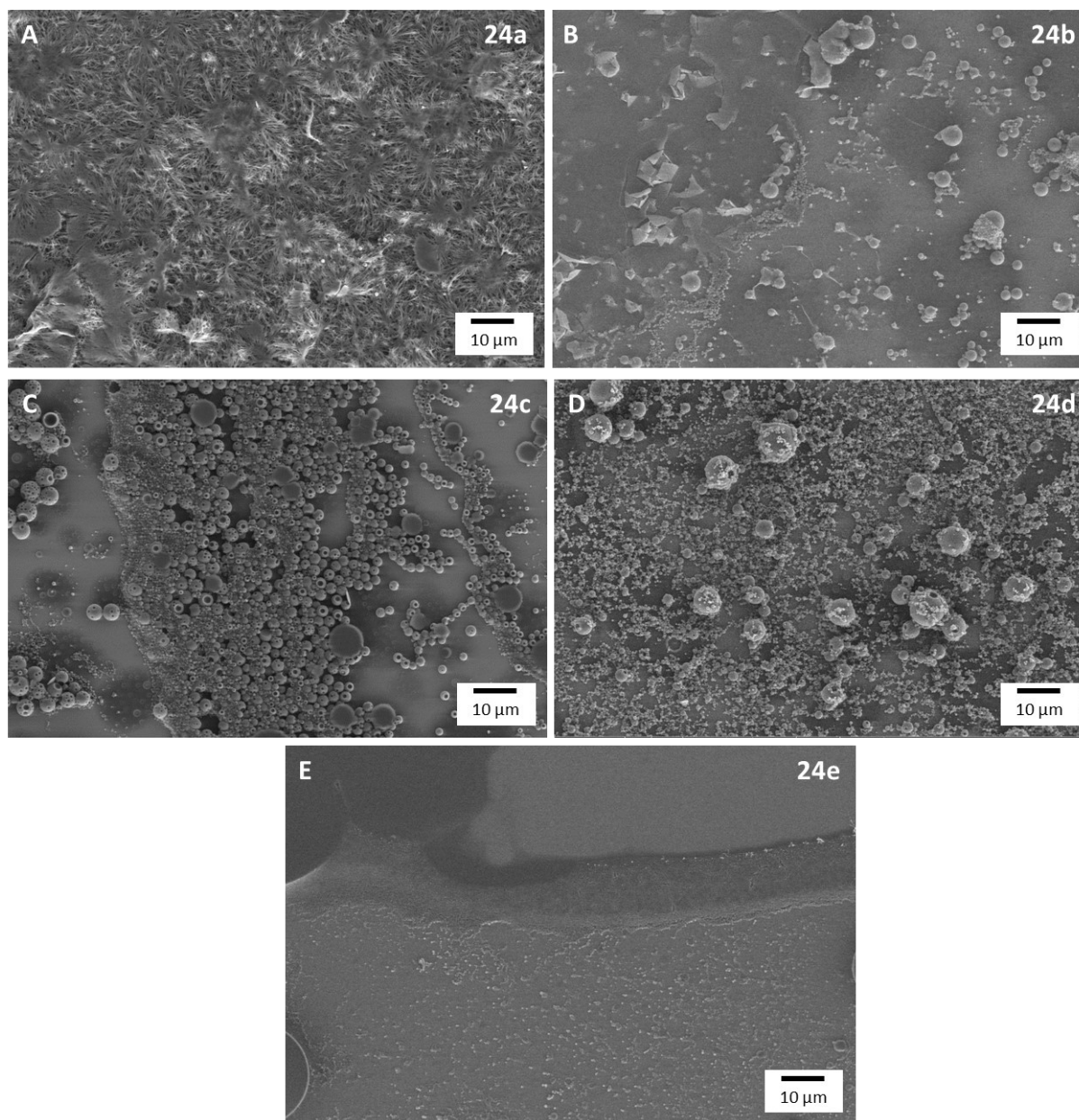
Figure 65: SEM micrographs of supramolecular structures of **24a-e** prepared by self-assembly upon cooling and evaporation at a concentration of 0.1 wt% in an 8:2 (w/w) THF/H$_2$O solvent mixture.

24a-e are optically completely soluble in an 8:2 (w/w) THF/H$_2$O solvent mixture. However, in contrast to the NPA/H$_2$O solvent mixture, no supramolecular fibers are formed from a THF/H$_2$O solvent mixture by self-assembly upon cooling and evaporation. The SEM micrographs show spherical particles, vesicles or indefinable structures. **24c** forms micrometer-sized vesicles, whereas **24b, 24d** and **24e** show a mixture of spherical particles and vesicles with a size of 0.5-1.5 µm. Fiber-like structures can only be observed in the case of **24a**. Here it looks like the fibers start to grow from several central

points, where evaporation takes place first. However, single spherical particles can also be seen. The same morphology is observed at lower BTA concentrations. Therefore, the formation of spherical particles does not occur due to the incomplete dissolution of the BTAs in the THF/H_2O solvent mixture.

Figure 64 and **Figure 65** clearly show what influence the solvent system has on the self-assembly behavior of **24a-e**. Besides the choice of solvent, the chemical structure also plays a decisive role in the formation of supramolecular structures. For that reason, the supramolecular structures of **24a** and **24e**, which differ in the length of the alkyl spacer length, are exemplarily shown for both self-assembly processes.

Figure 66 shows SEM micrographs of supramolecular fibers of **24a** formed by self-assembly from a 9:1 (w/w) IPA/H$_2$O solvent mixture and the corresponding fiber diameter histograms.
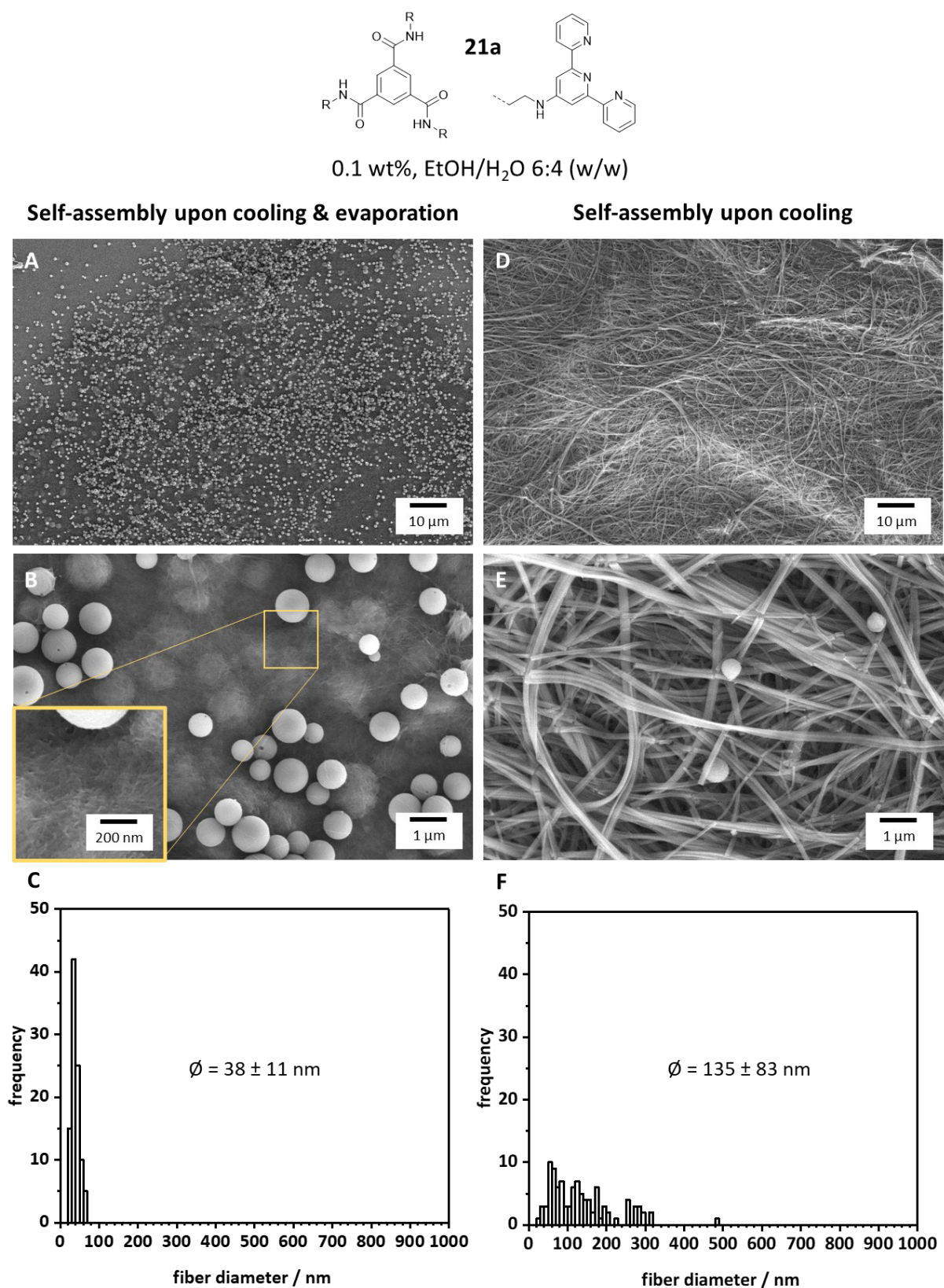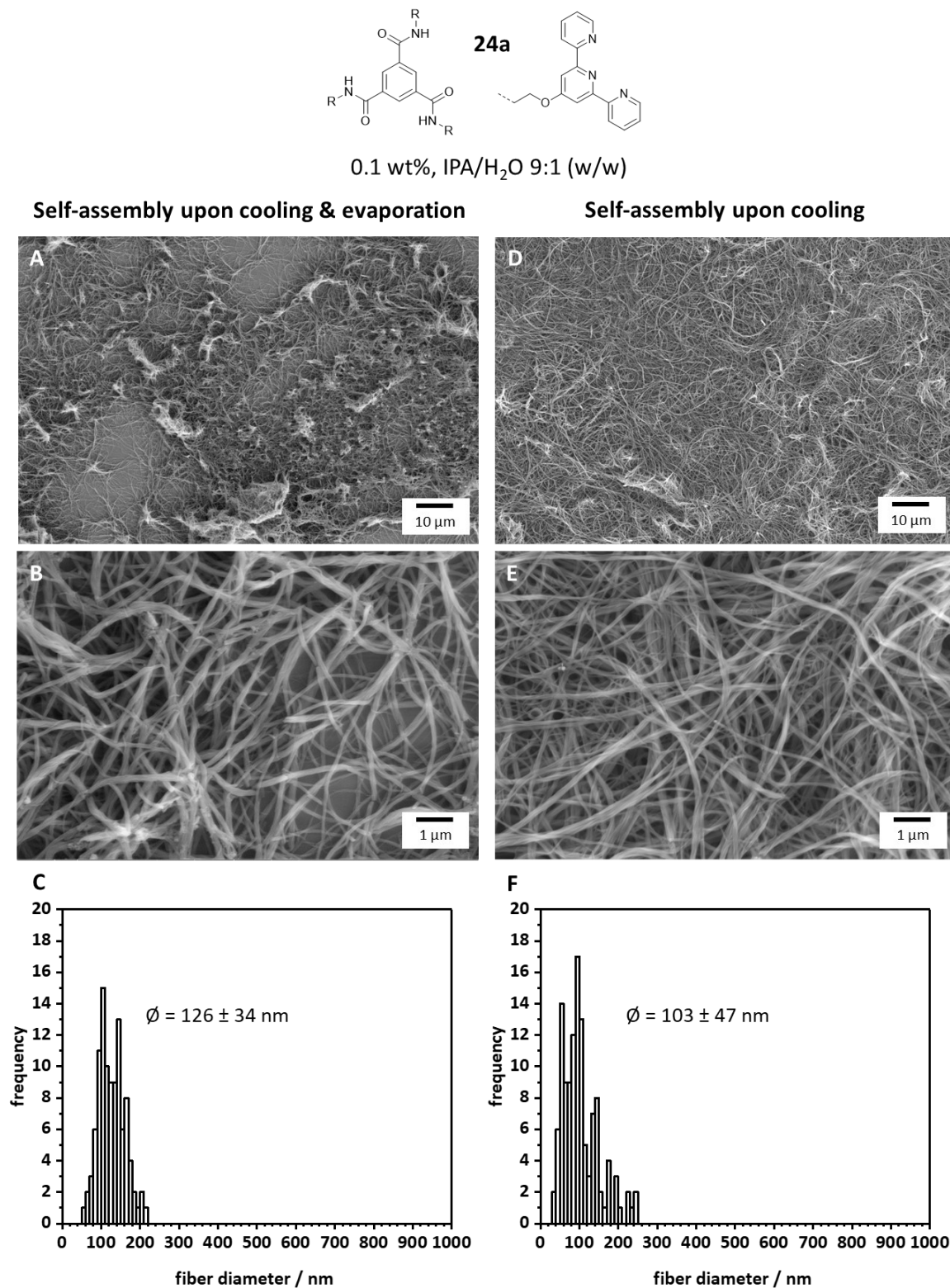

Figure 66: SEM micrographs of supramolecular fibers of **24a** prepared by self-assembly upon cooling and evaporation (**A, B**) and self-assembly upon cooling (**D, E**) at a concentration of 0.1 wt% in a 9:1 (w/w) IPA/H$_2$O solvent mixture. The corresponding fiber diameter histograms (**C, F**) are based on the evaluation of at least 100 fibers.

As shown in **Figure 66**, supramolecular fibers of **24a** are formed from a 9:1 (w/w) IPA/H_2O solvent mixture by self-assembly upon cooling and evaporation as well as by self-assembly upon cooling at a concentration of 0.1 wt%. The fiber diameter is in the same order of magnitude for both self-assembly methods, with a value of about 100-120 nm. The fiber histograms show a rather narrow distribution of the fiber diameters. Most fibers have a length in the range of 10-100 µm. The formation of supramolecular nanofibers took place within about 60 min for both methods. Similar self-assembly behavior was observed when using EtOH/H_2O or NPA/H_2O solvent mixtures in a ratio of 9:1 (w/w). The fiber diameter of the BTA fibers using these solvent systems is also in the range of approx. 100 nm.

In comparison to **24a**, **Figure 67** shows SEM micrographs of supramolecular fibers of **24e**, which has the longest alkyl spacer, formed by self-assembly from a 9:1 (w/w) NPA/H_2O solvent mixture.

24e

0.1 wt%, NPA/H_2O 9:1 (w/w)

Self-assembly upon cooling & evaporation

Self-assembly upon cooling

$\emptyset$ = 103 ± 36 nm

$\emptyset$ = 195 ± 85 nm

Figure 67: SEM micrographs of supramolecular fibers of **24e** prepared by self-assembly upon cooling and evaporation (**A, B**) and self-assembly upon cooling (**D, E**) at a concentration of 0.1 wt% in a 9:1 (w/w) NPA/H_2O solvent mixture. The corresponding fiber diameter histograms (**C, F**) are based on the evaluation of at least 100 fibers.

24e can be dissolved completely at a concentration of 0.1 wt% in a 9:1 (w/w) NPA/H_2O solvent mixture after heating for a longer period of time at 75 °C. As shown in **Figure 67**, supramolecular fibers are obtained by both self-assembly processes. In the case of self-assembly upon cooling, supramolecular fibers of **24e** are only formed if the BTA solution is stored at -18 °C for several days. The fibers assembled by cooling and evaporation of the solvent have a smaller fiber diameter (103 ± 36 nm) than the fibers formed upon cooling the solution (195 ± 85 nm). In addition, the distribution of the fiber diameter during self-assembly upon cooling is significantly broader. Supramolecular fibers with larger fiber diameters are more linear. Independent of the self-assembly process, the fiber length is in the range of a few micrometers to a maximum of 50 μm.

Even in the case of the structurally very similar **24b-d**, supramolecular fibers were obtained by self-assembly. However, only via self-assembly upon cooling fibers are formed for each **24a-e**, whereas during self-assembly upon cooling and evaporation, spherical particles sometimes appear in addition to or instead of supramolecular fibers. These particles have a diameter of 0.4-1.5 μm. A first assumption was that the BTA did not dissolve completely in the solvent mixture, although the solution was optically clear. However, the particles were detected even at lower concentrations or different ratios of the solvents. The treatment of the BTA solution with ultrasound did not bring any change either. It is therefore assumed that both fibers and spherical particles are formed side by side during self-assembly, which is not desirable for further applications.

A clear difference between **24a-e** regarding self-assembly is the duration of fiber formation. The shorter the alkoxy spacer, the faster the self-assembly takes place. This applies to both variants of self-assembly. However, the time factor for self-assembly upon cooling is more pronounced since **24c** assembles only after one day and **24d-e** even after several days stored at -18 °C. The fiber diameter and the corresponding fiber diameter distributions for **24b-e** are slightly larger or broader in the case of self-assembly upon cooling compared to self-assembly upon cooling and evaporation. Furthermore, the choice of solvent plays a decisive role in the formation of supramolecular nanofibers. Although the investigated solvents EtOH, IPA and NPA do not differ very much in their chemical structure and polarity, fibers are not formed in all cases in combination with a certain amount of water. In addition, the ratio of the solvents must be precisely adjusted; otherwise, despite the complete dissolution of the BTAs, no fibers but spherical particles or indefinable structures are formed.
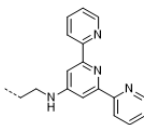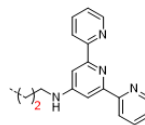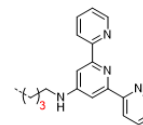
3.2.3 Conclusion of terpyridine-containing benzenetrisamides
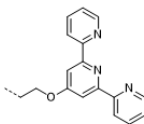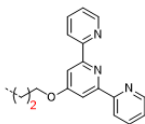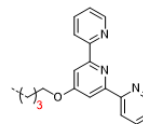
This section demonstrated that a series of BTAs with three terpyridine substituents can be straightforwardly synthesized in a two-step synthesis. This includes **21a-c**, which all exhibit three terpyridine substituents and only differ in the length of an alkylamine spacer between the amide and terpyridine unit, and **24a-e**, which have an alkoxy spacer of different length instead of the alkylamine spacer. All compounds were clearly identified by common analytic methods of organic chemistry, obtained in high purity and, with a few exceptions, in high yield. FT-IR measurements revealed that the amide absorption vibrations of **24a-e** are in the characteristic wavenumber range indicating threefold hydrogen bonds and thus the formation of columnar structures. In the case of **21a-c**, no formation of columnar structures is expected due to a significant shift of the N-H stretching vibration to higher wavenumbers compared to that of **24a-e**. Additionally, the characteristic amide absorption vibrations of **24a-e** are much sharper and more pronounced than those of **21a-e**. For these reasons, the newly synthesized BTAs with alkoxy spacer are expected to show better self-assembly into supramolecular fibers than the BTAs with alkylamine spacer. All terpyridine-containing BTAs exhibit high thermal stability due to decomposition at temperatures above 300 °C. Here, increasing stability from **24a** to **24e** was observed with an increasing length of the alkoxy spacer. Phase transitions were difficult to measure or were not strongly pronounced; however, they were sufficient for further applications.
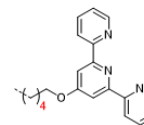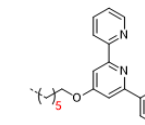
Since morphology control of the terpyridine-substituted BTAs plays a key factor, their self-assembly behavior was comprehensively investigated. Therefore, solubility experiments of **21a-c** and **24a-e** in different organic solvents and solvent mixtures were performed first. Notable differences in solubility were observed for **21a-c** and **24a-e** due to the different kinds and lengths of the alkylamine or alkoxy spacer. Especially mixtures of organic solvents and water, such as EtOH/H_2O or IPA/H_2O at certain ratios, were highly suitable for the complete dissolution of **21a**, **21b** and **24a-e**. As a clear trend in solubility, it was observed that the solubility of **24a-e** in the four selected solvents decreased with increasing alkyl spacer length. In pure water, all terpyridine-containing BTAs were completely insoluble, which is beneficial for the later immobilization of AuNPs from aqueous media. All relevant data of the self-assembly results are provided in **Table 5**.

Table 5: Summary of self-assembly results of **21a-c** and **24a-e**. Supramolecular fibers were generated from different solvent systems. The corresponding average fiber diameter is given with a standard deviation. For **21a, 24b** and **24c**, spherical particles were observed in addition to fibers during self-assembly upon cooling and simultaneous evaporation of the solvent; in the case of **21b** and **21c**, even only particles ([a] fiber diameter not possible to determine).

Abbr.		21a		21b		21c
Substituent						
		Morphology	Fiber diameter [nm]	Morphology	Fiber diameter [nm]	Morphology	Fiber diameter [nm]
Fiber preparation	Self-assembly upon cooling & evaporation	fibers + particles	38 ± 11	particles	-	particles	-
	Self-assembly upon cooling	fibers	135 ± 83	fibers	85 ± 26	fibers	850 ± 310

Abbr.		24a		24b		24c
Substituent						
		Morphology	Fiber diameter [nm]	Morphology	Fiber diameter [nm]	Morphology	Fiber diameter [nm]
Fiber preparation	Self-assembly upon cooling & evaporation	fibers	126 ± 34	fibers + particles	113 ± 35	fibers + particles	_[a]
	Self-assembly upon cooling	fibers	103 ± 47	fibers	175 ± 86	fibers	95 ± 28

Abbr.		24d		24e
Substituent				
		Morphology	Fiber diameter [nm]	Morphology	Fiber diameter [nm]
Fiber preparation	Self-assembly upon cooling & evaporation	fibers	248 ± 106	fibers	103 ± 36
	Self-assembly upon cooling	fibers	371 ± 197	fibers	195 ± 85

After self-assembly upon cooling and simultaneous evaporation of the solvent, some of the terpyridine-containing BTAs formed a mixture of supramolecular fibers and spherical particles or vesicles, whereas the rest of the BTAs formed supramolecular nanofibers without additional particles. The undesired spherical particles were detected independently of the BTA concentration and the choice of solvent. The cause of the formation of the spherical particles or vesicles has not yet been clarified. In contrast, during self-assembly upon cooling, only supramolecular fibers were obtained. For most terpyridine-containing BTAs, the average fiber diameter was in a range of about 80-150 nm. Only **21c**, which was not completely dissolved, forms significantly larger fibers. The supramolecular fibers of the **21a-c** have a significantly smaller fiber diameter and a narrower fiber diameter distribution compared to the **24a-e**.

Since the self-assembly of **24a** from an alcohol/water mixture in a ratio of 9:1 (w/w) upon cooling and evaporation as well as upon cooling always leads to a homogeneous nanofiber formation and the fibers are formed the fastest compared to all other BTAs **21a-c** and **24b-e**, further experiments are carried out with **24a**.

4 Functional microfiber - nanofiber composites

To make use of supramolecular nanofibers, they can be straightforwardly incorporated into existing nonwovens or woven fabrics. A proper combination of both leads to polymer microfiber - supramolecular nanofiber composites with sufficient mechanical stability. These composites can be easily used and evaluated in terms of functionality and reusability. Also, the functionality introduced by the supramolecular nanofibers can then better be determined and rated.

In the following chapter, two different approaches were used for the preparation of functional polymer microfiber – supramolecular nanofiber composites. In both cases, polymer fibers are used as scaffold structures and are combined with supramolecular pyridine- or terpyridine-containing BTA fibers.

(i) In the first approach (**chapter 4.1**), the fabrication and characterization of microfiber-nanofiber composites consisting of a polymer woven fabric and *in situ* formed supramolecular nanofibers based on pyridine-containing BTAs is described.

(ii) The second approach (**chapter 4.2**) is clearly different and deals with composite nonwovens prepared by the wet-laid technique. For this, a fiber dispersion mixture composed of short polymer microfibers and supramolecular terpyridine-substituted BTA nanofibers was deposited in the form of a thin, compact sheet.

All resulting composite nonwovens were characterized regarding their morphology, mechanical stability and shape persistence in aqueous media and were compared to each other.

4.1 Composites via *in situ* formation of supramolecular nanofibers within polymer fabrics

In recent works at our department, Misslitz et al. and Weiss et al. prepared mechanically stable microfiber-nanofiber composites composed of a polymer scaffold and non-functional supramolecular BTA fibers with aliphatic or alkoxy substituent for air filtration applications. These works mainly focused on particle filtration from air by physical means. Here, analogous mechanically stable microfiber-nanofiber composites with functional pyridine-substituted BTAs should be prepared. In particular, the peripheral functionality of the BTAs allows them to be used for the immobilization of metal NPs from a liquid media. [45,46]

In contrast to the fundamental investigation of supramolecular fiber formation in **chapter 3** outlined before, composite preparation relies on the self-assembly of supramolecular fibers *in situ* within a polymeric fabric. The concept of this process is presented in **Figure 68**.

In detail, a defined concentration of the BTA compound is completely dissolved in a suitable solvent at elevated temperature, resulting in a clear solution. The polymer fabric scaffold is completely immersed in the hot BTA solution. Afterwards, the fabric is removed from the BTA solution after it is completely soaked. Upon removing the scaffold, the solvent starts to cool and evaporate and the self-assembly of the BTA to supramolecular fibers takes place within the microfibers of the polymer fabric. After complete drying, microfiber-nanofiber composites are obtained.
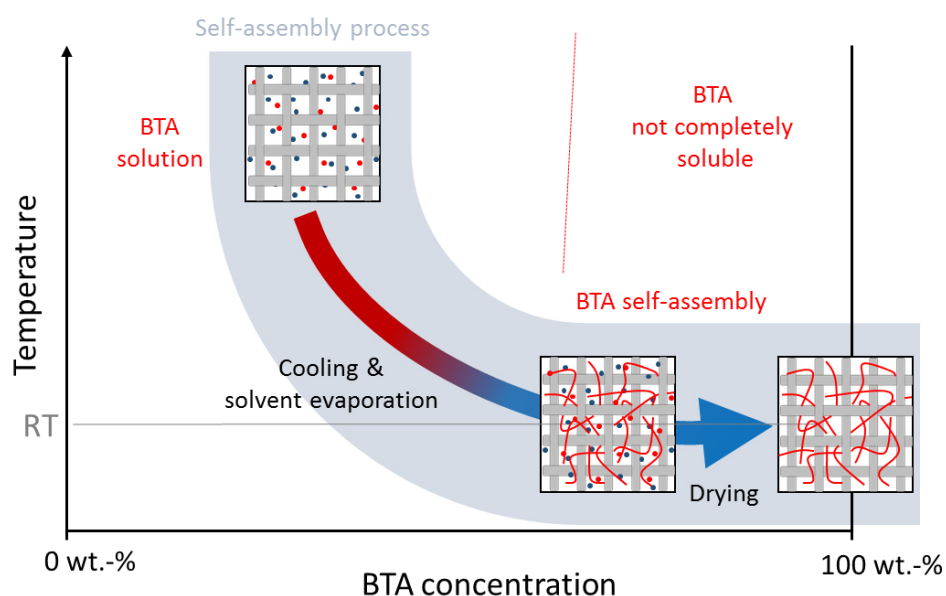
Figure 68: Schematic representation of the *in situ* formation of supramolecular nanofibers within a polymer fabric. The fabric scaffold (grey) is immersed into a BTA solution consisting of solvent (blue dots) and dissolved BTA molecules (red dots) and removed after a short time. Upon cooling and evaporation of the solvent, supramolecular nanofibers (red lines) are formed by self-assembly within the fabric scaffold. Complete evaporation of the solvent results in microfiber-nanofiber composites.

Based on the previous self-assembly studies of all BTAs with pyridine or terpyridine substituents, the pyridine-substituted BTA **3a** was selected for the preparation of the composites, as this compound can form supramolecular structures very rapidly by self-assembly upon cooling and solvent evaporation.

Woven fabrics were selected as scaffold structures since they consist of a single layer with a defined mesh size, allowing for evaluating the supramolecular fiber formation in a straightforward manner. To investigate the influence of the polymer woven fabrics, we selected three different materials, including polypropylene (PP), polyester and polyamide (PA). The different polymer materials can possibly influence the nucleation process noticeably and lead to different formation and stability of supramolecular fibers in the meshes of the polymer woven fabric. In addition, mesh sizes of 100, 200 and 400 µm were chosen to check to which extent the different mesh sizes affect the formation and homogenous distribution of supramolecular fibers in the empty meshes. The woven fabrics were commercially available from Buddeberg. Each woven fabric was cut into squares of 10 cm x 10 cm for further use. **Figure 69** shows examples of PA fabrics with different mesh sizes.
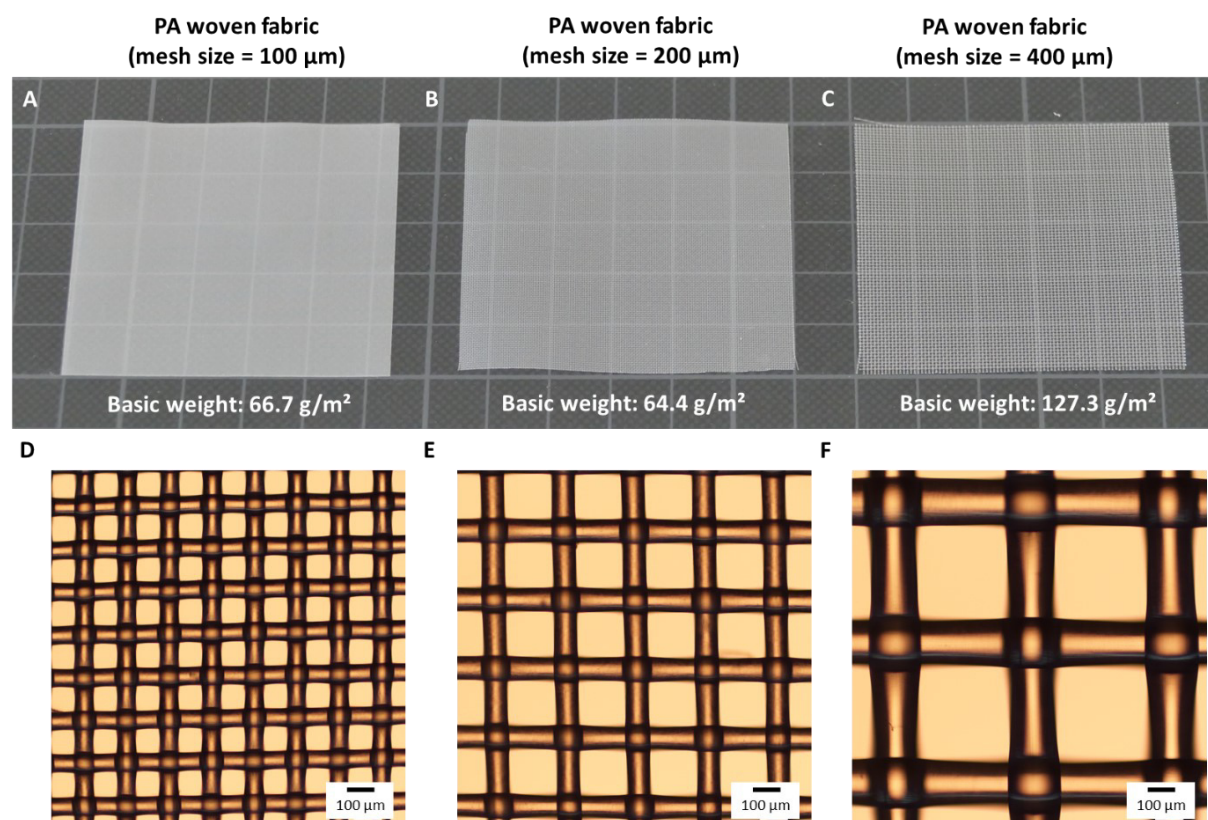
Figure 69: Photographs (**A-C**) and optical microscope images (**D-F**) of PA woven fabrics used for the preparation of microfiber-nanofiber composites containing supramolecular BTA nanofibers. (**A+D**) PA woven fabric with a thickness of 0.159 mm and a basis weight of 66.7 g/m², (**B+E**) PA woven fabric with a thickness of 0.196 mm and a basis weight of 64.4 g/m², (**C+F**) PA woven fabric with a thickness of 0.388 mm and a basis weight of 127.3 g/m².

General preparation of composites

To study the concentration-dependent formation of BTAs in woven fabrics, a BTA solution of **3a** with a concentration ranging from 0.2 to 0.5 wt% was prepared at a temperature of 75 °C. Three environmentally friendly alcohol/water mixtures (EtOH/H_2O, IPA/ H_2O and NPA/H_2O), as well as a THF/H_2O mixture, were selected due to the high solubility of **3a** in these solvent mixtures and to investigate the influence of different solvent systems on the preparation of the composites. The ratio of all solvent systems was 8:2 (w/w) in each case, as this is the most beneficial ratio for dissolving **3a** and for the further process.

The clear and hot BTA solution was then filled into a custom-made immersion bath with a volume of about 200 mL and kept at the corresponding elevated temperature. For this, the immersion bath was placed in a thermostat. In addition, the immersion bath can be closed with a lid to prevent evaporation of the solvent and a change in BTA concentration. **Figure 70** shows the different steps of the preparation process of microfiber-nanofiber composites.
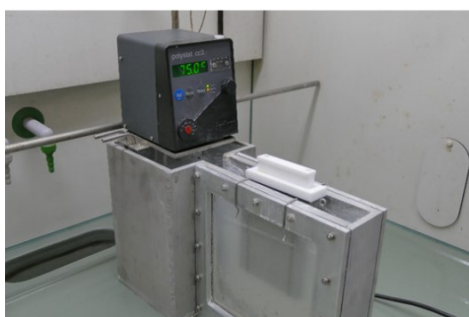
Figure 70: Preparation process of microfiber-nanofiber composites via *in situ* formation of supramolecular BTA nanofibers within the polymer fabric. (**A**) The polymer fabric was fixed in a metal frame with an open area of 8.5 cm x 8.5 cm. (**B**) Then, the fabric placed in the metal frame was immersed in the hot BTA solution for 30 s. (**C**) After complete soaking of the fabric with BTA solution, (**D**) the fabric was dried at ambient conditions resulting in a microfiber-nanofiber composite.

114

First, the fabric was fixed in a metal holding frame with an open area of 8.5 cm x 8.5 cm. Then the fabric placed in the metal frame was vertically immersed in the hot BTA solution for 30 s. During immersion, the fabric was soaked with the BTA solution. The handle of the metal frame closed the immersion bath completely so that evaporation of the solvent was prevented. In a final step, the fabric was removed from the immersion bath and dried in a horizontal position at ambient conditions until the solvent had completely evaporated (at least 60 min). It is important to fix the fabric as straight as possible so that it does not sag and areas with higher BTA concentration can form after horizontal drying. By cooling the BTA solution and evaporating the solvent, supramolecular fibers were formed in the defined meshes of the woven fabric.

Characterization of pyridine-functionalized composites

Preliminary tests were carried out to determine which of the previously mentioned polymer fabric materials and mesh sizes would give the best results. In this case, the best means in which composite the BTA fibers are most homogeneously distributed and most strongly anchored between the meshes. The PA woven fabric turned out to be the favorite, whereby it is assumed that interactions can occur between the amide groups of the PA fabric and the BTA, which allows for better bonding of the BTA fibers with the support fabric. The best mesh size figured out was 200 µm since, in contrast to a mesh size of 100 µm or 400 µm, the supramolecular fibers were very homogeneously distributed in the meshes and, at the same time, the meshes were not filled too much or too little. Furthermore, the highest anchorage of supramolecular fibers in or around the PA woven fabric was observed at 200 µm. In addition to different polymer woven fabrics, the concentration of the BTA solution and the solvent system were varied to investigate the influence on the morphology of the microfiber-nanofiber composites via SEM. Therefore, small pieces with an area of about 1.0 cm² were cut out at different positions of the composite and fixed with a carbon conductive tab on a SEM sample holder. Before measurement, the samples were sputter-coated with a 2.0 nm platinum layer using a Cressington sputter coater (208HR, 40 mA). SEM micrographs were recorded using a FEI Quanta FEG 250 at an acceleration voltage of 5 kV and in low-vacuum (40 Pa). For detection, a low-vacuum secondary electron (LFD) detector was used. The average fiber diameter was determined by measuring at least 100 fibers from SEM micrographs using the software *ImageJ*.

Figure 71 exemplarily shows a PA woven fabric without and with supramolecular nanofibers as a comparison.
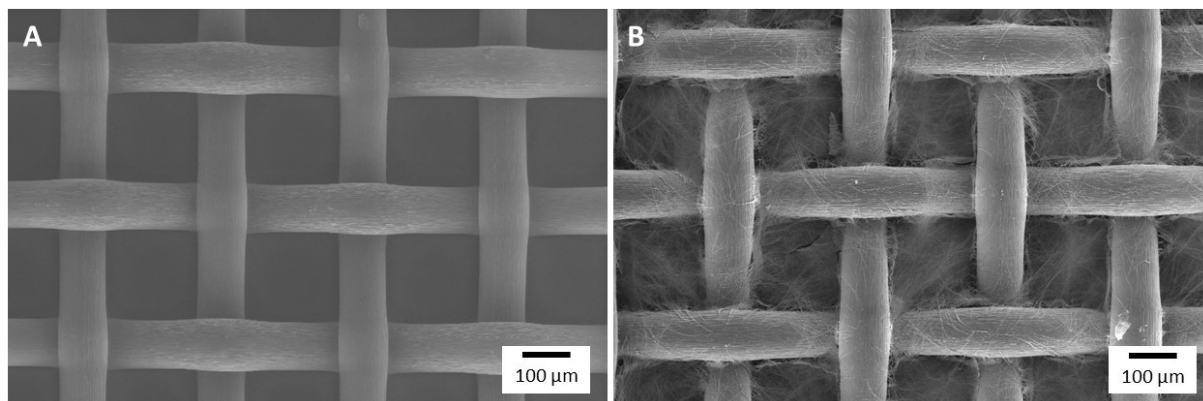
Figure 71: SEM micrograph of a PA woven fabric with a mesh size of 200 µm without supramolecular fibers (**A**). SEM micrograph of a PA woven fabric with a mesh size of 200 µm with supramolecular fibers resulting in a microfiber-nanofiber composite (**B**).

In the case of the neat PA woven fabric, you can see the evenly woven pattern very well and you can also notice that the fabric has a rather rough surface. After the *in situ* self-assembly process, the supramolecular BTA fibers largely fill the empty meshes of the PA woven fabric. In addition, the BTA fibers partially cover or wrap the existing PA fabric structure.

Various parameters, such as concentration, temperature or solvent, can significantly influence the overall morphology of the composites. The influence of the solvent system on the morphology of the composites is demonstrated in **Figure 72** and **Figure 73** for **3a**. Here, the polarity, as well as the evaporation rate of the solvent, plays a decisive role. In **Figure 72A**, a microfiber-nanofiber composite, which was prepared by immersing the PA woven fabric in a 0.5 wt% **3a** in EtOH/H_2O (8:2, w/w) solution, is shown at different magnifications.

Figure 72: SEM micrographs of a microfiber-nanofiber composite containing supramolecular nanofibers of **3a** at different magnifications (**A-C**). The composite was processed from an 8:2 (w/w) EtOH/H₂O mixture (0.5 wt% of **3a**) and showed supramolecular fibers with an average fiber diameter of 143 ± 53 nm. The fiber histogram (**D**) is based on the evaluation of at least 100 fibers.

The BTA fibers completely fill the meshes of the PA woven fabric and only minimal cracks or flaws can be observed. **Figure 72B** shows that the BTA fibers are spanned over the whole PA woven fabric. Additionally, there are more and more evaporation points on the PA woven fabric where the solvent has evaporated first and self-assembly started. Within the meshes, a dense network of BTA fibers is formed, which has an average fiber diameter of 143 ± 53 nm.

In contrast, after immersion of the PA woven fabric in a 0.5 wt% **3a** in THF/H₂O (8:2, w/w) solution, a composite with a large number of cracks in the meshes is obtained (**Figure 73**). This effect cannot be clearly explained so far. It is assumed that here, these cracks are formed due to different solvent evaporation than with an EtOH/H₂O mixture. In addition, the adhesion between the BTA fibers and the PA woven fabric is significantly lower than for the previous solvent system EtOH/H₂O (8:2, w/w), which increases the crack formation. The supramolecular fibers have an average fiber diameter of 96 ± 29 nm.

Figure 73: SEM micrographs of a microfiber-nanofiber composite containing supramolecular nanofibers of **3a** at different magnifications (**A-C**). The composite was processed from an 8:2 (w/w) THF/H$_2$O mixture (0.5 wt% of **3a**) and showed supramolecular fibers with an average fiber diameter of 143 ± 53 nm. The fiber histogram (**D**) is based on the evaluation of at least 100 fibers.

After the preparation and SEM investigation of the microfiber-nanofiber composites, the extent to which the composites are resistant to different solvents and retain their shape or morphology was investigated. Especially the resistance in aqueous media is of great importance for further application since the further immobilization of NPs as well as catalytic reaction should be carried out in aqueous media. For this purpose, the composites were immersed in various solvents and the solutions were stirred for 24 h. In most organic solvents, the supramolecular fibers are partly dissolved, resulting in a very inhomogeneous morphology of the composites. In aqueous media, the BTA fibers are completely insoluble. However, the BTA fibers detach from the PA fabric upon stirring the solution and then float around in the water. **Figure 74** shows how the morphology of the composite looks before and after immersion into aqueous media.
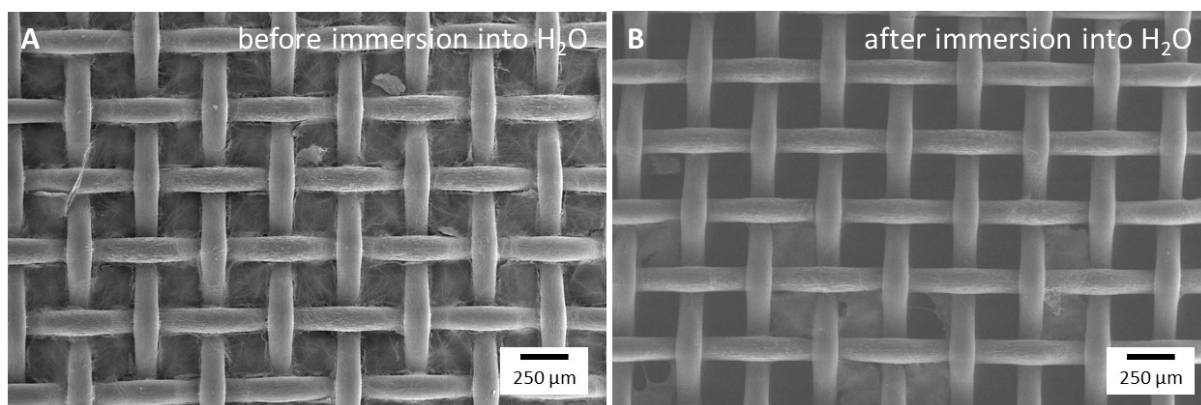
Figure 74: SEM micrographs of microfiber-nanofiber composites containing supramolecular nanofibers of **3a** before (**A**) and after (**B**) immersion into aqueous media. After immersing the composite in aqueous media, most of the fibers detach from the PA fabric resulting in empty meshes again.

Since preservation of the composite morphology in an aqueous solution is particularly necessary to immobilize NPs from aqueous media, different approaches were pursued to improve the adhesion of the BTA nanofibers to the PA woven fabric. The first approach was to soak the PA woven fabric in the solvent used later to remove various additives on the surface of the fabric. However, the extraction of the woven fabric did not contribute to any improvement of the mechanical stability. Short immersion of the woven fabric in aqueous media prior to the immersion in the BTA solution resulted in a slight improvement of the adhesion.

Stabilization of pyridine-based supramolecular nanofibers via simultaneous self-assembly of functional and non-functional BTAs

As outlined above, microfiber-nanofiber composites based on PA woven fabrics and functional pyridine-based **3a** could be successfully prepared. However, the hierarchical structure features an insufficient stability when exposed to liquid media. This instability is attributed to an insufficient adhesion of the functional supramolecular fibers to the PA woven fabric. To improve the stability of the fibers within the composite, a second non-functional BTA **25** was selected, which is known to form stable composites, as demonstrated in previous works. [46] These non-functional BTA fibers are expected to form supporting structures for fibers of **3a**. Since both BTAs can intrinsically form *in situ* fibers, both compounds were dissolved and self-assembled simultaneously. Both BTAs feature a very different self-assembly behavior since **25** can be processed from pure organic solvents such as 2-butanone, whereas **3a** can only be processed from alcohol/water mixtures. Additionally, **25** is known to form columnar stacks in contrast to **3a**. For that reason, it is highly unlikely that the different building blocks will incorporate into a co-assembled fibrous structure. Rather it is assumed that both compounds assemble individually into fibers in a self-sorted manner.

The general supposed hierarchical composite structure is shown in **Figure 75**. Here the BTA **25** fibers are proposed to act as additional support fibers for **3a**. The synthesis and characterization of **25**, which carries an ethylhexyl substituent instead of a pyridine one, is described in literature. [25]
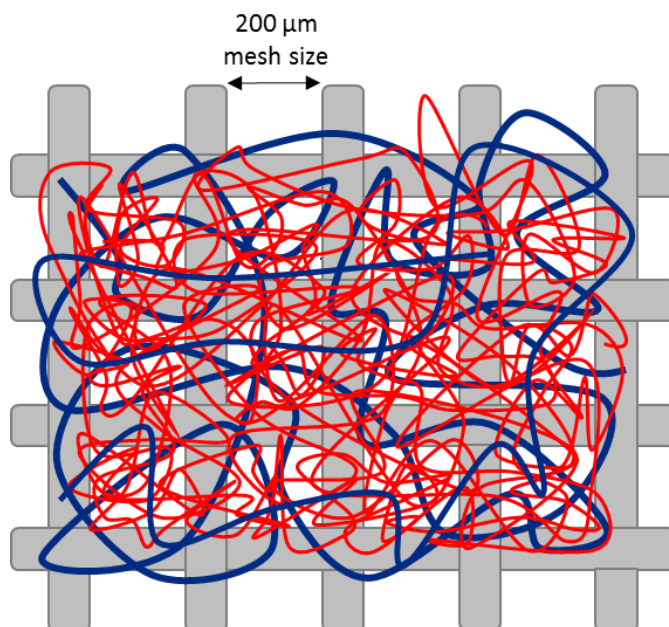
Figure 75: Scheme of the hierarchical structure of microfiber-nanofiber composites consisting of a PA fabric (grey), aliphatic BTA fibers (blue) and pyridine-functionalized nanofibers (red).

The PA woven fabric serves as a scaffold structure for the aliphatic BTA **25**, which in turn is to act as a scaffold for the pyridine-functionalized BTA fibers. The use of aliphatic BTA fibers is expected to increase the stability of pyridine-containing BTA fibers.

Prior to the investigation of the simultaneous self-assembly of both compounds, the self-assembly behavior of **25** in the used PA woven fabric was investigated first. For that reason, we have prepared and processed from a 1.0 wt% BTA solution of **25** in 2-butanone. The resulting composite is shown in **Figure 76** at different magnifications.
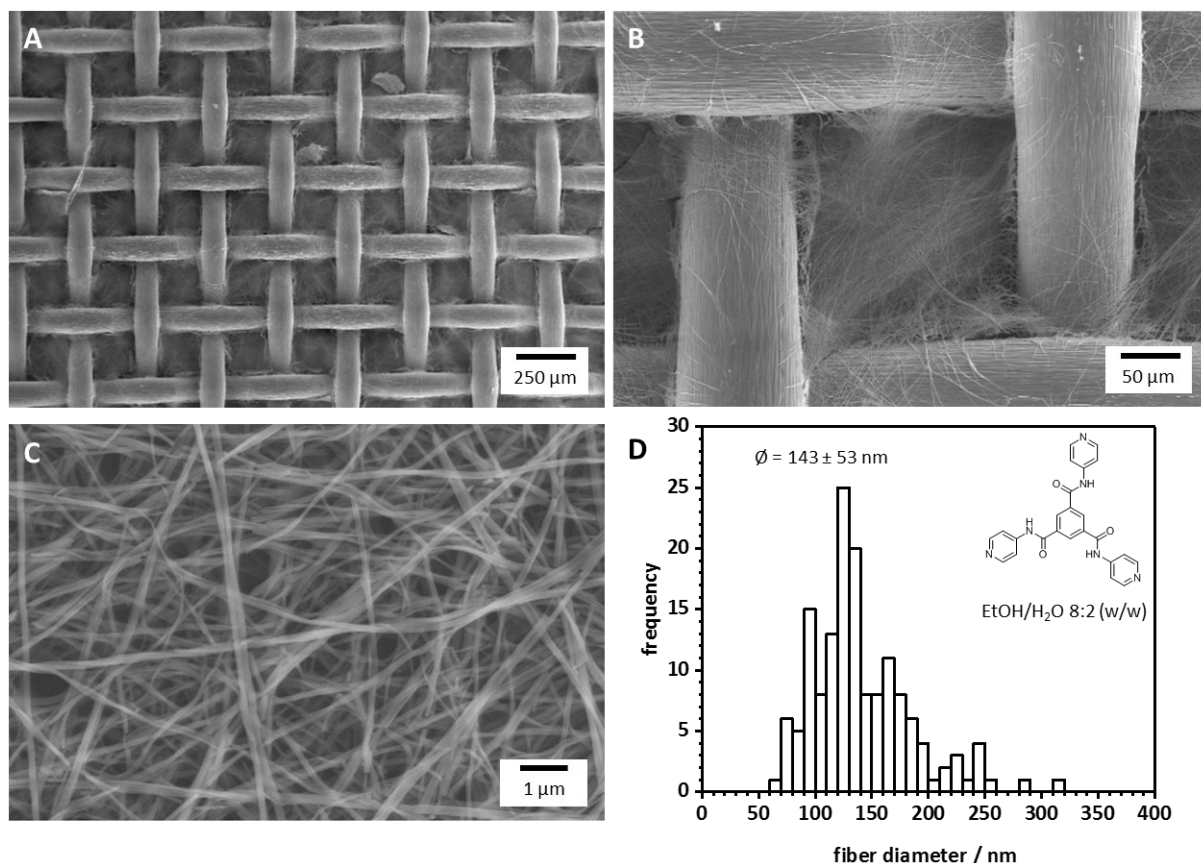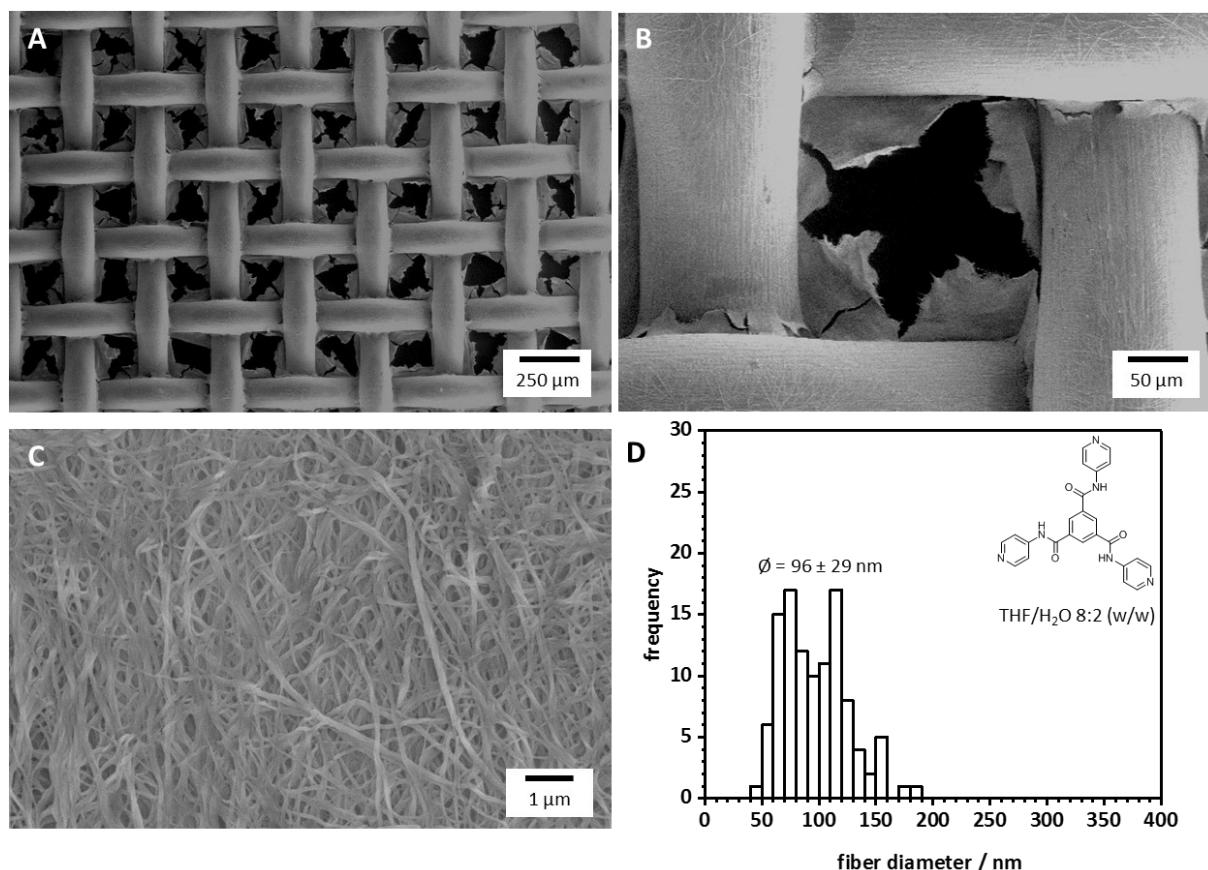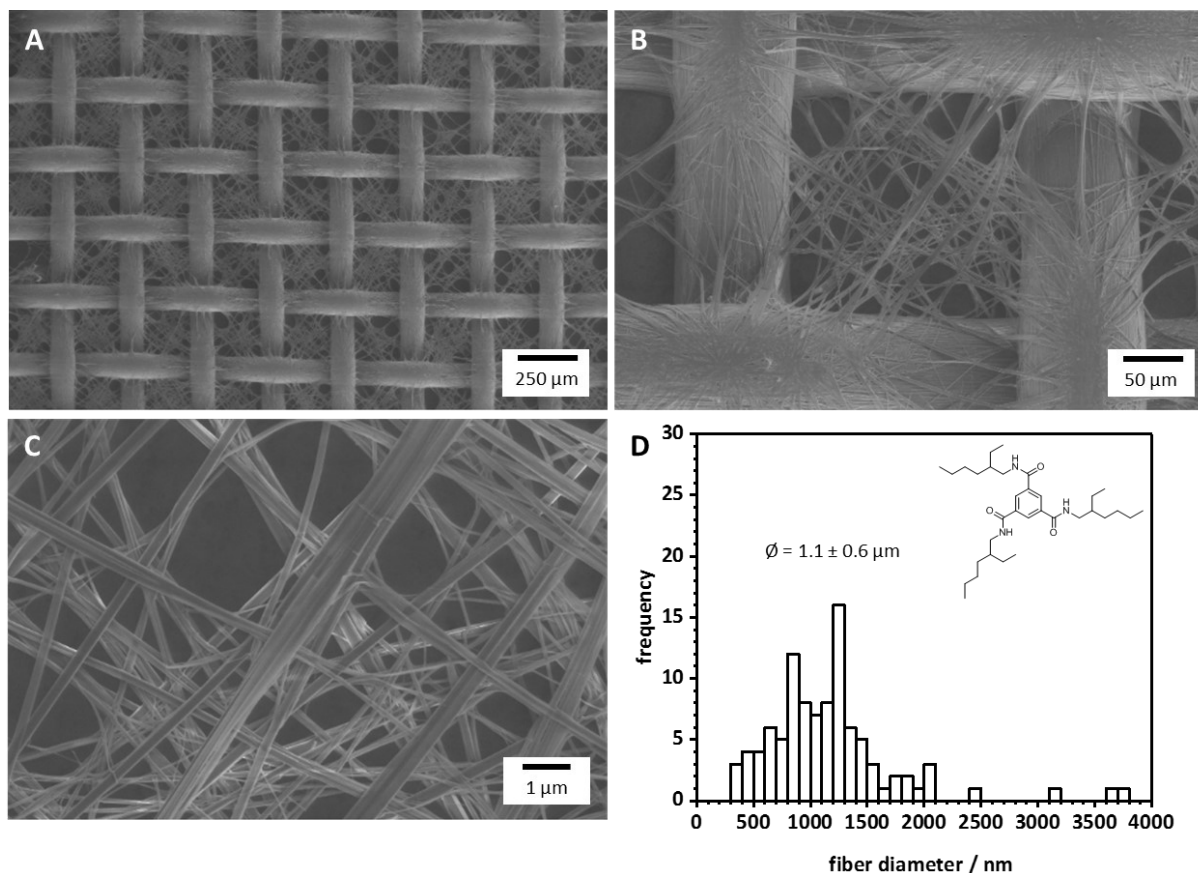

Figure 76: SEM micrographs of a microfiber-nanofiber composite containing supramolecular fibers of **25** at different magnifications (**A**-**C**). The composite was processed from 2-butanone (1.0 wt% of **25**) and showed supramolecular fibers with an average fiber diameter of 1.1 ± 0.6 µm. The fiber histogram (**D**) is based on the evaluation of at least 100 fibers.

From **Figure 76**, it can be clearly seen that the meshes of the PA woven fabric are filled very homogeneously with supramolecular fibers of **25**. In contrast to the composite with **3a** fibers, the meshes are not so densely filled. The bonding between the PA woven fabric and the BTA fibers is clearly improved and no cracks or defects can be observed. In aqueous media, the morphology of the composite is completely preserved and no BTA fibers detach from the PA woven fabric during stirring of the solution. These results are promising to be **25** used as a supporting supramolecular fiber component for **3a**.

For that reason, different combinations of the aliphatic **25** and the pyridine-functionalized **3a** were investigated. In addition to the molar ratio of the two BTAs, the solvent systems and the total BTA concentration were varied to verify which parameters are the most suitable to obtain a homogeneous composite that fully retains its structure in aqueous medium. After numerous screening experiments,

121

a total concentration of 1 wt% BTA in solution with a molar ratio **3a:25** of 4:6 mol% was determined as the most suitable parameter. Three different solvent mixtures containing a total BTA content of 1 wt% **3a:25** (4:6 mol%) were prepared for the fabrication of the corresponding microfiber-nanofiber composites.

Figure 77 shows the SEM micrographs of the three microfiber-nanofiber composites, which were prepared from an EtOH/H$_2$O, IPA/H$_2$O or NPA/H$_2$O mixture with a ratio of 8:2 (w/w) at different magnifications and the corresponding fiber histograms.
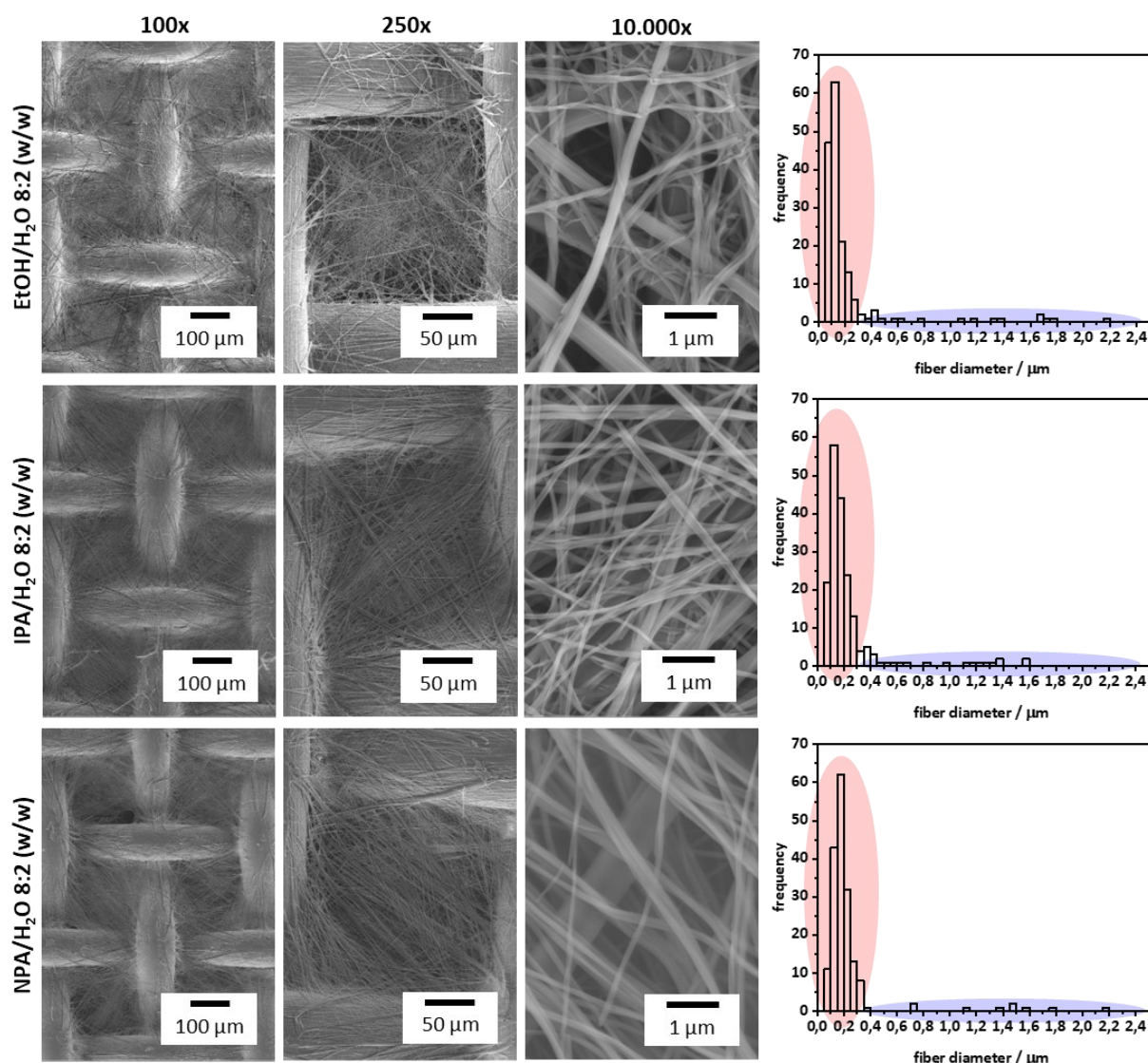
Figure 77: SEM micrographs of microfiber-nanofiber composites processed from different solvent mixtures at three different magnifications (100x, 250x, 10.000x). The composites were prepared from solutions comprising 1.0 wt% of a mixture of **3a** and **25** (4:6 mol%). The corresponding fiber diameter histograms are based on the evaluation of at least 150 fibers. Due to the two different BTAs, there is a bimodal fiber diameter distribution, which is marked in red (fibers of **3a**) and blue (fibers of **25**).

As can be seen from the SEM micrographs in **Figure 77**, the meshes of the composite, which was processed from an EtOH/H_2O mixture, are quite dense and homogeneously filled with supramolecular fibers. However, the adhesion of the nanofibers to the PA woven fabric is only weakly pronounced in some cases. Some cracks or defects, as well as several areas with higher fiber content, can be observed. The SEM micrographs of the composite, which was processed from IPA/H_2O, show a denser and more homogeneous filling of the openings. The supramolecular fibers are firmly fixed to the PA woven fabric via bridge points. No cracks are visible over the entire sample. The third composite, processed from NPA/H_2O, also shows a dense and homogeneous filling of all openings. A strong fixation of the supramolecular fibers to the PA woven fabric can be observed. Depending on the choice of solvent system, the adhesion of the BTA fibers is thus stronger or weaker. From the fiber histograms of all three composites, it is clearly noticeable that there is a bimodal distribution. This strongly suggests independent self-assembly of **3a** and **25**. The thin fibers with a diameter in the range of 60-300 nm can most likely be assigned to **3a**, whereas the thicker fibers in the range of 400 nm to 2 μm should be fibers of **25**.

Another interesting aspect is the content of supramolecular BTA fibers in the PA woven fabric. Although it is not possible to distinguish between the aliphatic **25** and the pyridine-containing **3a**, since immobilization is not possible, it is interesting to know what BTA content is required to receive a homogenous composite for further applications. The BTA fiber content in the composite was determined via gravimetric analysis. Therefore, the polymer woven fabric was weighed both before and after the immersion process. The fiber content could be calculated from the difference between both values. The gravimetrical values and the corresponding deviations are each based on six samples. The values are 7.2 ± 2.4 wt% in EtOH/H_2O (8:2, w/w), 4.7 ± 3.5 wt% in IPA/ H_2O (8:2, w/w) and 3.5 ± 0.8 wt% in NPA/ H_2O (8:2, w/w). Thus, the fiber content within the three composites noticeably depends on the choice of the solvent. In addition, the BTA content is relatively low in relation to the entire composite. The preparation of the composites was performed several times to prove reproducibility. These results clearly show that the choice of solvents plays an important role in the fabrication of microfiber-nanofiber composites regarding the fixation of the supramolecular nanofibers to the polyamide fabric. The fiber diameter and the corresponding fiber diameter distribution also depend on the chosen solvent mixtures.

As explained previously, **3a** and **25** are assumed to self-assemble independently, which is already evident by the result of the bimodal distribution in the fiber histograms. To further verify these observations and to be able to make statements about where the other BTA fiber grows away from, Raman measurements were carried out by Holger Schmalz (Macromolecular Chemistry II, University of Bayreuth). Raman measurements were performed on a combined Raman-imaging/scanning force microscope system (Witec Alpha 300 RA+) with a UHTS 300 spectrometer and a back-illuminated Andor Newton 970 EMCCD camera. Raman spectra were obtained using an excitation wavelength of λ = 532 nm and an integration time of 0.5 s/pixel (100x objective). All spectra were subjected to a

cosmic ray removal routine and baseline correction. The Raman spectra of the individual self-assembled BTA fibers were recorded as references to determine the spatial distribution of **3a** and **25** (**Figure 78A**).

Since the Raman spectra of the two BTAs are clearly different at individual peaks, it is possible to perform a mapping of a small area of the composite so that the distribution of the different BTA fibers is shown at the end. The Raman spectrum of **3a** (red) shows a clear signal from the C=N bonding at a wavenumber of 1610-1680 cm^{-1}. A clear distinction between the spectra of the two BTAs is possible by the aliphatic vibration region at a wavenumber range of 2800-3000 cm^{-1}. Here, only a signal is observed for **25**.
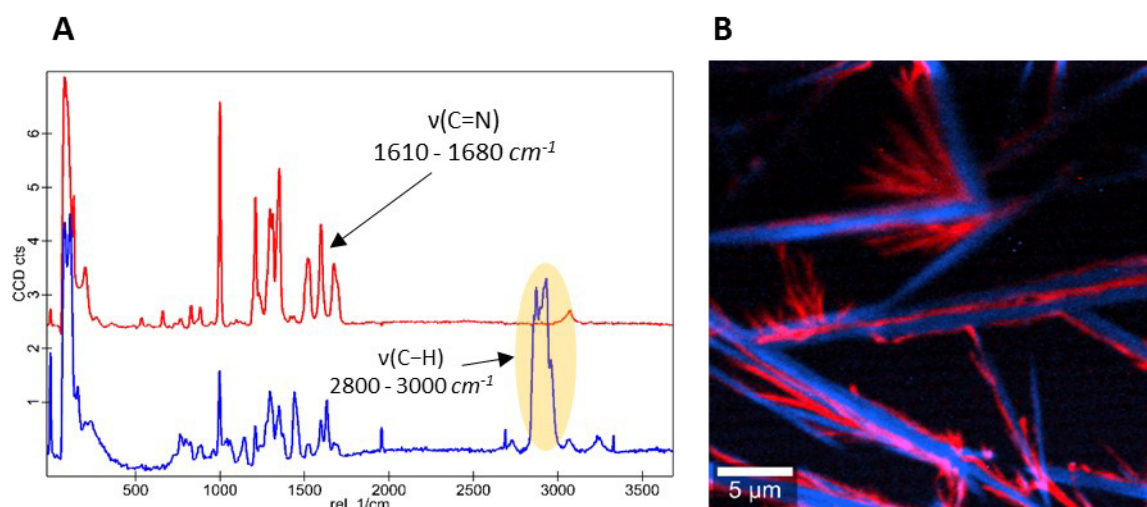
Figure 78: Raman-imaging microscopy study: (**A**) Comparison of the Raman spectra of **3a** (red) and **25** (blue). The Raman spectra of **3a** and **25** differ in some characteristic peaks, wherefore a mapping can be performed showing the spatial distribution of both fibers. (**B**) Distribution mapping of **3a** (red) and **25** (blue) fibers of a sample consisting of a 0.5 wt% mixture of **3a** and **25** (4:6 mol%) processed from NPA/H$_2$O (8:2).

As shown in **Figure 78B**, the supramolecular fibers of **3a** and **25** can clearly be distinguished by confocal Raman imaging. Notably, they are self-assembled next to each other. Since the substrate is not statistically covered with individual fibers, one may conclude that the fibers of **25** build up a scaffold for fibers of **3a**, which are placed next to or on top of the fibers of **25**. It can also be assumed that the aliphatic fibers must be formed before those of **3a** at the chosen self-assembly conditions since the fibers of **3a** are on or around the aliphatic fibers of **25**. In addition, it is noticeable that **3a** self-assembles especially in the corners or in places of high material density, as one may expect from the classical nucleation theory. Thus, the high surface of solid nanoobjects of **25** may act as nucleation sites for the self-assembly of **3a**.

In contrast to the microfiber nanofiber composites, which only exist of pyridine-functionalized nanofibers, the composites containing both aliphatic **25** and the pyridine-containing **3a** fibers are significantly more stable in water. This finding may be expected since the supramolecular nanofibers of **25** act as additional and more dense support fiber for **3a**. This is shown in **Figure 79**. Here the SEM micrographs before and after immersion of the composite into water can be compared.
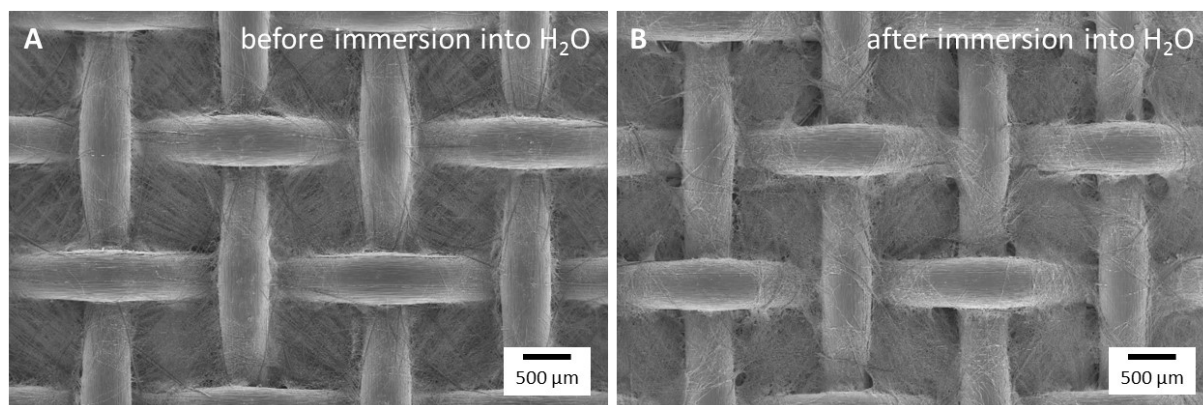
Figure 79: SEM micrographs of a microfiber-nanofiber composite containing supramolecular fibers of **3a** and **25** before (**A**) and after immersion (**B**) into aqueous media for 24 h at 60 rpm in a tumbling mixer. The BTA fibers keep stable within the PA fabric in an aqueous solution.

The morphology of the microfiber-nanofiber composite (processed from IPA/H_2O, 8:2 (w/w)) before and after exposure to water for 24 h shows no significant difference according to SEM micrographs. Hence, the supramolecular nanofibers remain almost completely stable connected to the PA woven fabric. The same behavior can be observed for composite prepared from NPA/H_2O, 8:2 (w/w), whereas several nanofibers on the edge of the composite prepared from EtOH/H_2O, 8:2 (w/w) detach from the PA woven fabric. In this case, the BTA fibers do not dissolve but are dispersed as single fibers in the water. For further applications like immobilization of NPs or catalysis, no BTA fibers at all should detach from the PA fabric. For that reason, the developed system can only be used in the immobilization of NPs or in catalysis to a limited extent.

4.2 Composite nonwovens via wet-laid technique

A very novel approach, which was investigated for the first time, comprises the preparation of compact sheets of composite nonwovens (hereinafter called "composite nonwoven sheet") composed of electrospun PAN short microfibers and supramolecular functional BTA nanofibers by a wet-laid technique. This approach is very different from the already conducted research with polymer and supramolecular fibers demonstrated at our department. In previous work, commercial polymer scaffolds were used or a polymer support was prepared by electrospinning of polymer solutions. Non-functional supramolecular fibers were formed *in situ* within the scaffold structure after immersion into a BTA solution. These composite nonwovens are highly suitable for air filtration applications and feature superior filtration efficiencies for particulate matter due to their improved mesoscopic fiber morphology.[44,45] In contrast, in this approach, compacted sheets are prepared by a sheet forming process using a mixture of short electrospun polymer fibers and functional supramolecular BTA fibers. Such compact sheets are highly beneficial since they feature a higher robustness and compactness than composite nonwovens based on regular electrospun polymer fibers. Moreover, integrated functional supramolecular nanofibers within these compact sheets are expected to feature a high functionality due to a high active surface area. Here, their functionality will be demonstrated by the immobilization of AuNPs, which can further be used for catalysis.

To achieve these compact sheets, a stable and homogenous polymer fiber dispersion is required for the wet-laid process. A stable polymer fiber dispersion is obtained by using short polymer fibers due to the absence of fiber entanglements. Mixing this polymer fiber dispersion with a homogenous BTA solution leads to the *in situ* formation of supramolecular BTA nanofibers in the mixture. After the solution is removed by soaking through a membrane, the fiber dispersion mixture results in a homogenous and mechanically stable composite nonwoven sheet. The individual process steps are shown in **Figure 80**.
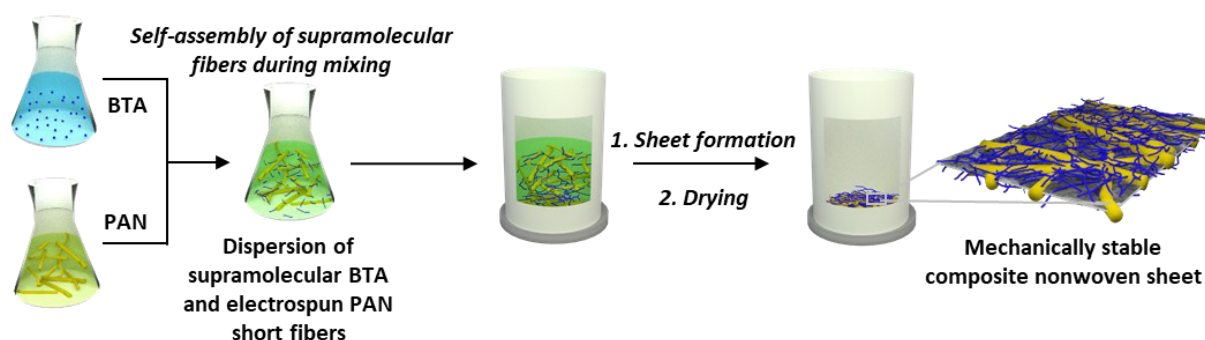
Figure 80: Schematic representation of the preparation process of mechanically stable composite nonwoven sheets composed of electrospun PAN short microfibers (yellow fibers) and supramolecular functional BTA nanofibers (blue fibers). Reprinted (adapted) with permission from [138] © 2021 American Chemical Society.

For the preparation of composite nonwoven sheets by the wet-laid technique, two materials, a commercially available PAN-based polymer and a terpyridine-containing BTA, were selected.

Polymer short fibers: The preparation of the polymer short fibers was carried out by Chen Liang (Macromolecular Chemistry II, University of Bayreuth) and the characterization of these polymer short fibers was carried out by myself. A PAN copolymer with < 7 % methyl acrylate and a molecular weight of M_n = 80.000 g/mol (hereinafter called "PAN") was selected as polymer material due to its good electrospinnability and sufficient wettability with water, which is required for the cutting process of PAN fibers in aqueous media. For cutting, the electrospun PAN nonwovens were placed in water at a concentration of 0.05 wt% and cut with a blender until a homogeneous PAN short fiber dispersion was received. After electrospinning and cutting, a stable homogenous fiber dispersion in water can be prepared. Details on the electrospinning process and the preparation of the electrospun PAN short fiber dispersion are depicted in the experimental section (**chapter 7**).

SEM micrographs of the as-spun PAN fibers and the PAN short fibers are shown in **Figure 81.** The length of the PAN short fibers was determined to be 442 ± 171 µm and their diameter to be 1.10 ± 0.28 µm.
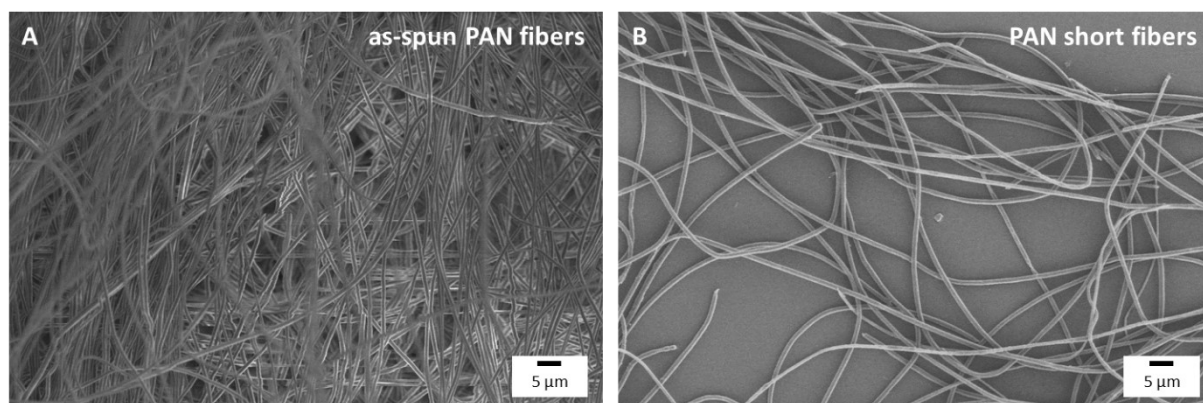
Figure 81: SEM micrograph of randomly oriented as-spun PAN microfibers (**A**) and electrospun PAN short fibers (**B**), received after cutting in a blender. Reprinted (adapted) with permission from [138] © 2021 American Chemical Society.

Functional supramolecular fibers: The terpyridine-containing BTAs were found to be highly suitable in terms of fiber formation as described in **chapter 3.2** and due to their potential to provide an attractive interaction with metal ions or NPs. Here, **24a** was selected for the preparation of the composite nonwoven sheets based on the previous self-assembly studies for all BTAs with pyridine or terpyridine substituents. **24a** is able to form uniform supramolecular nanofibers with a diameter of approximately 100 nm by self-assembly upon cooling (**Figure 82**). Moreover, the proposed columnar stacking of **24a-e** indicates a high density and access to the peripheral functional terpyridine groups.
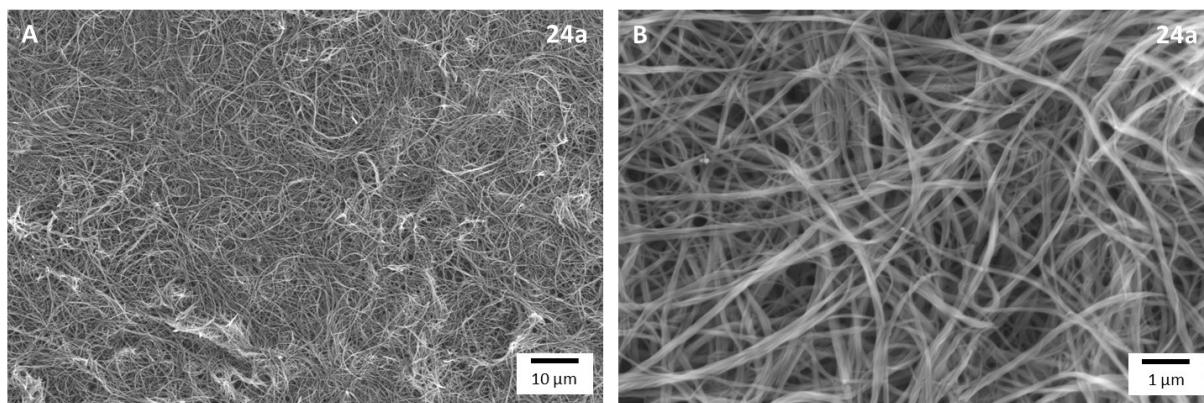
Figure 82: SEM micrographs of supramolecular BTA nanofibers of **24a** received after self-assembly upon cooling from an IPA/H$_2$O (9:1, w/w) solvent mixture at two magnifications (**A**+**B**).

Screening experiments on lab scale

To demonstrate and evaluate the general feasibility of the new approach and to determine the importance of relevant parameters such as the volume ratio of PAN fiber dispersion and BTA solution and the total volume of the fiber dispersion in the preparation of composite nonwoven sheets, screening experiments were first carried out in a small volume on lab scale.

Therefore, the electrospun PAN short fibers were mixed with a freshly prepared solution of **24a** in IPA/H$_2$O (9:1, w/w). Upon mixing, **24a** completely self-assembles into supramolecular nanofibers due to a change in solubility of **24a** in the mixture. After the preparation of the PAN/BTA **24a** fiber dispersion, the mixture was filtered through a frit (∅ = 3.7 cm), which was equipped with three layers of filter paper and, on top, a fine-meshed metal net to reduce the filtration speed that ensures a homogenous deposition of the fibers. The residual solvent was removed under reduced pressure. Drying of the composite nonwoven sheet was achieved in a vacuum drying oven. The volume ratio of the PAN dispersion and BTA solution, as well as the total volume of the PAN/BTA **24a** fiber dispersion, were changed to investigate the influence on the morphology and mechanical stability of the composite nonwovens **c1-6** and to find suitable parameters for the preparation of composite nonwovens on a technical scale.

Influence of the volume ratio of PAN fiber dispersion and BTA solution

Prior to the following experiments, several reference sheets composed of neat PAN fibers were prepared in the same way. Every neat PAN sheet showed insufficient robustness, as it was partially destroyed directly when touched with tweezers. This renders the neat reference to be insufficient to be examined further. To investigate the influence on the morphology of the composite nonwoven sheets, different volume ratios of the PAN short fiber dispersion to the BTA solution were chosen. As volume ratios 3:1, 1:1 and 1:3 were selected.

In all cases, a total volume of 40 mL and the same concentration of the PAN fiber dispersion (0.05 wt%) and BTA **24a** solution (0.1 wt%) were used. This finally results in composite nonwoven sheets with a PAN:BTA **24a** ratio of 0.2:1 (**c1**), 0.6:1 (**c2**) and 1.9:1 (**c3**). During the preparation of composite nonwoven sheets **c1** and **c2**, gel formation takes place due to changes in solubility of **24a** in the PAN/BTA **24a** fiber dispersion. Most probably, gel formation prevents a good and homogenous sheet forming process. This is observed during the handling of the composite nonwoven sheet, which was found to be significantly poorer for **c1** and **c2** than for composite nonwoven sheet **c3** with a PAN/BTA **24a** ratio of 1.9:1 due to the higher BTA fiber amount. Composite **c1** and **c2** are already destroyed upon touching it carefully with tweezers.

Figure 83 shows SEM micrographs of the composite nonwoven sheets **c1-3**, which significantly differ in their morphology due to the different PAN:BTA **24a** ratios in the composite nonwovens**.**
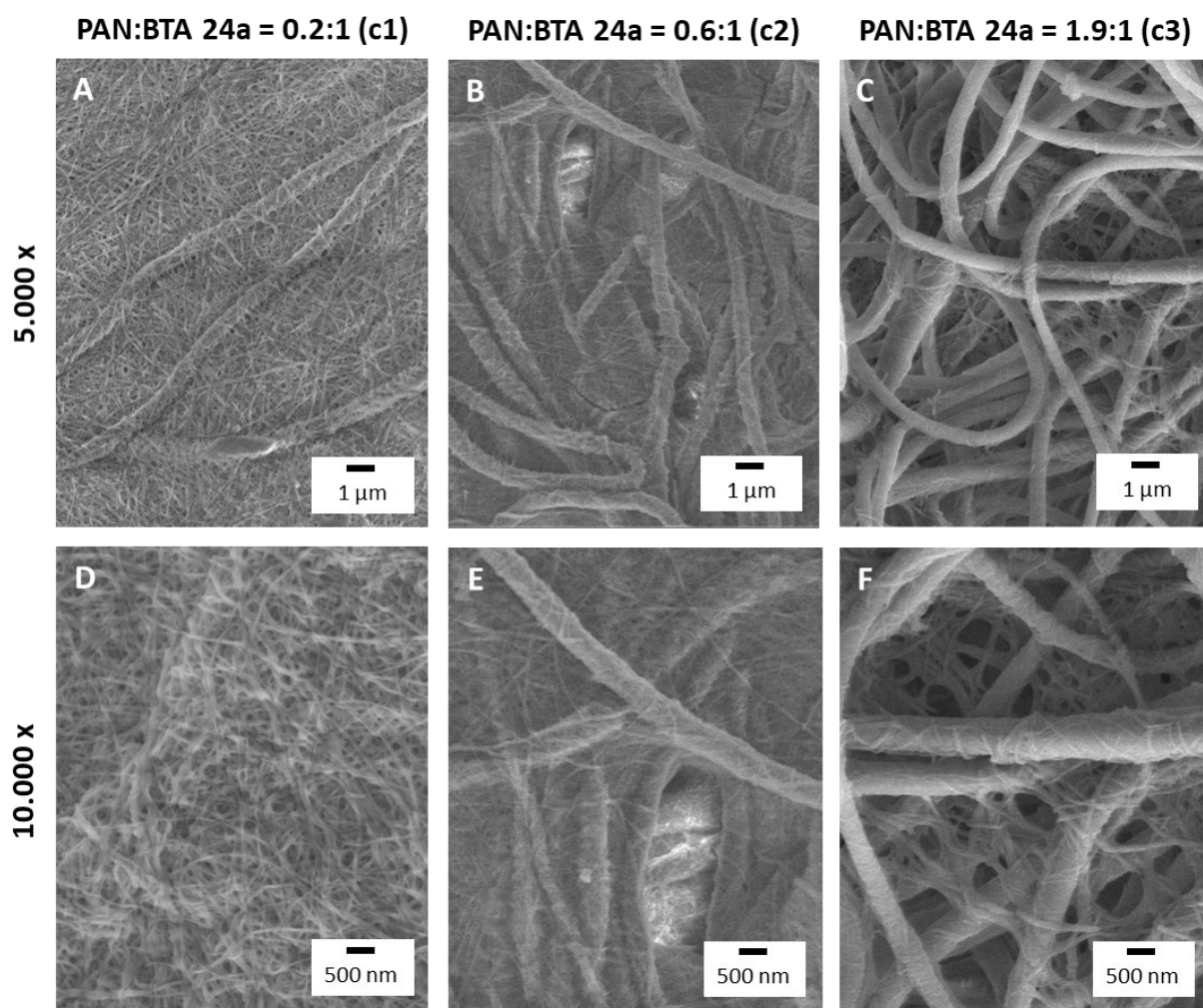
Figure 83: SEM micrographs of composite nonwovens sheets **c1-3** composed of different ratios of PAN microfibers and BTA **24a** nanofibers at two different magnifications.

A decrease in the BTA fiber amount in **Figure 83** from composite nonwoven sheet **c1** to **c3** can be clearly observed. At a PAN:BTA **24a** ratio of 0.2:1, the PAN fibers are only partially visible. At a ratio

of 0.6:1, the PAN fibers are still completely surrounded by BTA fibers and an interpenetrating network of BTA fibers is still present. In the case of a PAN:BTA **24a** ratio of 1.9:1, both the PAN and BTA fibers are clearly visible and a network of BTA fibers is formed between the PAN fibers, however, to a smaller extent. Since a too dense interpenetrating network of BTA fibers is expected to be unfavorable for the proposed filtration application, for further studies, a PAN:BTA **24a** ratio of 1.9:1 was selected, in which the PAN fiber amount is comparable to that of the BTA fiber amount. In addition, it was found that the fiber morphology of the pure PAN and BTA fibers does not differ from the morphology of the PAN and BTA fibers in the composite nonwoven sheets.

Influence of the total volume of fiber dispersion

After the determination of the suitable PAN/BTA **24a** ratio, efforts were made to evaluate the necessary volume of the dispersion to prepare a homogenous and robust composite nonwoven sheet. Therefore, the total volume was varied between 10-40 mL PAN/BTA **24a** fiber dispersion while the other parameters were kept constant. Already when filtering off the fiber dispersion, it was noticeable that particularly 10 mL is a too small volume to obtain a uniform composite nonwoven sheet (**c4**). Some parts of the metal mesh on which the fibers are deposited are still visible so that a continuous composite nonwoven sheet is not obtained. A total volume of 20 mL or 30 mL was found to be sufficient to obtain a nearly homogeneous pinhole-free nonwoven sheet **c5** and **c6**. However, a volume of 40 mL results in composite nonwoven sheet **c3** with a thickness of approximately 120 µm, which was found to be the best and most suitable composite to handle. **Figure 84** shows the thickness of the composite nonwoven sheet as a function of the total volume of PAN/BTA **24a** fiber dispersion. Here, a linear increase in the thickness of the composite nonwoven sheets with increasing total volume in the range of 10-40 mL is clearly evident, which allows for a convenient adjustment of the sheets' thickness using these conditions if necessary.
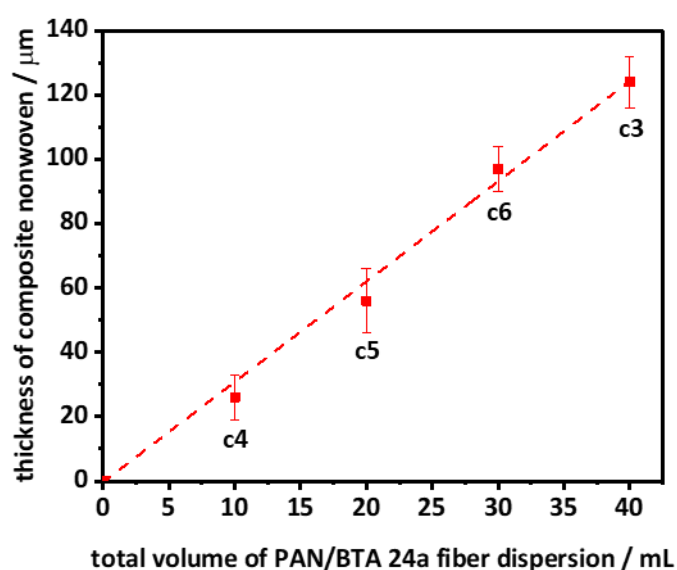
Figure 84: Plot of the thickness of composite nonwovens **c3-6** in relation to the total volume of the PAN/BTA **24a** fiber dispersion.

The composition of the PAN short fiber dispersion, the BTA **24a** solution and the PAN/BTA **24a** fiber dispersion for the preparation of the composite nonwoven sheets **c1-c6** and the reference sheet, as well as the thickness of the prepared sheets, are summarized in **Table 6**.

Table 6: Composition of the PAN dispersion, BTA **24a** solution and PAN/BTA **24a** dispersion for the wet-laid process in a small volume on lab scale using a frit (∅ = 3.7 cm) and the corresponding thickness of the resulting composite nonwoven sheets **c1-6** and reference PAN sheet.

| Sample | Composition of dispersions | | | | | | Composite nonwoven |
| | PAN dispersion | | BTA **24a** solution | | PAN/BTA **24a** dispersion | | |
	Conc. [wt%]	Vol. [mL]	Conc. [wt%]	Vol. [mL]	Total volume [mL]	Ratio of PAN:BTA **24a**	Thickness [µm]
Reference	0.05	30	-	-	30	-	132 ± 6
c1	0.05	10	0.1	30	40	0.2:1	67 ± 6
c2	0.05	20	0.1	20	40	0.6:1	144 ± 13
c3	0.05	30	0.1	10	40	1.9:1	124 ± 8
c4	0.05	7.5	0.1	2.5	10	1.9:1	26 ± 7
c5	0.05	15	0.1	5	20	1.9:1	56 ± 10
c6	0.05	22.5	0.1	7.5	30	1.9:1	97 ± 7
c3	0.05	30	0.1	10	40	1.9:1	124 ± 8

Transfer from lab scale to technical scale

As the screening experiments demonstrated that composite nonwoven sheets composed of electrospun PAN short fibers and supramolecular BTA nanofibers can be successfully prepared by the wet-laid technique together with suitable parameters for their composition, the wet-laid process was scaled up to technical scale. The procedure is similar to the experiments on lab scale. However, this time the PAN/BTA **24a** fiber dispersion was prepared by two different approaches - route A and route B (see **Figure 85**). These different routes were chosen to investigate the influence of the BTA component as a fiber dispersion (route A) or as a solution (route B) on the final morphology and the robustness of the composite nonwoven sheets.

I. Preparation of fiber dispersion
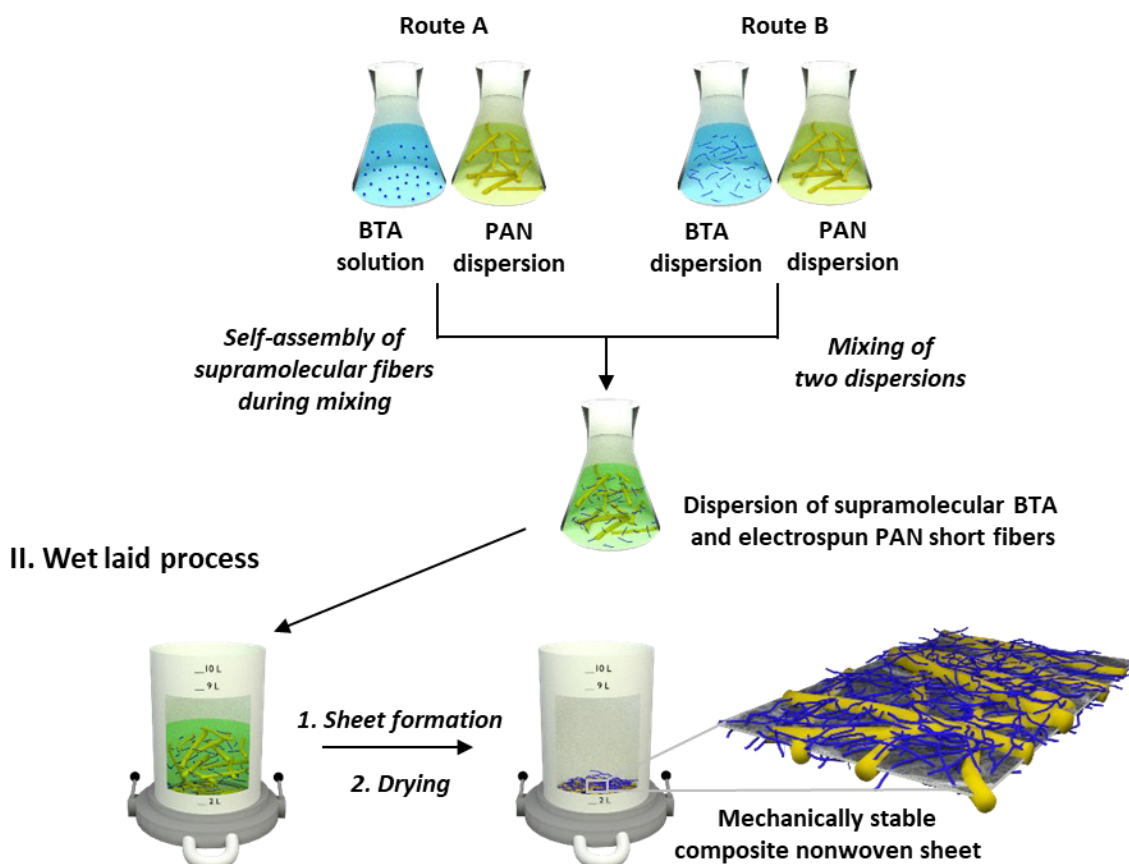
Figure 85: Schematic representation of the preparation process of mechanically stable composite nonwoven sheets composed of electrospun PAN short microfibers (yellow fibers) and supramolecular functional BTA **24a** nanofibers (blue fibers) on technical scale. Two different routes A and B were chosen to prepare dispersions of PAN microfibers and BTA **24a** nanofibers, which were further processed by wet-laid technique (sheet forming process, step II) into mechanically stable composite nonwovens. Reprinted (adapted) with permission from [138] © 2021 American Chemical Society.

Route A is comparable as described for the previous screening experiments, i.e., the use of a homogenous BTA **24a** solution in IPA/H$_2$O (9:1, w/w). For this, **24a** was dissolved in the solvent mixture at 75 °C. After cooling the BTA solution to room temperature, it was directly mixed with the PAN short fiber dispersion. Upon mixing, supramolecular nanofibers are immediately formed *in situ* due to a change in solubility of **24a** in the mixture. The concentration of the **24a** solution was varied between 0.01 wt% and 0.1 wt%, whereas the concentration of PAN fiber dispersion was kept constant to receive composite nonwovens with different compositions.

In route B, supramolecular BTA nanofibers were prepared by self-assembly upon cooling and subsequently mixed with a dispersion of electrospun PAN short fibers. For this, 0.05 wt% of **24a** was completely dissolved in IPA/H$_2$O (9:1, w/w) mixture at 75 °C. Afterwards, the BTA solution was cooled to room temperature resulting in the formation of BTA fibers within 24 h (see **Figure 82**). These supramolecular fibers were then mixed with the PAN short fiber dispersion.

In contrast to the lab scale, the sheet-forming process on technical scale was performed on a HAAGE BB sheet former, which is equipped with a sheet forming column and a vacuum pump and enables the formation of composite nonwoven sheets with a diameter of 20 cm and a significantly larger area of approximately 300 cm². This is important and helpful since numerous test specimens for i.a. mechanical tensile tests can be prepared from such a large-area composite nonwoven sheet, ensuring better comparability of the individual specimens. In addition, the preparation process of composite nonwoven sheets is more consistent and reproducible due to several process stages that can be selected via levers at the HAAGE BB sheet former. To prepare these composite nonwoven sheets, a total volume of the PAN/BTA **24a** fiber dispersion of around 3.7 L was used instead of 40 mL PAN/BTA **24a** fiber dispersion applied on lab scale. For this purpose, the PAN short fiber dispersion and BTA **24a** fiber dispersion (route A) or solution of **24a** (route B) were diluted with appropriate amounts of additional solvent (IPA and water) so that finally, comparable amounts of BTA and PAN fibers were obtained in the composite nonwoven sheets.

After filtration of the PAN/BTA **24a** fiber dispersion, the resulting composite nonwoven sheets, composed of different ratios of PAN short microfibers and supramolecular BTA **24a** nanofibers (hereinafter named **c7-10**), were dried at 60 °C in a vacuum dryer. The detailed experimental procedure can be found in the experimental section (**chapter 7**). Details on the composition of the dispersions, as well as the composition and thickness of the resulting composite nonwoven sheets **c7-10** and the reference PAN sheet, are summarized in **Table 7**.

Table 7: Composition of the PAN dispersion, BTA **24a** solution (route A) or BTA **24a** fiber dispersion (route B) and PAN/BTA **24a** dispersion for the wet-laid process and the composition and thickness of the resulting composite nonwoven sheets **c7-10**. In addition, values of a wet-laid nonwoven consisting only of electrospun PAN short fibers are given as reference. Reprinted (adapted) with permission from [138] © 2021 American Chemical Society.

Sample	Composition of dispersions					Composite nonwoven	
	PAN dispersion		BTA **24a** solution		PAN/BTA **24a** dispersion	Ratio of PAN:BTA **24a**[3]	Thickness [μm]
	Conc. [wt%]	Vol. [mL]	Conc. [wt%]	Vol. [mL]	Ratio of PAN:BTA **24a**		
Reference	0.05	838	-	-	-[1]	-	61 ± 5
c7 (route A)	0.05	838	0.01	419	12:1[2]	>12:1	66 ± 2
c8 (route A)	0.05	838	0.05	419	2.4:1[2]	3:1	74 ± 4
c9 (route A)	0.05	838	0.1	419	1.3:1[2]	1.3:1	82 ± 6
c10 (route B)	0.05	838	0.05	419	2.4:1[2]	3.8:1	68 ± 3

[1] Volume for the preparation of the reference sheet = 3334 mL (838 mL of PAN dispersion, 1742 mL of IPA and 754 mL of H_2O)
[2] Volume for the preparation of the composite nonwoven sheet = 3744 mL (838 mL of PAN fiber dispersion, 410 mL of BTA **24a** solution, 1742 mL of IPA and 754 mL of H_2O) [3] Determined by ^1H-NMR.

The BTA **24a** content within the composite nonwoven sheets was determined by ^{1}H-NMR measurements. Therefore, a calibration was established by dissolving different masses (0.5 mg, 2.5 mg, 5.0 mg and 7.5 mg) of BTA **24a** powder together with 3 mg of dissolved dimethyl terephthalate as a reference in 1 mL deuterated DMSO. Dimethyl terephthalate was chosen as a reference since its peaks do not overlap with the peaks of **24a**. A linear correlation for the calibration was established by plotting the ratio of the two integral $I_{BTA\ 24a}$ at 4.41 ppm and the integral $I_{Reference}$ at 3.87 ppm against the corresponding amount of BTA **24a**. A subsequent linear regression (**Figure 86**) accurately matches the data points.
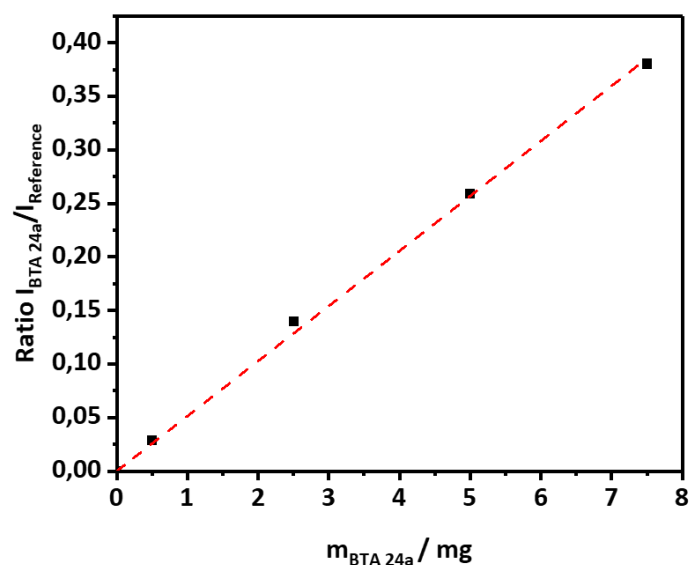
Figure 86: Calibration plot of the ratio of the two integrals $I_{BTA\ 24a}$ at 4.41 ppm and $I_{Reference}$ at 3.87 ppm against the mass of **24a**. Reprinted (adapted) with permission from [138] © 2021 American Chemical Society.

After completely dissolving 10 mg of each composite nonwoven sheet in deuterated DMSO, the corresponding ^{1}H-NMR spectra were measured (**Figure 87**).

Route A
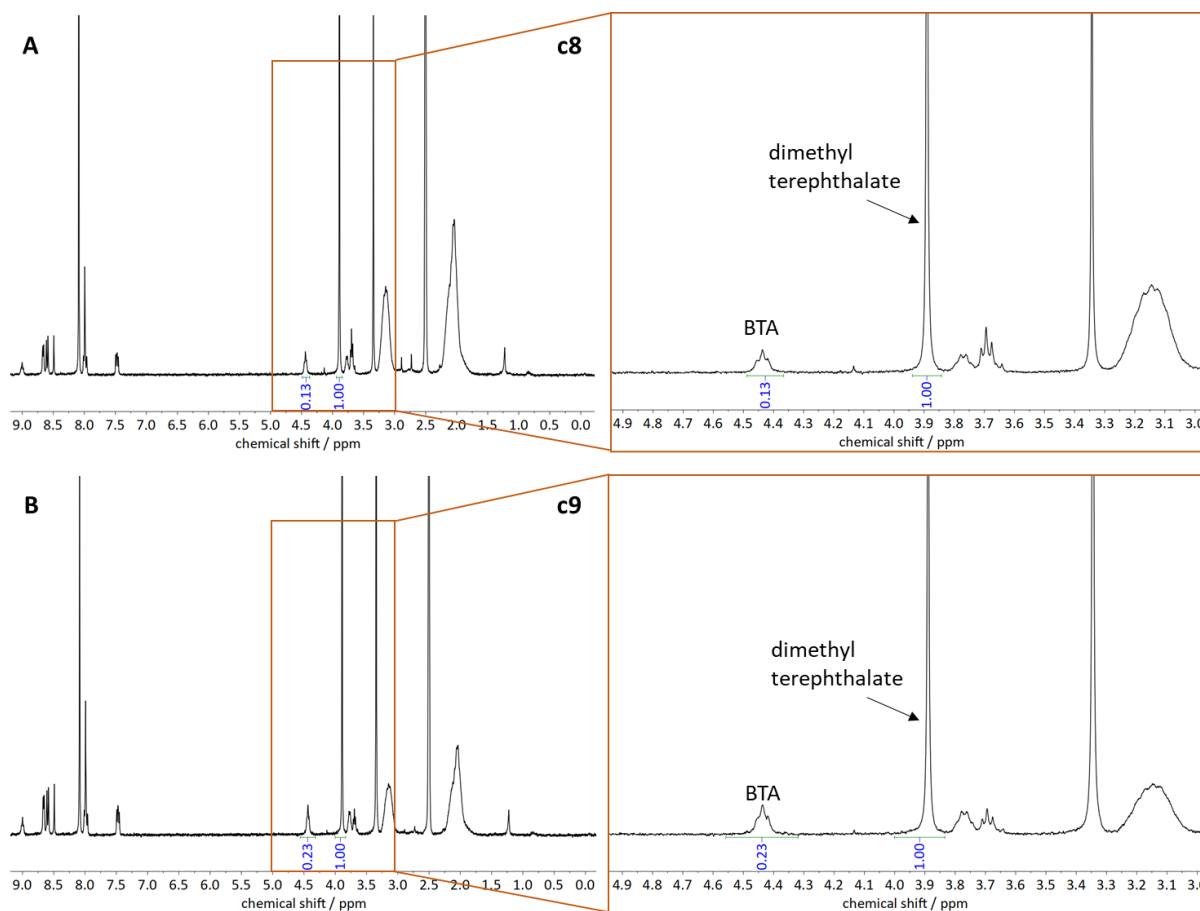
Route B
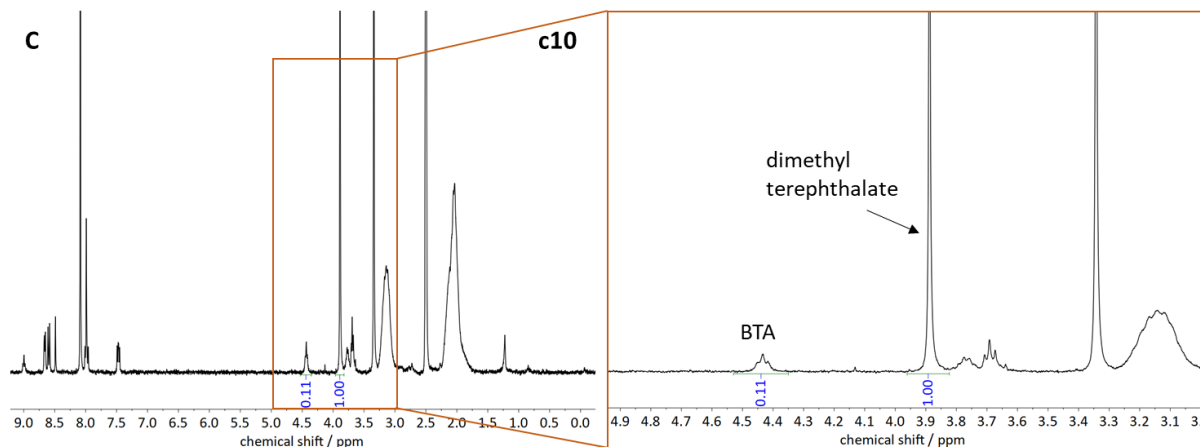
Figure 87: NMR spectra of composite nonwoven sheets **c8** (**A**) and **c9** (**B**) prepared via route A and **c10** (**C**) prepared via route B with 3 mg dimethyl terephthalate added as reference measured in DMSO-d_6. Reprinted (adapted) with permission from [138] © 2021 American Chemical Society.

The NMR spectrum of composite nonwoven sheet **c7** showed no peaks of **24a** due to a too low amount of **24a** within the composite nonwoven sheet. For the other cases, the BTA **24a** content (in mg) within the composite nonwoven sheets **c8**, **c9** and **c10** could be read from the established calibration line after the determination of $I_{BTA\ 24a}$ from the corresponding spectra.

For example, the ratio $I_{BTA\ 24a}/I_{Reference}$ is 0.13 in the case of composite nonwoven sheet **c8**. The BTA amount within a 10 mg sample of this sheet is 2.5 mg. This results in a PAN fiber amount of 7.5 mg and a PAN:BTA **24a** ratio of about 3:1. Importantly, for these composite nonwoven sheets **c8**, **c9** and **c10**, a similar composition was found as in the PAN:BTA **24a** dispersions. This leads to the conclusion that almost all BTA nanofibers and PAN microfibers are present in the final composite nonwoven sheets and no BTA remains dissolved or hardly any fibers are lost during the preparation process.

Morphology of composite nonwoven sheets c7-9

As shown before, the influence of the total fiber dispersion volume and the volume ratio of PAN fiber dispersion to BTA solution were identified as important parameters influencing the stability and robustness of the composite nonwoven sheets. To compare the fiber morphology of lab scale with that of technical scale as a function of the BTA concentration, SEM measurements on different samples and at several positions of the composite nonwoven sheets **c7-9** were carried out. **Figure 88** shows the top view of the composite nonwoven sheets **c7-9** and the neat PAN nonwoven as reference.

Sheet top view

Figure 88: SEM micrographs showing a top view of the composite nonwoven sheets **c7-9** composed of different ratios of PAN short microfibers and supramolecular BTA **24a** nanofibers and a reference sheet composed only of PAN short fibers (**A-D**). Reprinted (adapted) with permission from [138] © 2021 American Chemical Society.

In general, an overall homogenous distribution of PAN microfibers and BTA **24a** nanofibers within the composite nonwoven sheets can be observed. In the case of composite nonwoven sheet **c7**, mostly PAN short fibers are visible and only a few BTA **24a** fibers can be found on the surface of the PAN microfibers. With an increasing concentration of **24a** in the composite nonwoven sheets **c8** and **c9**, the PAN fibers are more surrounded by BTA **24a** fibers and a denser interpenetrating BTA **24a** fiber network is formed. Here, the supramolecular fibers entangle closely with the PAN microfibers. The average diameter of the BTA **24a** nanofibers in these composite nonwoven sheets was 82 ± 25 nm. This diameter is thus about 20 nm lower compared to the BTA **24a** nanofibers obtained after self-assembly upon cooling (see **chapter 3.2.2**). A possible explanation is that upon mixing the BTA **24a** solution with the PAN short fibers, the PAN fibers may act as a nucleation site and thus increasing the nucleation density. A more likely explanation is the rapid change in solubility resulting in BTA nanofibers with a slightly smaller diameter. Here, the processing conditions are different from the self-assembly of neat **24a** described before.

Besides the sheet top view, SEM micrographs of the cross-section of the cut composite nonwoven sheet **c8** at two different magnifications were taken (**Figure 89**). Such a cross-section enables more precise statements about the arrangement of the BTA and PAN fibers across the composite nonwoven sheet.
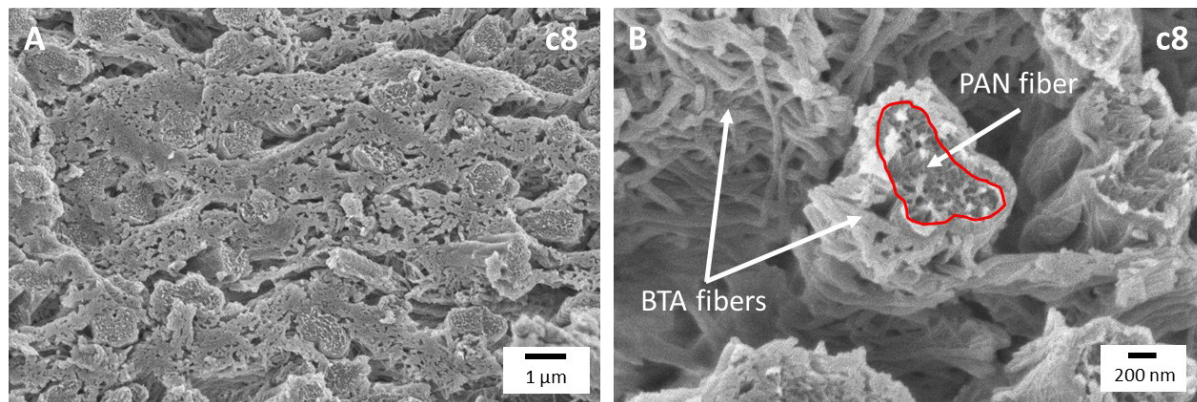
Figure 89: SEM micrographs showing a cross-section of composite nonwoven sheet **c8** at two magnifications (**A** and **B**). Areas of BTA fibers and a PAN fiber (area inside the red line) are shown. Reprinted (adapted) with permission from [138] © 2021 American Chemical Society.

The cross-section of composite nonwoven sheet **c8** also demonstrates the dense connection of the supramolecular nanofibers with the PAN microfibers and the surrounding of PAN microfibers with BTA **24a** nanofibers. Compared to the lab scale process, it seems that a slightly more homogeneous distribution of the PAN and BTA fibers can be observed in the composite nonwoven sheets prepared on technical scale. In addition, a SEM micrograph of a neat PAN nonwoven sheet could be taken since slightly better stability of the reference sheet is achieved due to the more defined processing than on lab scale.

When comparing the morphology of composite nonwovens **c8** and **c10** shown in **Figure 90**, which differ in the preparation of the PAN/BTA fiber dispersion by using the different routes A and B, it is noticeable that both composite nonwoven sheets look similar from a first glance. A closer look revealed that the composite nonwoven sheet **c10** prepared via route B exhibits a more inhomogeneous distribution of supramolecular BTA fibers and electrospun PAN short fibers over the whole sample. Thus, composite nonwoven sheet **c8** is preferred for further use.

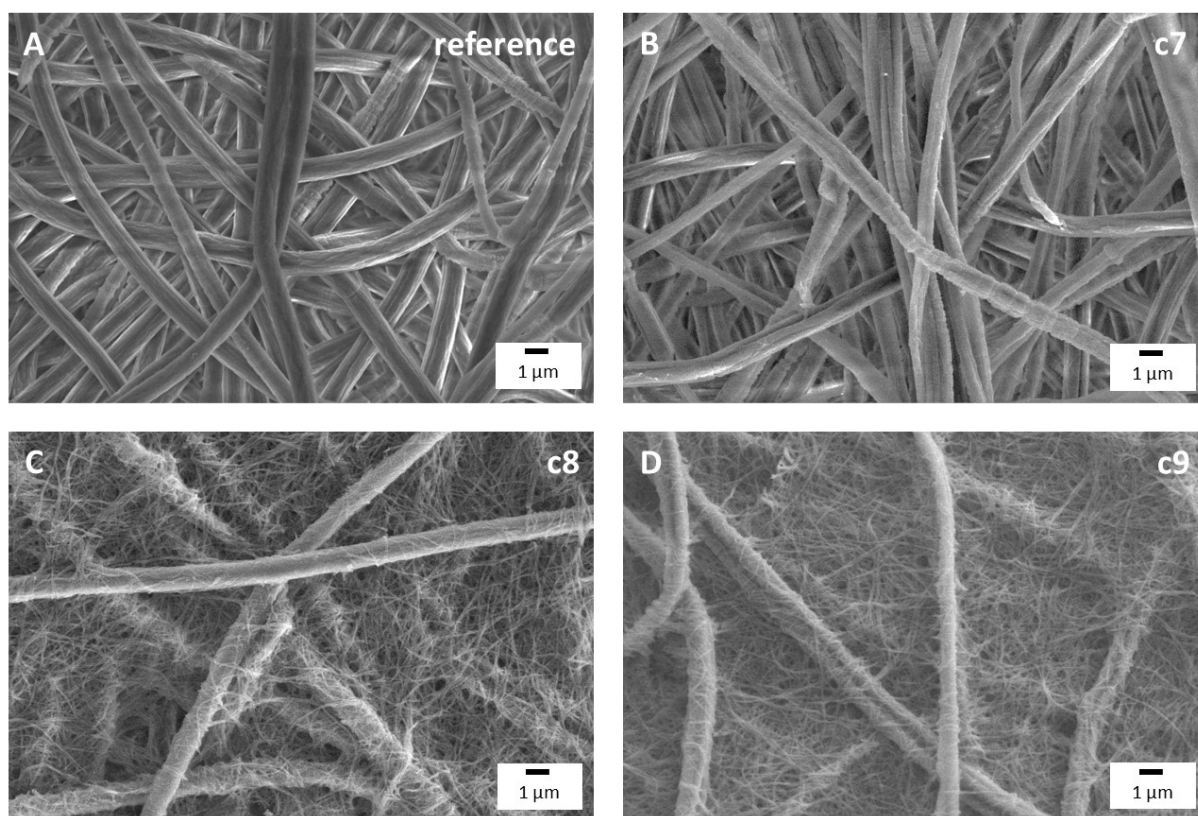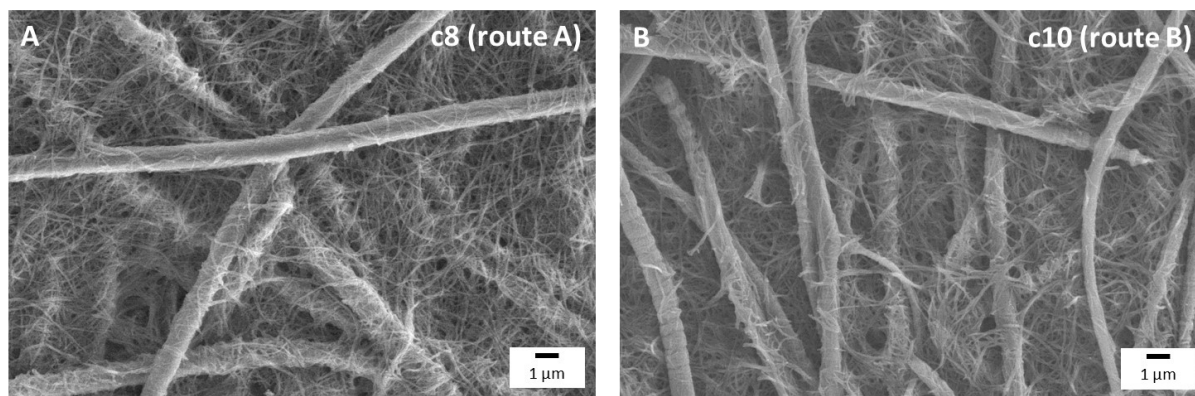**Figure 90:** SEM micrographs showing a top view of the composite nonwoven sheets **c8** and **c10** composed of the same ratios of PAN short microfibers and supramolecular BTA **24a** nanofibers. However, composite nonwoven **c8** was prepared by route A (**A**), whereas **c10** was prepared by route B (**B**).

Pore size, nonwoven density and porosity of composite nonwoven sheets c7-9

For the use of nonwovens in practical applications, besides the nonwovens' morphology, the pore size and porosity of the composite nonwovens are important characteristics. For instance, the mean pore size is used to estimate the ease of accessibility of the nonwoven and the porosity represents the ratio of void volume to total volume in the composite nonwoven sheet. For filtration applications, a smaller pore size resembles a larger number of fibers present in the nonwoven. This, in turn, increases the probability of the deposition of small particles on the fibers from different media. Easier accessibility within the composite nonwoven is achieved with larger pore sizes, which is especially important for catalytic applications. High porosity is commonly beneficial for filtration as well as for catalytic applications to ensure a high mass transfer to the functional surface within the composite nonwovens.

Pore size evaluation: The mean flow pore size of the composite nonwovens **c7-10** and a reference nonwoven was determined using a porometer (PSM 165/H, Dresden, Germany). The experimental procedure is described in detail in the experimental section (**chapter 7**).

Figure 91 shows the mean flow pore size in dependence on the BTA **24a** concentration. It can be observed that the pore size is reduced more than one order of magnitude from 4.86 ± 1.74 µm for the reference nonwoven to 0.36 ± 0.03 µm for composite nonwoven **c10** (also see **Table 8**) due to the presence of the interpenetrating supramolecular fiber network of **24a**.
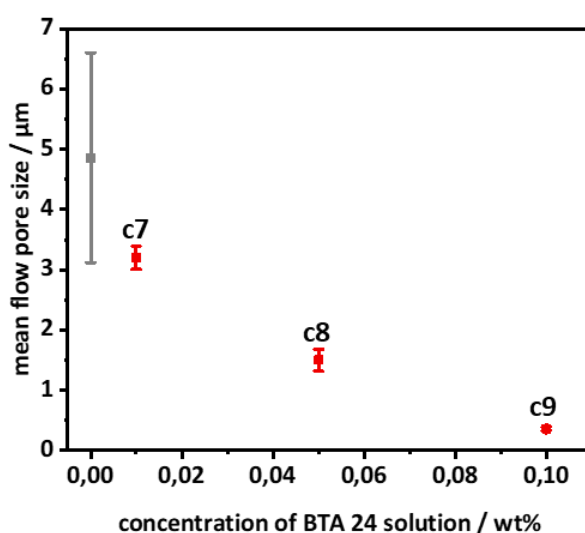
Figure 91: Mean flow pore sizes of the composite nonwovens **c7-c9** (red symbols) with different BTA **24a** contents and the reference nonwoven without BTA **24a** (grey symbol). At least two samples were measured and averaged. The error bars denote the standard deviation. Reprinted (adapted) with permission from [138] © 2021 American Chemical Society.

Nonwoven density and porosity determination: The nonwoven densities were determined from the size (measured using a Vernier caliper) and the weight (measured using a microbalance) of the composite nonwoven sheets. Porosity was calculated according to **equation 4** from the measured nonwoven density $\rho_{nonwoven}$ and the theoretical density of the corresponding compact sample.

$$\text{Porosity (\%)} = \left(1 - \frac{\rho_{nonwoven}}{\rho_{BTA}\varphi_{BTA} + \rho_{PAN}\varphi_{PAN}}\right) \cdot 100 \qquad \textbf{4}$$

The density of PAN (1.184 g/cm³) and an estimated density of BTA **24a** ($\sim$1.1 g/cm³) based on literature values of BTA[139] were used together with the respective weight fractions of PAN (φ_{PAN}) and BTA **24a** (φ_{BTA}) in the nonwovens. The weight fractions were determined by ¹H-NMR measurements.

The nonwoven density of composite sheets **c7-9** increased with an increasing concentration of BTA **24a** nanofibers from 0.18 g/cm³ for the reference nonwoven to 0.24 g/cm³ for composite nonwoven **c9** (**Figure 92A**). In contrast, the porosity slightly decreased with an increasing concentration of BTA **24a** nanofibers from 85 % to 79 % (**Figure 92B**).
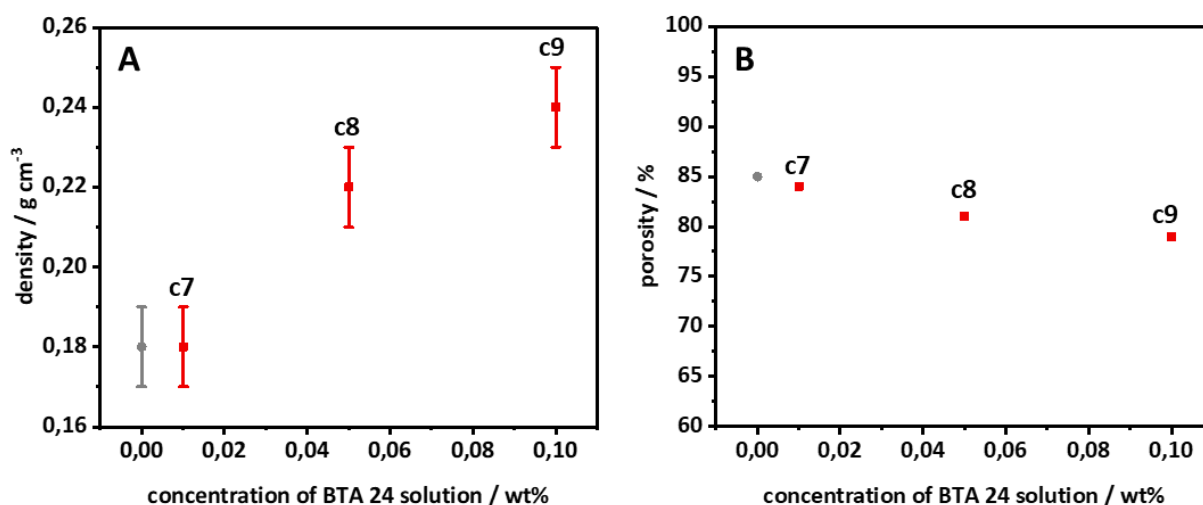
Figure 92: Density measurements (**A**) and porosity calculations (**B**) for the composite nonwovens **c7-9** (red symbols) and the reference nonwoven composed only of electrospun PAN short fibers (grey symbol). Reprinted (adapted) with permission from [138] © 2021 American Chemical Society.

Table 8 summarizes the density, mean flow pore size and porosity of composite nonwovens **c7-10** and the reference nonwoven.

Table 8: Summary of the composite nonwoven density, pore size and porosity.

Sample	Density (g/cm³)	Mean flow pore size (µm)	Porosity (%)
Reference	0.18 ± 0.01	4.86 ± 1.74	85
c7	0.18 ± 0.00	3.20 ± 0,19	84
c8	0.22 ± 0.01	1.50 ± 0.18	81
c9	0.24 ± 0.01	0.36 ± 0.03	79
c10	0.24 ± 0.03	1.61 ± 0.17	79

*Mechanical properties of composite nonwoven sheets **c7-10***

Besides the previously mentioned characteristics, the mechanical properties of the composite nonwovens play an essential role since the mechanical stability should be high enough to prevent disintegration or destruction of the composite nonwoven during catalytic reactions. Moreover, this also allows the reuse of the composite nonwovens. Tensile tests on composite nonwoven sheets **c7-10** were carried out to obtain values for comparing the mechanical properties of the different composite nonwoven sheets and enable to study the influence and interplay of the interpenetrating BTA **24a** nanofibers with the PAN short microfibers. These tests were performed on cut strips with dimensions of 3.0 x 0.3 cm. Five specimens were measured from each composite nonwoven sheet to ensure reproducibility. To compare the mechanical properties of the different nonwoven sheets, the ultimate strength and the behavior of the stress-strain curve at the beginning of the measurements were examined.

Figure 93 shows the stress-strain curves of composite nonwovens **c7-9** and a neat PAN nonwoven sheet as a reference.
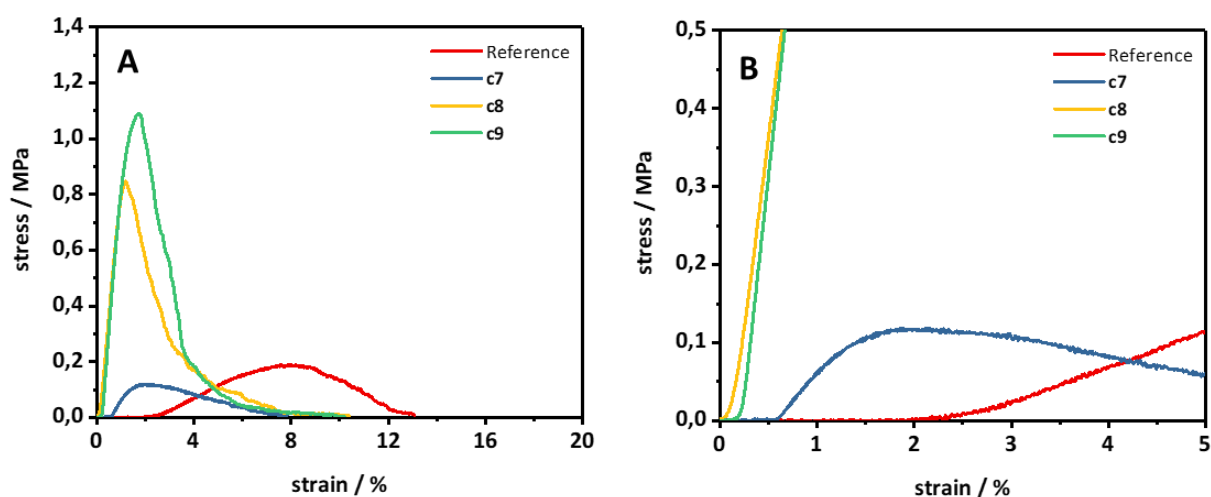
Figure 93: Stress-strain curves of composite nonwoven sheets **c7-9** composed of PAN short microfibers and supramolecular BTA **24a** nanofibers and a reference nonwoven sheet composed only of PAN short fibers. Graph **B** shows a magnification of **A** in the stress of up to 0.5 MPa and the strain to 5 %. Reprinted (adapted) with permission from [138] © 2021 American Chemical Society.

The reference nonwoven sheet and composite nonwoven sheet **c7** show poor mechanical properties. The ultimate strength of these nonwovens is below 0.2 MPa and is attributed to weak interconnections of the polymer fibers in the composite nonwoven. At the beginning of the measurement, a differently pronounced shift in the stress-strain curves can be observed, which is attributed to a fiber alignment and disentanglement. In the case of **c7**, this behavior is less pronounced due to the presence of supramolecular **24a** fibers. With increasing BTA **24a** fiber concentration, an ultimate strength of 0.78 ± 0.19 MPa and 1.09 ± 0.15 MPa was determined for the composite nonwovens **c8** and **c9**, which were larger by a factor of 4 and 5, respectively. These results demonstrate that the BTA **24a** fiber

amount within composite nonwoven **c8** noticeably improves the overall mechanical properties of the composite nonwovens. A further increasing amount of BTA **24a** nanofibers as in composite nonwoven **c9** only slightly improves the mechanical properties, indicating a possible limit of maximum ultimate strength.

A comparison of the mechanical properties of composite nonwovens **c8** and **c10**, which differ only by their preparation via routes A and B, is shown in **Figure 94**. Remarkably, despite the same composition and a comparable morphology (see **Figure 90**) of composite nonwoven sheets **c8** and **c10**, different mechanical properties can be observed. Composite nonwoven sheet **c10** shows only about half the ultimate strength with 0.43 ± 0.03 MPa compared to **c8** with 0.78 ± 0.19 MPa. In addition, as previously described, a significant shift in the stress-strain curve is present at the beginning of the measurement of **c10**, which also indicates alignment and disentanglement of the (polymer) fibers. These findings can possibly be attributed to the more inhomogeneous distribution of the supramolecular BTA fibers in the composite nonwoven **c10**.
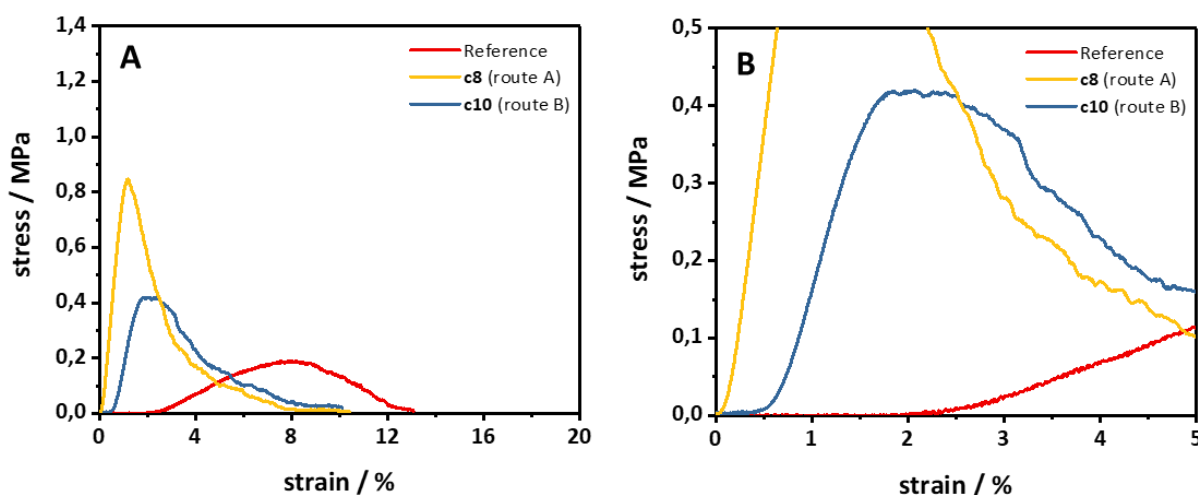
Figure 94: Stress-strain curves of composite nonwovens **c8** (route A) and **c10** (route B) composed of PAN short microfibers and supramolecular BTA **24a** nanofibers as well as a reference nonwoven composed only of PAN short fibers. Graph **B** shows a magnification of **A** in the stress of up to 0.5 MPa and the strain to 5 %.

These findings demonstrate that compact sheets of composite nonwovens prepared via route A show an unexpected superior mechanical performance compared to composite nonwoven sheets comprising the same composition via route B. Therefore, composite nonwoven sheets prepared via route A will be used for further applications.

Wettability of composite nonwoven sheets c7-9

Since the composite nonwovens are intended to be used in aqueous media for further applications, wettability with water as well as shape persistence in aqueous media are of great importance. High wettability of the composite nonwovens indicates an attractive interaction of PAN microfibers and supramolecular BTA **24a** nanofibers with water. It also promotes the transport of educts and products from the aqueous media to the fiber surface in catalytic reactions. A drop shape analyzer was used to visualize the penetration of a water droplet on the composite nonwovens **c7-9** and a reference nonwoven. Time-dependent investigations revealed that the water droplet completely penetrates into the nonwovens within a few seconds, which is considered a noticeable wetting behavior and is present in all samples (**Figure 95**). Full droplet penetration takes longer with an increasing amount of BTA **24a** nanofibers. However, it is still fully accomplished after about 11 s for composite nonwoven **c9**. This effect is mainly attributed to the decreasing pore size of the composite nonwovens, as shown before. For further application, the wettability with water for all composite nonwoven sheets is given in a reasonable manner that NP immobilization from aqueous medium or catalytic reactions in aqueous medium can be carried out.
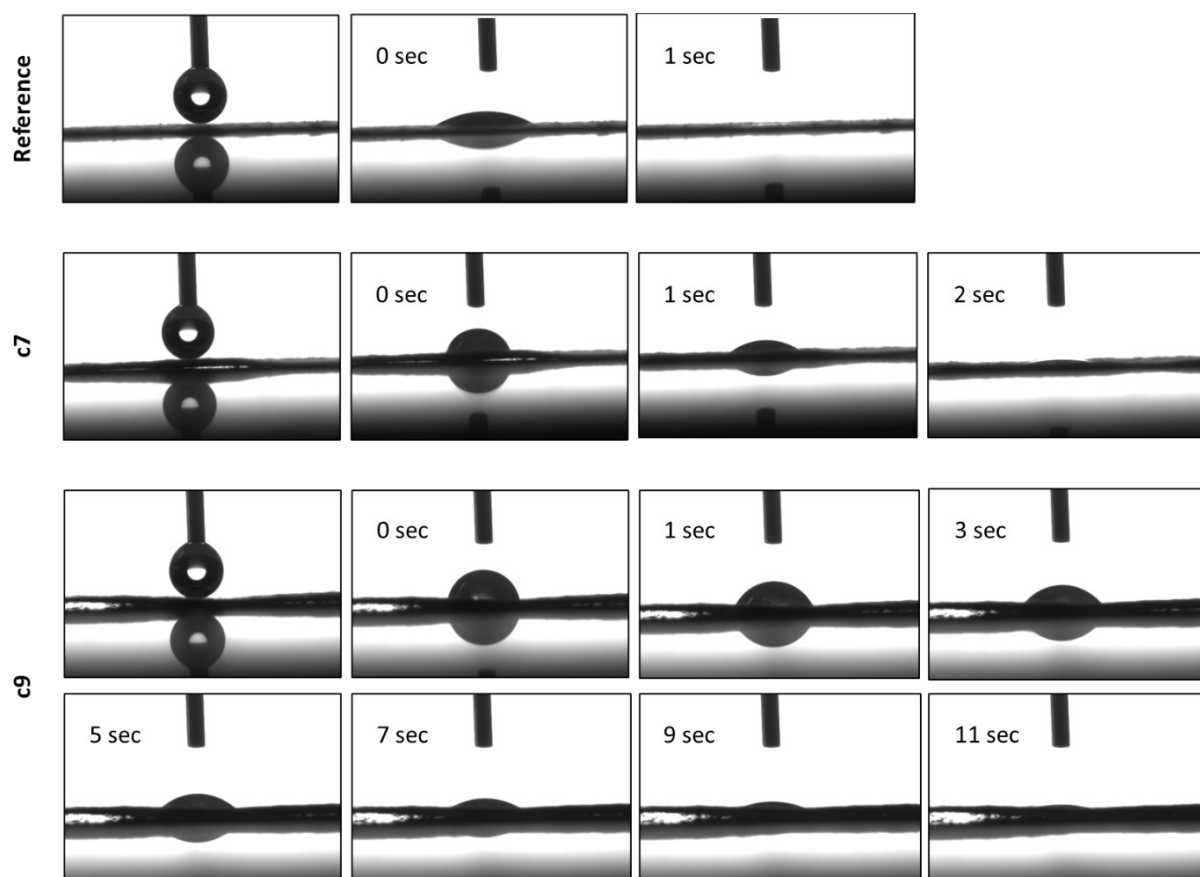
Figure 95: Contact angle measurements of the reference nonwoven and composite nonwoven sheets **c7** and **c9**. A water droplet was placed on the nonwoven and then photos of the droplet were taken at short time intervals. Reprinted (adapted) with permission from [138] © 2021 American Chemical Society.

*Shape persistence of composite nonwoven sheets **c7-c9** in water*

To use and reuse the composite nonwoven sheets in liquid media, shape-persistent nonwovens are beneficial. Therefore, the composite nonwoven sheets **c7-c9** were placed in water and shaken for 0, 1 and 24 h (**Figure 96**).
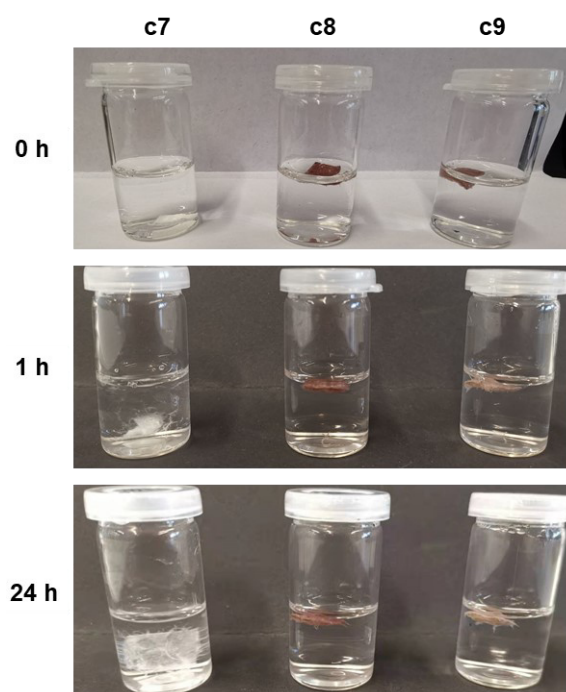
Figure 96: Shape persistence experiments of composite nonwoven sheets **c7-c9** were carried out in water for 24 h upon shaking at 500 rpm. Photos of **c7-c9** were taken after 0, 1 and 24 h, respectively. Reprinted (adapted) with permission from [138] © 2021 American Chemical Society.

As shown in **Figure 96**, no or only poor shape persistence was observed after stirring a 1 x 1 cm sample of the reference nonwoven and composite nonwoven **c7** for several hours at 500 rpm. In contrast, the shape was preserved for several hours with a higher amount of BTA **24a** nanofibers in the composite nonwovens **c8** and **c9**. Thus, the increasing amount of BTA fibers significantly improves the shape persistence of the composite nonwoven sheets.

4.3 Conclusion of functional microfiber-nanofiber composites

Microfiber-nanofiber composites containing supramolecular fibers of **3a** were successfully prepared via *in situ* formation of supramolecular nanofibers within the meshes of a PA woven fabric by self-assembly upon cooling and simultaneous solvent evaporation. Here, especially the solvent system has a strong influence on the morphology of the composite, including the homogenous distribution of BTA fibers and the BTA fiber diameter. The composite showed insufficient stability in aqueous media due to the low adhesion of the supramolecular fibers to the PA woven fabric. Fibers of **3a** detached from the PA fabric and were dispersed in the water. To improve the stability of the **3a** fibers in the composite, the non-functional BTA **25**, which is known to form stable composites, was selected as a supporting structure for fibers of **3a**. The best composite, showing a homogenous BTA fiber distribution morphology of **3a** and **25** within the whole composite, was obtained using an IPA/H_2O (8:2, w/w) mixture and a concentration of 1.0 wt% mixture of **3a** and **25** (4:6 mol%). Based on a bimodal fiber distribution and by additionally performed co-localized Raman measurements, it was confirmed that **3a** and **25** self-assemble independently, which is presumably, among others, due to the different crystal structures of the two compounds. Despite the second scaffold structure, no fully mechanical stability in aqueous media could be established. Some BTA fibers detach from the PA fabric, especially at the edges of the composites. However, the BTA fibers do not dissolve but are dispersed as single fibers in the water. This behavior is not desirable for use in further applications like immobilization of NPs or catalysis. For that reason, the developed system can only be used in the immobilization of NPs or in catalysis to a limited extent.

In contrast, mechanically stable composite nonwoven sheets comprising electrospun PAN short microfibers and supramolecular BTA nanofibers were successfully prepared for the first time by combining electrospinning, self-assembly and the wet-laid process. It was demonstrated that this combination is highly suited to achieve mechanically stable composite nonwoven sheets with a homogenous fiber morphology due to the formation of an interpenetrating network of supramolecular BTA nanofibers and PAN microfibers. Besides the ratio of PAN dispersion and BTA solution, the total volume of the PAN/BTA fiber dispersion plays an important role in the sheet forming process. Too low amount of BTA **24a** fibers in the composite nonwoven sheets leads to poor mechanical properties of the composites, whereas too high BTA concentration can be unfavorable in the sheet-forming process due to gel formation and can lead to a too dense BTA fiber network within the composite nonwoven sheets. The best composite nonwoven sheet, showing a homogenous distribution of BTA nanofibers and PAN microfibers with the whole composite, was obtained using a PAN/BTA **24a** ratio of about 2-3:1. SEM measurements showed that the BTA **24a** fibers are densely connected to the PAN fibers and surround the PAN fibers. In addition, it was found that the fiber morphology of the neat PAN and BTA fibers is similar to the morphology of the PAN and BTA fibers in the composite nonwoven sheets. The BTA fiber diameter in the composite nonwoven sheet is slightly smaller than that of the BTA fibers formed by self-assembly upon cooling. The total volume of the PAN/BTA **24a** fiber dispersion

significantly influences the thickness of the sheet and also plays a role in the homogeneity of the fibers in the resulting composite nonwoven sheets.

After determining the basic parameters on lab scale, the sheet-forming process was also successfully transferred to technical scale using the Haage BB sheet former enabling an easier and more reproducible preparation process of the sheets with a significantly larger diameter of 20 cm. Two different routes A and B were investigated on technical scale with respect to the morphology and robustness of the composite nonwoven sheets. In route A, the BTA **24a** solution was mixed with PAN short microfibers, whereas in route B, already self-assembled BTA **24a** nanofibers were mixed with PAN short microfibers. The chosen route showed no significant difference with respect to the morphology of the composite nonwoven sheets. Surprisingly, the composites prepared by route B showed significantly lower mechanical properties. Therefore, composite nonwoven sheets prepared via route A will be used for further applications. In general, an increasing amount of BTA nanofibers within the composite nonwovens significantly improve the mechanical properties and the shape persistence, which clearly improves the use and reusability of the composite nonwoven sheets. In addition, all composite nonwovens showed good wettability with water, which is beneficial for further applications such as the immobilization of NPs from aqueous media.

5 Immobilization of gold nanoparticles and ions on functional supramolecular nanofibers

In this chapter, the functionality of the pyridine- and terpyridine-substituted BTA nanofibers is demonstrated and discussed by the immobilization of AuNPs and Au ions. AuNPs were exemplarily selected as material since AuNPs can straightforwardly be synthesized according to known procedures, show high catalytic activity and allow for a comparison with findings in literature due to a large number of publications. In addition to the widely used citrate-stabilized AuNP dispersions, a polyvinyl-pyrrolidone (PVP) stabilized AuNP dispersion (hereinafter referred to as PVP@AuNP) was selected to investigate the influence of the different stabilizing ligands on the immobilization behavior. The latter was provided as spray-dried PVP@AuNP powder by the Chair of Macromolecular Chemistry II, University of Bayreuth, and was used to prepare an aqueous dispersion of PVP stabilized AuNPs. The average PVP@AuNP diameter of 16.5 ± 2.9 nm was determined by TEM measurements in previous works. [75] Citrate stabilized AuNPs (hereinafter referred to as Citrate@AuNP) with a diameter of 30 nm were acquired from Aldrich. For the *in situ* formation of AuNPs, tetrachloroauric (III) acid was used as a precursor and NaBH$_4$ as a reducing agent.

Parameters such as the AuNP/ion uptake capacity, the rate of AuNP/ion adsorption and the leaching behavior of the immobilization of AuNPs from the fibers play a crucial role in various applications such as the removal of contaminants or catalysis. In particular, the targeted immobilization of AuNPs in functional and macroscopically large nonwoven composites enables the preparation of catalytically active materials, which, in contrast to simply dispersed AuNPs, can be more easily removed from the reaction solution after catalysis and reused several times. Immobilization of AuNPs enables a homogenous distribution of the AuNPs and prevents agglomeration on the fibers to ensure a high active surface of the AuNPs. Furthermore, the catalytic system should show a high degree of reusability without loss of catalytic activity. For that reason, AuNPs should not detach in aqueous or organic media, which makes their recovery difficult and the AuNPs may be released into the environment in an uncontrolled manner.

To comprehensively investigate and evaluate the nanofibers' functionality and the above parameters, four different ways of AuNP immobilization were chosen:

i) Simple mixing of BTA fibers or a BTA fiber dispersion with a AuNP dispersion
ii) Immersion in a AuNP dispersion of composite nonwoven sheets comprising these functional BTA nanofibers
iii) Filtration of a AuNP dispersion through a supramolecular functional BTA fiber network or a composite nonwoven sheet
iv) *In situ* formation of AuNPs on supramolecular BTA fibers or within composite nonwoven sheets comprising these functional BTA nanofibers

In **chapter 5.1**, the immobilization of AuNPs on *supramolecular nanofibers of BTAs with pyridine substituents* is described. Here, the influence of the number of pyridine substituents in the BTA molecule on the immobilization behavior is investigated.

Chapter 5.2 describes the immobilization of AuNPs on *supramolecular nanofibers of BTAs with terpyridine substituents*. Here, we investigate how immobilization on pure BTA nanofibers differs from immobilization on composite nonwoven sheets and how the composite nonwoven sheets perform in immobilization of AuNP via immersion and filtration.

In **chapter 5.3**, the *in situ formation of AuNPs on supramolecular nanofibers of BTAs with terpyridine substituents* is discussed. Here, the *in situ* formation is investigated on pure BTA nanofibers and in the composite nonwoven sheets.

5.1 Immobilization of AuNPs on supramolecular fibers of BTAs with pyridine substituents

In a first step, the capability of BTAs with pyridine substituents to absorb AuNPs was investigated. Particularly, the question was addressed to which extent BTAs with a different number of pyridine substituents are able to immobilize AuNPs. Here, it is expected that with an increasing number of pyridine moieties in the periphery of the molecules from one, two to three, the density of the active moieties on the supramolecular fibers' surface increases and thus improves the AuNP capability. Consequently, the BTAs with aliphatic substituents **9a-c** and **16a-c** are expected to be less efficient for the AuNP immobilization on the supramolecular fibers due to their nonpolar character. For that reason, immobilization experiments were performed using supramolecular fibers of **9a** and **16a**, which carry a different number of pyridine and *tert*-butyl substituents, fibers of **9b** and **16b**, which exhibit ethylhexyl instead of *tert*-butyl substituents as well as supramolecular fibers of **3a**, which carries three pyridine substituents. To validate the concept of AuNP immobilization, experiments were carried out with these pyridine-containing BTAs and two aliphatic BTAs **26** (three *tert*-butyl substituents) and **25** (three ethylhexyl substituents), which were chosen as reference compounds.

For the absorption experiments, all supramolecular fibers were prepared by self-assembly upon cooling and subsequent isolation of the BTA fibers by filtration. Here, we are aware that the fiber thickness and thus the active moieties on the supramolecular fiber surface vary depending on the BTA. However, to standardize the procedure, 1 mg of the isolated and dried BTA fibers was added to 3 mL of an aqueous PVP@AuNP dispersion and mixed for 5 min. The fibers were then filtered off using a PTFE (polytetrafluoroethylene) syringe filter. Non-bonded AuNPs were removed by a subsequent washing step by filtering 2 mL of water through the PTFE syringe filter. UV/Vis spectra were recorded in a range of 300-800 nm from each of the filtrates. The preparation of Au-loaded BTA fibers is schematically shown in **Figure 97**.
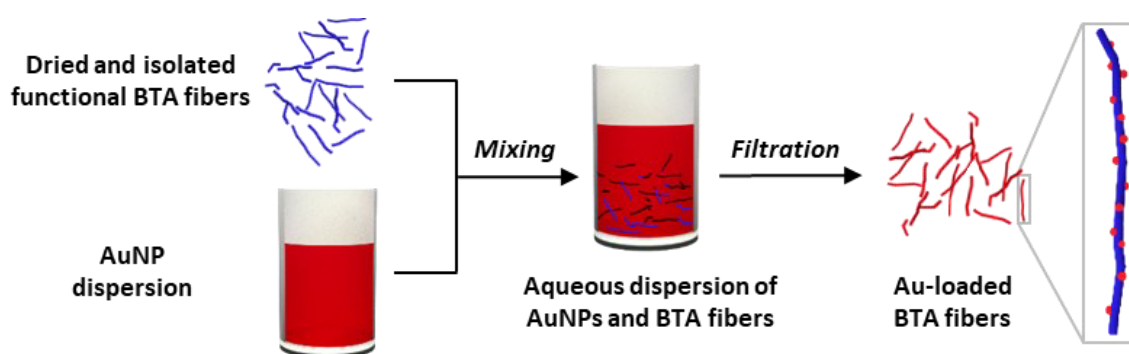
Figure 97: Schematic representation of the preparation process of Au-loaded pyridine-containing supramolecular BTA nanofibers. Dried and isolated functional BTA fibers (blue fibrous structures) are mixed with an aqueous AuNP dispersion (red). During mixing, the AuNPs (red dots) can adsorb on the BTA fiber surface. After filtration, isolated Au-loaded BTA fibers (red fibrous structures) are obtained. On the right side of the schematic, a magnification of a single BTA fiber with immobilized AuNPs (red dots) is shown.

The adsorption efficiency of AuNPs on the BTA nanofibers was calculated based on UV/Vis measurements, comparing the absorption values of the filtrate ($A_{filtrate}$) and the initially employed PVP@AuNP dispersion as reference (A_0) at a wavelength of 524 nm. This is the absorption maximum of the PVP@AuNPs, which occurs at a certain wavelength depending on the AuNP diameter. Therefore, 1 mL of the PVP@AuNP dispersion (1 g/L) and 1 mL of the filtrate (after immobilization) were measured. The adsorption efficiency (AE) at 524 nm is calculated according to **equation 5**:

$$\mathbf{AE_{524\,nm}}\,(\%) = \left(1 - \frac{\mathbf{A_{filtrate}}}{\mathbf{A_0}}\right) \cdot \mathbf{100} \qquad\qquad \mathbf{5}$$

Additionally, ICP-OES measurements of the same samples were performed to calculate and compare the adsorption efficiency to UV/Vis measurements. The adsorption efficiency is calculated according to **equation 6** using the concentration of the filtrate ($c_{filtrate}$) and the PVP@AuNP dispersion as reference (c_0):

$$\mathbf{AE}\,(\%) = \left(1 - \frac{\mathbf{c_{filtrate}}}{\mathbf{c_0}}\right) \cdot \mathbf{100} \qquad\qquad \mathbf{6}$$

Based on (i) the adsorption efficiency, (ii) the Au amount of 1 mL PVP@AuNP dispersion and (iii) the volume of PVP@AuNP dispersion used for immobilization of AuNPs ($V_{PVP@Au}$), the Au amount on BTA nanofiber can be calculated according to **equation 7**:

$$\mathbf{m_{Au}}\,(\mathbf{\mu g}) = \mathbf{AE} \cdot \mathbf{m_{Au\,1\,mL\,PVP@AuNP}} \cdot \mathbf{V_{PVP@Au}} \qquad\qquad \mathbf{7}$$

The Au amount within 1 mL of PVP@AuNP dispersion ($m_{Au\,1\,mL\,PVP@AuNP}$) was determined by ICP-OES measurement and is 30 ± 5 µg Au.

The results of the immobilization experiments, including the UV/Vis spectra of filtrates after immobilization of PVP@AuNP on the supramolecular fibers of **3a**, **9a**, **16a** and **26** and a table summarizing the adsorption efficiencies calculated from UV/Vis and ICP-OES data as well as the Au amount immobilized on the BTA fibers, are shown in **Figure 98**.

From the UV/Vis spectra shown in **Figure 98**, it can be clearly seen that with an increasing number of aliphatic substituents (from **3a** to **26**), the maximum absorption at a wavelength of 524 nm increases. The smaller the difference between the absorption of initially employed PVP@AuNP dispersion (shown in red) and the corresponding filtrate, the lower the adsorption efficiency of AuNPs on the supramolecular fibers.
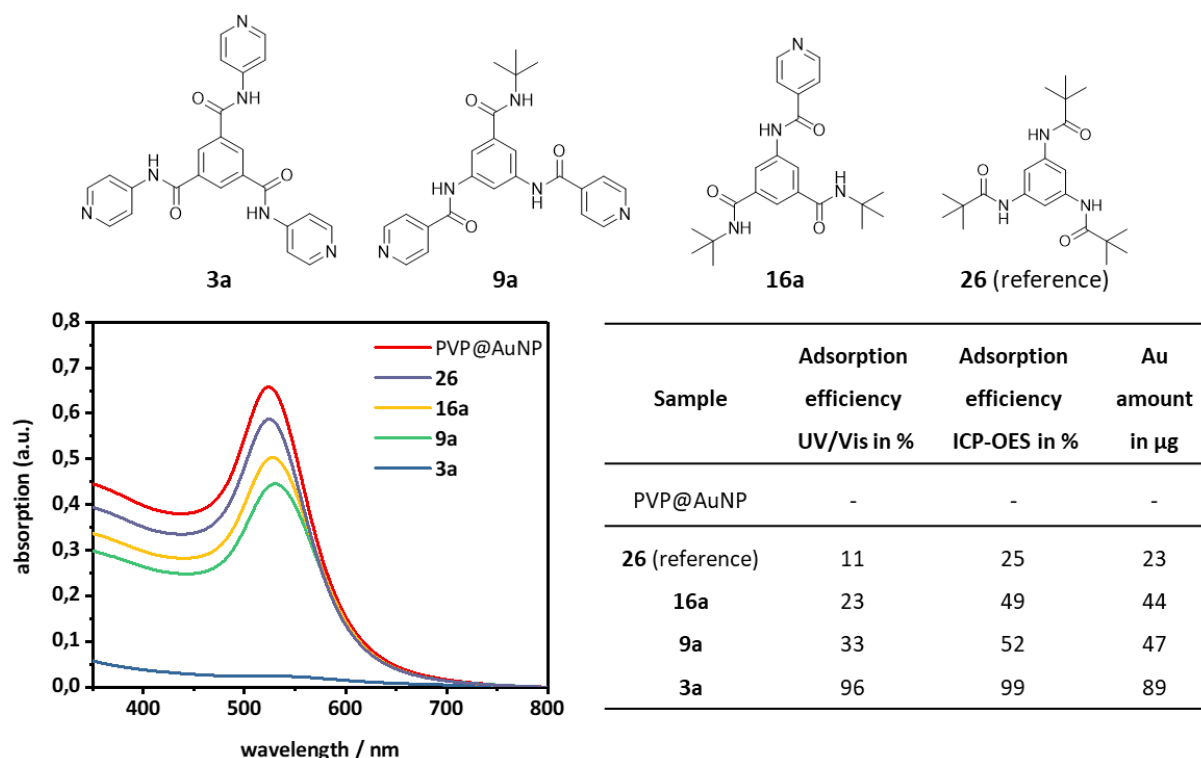
Figure 98: Comparison of the immobilization of PVP@AuNPs on supramolecular BTA fibers with different numbers of pyridine and *tert*-butyl substituents. The number of pyridine substituents continuously decreases from **3a** (three pyridine substituents) to **26** (no pyridine substituents). The Au amount was calculated based on the ICP-OES measurements (1 mL PVP@AuNP contains 30 µg).

Nearly all AuNPs were immobilized on the fibers of **3a** within 5 min, as evidenced by the complete optically decolorization of the AuNP dispersion resulting in almost no absorption. In contrast, a much smaller amount of AuNPs was immobilized on the supramolecular fibers of **9a**, **16a** and **26**, since a distinct absorption signal of the AuNPs at a wavelength of 524 nm is present. Thus, the adsorption efficiency decreases with a decreasing number of pyridine substituents. However, the difference in the adsorption efficiency between **3a** and **9a** is much larger than expected, although **9a** carries only one pyridine substituent less. We assume that already one *tert*-butyl group strongly influences the two pyridine moieties to some extent resulting in a significantly lower immobilization of AuNPs. Interestingly, for **9a**, **16a** and **26**, the adsorption efficiency calculated from ICP-OES data according to **equation 6** is higher than the efficiencies calculated from UV/Vis data according to **equation 5**. The adsorption efficiencies from UV/Vis and ICP-OES differ by about 20 % for **9a** and **16a** and about 15 % for **26**. The difference in adsorption efficiency between **9a** and **16a** is relatively small at about 3 %, according to ICP-OES measurements. On the reference fibers of **26**, only 25 % of the AuNPs were adsorbed due to the lack of functionality. More importantly, those deposited AuNPs can be easily removed again from the fiber surface by applying a subsequent washing step with water, demonstrating that the AuNPs are not firmly bound. In the case of **26**, only physisorption can take place, whereas, in the presence of pyridine substituents, chemisorption is possible.

The UV/Vis spectra of **3a**, **9b**, **16b** and **25**, the adsorptions efficiencies calculated from the UV/Vis and ICP-OES data and the immobilized Au amount on the supramolecular BTA fibers are shown and given in **Figure 99**.

Sample	Adsorption efficiency UV/Vis in %	Adsorption efficiency ICP-OES in %	Au amount in µg
PVP@AuNP	-	-	-
25 (reference)	15	28	25
16b	27	45	41
9b	36	54	49
3a	96	99	86
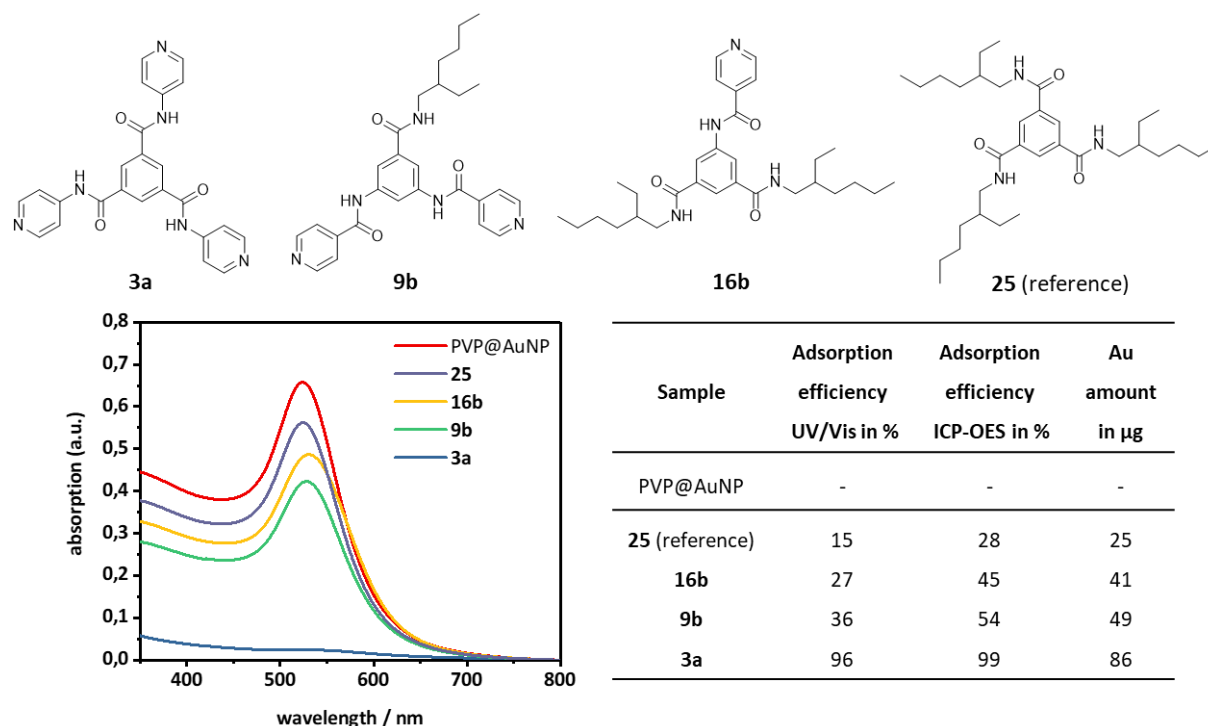
Figure 99: Comparison of the immobilization of PVP@AuNPs on supramolecular BTA fibers with different numbers of pyridine and ethylhexyl substituents. The number of pyridine substituents continuously decreases from **3a** (three pyridine substituents) to **25** (no pyridine substituents). The Au amount was calculated based on the ICP-OES measurements (1 mL PVP@AuNP contains 30 µg).

The calculated adsorption efficiencies of **9b**, **16b** and **25**, based on the UV-Vis and ICP-OES measurements, are almost identical to those of the former series of **9a**, **16a** and **26**. Based on the UV/Vis measurements, the adsorption efficiencies of the BTAs with ethylhexyl substituents (**9b**, **16b** and **25**) are each only about 3 % higher than the efficiencies of the corresponding BTAs with *tert*-butyl substituents (**9a**, **16a** and **26**). Thus, the two different aliphatic substituents in the BTA structure hardly affect the immobilization behavior of AuNPs.

In addition to the adsorption efficiency, a homogeneous distribution of AuNPs on the fiber surface is of great importance. A straightforward method to study the distribution of AuNPs and possible AuNP agglomeration on the supramolecular fibers is provided by SEM. **Figure 100** shows exemplary SEM micrographs of **3a**, **9a**, **16a** and **26** after immobilization of AuNPs.
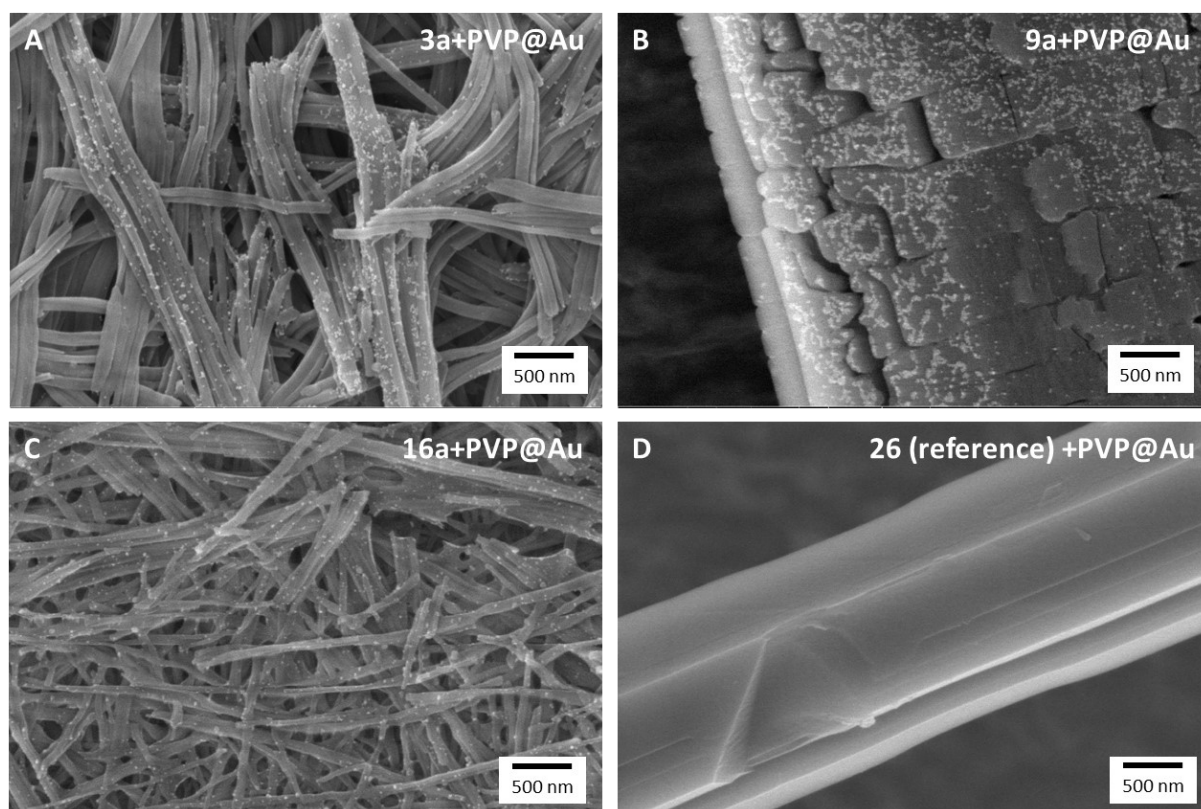
Figure 100: SEM micrographs of Au-loaded supramolecular BTA fiber of **3a** (**A**), **9a** (**B**), **16a** (**C**) and reference **26** (**D**). In micrographs **A-C**, AuNPs can be observed very well, whereas no AuNPs can be observed in micrograph **D**.

In **Figure 100A-C**, the adsorbed AuNPs are visible as bright spots on the supramolecular BTA fibers. The AuNPs are very homogeneously distributed without agglomeration on the fibers of **3a** and **16a**, whereas on the large thick fiber of **9a**, partial agglomeration of individual AuNPs into clusters can be detected. However, AuNP adsorption may also be affected by the different fiber structures of **3a** compared to **9a**, resulting in the aforementioned agglomeration of particles in the case of **9a**. In **Figure 100D**, no AuNPs are found on the supramolecular fiber of reference BTA **26** since the AuNPs were completely removed during the washing step after the immobilization of AuNPs.

5.2 Immobilization of AuNPs on supramolecular fibers of BTAs with terpyridine substituents

As shown before, AuNP adsorption was investigated by using isolated and dried pyridine-functionalized BTA nanofibers, which were subsequently mixed with an aqueous AuNP dispersion (see **Figure 97**). Here, for AuNP immobilization, a supramolecular terpyridine-functionalized BTA fiber dispersion was directly mixed with an aqueous AuNP dispersion. For this purpose, a BTA fiber dispersion was prepared by dissolving 50 mg **24a** in a 50 g mixture of IPA/H$_2$O 9:1 (w/w) at 75 °C under stirring until a clear solution (0.1 wt%) was obtained. After cooling to room temperature and aging the sample for around 1 h, the solution turned turbid due to the formation of supramolecular nanofibers. A PVP@AuNP dispersion with a concentration of 1 g/L was obtained by dispersing 200 mg PVP@Au powder in 200 g Milli-Q water. This dispersion contains 30 ± 5 µg Au per mL dispersion according to ICP-OES measurements (see **chapter 5.1**). 5 mL of the **24a** fiber dispersion (0.1 wt%) were mixed with different volumes of PVP@AuNP dispersion (1 g/L) in a glass vial for 5 min in an IKA Vibrax VXR basic at 500 rpm. As a reference experiment, 5 mL of the aliphatic **25** fiber dispersion was mixed with 5 mL of a PVP@AuNP dispersion in an analogous manner. The mixtures were filtered off through a Büchner funnel with a cellulose filter paper (Rotilabo®-Round filter, type 603a Cellulose, Ø = 55 mm) and washed with Milli-Q water in a subsequent washing step. The preparation process of Au-loaded terpyridine-functionalized BTA fibers is shown schematically in **Figure 101**.
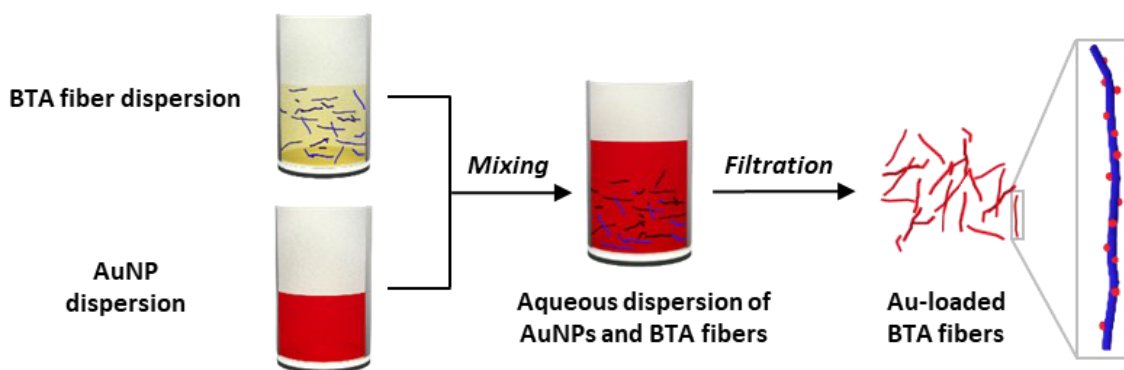
Figure 101: Schematic representation of the preparation process of Au-loaded terpyridine-functionalized supramolecular BTA nanofibers. A BTA fiber dispersion (BTA: blue fibrous structures, solvent: yellow) is mixed with an aqueous AuNP dispersion (red). During mixing, the AuNPs can adsorb on the BTA fiber surface. After filtration, isolated Au-loaded BTA fibers (red fibrous structures) are obtained. On the right side of the schematic, a magnification of a single BTA fiber with immobilized AuNPs (red dots) is shown.

To investigate and evaluate the distribution of AuNPs and possible AuNP agglomeration on the supramolecular fibers, TEM measurements were carried out, which provide a better resolution in contrast to SEM. Due to the more complex preparation effort and the limited observable section, TEM micrographs were only taken of selected samples exhibiting individual BTA nanofibers with sufficiently thin fiber diameter. **Figure 102** shows exemplary TEM micrographs of supramolecular fibers of **24a** with immobilized AuNPs on the fiber surface, as well as supramolecular fibers of the aliphatic BTA **25** as reference.
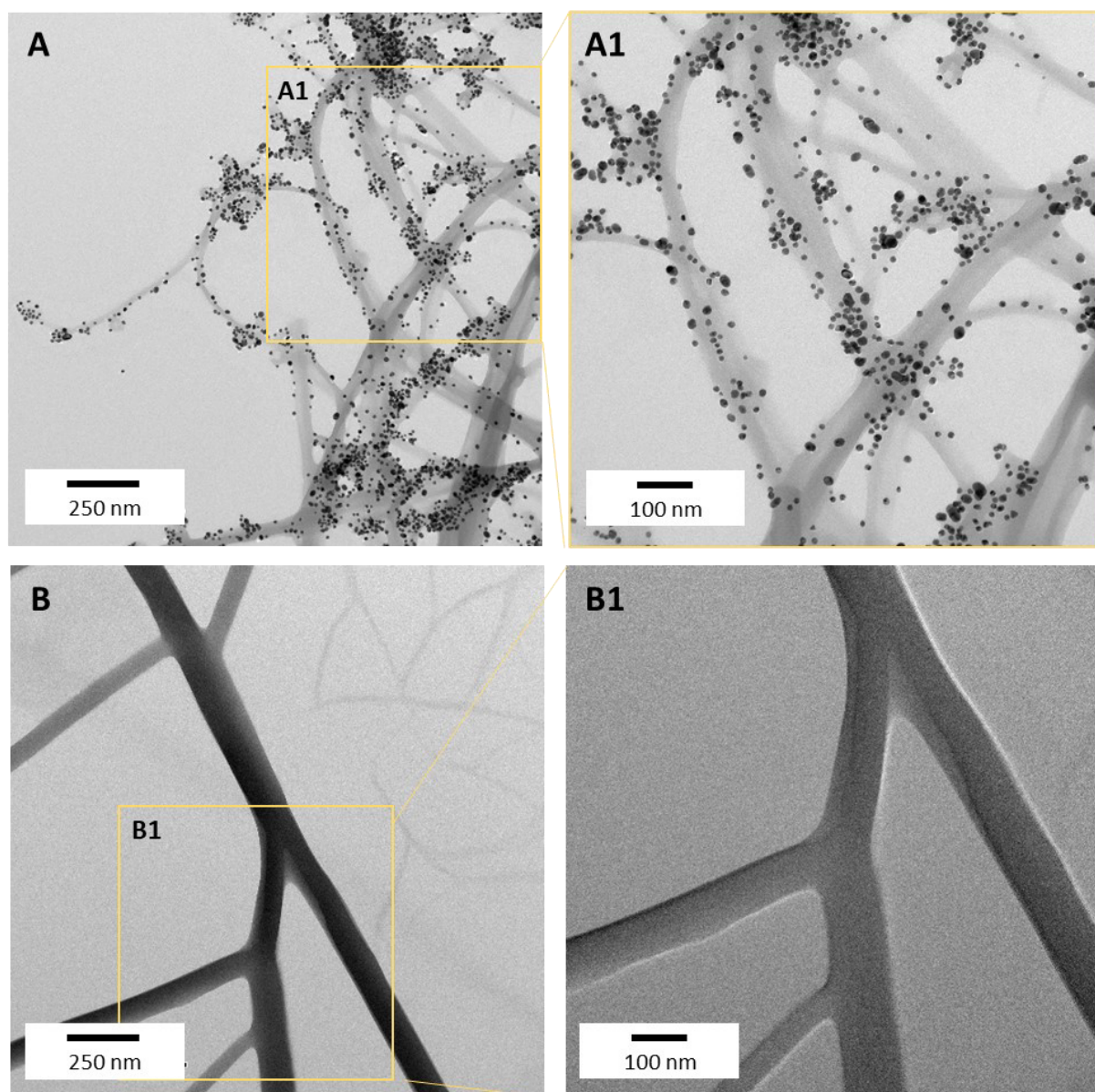
Figure 102: Immobilization of PVP@AuNPs on supramolecular BTA fibers by mixing 5 mL BTA fiber dispersion with 5 mL PVP@AuNP dispersion (1 g/L) for 5 min. (**A**, **A1**) Representative TEM micrographs of **24a** (terpyridine-functionalized) nanofibers after immobilization of AuNPs at two different magnifications. (**B**, **B1**) Representative TEM micrographs of **25** (aliphatic) nanofibers after immobilization of AuNPs at two magnifications.

The AuNPs are very homogeneously distributed on the supramolecular fibers of **24a** and no agglomeration of AuNPs can be observed (**Figure 102A**). In contrast, no AuNPs at all can be found on the supramolecular fibers of **25** (**Figure 102B**). This is in agreement with the findings in **chapter 5.1**, where it was demonstrated by UV/Vis measurements that AuNPs cannot be immobilized on the aliphatic supramolecular fibers of **25** due to the lack of functional groups. Here, if at all, only simple and weak physisorption may take place.

Further evidence for the adsorption capability is provided by UV/Vis spectra shown in **Figure 103**. For this purpose, UV/Vis spectra of the initially employed PVP@AuNP dispersion and the filtrates after

immobilization of AuNPs on the terpyridine-functionalized nanofibers of **24a** and the aliphatic supramolecular fibers of **25** (**reference 2**) were measured.

No absorption can be observed for the PVP@AuNP dispersion after 5 min of mixing with the terpyridine-functionalized **24a** fibers. Thus, almost all AuNPs were immobilized on the supramolecular fibers of **24a**. The adsorption efficiency of AuNPs, which was calculated again according to **equations 5** and **6** (see **chapter 5.1**), is larger than 99 %. In contrast, the absorption of the PVP@AuNP dispersion after mixing with the fiber dispersion of **25** is only slightly lower than the absorption of the initially employed PVP@AuNP dispersion. Therefore only a very small part of the AuNPs was adsorbed and the observations from the TEM micrographs were confirmed by the UV/Vis and ICP-OES measurements. The adsorption efficiency of AuNPs is only about 16 % for **25** and thus agrees well with the value obtained for **25** from UV/Vis measurements in **chapter 5.1**. However, nearly all AuNPs are removed from the supramolecular fibers of **25** after the washing step (AE of 6 %). The adsorption efficiencies calculated from the UV/Vis and ICP-OES data agree very well in both cases.
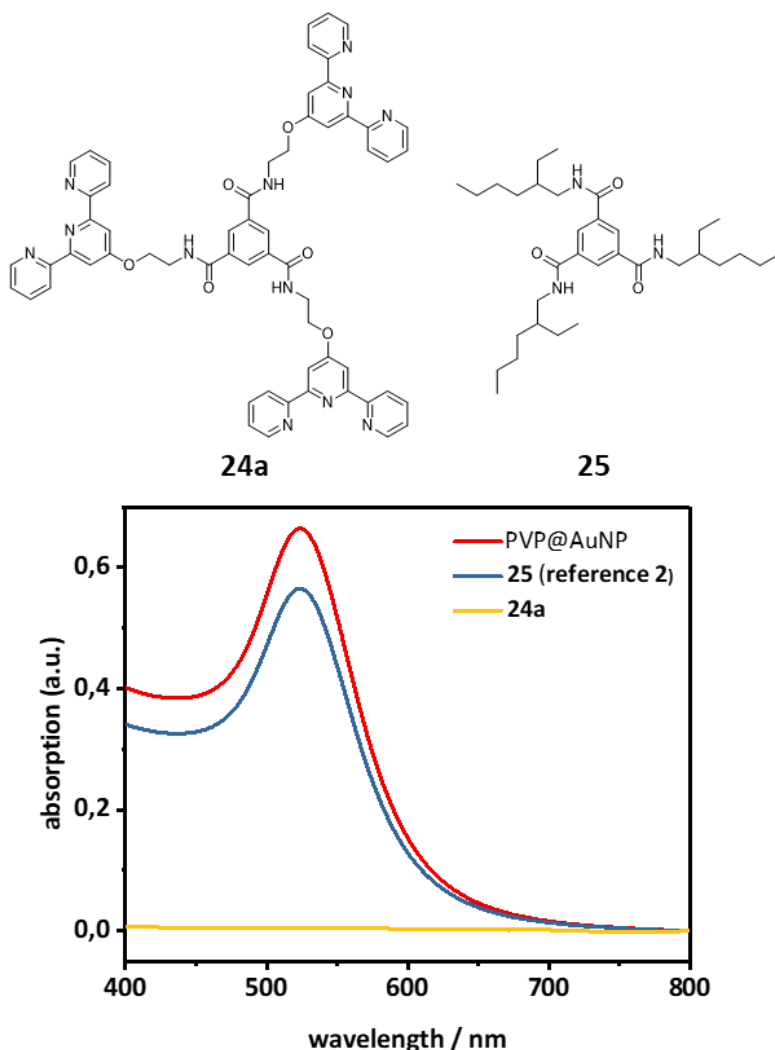
Figure 103: UV/Vis spectra of the initially employed PVP@AuNP dispersion (red) and the PVP@AuNP dispersion after immobilization of AuNPs on the aliphatic supramolecular fibers of **25** (blue) and the terpyridine-functionalized nanofibers of **24a** (yellow).

*Maximum Au uptake capacity on supramolecular fibers of **24a** within 5 min*

Due to these promising results, **24a** was studied in more detail regarding the maximum Au uptake capacity. Therefore, different volumes of a freshly prepared aqueous PVP@AuNP dispersion (1 g/L) in a range from 5-30 mL were mixed with a constant volume of 5 mL of a **24a** fiber dispersion (0.1 wt%, corresponds to 4 mg **24a**) in a glass vial for 5 min at 500 rpm. The mixture was filtered off through a Büchner funnel with a cellulose filter paper (Rotilabo®-Round filter, type 603a Cellulose, $\varnothing$ = 55 mm) and washed with Milli-Q water in a subsequent washing step. To determine the AuNP content, which was deposited on the cellulose filter only, 5 mL of the PVP@AuNP dispersion was filtered off over a pristine cellulose filter paper. The different mixtures of PVP@AuNP dispersion and **24a** fiber dispersion are referred to as formulations **f1-f5** in the following. UV/Vis and ICP-OES measurements were carried out from formulations **f1-f5** and **references 1** and **2** after filtration.

Table 9: Composition of the different formulations **f1-f5** composed of 5 mL BTA fiber dispersion and different volumes of PVP@AuNP dispersion as well as two reference formulations. Here, 5 mL of the PVP@AuNP dispersion were filtered through the neat cellulose filter paper (**reference 1**) and 5 mL of the aliphatic **25** fiber dispersion were mixed with 5 mL of PVP@AuNP dispersion (**reference 2**).

	Formulation	Volume BTA in mL[a]	Volume PVP@AuNP in mL[b]
	Cellulose filter paper (**reference 1**)	-	5
	Aliphatic BTA **25** (**reference 2**)	5	5
5 min mixing	f1	5	5
	f2	5	10
	f3	5	15
	f4	5	20
	f5	5	30

[a] 1 mL BTA fibers dispersion contains 0.8 mg BTA fibers; [b] 1 mL PVP@AuNP dispersion (1 g PVP@Au powder per liter water) contains 30 ± 5 µg Au.

The resulting supramolecular nanofiber networks with the immobilized AuNPs on top of the cellulose filter paper after filtration of formulations **f1-f5** and the neat cellulose filter paper as **reference 1** are shown in **Figure 104**. Additionally, the corresponding UV/Vis spectra of the filtrates of formulations **f1-f5** and a graph showing the deposited Au amount on the supramolecular fibers as a function of PVP@AuNP dispersion volume are given.

Figure 104A shows that the PVP@AuNP dispersion after filtration through the neat cellulose filter paper contains its red color while the cellulose filter paper is non-colored, which indicates no or only minimal adsorption of AuNPs. In all other cases (**f1-f5**), a distinct red coloration of the cellulose filter paper can be seen due to the Au-loaded supramolecular fiber network of **24a** deposited on top of the filter paper. The filtrates of **f1-f3** are colorless, indicating adsorption of a large quantity of AuNPs onto the fibers of **24a**. On the other hand, filtrates of **f4** and **f5** show a slight red coloration, indicating incomplete adsorption of the AuNPs. These observations were quantified by the corresponding UV/Vis spectra shown in **Figure 104B**. No or very low absorption can be observed in the case of the filtrates of **f1-f3**. With an increasing volume of PVP@AuNP dispersion, higher adsorption intensities are determined, which in turn means lower adsorption efficiencies of AuNPs. The adsorption efficiencies with values between 60-99 %, determined by both methods (UV/Vis and ICP-OES measurements), are in good agreement.
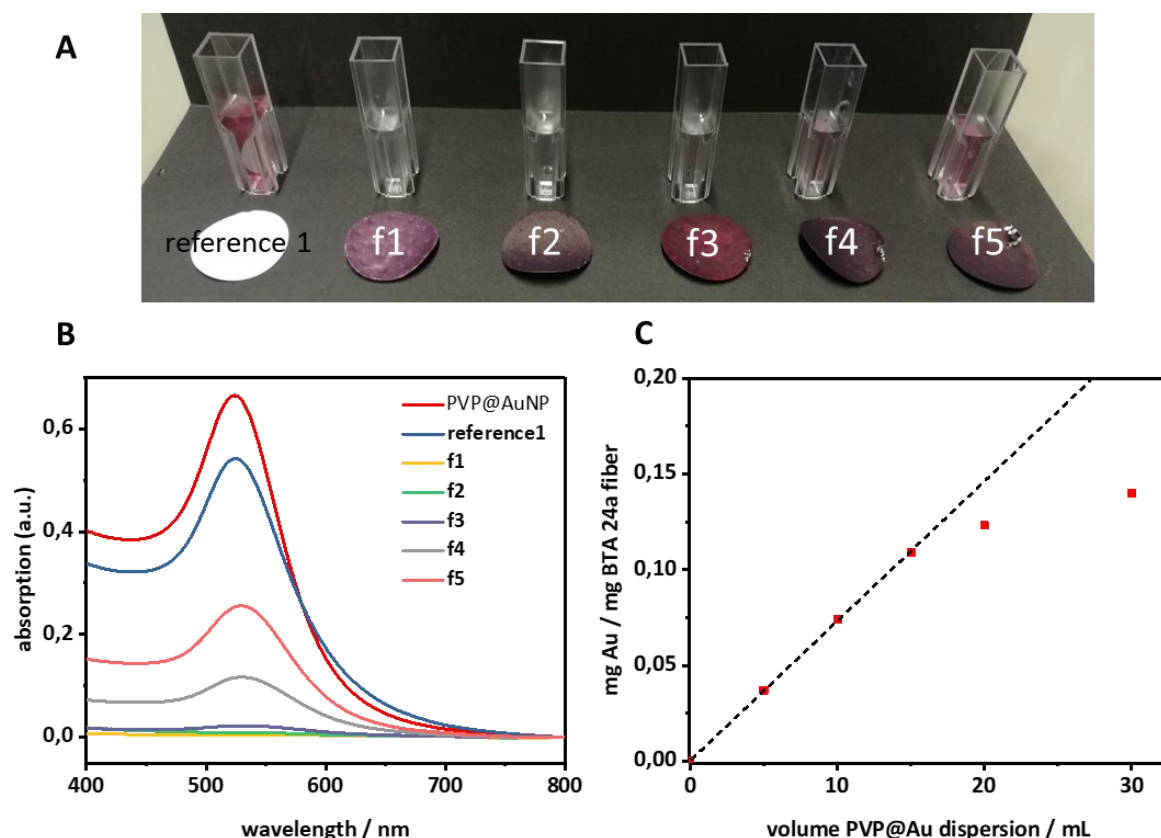
Figure 104: Study of the maximum Au uptake capacity of **24a** nanofibers with PVP@AuNPs within 5 min. (**A**) Representation of the UV/Vis samples prepared after filtration of different formulations **f1-f5** (5 mL **24a** nanofiber dispersion (corresponds to 4 mg BTA) + 5-30 mL PVP@AuNP dispersion) and the corresponding supramolecular nanofiber networks on top of the cellulose filter paper. The immobilization of AuNPs on a neat cellulose filter paper was carried out as a reference experiment (**reference 1**). (**B**) UV/Vis spectra of the initially employed PVP@AuNP dispersion (red), the PVP@AuNP dispersions after filtration of formulations **f1-f5** and the PVP@AuNP dispersion after filtration through a neat cellulose filter paper (**reference 1**). (**C**) Normalized deposited Au amount per mg **24a** fibers within 5 min in dependence of PVP@AuNP dispersion volume. The black dashed line represents a linear fit corresponding to the theoretically available Au amount in the AuNP dispersion (normalized to the BTA amount).

The AE of AuNPs with formulations **f1-f3** was found to be close to 100 %. Here, the deposited Au amount on the supramolecular BTA fibers of **24a** increases almost linearly in the range of 0-15 mL PVP@AuNP dispersion, as shown in **Figure 104C**. The black dashed line represents a linear fit corresponding to the theoretically available amount of Au in the dispersion (normalized to the BTA amount). This maximal Au amount on the supramolecular fibers of **24a**, which can be deposited, is almost identical to the determined deposited Au amount up to a PVP@AuNP dispersion volume of 15 mL and consequently corresponds to an AE of ∼ 100 %. With increasing volume of PVP@AuNP dispersion, the determined Au amount on the BTA fibers (red dots) deviates from the theoretical maximal Au amount on the supramolecular fibers of **24a**, demonstrating that the full capacity for the BTA fibers under these conditions is almost reached. For instance, an AE of about 80 % was determined for **f4** (20 mL PVP@AuNP dispersion) and about 60 % for **f5** (30 mL PVP@AuNP dispersion). The Au uptake capacity within 5 min ranges from 37 μg Au per mg **24a** fiber in the case of **f1** to 140 μg Au per mg **24a** fiber in the case of **f5**. Thus, a very high Au amount can already be immobilized on the supramolecular fibers of **24a** within such a short exposure time.

To verify that the neat cellulose filter paper does not significantly contribute to the AuNP deposition, reference experiments were performed. It was found that the neat cellulose filter paper initially adsorbs only a small amount of AuNPs (AE of around 20 %) as determined by UV/Vis and ICP-OES measurements. This is attributed to several hydroxyl groups within the cellulose structure, which may give rise to a weak interaction of the AuNPs with these groups. However, the AuNPs are almost completely removed after the washing step with Milli-Q water (AE of ∼ 8 %), which explains the white color of the cellulose filter paper shown in **Figure 104A**. In contrast to the neat cellulose filter paper or the aliphatic fibers of **25**, UV/Vis measurements and ICP-OES measurements revealed no leaching of AuNPs from the supramolecular **24a** fibers during the washing step with Milli-Q water. Here, chemisorption between the terpyridine moieties and the Au atoms takes place, whereas, in the case of the cellulose filter paper or the aliphatic **25** fibers, only very weak physisorption is present. This demonstrates that supramolecular nanofibers of **24a** are a very promising candidate for the efficient immobilization of AuNPs without leaching of immobilized AuNPs.

*Maximum Au uptake capacity on supramolecular fibers of **24a** within 24 h*

The above-discussed results with formulations **f1-f5** were obtained with a short exposure time of the AuNP dispersion with the supramolecular nanofibers of only 5 min and subsequent filtration of this mixture. To get a deeper insight into the maximum Au capacity with increasing exposure time, 10-200 mL PVP@AuNP dispersion were mixed with 1 mL **24a** fiber dispersion each (formulations **f7-f12**, see **Table 10**).

Table 10: Composition of the different formulations **f6-f11** composed of 1 mL BTA fiber dispersion and different volumes of PVP@AuNP dispersion.

	Formulation	Volume BTA in mL[a]	VolumePVP@AuNP in mL[b]
24 h mixing	f6	1	10
	f7	1	20
	f8	1	50
	f9	1	75
	f10	1	100
	f11	1	200

[a] 1 mL BTA fibers dispersion contains 0.8 mg BTA fibers; [b] 1 mL PVP@AuNP dispersion (1 g PVP@Au powder per liter water) contains 30 ± 5 μg Au.

The UV/Vis spectra of the PVP@AuNP dispersions after filtration of formulations **f6-11** and the corresponding graph representing the deposited Au amount on 0.8 mg nanofibers of **24a** as a function of the PVP@AuNP dispersion volume are shown in **Figure 105**.
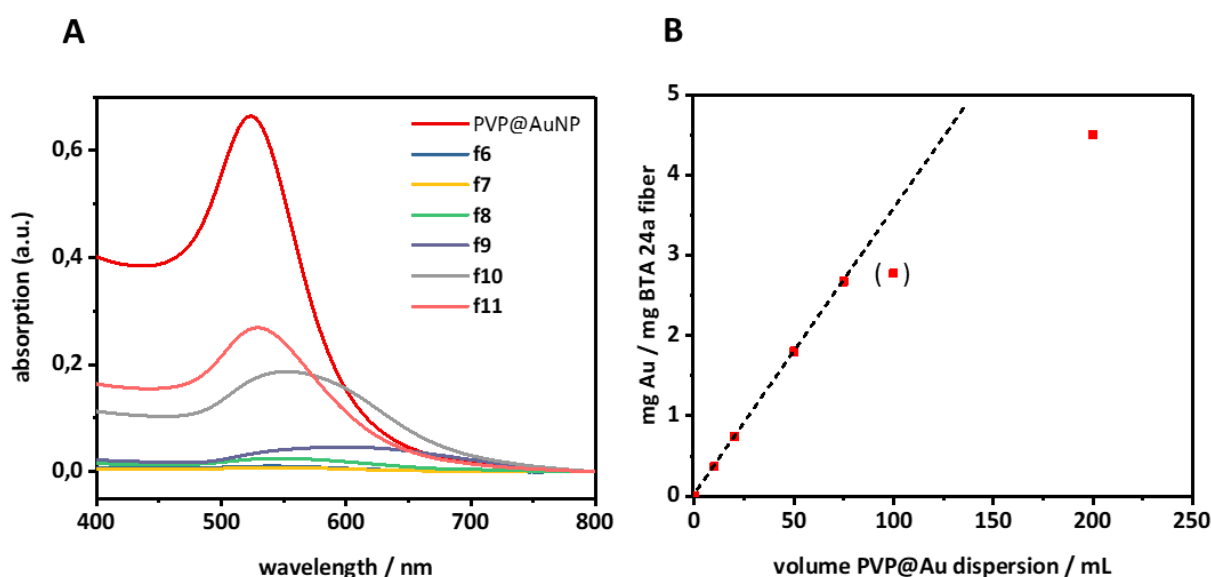
Figure 105: Study of the maximum Au uptake capacity of **24a** nanofibers with PVP@AuNPs within 24 h. (**A**) UV/Vis spectra of the initially employed PVP@AuNP dispersion (red) and the PVP@AuNP dispersion after filtration of **f6-f11** (1 mL **24a** nanofiber dispersion (corresponds to 0.8 mg BTA) + 10-200 mL PVP@AuNP dispersion). (**B**) Normalized deposited Au amount per mg **24a** fibers within 24 h in dependence of PVP@AuNP dispersion volume. The black dashed line represents a linear fit corresponding to the theoretically available Au amount in the AuNP dispersion (normalized to the BTA amount). The data point at 100 mL PVP@AuNP dispersion is bracketed since this value is actually expected to be at around 3 mg Au per mg **24a** fiber.

Figure 105 shows that a significantly higher Au amount can be adsorbed on the **24a** fibers if the BTA nanofiber dispersion is mixed with the PVP@AuNP dispersion for a period of 24 h. The black dashed linear fit is up to a PVP@AuNP dispersion volume of about 75 mL almost identical to the obtained data

points, for which an AE of nearly 100 % was determined. With increasing PVP@AuNP dispersion volume, a stronger deviation of the black dashed fit from the real deposited Au amount on the supramolecular fibers of **24a** is observed. At a volume of 200 mL, 60 % of the AuNPs were still adsorbed on the BTA fibers within 24 h, which corresponds to a Au uptake capacity of 4.5 mg Au per mg **24a** nanofiber. Thus, with a longer exposure time of the AuNP dispersion with the supramolecular **24a** nanofibers, a larger amount of AuNPs can be immobilized. The adsorption efficiencies determined from the UV/Vis and ICP-OES measurements correspond very well, except for **f9**. The 13 % deviation of the values with **f9** could have been caused by preparation errors in ICP-OES.

Table 11 summarizes the results of the adsorption efficiencies and the Au amount immobilized on **24a** nanofibers, which were calculated based on UV/Vis and ICP-OES measurements.

Table 11: Summary of the calculated adsorption efficiencies and corresponding Au amount immobilized on the supramolecular fibers of **24a**. Different volumes of PVP@AuNP dispersion were mixed with 5 mL or 1 mL **24a** fiber dispersion (0.1 wt%) each for 5 min (**f1-f5**) or 24 h (**f6-f11**). Two reference experiments were performed using a neat cellulose filter paper (**reference 1**) and an aliphatic **25** fiber dispersion (**reference 2**). The AEs of AuNPs on the nanofibers after the washing step were calculated based on UV/Vis and ICP-OES measurements. The last column shows the Au uptake capacity of 1 mg **24a** nanofibers in 5 min and 24 h, respectively.

	Formulation	Volume BTA in mL[a]	Volume PVP@AuNP in mL[b]	Adsorption efficiency UV/Vis in %	Adsorption efficiency ICP-OES in %	µg Au / mg BTA fiber
	Cellulose filter paper (**reference 1**)	-	5	8	8	-
5 min mixing	Aliphatic BTA **25** (**reference 2**)	5	5	6	6	2
	f1	5	5	99	99	37
	f2	5	10	99	99	74
	f3	5	15	97	97	109
	f4	5	20	82	82	123
	f5	5	30	62	60	140
24 h mixing	f6	1	10	98	99	369
	f7	1	20	99	99	742
	f8	1	50	96	96	1804
	f9	1	75	95	82	2675
	f10	1	100	75	75	2797
	f11	1	200	60	62	4500

[a] 1 mL BTA fibers dispersion contains 0.8 mg BTA fibers; [b] 1 mL PVP@AuNP dispersion (1 g PVP@Au powder per liter water) contains 30 ± 5 µg Au.

A significant feature, which can be found in **Figure 106A**, is that the maximum absorption of the UV/Vis spectra, except for the filtrate of **f11**, is shifted to higher wavelengths. This finding is in strong contrast to that in **Figure 104** and indicates that agglomeration of AuNPs in the measured filtrates takes place within the period of 24 h. Therefore, it may be assumed that the AuNPs on the BTA fibers are also deposited in the form of larger agglomerates beside individual AuNPs. For this reason and to investigate the distribution of AuNPs on the BTA fibers, the supramolecular fiber networks obtained after filtration of the different formulations through a cellulose filter paper were further analyzed by SEM and EDX measurements. **Figure 106** shows SEM micrographs of the supramolecular fiber networks obtained after filtration of **f1-f5** (for simplicity hereinafter further referred to as **f1-f5**) and **reference 1**. It can be clearly seen that no AuNPs were immobilized on the neat cellulose filter paper after washing. SEM micrographs of **f1-f5**, however, revealed a homogenous distribution of the AuNPs on the nanofibers of **24a** for all supramolecular fiber networks **f1-f5**. With an increasing volume of PVP@AuNP dispersion, the nanofibers are covered with a higher number of AuNPs. However, the SEM micrographs indicate that no significant agglomeration of AuNPs can be observed after exposure to the AuNP dispersion for 5 min. These findings go in line with the previously determined absorption measurements.
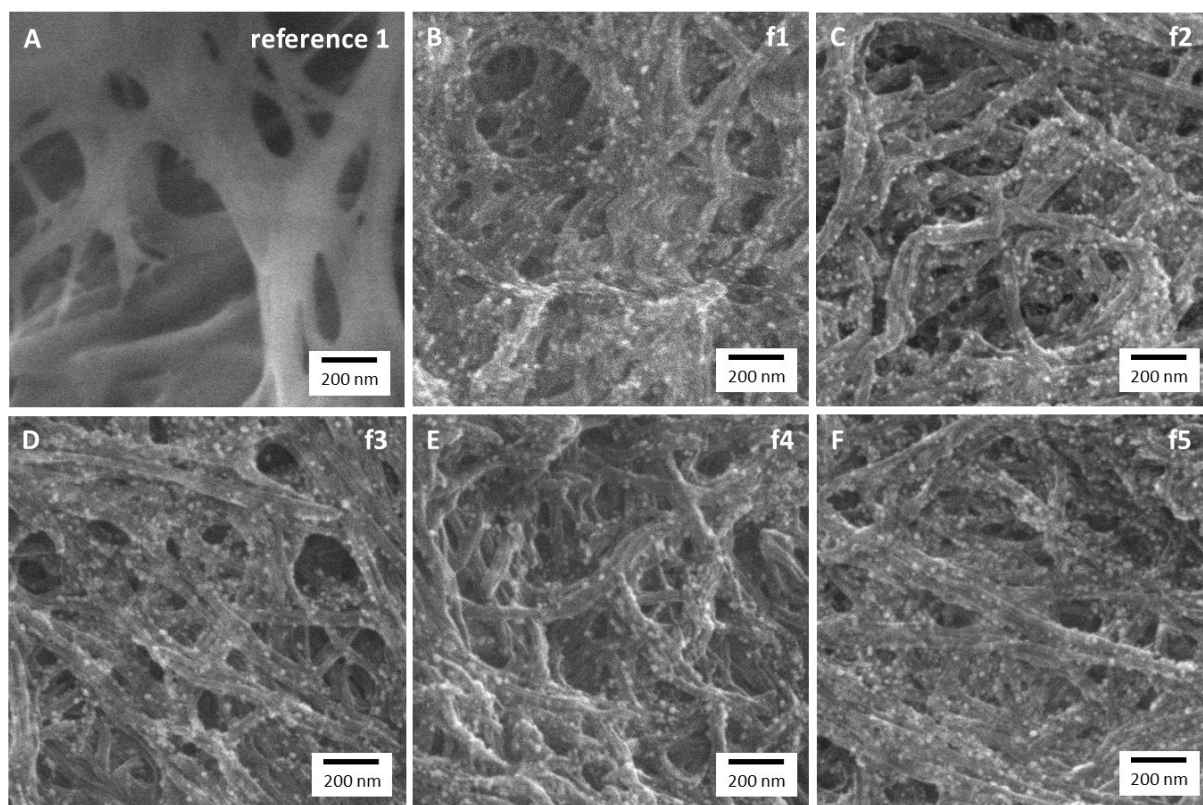
Figure 106: SEM micrographs of the supramolecular fiber networks with immobilized AuNPs obtained after filtration of **f1-f5** and a neat cellulose filter paper (**reference 1**) after filtration of a PVP@AuNP dispersion through the filter paper (**A-F**).

To further provide evidence for the AuNP distribution on the BTA fibers and quantitatively compare the Au amount adsorbed on the BTA fibers, EDX measurements were performed. A section of the supramolecular fiber network was analyzed specifically in view of the element Au, whereby a mapping of this section was obtained. Exemplarily, the SEM micrograph with EDX mapping and the summarized EDX spectra of all data points of the measured section are shown for the neat cellulose filter paper (**reference 1**) and supramolecular fiber networks after immobilization of AuNPs and filtration of **f1** und **f5** in **Figure 107**.
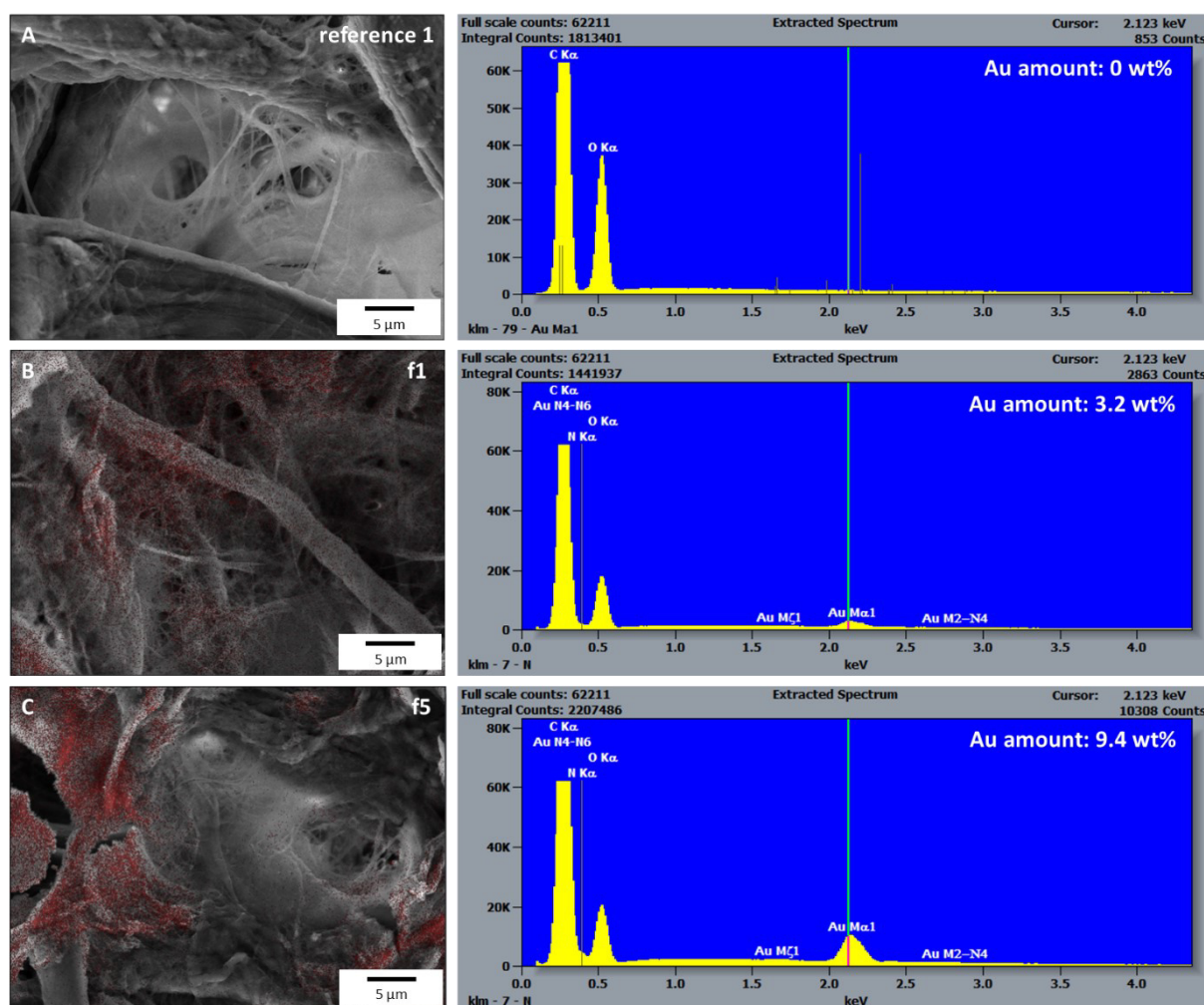
Figure 107: SEM micrographs with EDX mapping showing the Au distribution (red dots) on the **24a** nanofibers (**A-C**, left) and the corresponding EDX spectra (**A-C**, right) of a **reference 1** formulation (neat cellulose filter paper) and formulations **f1** and **f5**. No AuNPs were detected on the neat cellulose filter paper.

As expected, no AuNPs were detected on the neat cellulose filter paper using EDX. A Au peak is clearly visible in the other EDX spectra. Here, the intensity of the characteristic Au peaks significantly increased from **f1** to **f5** since, in the case of **f5**, a higher Au amount was immobilized on the supramolecular fibers of **24a**. After filtration of formulation **f1**, a Au amount of 3.2 wt% could be detected in the examined section of the supramolecular fiber network. The Au content after filtration

of formulation **f5**, where the largest PVP@AuNP volume was used, is highest at 9.4 wt%. The EDX data thus confirm the values determined from the UV/Vis and ICP-OES measurements.

Looking at the supramolecular fiber networks (**f6-f11**), where larger amounts of PVP@AuNP dispersion were used for adsorption experiments, a significantly higher number of AuNPs on the BTA fibers can be observed (**Figure 108**).

In particular cases such as the supramolecular fiber networks **f9-11**, the number of AuNPs completely covers the individual BTA fibers. Here, as shown in **Figure 108D-F**, spots of AuNP agglomeration are visible. This finding is attributed to the additional deposition of AuNP agglomerates during the course of the extended 24 h exposure to the AuNP dispersion.
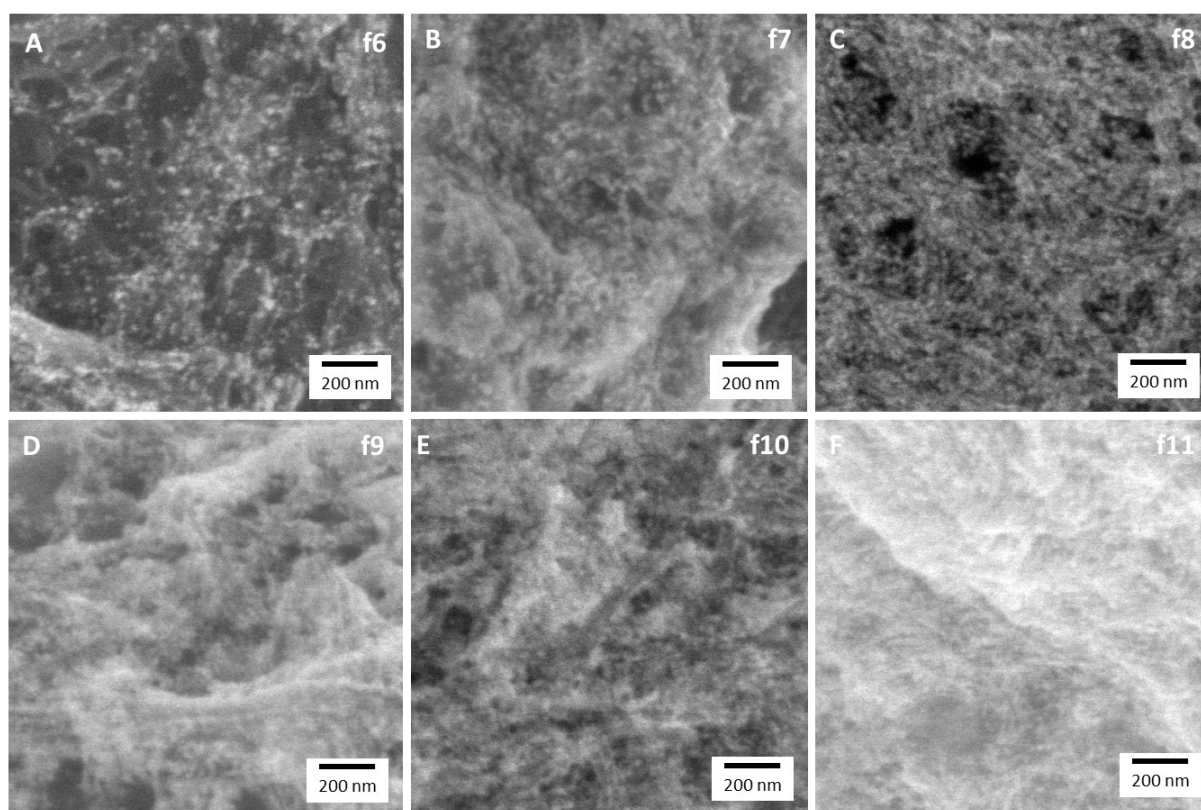
Figure 108: SEM micrographs of the supramolecular fiber networks with immobilized AuNPs obtained after filtration of **f6-f11**.

In view of the use of such supramolecular fiber networks for catalytic purposes, the deposition of individual non-agglomerated AuNPs is expected to be the most beneficial composite with the most active AuNP species. For this purpose, the highest possible Au uptake capacity only makes sense if there is no agglomeration of AuNPs. Therefore, for catalytic application, it is of great relevance to immobilize AuNPs within a short period of exposure to the AuNP dispersion to prevent the deposition of agglomerates.

Immobilization of AuNPs on supramolecular BTA fibers by filtration

The previous experiments were carried out to determine the maximum Au capacity of supramolecular **24a** fibers within 5 min or 24 h. The following experiments aim to determine the deposition of AuNPs only by passing a AuNP dispersion through a previously formed supramolecular fiber network of **24a**. This represents a more straightforward and faster immobilization method for the preparation of a catalytic system than the methods mentioned above. In particular, the question is addressed how the immobilization of AuNPs differs in terms of adsorption efficiency and homogeneous distribution of AuNPs on supramolecular fibers from the procedure used before.

For this purpose, the following procedure, which is schematically shown in **Figure 109**, was conducted using a reusable PTFE syringe filter holder. A PTFE membrane on which the BTA fibers can be deposited is inserted into the PTFE syringe filter holder.

1. Preparation of a supramolecular BTA fiber network by filtration of 4 mL of a 0.1 wt% **24a** fiber dispersion (corresponds to 3.2 mg **24a** fibers)
2. Exchange and removal of the organic solvent by filtration of 4 mL H_2O
3. Filtration of 1 mL AuNP dispersion (Filtrate)
4. Washing step I to remove non-adsorbed AuNPs by filtration of 3 mL H_2O (Washing solution I)
5. Washing step II to verify that potential leaching was completed by filtration of additional 2 mL H_2O (Washing solution II)
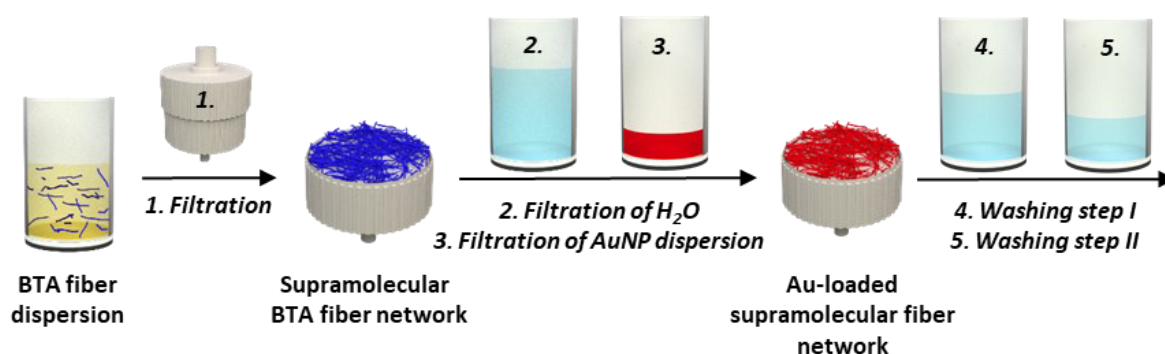
Figure 109: Schematic representation of the preparation process of a Au-loaded terpyridine-functionalized supramolecular BTA nanofiber network. A BTA fiber dispersion (BTA: blue fibrous structure, solvent: yellow) is filtered off with a reusable PTFE syringe filter holder to obtain a supramolecular BTA fiber network on top of a PTFE membrane. To completely exchange and remove the solvent of the BTA fiber dispersion, H_2O (light blue) is filtered through the fiber network, followed by an aqueous AuNP dispersion (red). During filtration of the AuNP dispersion, AuNPs can adsorb on the BTA fiber surface resulting in a Au-loaded supramolecular BTA fiber network (red fibrous structure). After AuNP deposition, two washing steps with H_2O were carried out to remove non-adsorbed AuNPs and check for leaching of AuNPs.

The filtration experiments were performed with PVP@AuNP dispersion (30 µg Au/mL) and Citrate@AuNP dispersion (4 µg Au/mL) to investigate the influence of the different stabilizing ligands of the AuNPs on the immobilization behavior.

For all Filtrates and Washing solutions I and II, UV/Vis measurements were carried out as described before. The filtration efficiency can be calculated analogously to the adsorption efficiency according to **equation 5** (see **chapter 5.1**). For this, the absorption maxima of the initially employed AuNP dispersion are compared with the absorption intensities of the Filtrates and Washing solutions I and II at 524 nm, respectively. As a reference experiment, filtration without BTA fibers was performed by starting directly with step 3.

Figure 110 shows the UV/Vis spectra of the initially employed PVP@AuNP dispersion, the Filtrates and Washing solutions I and II of the reference experiment without BTA fibers and the filtration experiments with a supramolecular fiber network of **24a**.
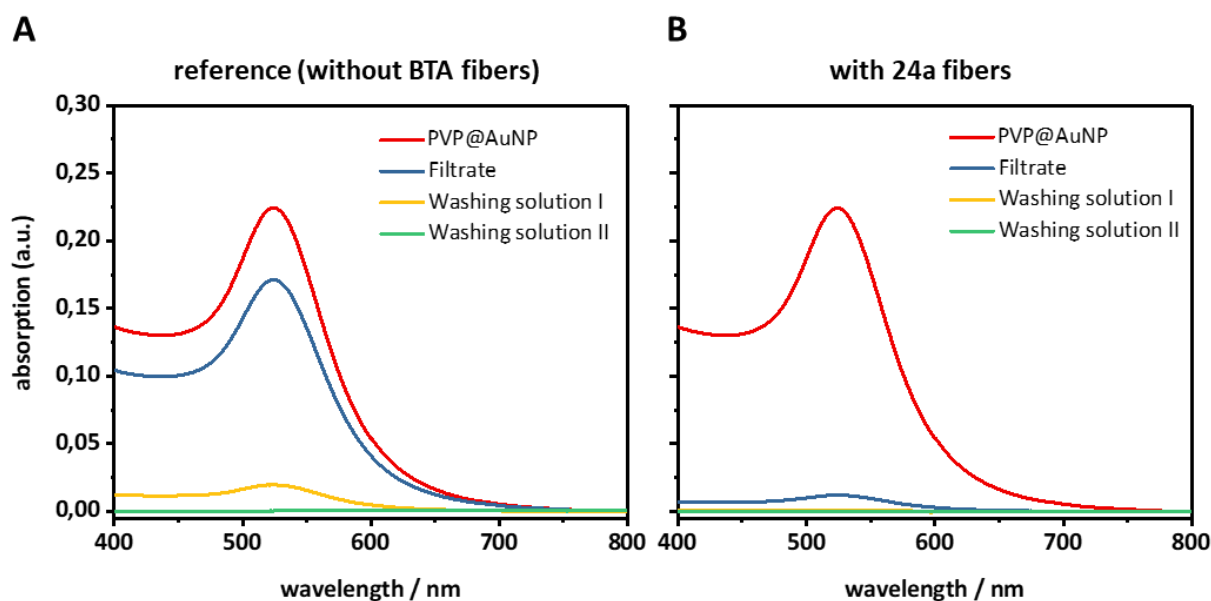
Figure 110: UV/Vis spectra of the initially employed PVP@AuNP dispersion (red), Filtrates (blue) and Washing solutions I (yellow) and II (green); (**A**) reference experiment without BTA fibers, (**B**) filtration experiment with 3.2 mg **24a** fibers.

As can be clearly seen from **Figure 110**, the UV/Vis spectra of the Filtrates and Washing solutions I and II of the reference experiment without BTA fibers (**Figure 110A**) differ significantly from the UV/Vis spectra of those in the filtration experiment with BTA fibers (**Figure 110B**). The absorption peak of the Filtrate (blue) is much stronger without BTA fibers, which means a lower filtration efficiency. In total, 24 % of the AuNPs were filtered out with the neat PTFE membrane, whereas about 95 % of the AuNPs were filtered out with BTA fibers. It is also noticeable that only in the case of the reference experiment a clear absorption peak of Washing solution I (yellow) is visible. About 65 % of the AuNPs deposited at the PTFE membrane were released again by subsequent washing with water. This behavior cannot be observed in the presence of the BTA fibers. The absorption of Washing solution II (green) is nearly zero in both cases, which indicates no leaching of AuNPs. The PTFE membrane cannot immobilize AuNPs, but it is reasonable to assume that the AuNPs were filtered out due to their small pore size. Further

washing of the PTFE membrane with larger amounts of water removes the AuNPs more or less completely. In contrast, the AuNPs do not detach from the supramolecular fibers.

As shown in **Figure 111**, the surface of the supramolecular **24a** fibers is homogeneously covered with a large number of AuNPs, which have a size of about 16.5 nm.
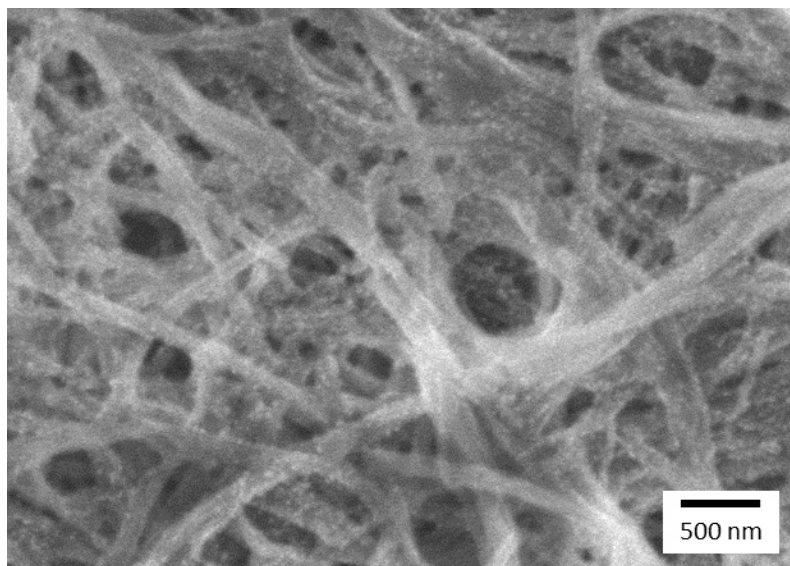
Figure 111: SEM micrograph of the supramolecular **24a** fiber network with immobilized AuNPs after filtration of 1 mL PVP@AuNP dispersion (30 µg Au/mL). The AuNPs with an average diameter of 16.5 nm are homogenously distributed on the surface of the supramolecular **24a** fibers.

In order to investigate the influence of different stabilization ligands of AuNPs on the filtration performance, Citrate@AuNPs (4 µg Au/mL) were also used instead of PVP@AuNPs for the following filtration experiments. The corresponding UV/Vis spectra of the initially employed Citrate@AuNP dispersion, the Filtrates and the Washing solutions I and II of the reference experiment without BTA fibers and the filtration experiment with supramolecular fiber network are shown in **Figure 112**.

A

B
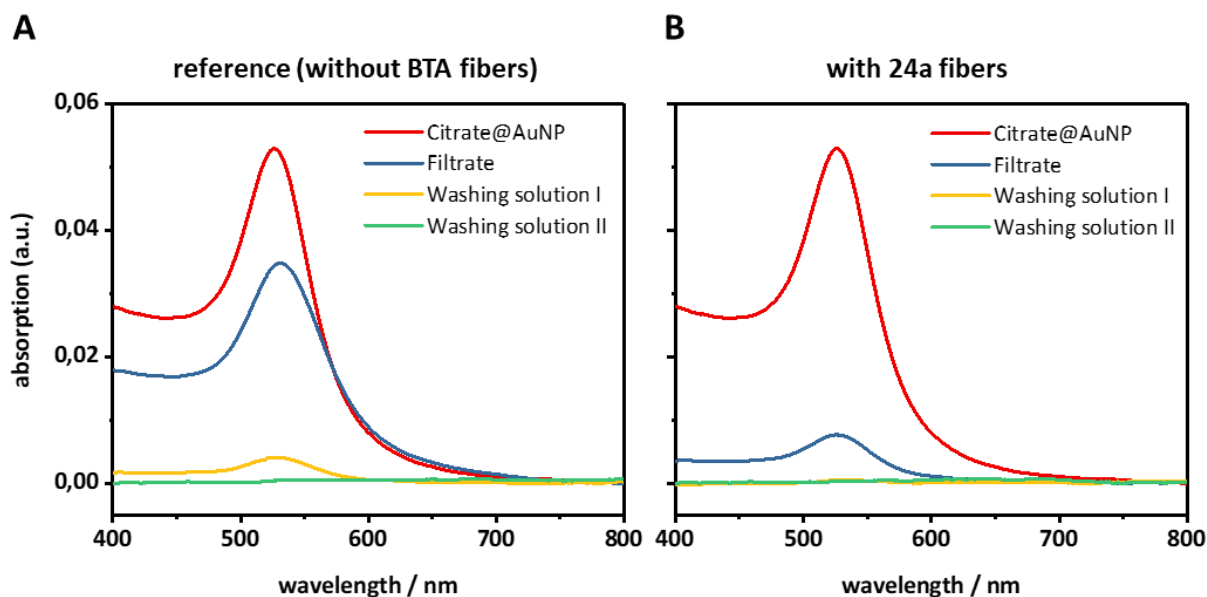
Figure 112: UV/Vis spectra of the initially employed Citrate@AuNP dispersion (red), Filtrates (blue) and Washing solutions I (yellow) and II (green); (**A**) reference experiment without BTA fibers, (**B**) filtration experiment with 3.2 mg **24a** fibers.

With Citrate@AuNPs, the same trend can be seen as before with PVP@AuNPs. Only in the presence of the BTA fibers most AuNPs are adsorbed and filtered out of the dispersion. In the case of the reference experiment, only 34 % of the AuNPs were filtered out with the neat PTFE membrane, whereas about 86 % of the AuNPs were filtered out with the supramolecular BTA fiber network by just passing the AuNP dispersion through the filter medium. A slight shift of the absorption maximum of the Filtrate (blue) to higher wavelengths is noticeable in the reference experiment, which indicates possible agglomeration of the AuNPs as observed and described before. Through the PTFE membrane, the AuNPs were only filtered out but not immobilized, whereas the AuNPs were efficiently immobilized on the surface of the BTA fibers and as long as the surface is not completely covered with AuNPs, no agglomeration occurs. About 25 % of the AuNPs were washed off the PTFE membrane by subsequent filtration of water. This behavior can be observed only slightly in the presence of the BTA fibers, although this is also within the error range of the measurement. The absorption of Washing solution II (green) is nearly zero in both cases, which indicates no leaching of AuNPs.

Figure 113 shows the distribution of AuNPs on the supramolecular fiber network of **24a**. The AuNPs with a diameter of 30 nm are mostly homogeneously distributed on the surface of the BTA fibers.
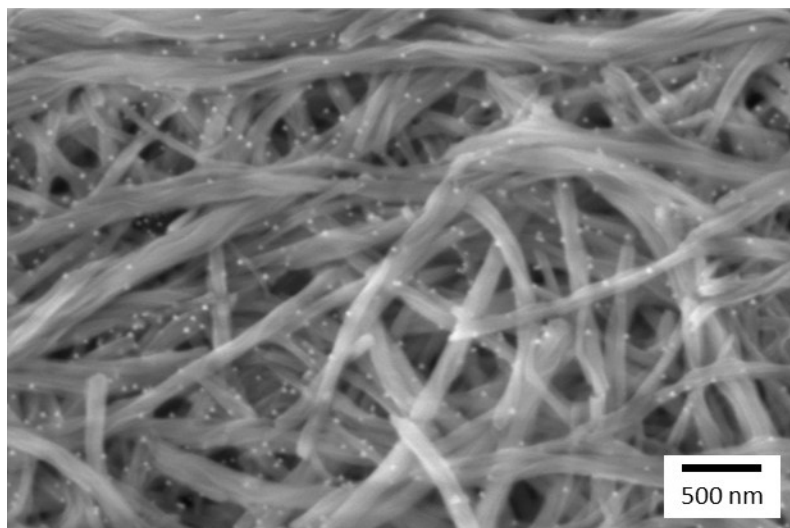
Figure 113: SEM micrograph of the supramolecular **24a** fiber network with immobilized AuNPs after filtration of 1 mL Citrate@AuNP dispersion (4 µg Au/mL). The AuNPs with an average diameter of 30 nm are homogenously distributed on the surface of the supramolecular **24a** fibers.

When comparing the differently stabilized AuNPs (PVP@AuNP and Citrate@AuNP), it is noticeable that the filtration efficiencies are high for both types, but in the case of PVP-stabilized AuNPs, about 10 % higher. Here it must be taken into account that the Au concentration of the PVP@AuNP dispersion with a value of 30 µg Au/mL is significantly higher than the concentration of the Citrate@AuNP dispersion with 4 µg Au/mL. Thus, it can be assumed that the filtration efficiency for PVP@AuNP is even higher since a larger Au amount is immobilized on the fibers under the same conditions.

Immobilization of AuNPs within a composite nonwoven sheet - Immersion vs. Filtration

Since a fiber network based only on supramolecular fibers of **24a** features a mechanically stable insufficient property, such structures can hardly be used for applications where mechanically integrity is required. For this reason, the composite nonwoven sheets **c7-c9**, composed of electrospun PAN short fibers and supramolecular **24a** fibers and prepared by the wet-laid technique (**chapter 4.2**), were used to overcome this issue and were investigated regarding the immobilization of AuNPs in the following experiments. A nonwoven sheet composed only of PAN short fibers was selected as a reference. AuNP immobilization was carried out either by immersing the composite nonwoven sheet in a PVP@AuNP dispersion (30 µg Au/mL) or by filtration of the PVP@AuNP dispersion through the composite nonwoven sheet. Both routes were investigated and compared in more detail in terms of AuNP adsorption or filtration efficiency and distribution of the AuNPs within the composite nonwoven sheet.

For the immobilization of AuNPs *via immersion*, a composite nonwoven sheet with an area of ~ 1 cm² was cut off from the large composite nonwoven sheets and was immersed into 3 mL of a PVP@AuNP dispersion for 16 h under shaking at 500 rpm (IKA Vibrax VXR basic), shown schematically in **Figure 114**. Afterwards, the composite nonwoven sheet was placed in Milli-Q water to remove non-bonded AuNPs and was dried under ambient conditions for further use.
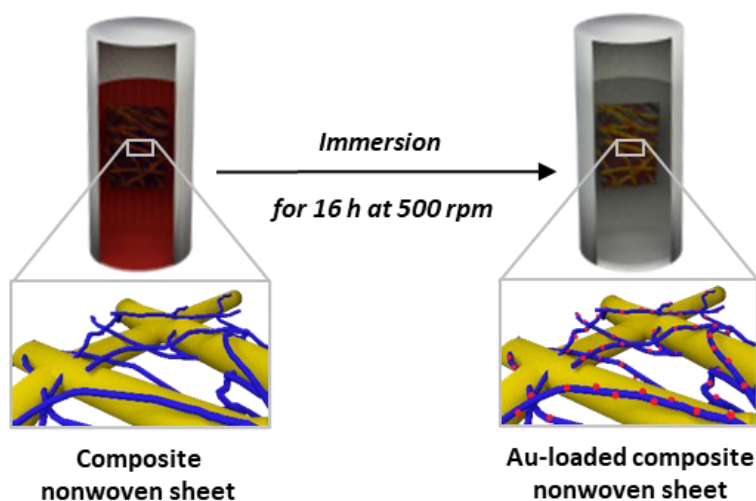
Figure 114: Schematic representation of the preparation process of a Au-loaded composite nonwoven sheet via immersion. A composite nonwoven sheet composed of PAN short fibers (yellow fibers) and terpyridine-functionalized BTA fibers (blue fibers) is placed in an aqueous PVP@AuNP dispersion (red) using tweezers. During immersion into the AuNP dispersion, the AuNPs can adsorb on the surface of functional BTA fibers (Au-loaded BTA fibers shown in red) within the composite nonwoven sheet. After removing the Au-loaded composite nonwoven sheet from the partly or entirely discolored AuNP dispersion, it is placed in Milli-Q water to remove non-bonded AuNPs. A section of the composite nonwoven sheet without and with AuNPs (red dots) is shown in magnification.

For the immobilization of AuNPs *via filtration*, a round piece with a diameter of 1.3 cm and a filtration area of 0.98 cm² was cut off from a large composite nonwoven sheet. Afterwards, 3 mL of a PVP@AuNP dispersion were passed through the reusable PTFE syringe filter using a syringe pump, followed by 3 mL of Milli-Q water to remove excess or non-adsorbed AuNPs. Then, 2 mL of Milli-Q water were filtered through the syringe filter to verify that leaching plays a minor role and the composite nonwoven sheet was completed. The preparation process is schematically shown in **Figure 115**.
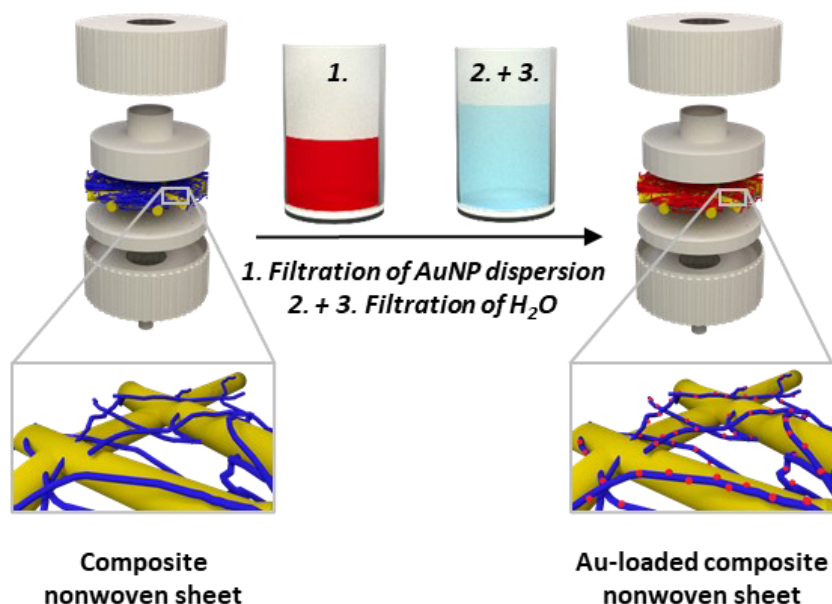
Figure 115: Schematic representation of the preparation process of a Au-loaded composite nonwoven sheet via filtration. A composite nonwoven sheet composed of PAN short fibers (yellow fibers) and terpyridine-functionalized BTA fibers (blue fibers) is placed in a reusable PTFE syringe filter holder. An aqueous PVP@AuNP dispersion (red) is filtered through the PTFE syringe filter holder using a syringe pump. During filtration of the AuNP dispersion, the AuNPs can adsorb on the surface of functional BTA fibers within the composite nonwoven sheet. For simplicity, the Au-loaded supramolecular BTA nanofibers are shown in red color. Subsequent filtration of Milli-Q water removes non-bonded AuNPs. The second filtration of Milli-Q water is carried out to verify the leaching behavior of AuNPs. A section of the composite nonwoven sheet without and with AuNPs (red dots) is shown in magnification.

To determine the adsorption or filtration efficiency, the absorption maxima of the initially employed AuNP dispersion at 524 nm were determined by UV/Vis measurements and compared to the absorption intensities of the AuNP dispersion after immersion or filtration. Additionally, ICP-OES measurements were carried out to evaluate the adsorption efficiencies and compare them with those obtained by UV/Vis measurements.

Figure 116 shows the UV/Vis spectra of the initially employed PVP@AuNP dispersion and the dispersions after immersion (left) or filtration (right) using the composite nonwoven sheets **c7-c9** and the reference nonwoven sheet.
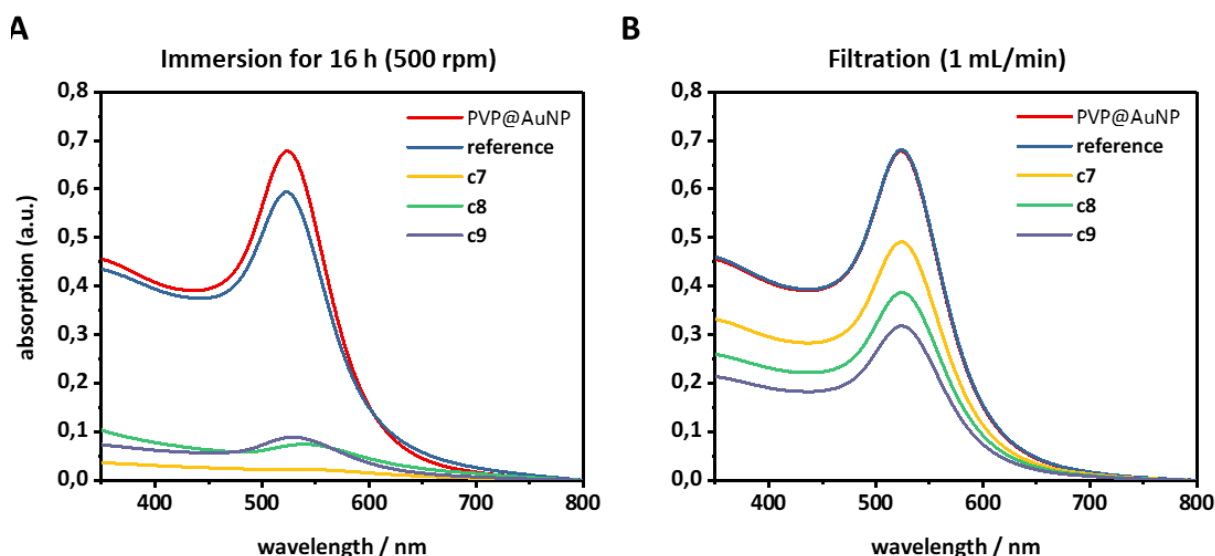
Figure 116: UV/Vis spectra of the initially employed PVP@AuNP dispersion (red) and the dispersions after immersion (**A**) and filtration (**B**) using composite nonwoven sheets **c7-c9** and a reference nonwoven sheet composed of pure PAN short fibers.

As already expected, only a very small amount of AuNPs was immobilized within the neat PAN nonwoven sheet as a reference. Approximately 12 % of the AuNPs were adsorbed via immersion, whereas no significant amount of AuNPs could be deposited by filtration. This finding can be explained by the lack of suitable functional groups interacting with the AuNPs. In contrast, the composite nonwoven sheets composed of PAN and **24a** fibers adsorbed significantly more AuNPs. Since the immobilization of AuNPs on the supramolecular BTA fibers depends on the number of terpyridine units and thus on the amount of BTA, composite nonwoven sheet **c9**, which exhibits the most BTA fiber content, should theoretically adsorb most AuNPs. This is also true for filtration but not for immobilization by immersion. As shown in the following **Table 12**, the highest immobilization by immersion was achieved with composite nonwoven sheet **c7**. An opposite trend in adsorption/filtration efficiencies can be observed when comparing the two immobilization methods. Via immersion, fewer AuNPs were adsorbed with an increasing amount of BTA fibers, whereas the filtration efficiency increased with higher BTA fiber content. In both cases, the adsorption efficiency was expected to increase with increasing BTA amount in the composite. Why this is not the case for the immersion process is still unclear.

To detect possible AuNP agglomeration and to investigate the distribution of AuNPs within the corresponding composite nonwoven sheets, SEM micrographs were taken after immersion (**Figure 117**) and after filtration (**Figure 118**).
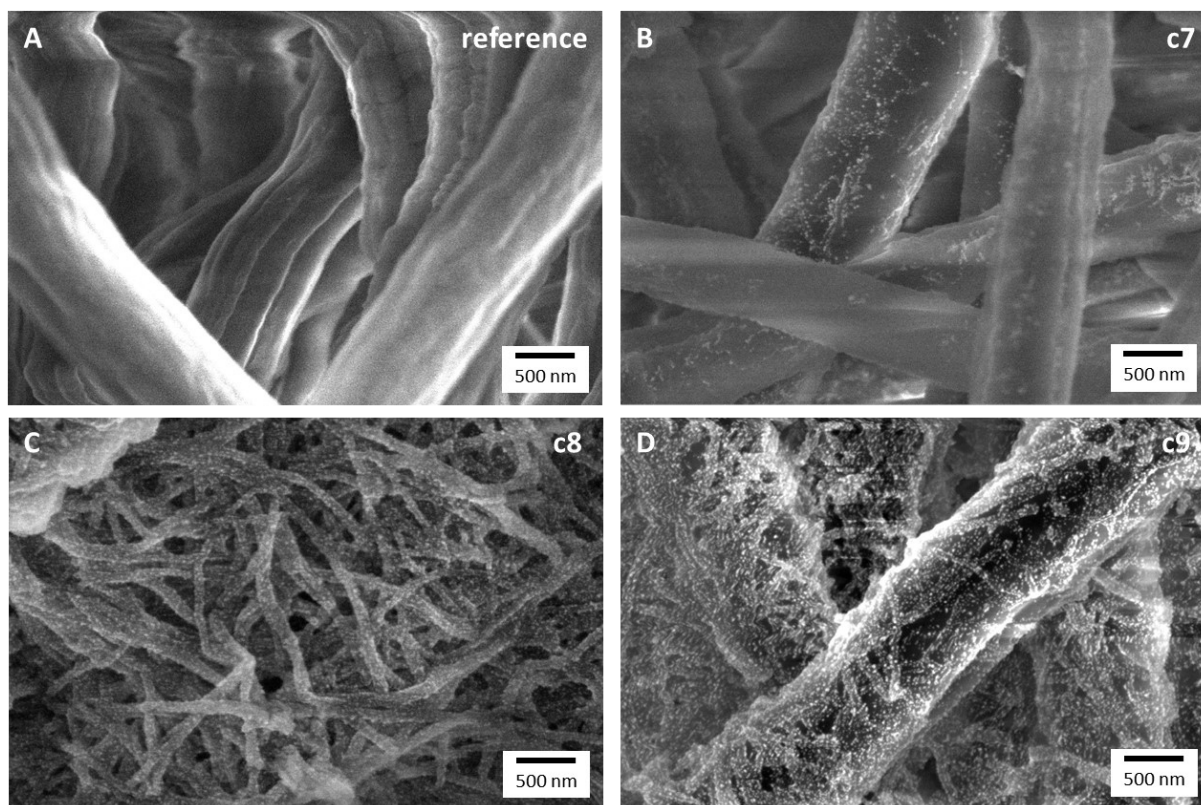
Figure 117: SEM micrographs of the reference nonwoven composed of PAN short fibers (**A**) and composite nonwoven sheets **c7-c9** (**B-D**) after immersion in a PVP@AuNP dispersion.

On the neat PAN fibers, only a very few AuNPs are visible. With an increasing BTA fibers amount, more immobilized AuNPs can be observed. AuNP agglomeration was found at some points in the composite nonwoven sheet **c7**, whereas in the case of composite nonwoven sheet **c8** or **c9**, the AuNPs are distributed very homogeneously on the supramolecular fibers and no agglomeration of AuNPs is visible. Interestingly, the adsorption efficiencies calculated from UV/Vis and ICP-OES measurements are significantly different in the case of the immersion method, whereas they are in very good agreement with the filtration method. The reason for this is unclear. Since the AuNP dispersion completely decolorized after immersion of composite nonwoven sheet **c7**, this indicates a very high adsorption efficiency as calculated from the UV/Vis measurements.

top side
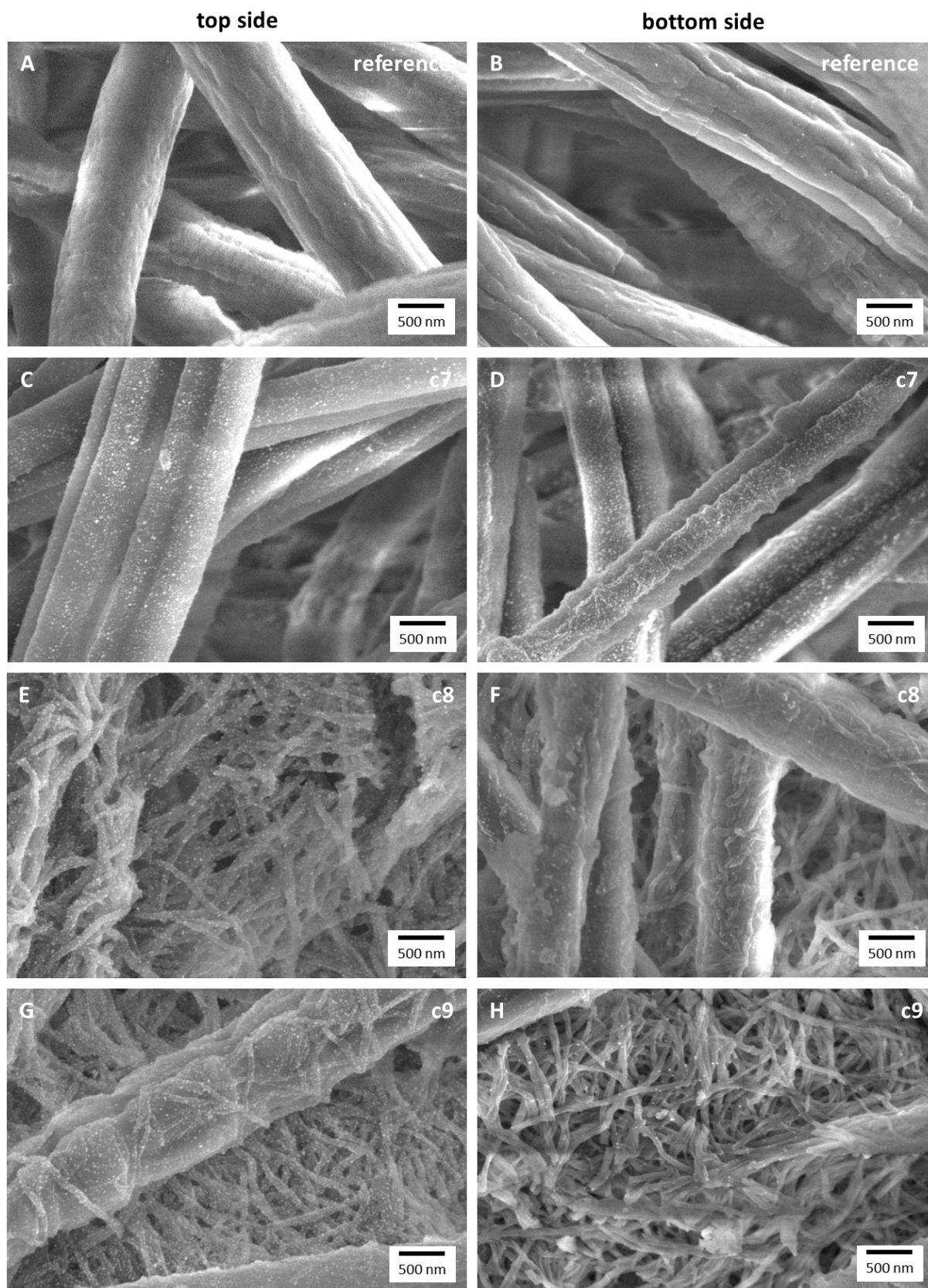
bottom side

Figure 118: SEM micrographs of the reference nonwoven sheet composed of PAN short fibers and composite nonwoven sheets **c7-c9** after filtration of a PVP@AuNP dispersion. The top side (left) and the bottom side (right) of the nonwoven sheets are shown, respectively.

Since a concentration gradient can potentially occur during filtration of the AuNP dispersion through a composite nonwoven sheet, both the top and bottom sides of the sheet were investigated by SEM with respect to AuNP distribution (**Figure 118**). When looking at the top side, the AuNP density increases with larger BTA content in the composite, similar to the immersion method. On the bottom side of the composite nonwoven sheets, a low number of AuNPs was determined with increasing BTA fiber contents (**c8** and **c9**), which indicates a concentration gradient. In the case of composite nonwoven sheet **c7** with the lowest BTA amount, no significant difference can be observed in the number of AuNPs on the top and bottom of the composites. These findings may be attributed to the different morphology of the composite nonwoven sheets and the resulting pressure build-up in the syringe filter holder. It can be assumed that in the case of **c7**, the pressure difference between the top and bottom sides of the composite is smaller than in the case of **c8** and **c9**, which means that the formation of a concentration gradient is not observed or is less pronounced. Here, further investigations would be necessary for more precise statements. **Table 12** summarizes the adsorption and filtration efficiencies as well as the corresponding Au amount immobilized within the composite nonwoven sheets **c7**-**c9** and the reference nonwoven sheet.

Table 12: Immobilization of PVP@AuNP on composite nonwovens with different amounts of BTA fibers. Based on the UV/Vis measurements of the AuNP dispersions after immersion or after filtration, the adsorption or filtration efficiency and the corresponding Au amount on the nonwovens were calculated. The pure PVP@AuNP dispersion contains 30 µg Au/mL and serves as a reference.

Sample	Adsorption efficiency UV/Vis in %	Adsorption efficiency ICP-OES in %	Au amount in µg[a]	Filtration efficiency UV/Vis in %	Filtration efficiency ICP-OES in %	Au amount in µg[a]
PVP@AuNP	-	-	-	-	-	-
reference	12	0	11	0	0	0
c7	97	54	87	28	29	25
c8	90	61	81	43	37	39
c9	87	52	78	53	52	48

[a] calculated based on the efficiencies from UV/Vis measurements; 1 mL PVP@AuNP dispersion (1 g PVP@Au powder per liter) contains 30 ± 5 µg gold.

Maximum Au uptake capacity within PAN/BTA composite nonwoven sheets

To compare the maximum Au uptake capacity of neat supramolecular **24a** nanofibers with that of a composite nonwoven sheet, 5 mL of a PVP@AuNP dispersion were filtered several times through composite nonwoven sheet **c8**, which was placed in a PTFE syringe filter holder, with a filtration speed of 1 mL/min until the absorption in UV/Vis measurements did not change anymore.

To determine the Au amount adsorbed, the filtrate was measured by UV/Vis spectroscopy each after two-times filtration of the AuNP dispersion. The corresponding UV/Vis absorption spectra, calculated efficiencies and immobilized Au amounts are shown in **Figure 119**.

	Sample	Filtration efficiency UV/Vis in %	Au amount in μg[a]
	reference	-	-
c8	After 2 cycles	62	93
	After 4 cycles	82	123
	After 6 cycles	92	138
	After 8 cycles	99	148

[a] 1 mL PVP@AuNP dispersion contains 30 μg Au per mL
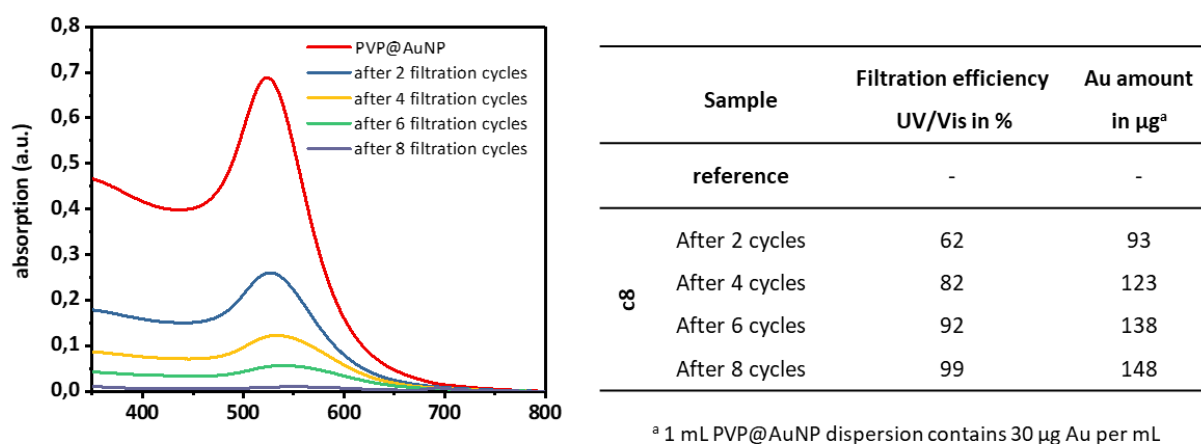
Figure 119: UV/Vis spectra of the filtrate after each double filtration through the composite nonwoven sheet **c8** and the corresponding filtration efficiencies and immobilized Au amounts.

After 5 mL of a PVP@AuNP dispersion was filtered twice (two filtration cycles) through the composite nonwoven sheet **c8**, 62 % of the AuNPs were already adsorbed within the composite nonwoven sheet, which corresponds to a Au quantity of 93 μg. After eight filtration cycles, even an efficiency of 99 % was achieved (corresponds to 148 μg Au). Assuming a completely homogeneous distribution of the BTA fibers in the composite nonwoven sheet, the filtration area (0.98 cm²) should comprise approximately 0.5 mg **24a** fibers. Normalizing the Au amount to 1 mg **24a** fibers, the Au uptake capacity corresponds to ~ 300 μg Au per mg **24a** fiber. This value is about twice as high as the Au uptake capacity of neat **24a** fibers after 5 min. However, the different experimental conditions (different contact times of AuNPs with composite) must be taken into account here, making a direct comparison difficult.

Interestingly, UV/Vis spectra after six or eight filtration cycles showed additional low absorption peaks at ~ 700 nm, indicating AuNP agglomeration. This observation could not be made in any of the previous UV/Vis spectra. SEM micrographs, which are shown in **Figure 120**, confirm this hypothesis. The supramolecular **24a** fibers are almost completely occupied with AuNPs, so that AuNPs may be adsorbed between or next to other AuNPs. However, in this case, agglomeration of AuNPs may also occur. The red circles show areas where AuNP agglomeration can be seen.
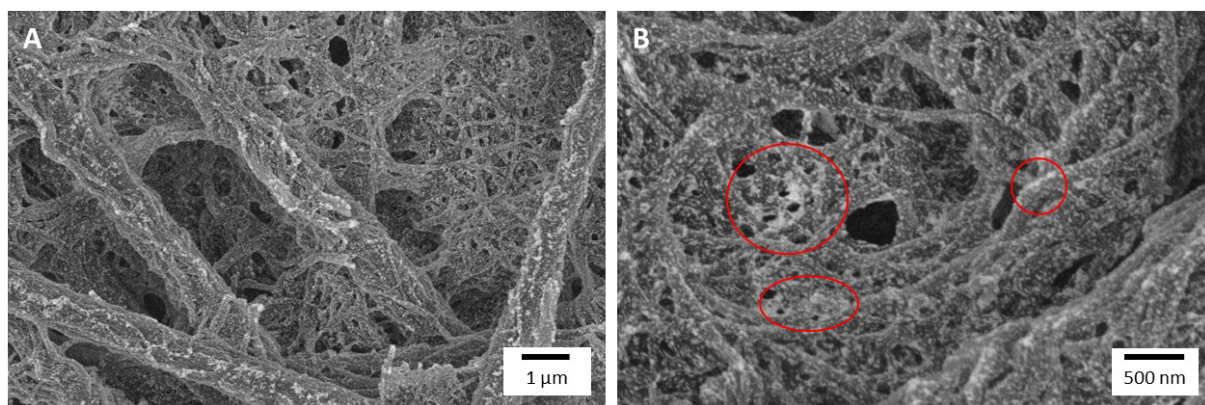
Figure 120: SEM micrographs of the composite nonwoven sheet **c8** after filtration of 5mL PVP@AuNP dispersion. Since the BTA fibers are very strongly occupied with AuNPs, agglomeration of the AuNPs (red circles) occurs.

5.3 *In situ* formation of AuNPs on supramolecular fibers of BTAs with terpyridine substituents

Finally, an interesting approach for AuNP immobilization is the *in situ* formation of AuNPs on supramolecular fibers. The advantage of this way is that, within a short time, extremely small AuNPs can be generated, which are directly stabilized by the support material and thus, no additional stabilizing ligands such as citrate or PVP are needed. The general applicability of this approach was first examined with single BTA fibers and subsequently transferred to a composite nonwoven sheet, which features sufficient mechanical stability to be used further in catalysis. Particular focus was given to a uniform AuNP formation and homogenous AuNP distribution on the surface of the supramolecular **24a** nanofibers.

Figure 121 shows the experimental procedure of the *in situ* formation of AuNPs on single BTA fibers. In detail, 1 mg fibers of **24a** were mixed with 1 mL of a 0.5 mM aqueous $HAuCl_4$ solution for 10 min while shaking. Afterwards, 1 mL of a 50 mM aqueous $NaBH_4$ solution was added and the mixture was filtered off after 3 min using a PTFE syringe filter holder.
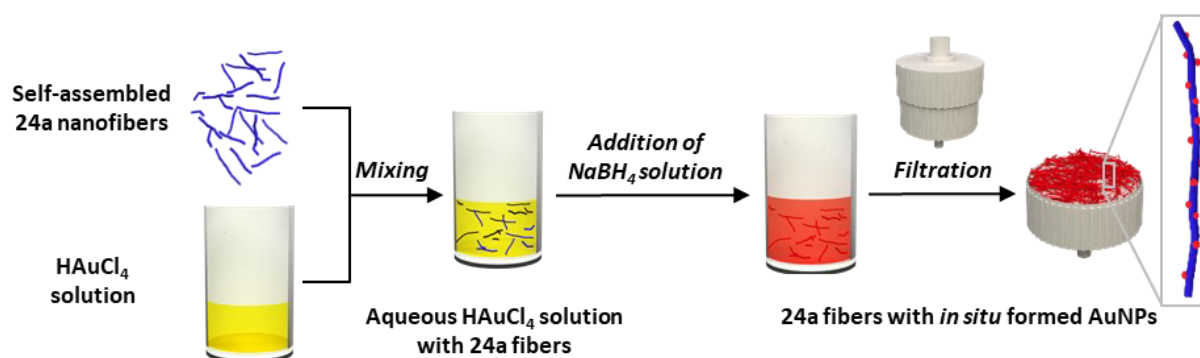
Figure 121: Schematic representation of the *in situ* formation of AuNPs on supramolecular **24a** fibers. In a first step, the self-assembled nanofibers of **24a** (blue fibrous structures) were mixed with a $HAuCl_4$ solution (yellow). During mixing, the Au ions can adsorb on the BTA fiber surface. Subsequent addition of an aqueous $NaBH_4$ solution results in *in situ* formation of AuNPs on the **24a** fiber surface (red fibrous structures). The solution also turns red since AuNPs are not only formed on the **24a** fiber surface. Afterwards, the Au-loaded **24a** nanofibers are filtered off using a PTFE syringe filter holder. On the right side of the schematic, a magnification of a single BTA fiber with *in situ* formed AuNPs (red dots) is shown.

Au ions were adsorbed on the supramolecular **24a** fibers within a short time, which was indicated by a slightly yellow coloring of the fibers. When $NaBH_4$ was added, a rapid color change was observed. The supramolecular fibers take on a brownish-red color indicating successful AuNP formation, verified by TEM measurements. For this purpose, the filtered brownish-red supramolecular **24a** fibers were redispersed in water and a droplet of this fiber dispersion was deposited on a TEM grid.

Figure 122 shows exemplarily a TEM micrograph of a single **24a** fiber with *in situ* formed AuNPs. The *in situ* formed AuNPs have a uniform particle size with an average diameter of 2.6 ± 0.6 nm and are very homogeneously distributed on the fiber surface. No agglomeration of AuNPs can be observed.
178
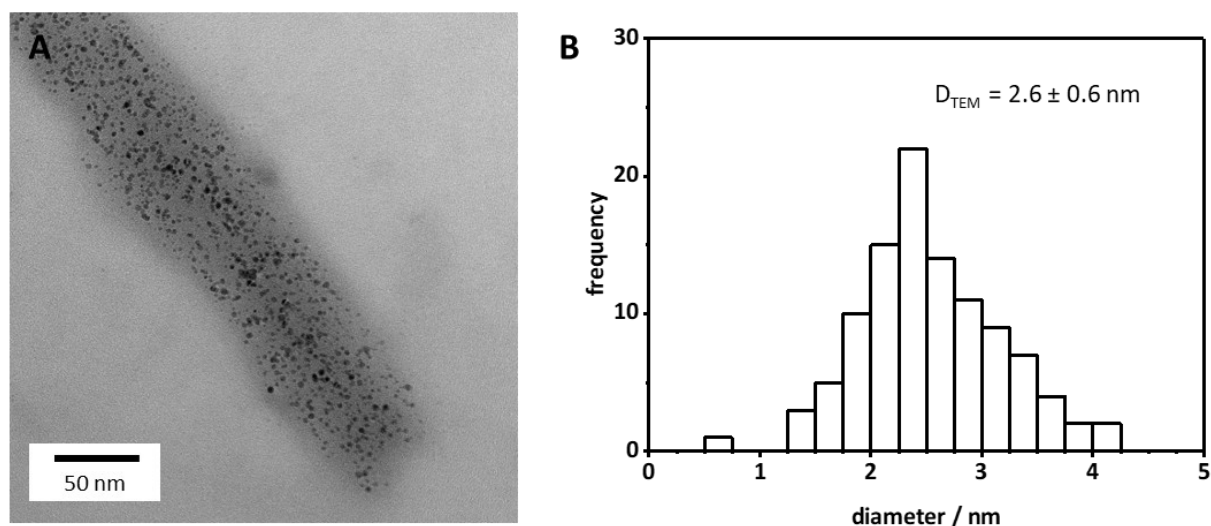
Figure 122: TEM micrograph of *in situ* formed AuNPs on a single supramolecular fiber of **24a** (**A**) and the corresponding AuNP size distribution (**B**). The *in situ* formed AuNPs exhibit an average diameter of 2.6 ± 0.6 nm and are homogenously distributed on the fiber surface.

After the general applicability of the *in situ* formation of AuNPs on single supramolecular **24a** fibers was successfully tested, the *in situ* AuNP formation was transferred to composite nonwoven sheets. Further experiments were carried out using composite nonwoven sheet **c8** to find the most suitable conditions for the *in situ* AuNP formation within composite nonwoven sheets. Therefore, the following parameters were varied:

(i)   *Volume of the Au precursor solution*

(ii)   *Concentration and volume of NaBH$_4$*

(iii)   *Exposure time before and after adding NaBH$_4$*

The *in situ* formation of AuNPs within the composite nonwoven sheets was performed by immersing the composites into a certain volume of Au precursor solution (HAuCl$_4$·3H$_2$O) and mixing it over a certain period of time (10, 60 or 240 min). After adding NaBH$_4$ as a reducing agent, the solution was shaken again for several minutes (3 or 10 min). Finally, the composite was removed from the solution and washed with MilliQ water. After complete drying under ambient conditions, the composite was examined by SEM. The Au content in the composite was determined via ICP-OES measurements by calculating the difference between the neat Au precursor solution and the supernatant solution. This amount corresponds to the amount of Au adsorbed.

As a reference experiment, the *in situ* AuNP formation was performed with a nonwoven sheet composed of neat PAN short fibers. No color change of the nonwoven could be detected since the PAN fibers are not able to immobilize AuNPs despite the nitrile groups. For all samples with composite nonwoven sheet **c8**, yellow coloration of the composite was observed within a short time. The more volume of Au solution was used, the stronger the yellow tone. By adding NaBH$_4$, a distinct change in the color of the composite from yellow to red/purple took place within a few seconds. This was a direct

indication of successful *in situ* AuNP formation. **Table 13** shows an overview of the different experiments performed to form *in situ* AuNPs within composite nonwoven sheet **c8**.

Table 13: Overview of the different performed experiments for the formation of *in situ* AuNPs within composite nonwoven sheet **c8**. The volume of the Au precursor solution (HAuCl$_4$·3H$_2$O, 0.5 mM), the concentration and volume of NaBH$_4$ solution, as well as the exposure time of the composite in the solution before and after adding NaBH$_4$ were varied, respectively.

Sample	Volume (HAuCl$_4$·3H$_2$O, 0.5 mM)	Concentration / Volume NaBH$_4$	Exposure time in aqueous HAuCl$_4$ solution	Exposure time in HAuCl$_4$ + NaBH$_4$ solution	Stability of composite
1	0.1 mL	7.5 mM / 1.0 mL	240 min	10 min	✓
2	0.25 mL	7.5 mM / 1.0 mL	240 min	10 min	✓
3	0.5 mL	7.5 mM / 1.0 mL	240 min	10 min	✓
4	0.75 mL	7.5 mM / 1.0 mL	240 min	10 min	✗
5	1.0 mL	7.5 mM / 1.0 mL	240 min	10 min	✗
6	0.5 mL	50 mM / 1.0 mL	60 min	10 min	✓
7	0.5 mL	25 mM / 1.0 mL	60 min	10 min	✓
8	0.25 mL	7.5 mM / 1.0 mL	60 min	10 min	✓
9	0.25 mL	7.5 mM / 1.0 mL	10 min	10 min	✓
10	2.0 mL	75 mM / 1.0 mL	10 min	3 min	✓
11	2.0 mL	75 mM / 2.0 mL	10 min	3 min	✓

In the first experimental series (samples 1-5), the volume of a 0.5 mM aqueous HAuCl$_4$ precursor solution was varied between 0.1 and 1.0 mL, whereas all other parameters were kept constant. It was found that using a large volume of HAuCl$_4$ solution results in a not completely stable and partially disintegrated composite nonwoven sheet **c8**. This may be attributed to the dissolution of the supramolecular fibers due to the acidic environment of the HAuCl$_4$ solution combined with the large volume of HAuCl$_4$ solution. Additionally, agglomeration of AuNPs was observed in several parts for all samples 1-5.

In further experiments, the volume of the HAuCl$_4$ solution and the concentration of NaBH$_4$ solution was varied and the exposure time of the composite in the HAuCl$_4$ solution and in the mixture of HAuCl$_4$ and NaBH$_4$ solution was reduced. **Figure 123** shows SEM micrographs of composite nonwoven sheet **c8** with *in situ* formed AuNPs using different experimental conditions.
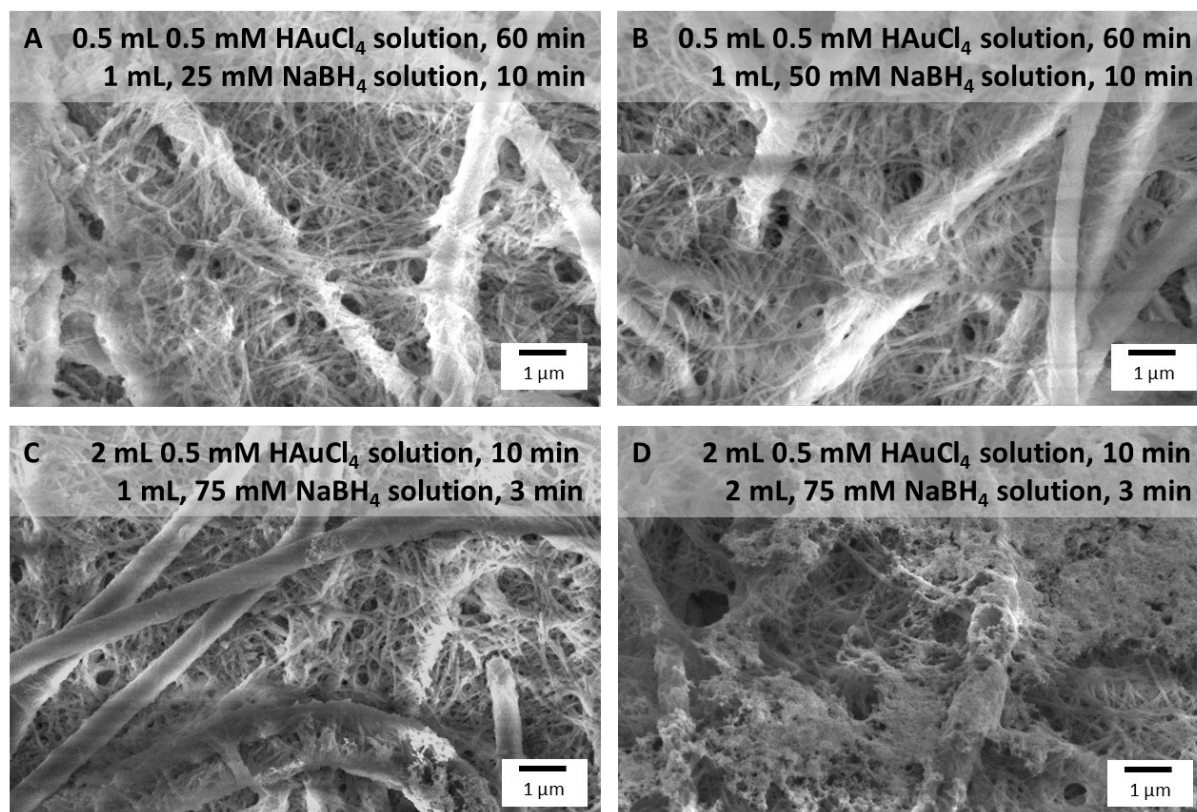
Figure 123: SEM micrographs from the top side of composite nonwoven sheet **c8** after *in situ* AuNP formation under different experimental conditions. Composite **c8** was immersed into 0.5 mL (**A+B**) or 2 mL (**C+D**) of a 0.5 mM HAuCl₄ solution for 60 min (**A+B**) or 10 min (**C+D**), followed by the addition of 1 mL of a 25, 50 or 75 mM (**A-C**) or 2 mL of a 75 mM (**D**) NaBH₄ solution. After 10 min (**A+B**) or 3 min (**C+D**), the composite was removed from the solution mixture; the morphology of composite nonwoven sheet **c8** remains the same after *in situ* formation of AuNPs. However, AuNP agglomeration can be observed in **C+D**.

All samples of composite nonwoven sheets **c8**, shown in **Figure 123**, remain their original morphology after *in situ* AuNP formation under the reported experimental conditions. Consequently, the concentration of the NaBH₄ solution has no influence on the morphology and stability of the composites. However, the different NaBH₄ concentrations influence the size and number of AuNPs formed as well as the volume of the HAuCl₄ solution. [140,141] A further finding is that an exposure time of 4 h of composite nonwoven sheet **c8** in the HAuCl₄ solution is too long, whereas the volume of the HAuCl₄ solution does not play a decisive role in the stability of the composite nonwoven sheet. In **Figure 123A** and **B**, no AuNP agglomeration can be observed due to the small AuNP size, whereas in **Figure 123C** and **D**, several large AuNP agglomerates can be found. These agglomerates possibly are formed since AuNPs were formed in solution rather than directly on the fibers. Subsequently, due to the lack of stabilizing ligands, the AuNPs form large agglomerates and deposit on the surface of the composites. To overcome this issue, the procedure of *in situ* formation within composite nonwovens was slightly modified.

Instead of adding $NaBH_4$ directly to the 0.5 mM aqueous $HAuCl_4$ solution, the composite nonwoven sheet was previously removed from the $HAuCl_4$ solution (1 mL) after an exposure time of 10 min and rinsed/washed with MilliQ water to remove non-bonded Au(III) ions. This did not affect the yellowish color of the composite (**Figure 124B**). The Au precursor solution was then evaporated for further ICP-OES measurements. To form AuNPs, the composite nonwoven sheet was placed in a 50 mM $NaBH_4$ solution so that AuNPs could only form directly within the composite nonwoven sheet and not in solution within a very short time. Within a few seconds, a color change from yellow to red took place (**Figure 124C**). Finally, the composite was washed with Milli-Q water to remove non-bonded AuNPs and $NaBH_4$ residues. The composite was dried at 40 °C in a vacuum drying oven for 1 h.
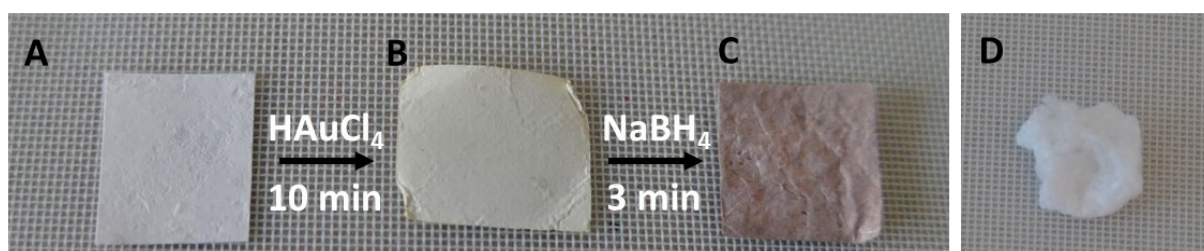
Figure 124: *In situ* formation of AuNPs within a composite nonwoven sheet. (**B**) Composite nonwoven sheet **c8** before the addition of $HAuCl_4$ solution, (**B**) composite nonwoven sheet **c8** with yellowish color after immersion into $HAuCl_4$ solution, (**C**) composite nonwoven sheet **c8** with red color after adding $NaBH_4$ indicating the formation of AuNPs, (**D**) neat PAN nonwoven after *in situ* AuNP formation. Reprinted (adapted) with permission from [138] © 2021 American Chemical Society.

TEM measurements were carried out to determine the distribution and size of the *in situ* formed AuNPs. Since the composite nonwoven sheet cannot be measured directly due to the dense fiber network, the composite was destroyed with a mixer to obtain single fibers, which could be applied to a TEM grid. **Figure 125** shows the TEM micrographs of single BTA fiber pieces. Very homogenous distribution of the *in situ* formed AuNPs on the BTA nanofiber surface and no agglomeration of AuNPs was observed according to TEM micrographs.

The average diameter of the AuNPs was found to be 2.4 ± 0.8 nm and is thus in very good agreement with the average diameter of *in situ* formed AuNPs determined before on single **24a** nanofibers. The AuNPs are only stabilized by the terpyridine units and no other ligands block the catalytically active surface of AuNPs.
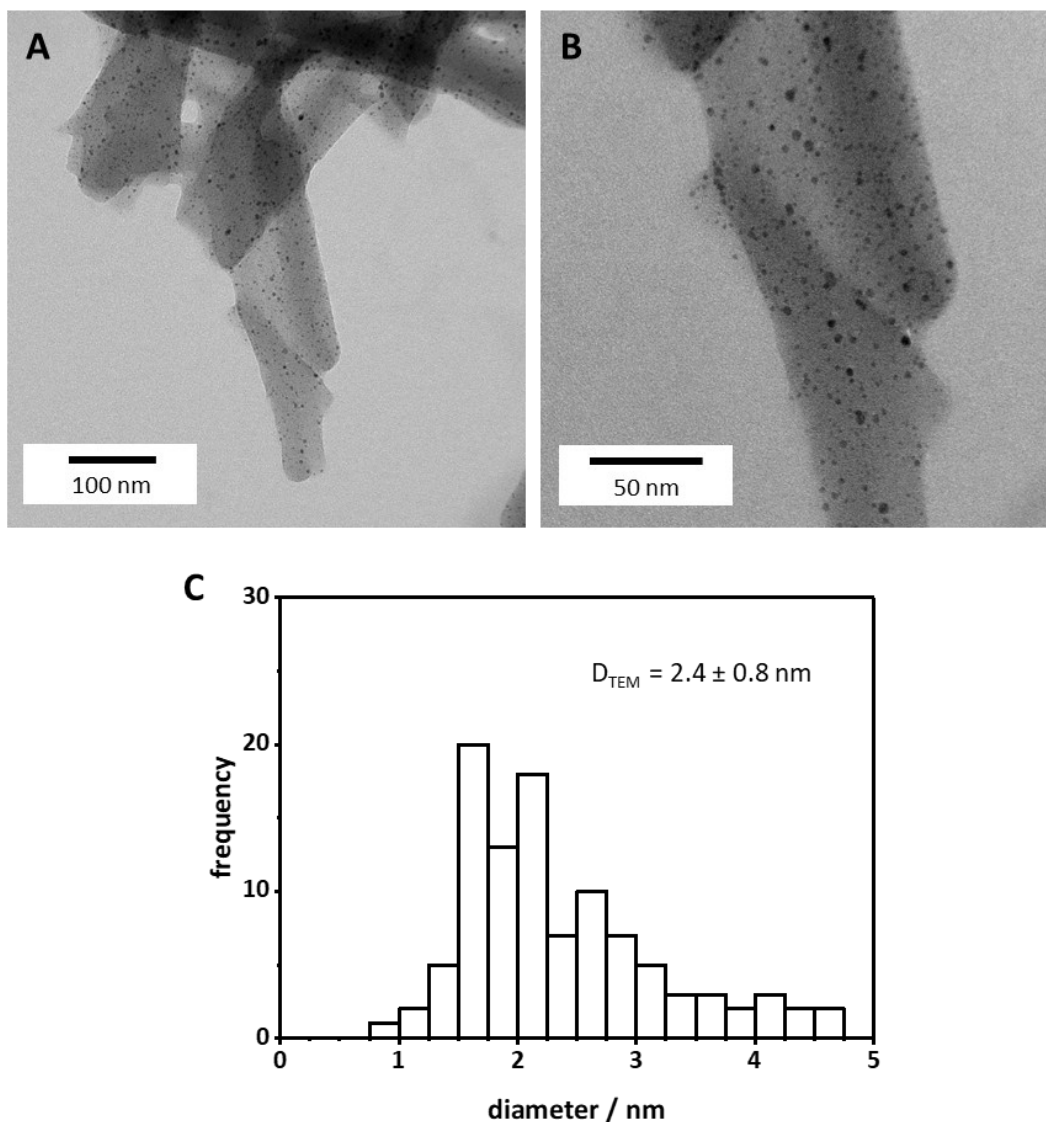
Figure 125: TEM micrograph of *in situ* formed AuNPs on a supramolecular fiber of **24a** (**A**) and the corresponding AuNP size distribution (**B**). The individual fibers were obtained by cutting a composite nonwoven into small pieces in a mixer. The average AuNP diameter is 2.4 ± 0.8 nm and the AuNPs are homogenously distributed on the fiber surface. Reprinted (adapted) with permission from [138] © 2021 American Chemical Society.

The Au content within composite nonwoven sheet **c8** was determined by ICP-OES measurements calculating the difference between the initial concentration of the aqueous $HAuCl_4$ solution before and the concentration after immersion of the composite nonwoven sheet. Within a short exposure time of 10 min, a Au amount of 50 µg was immobilized within composite nonwoven sheet **c8** with an area of around 1 cm².

5.4 Conclusion

The functionality of the pyridine- and terpyridine-substituted BTA nanofibers as efficient AuNP carrier was successfully demonstrated by four different ways of AuNP immobilization. UV/Vis and ICP-OES measurements were used to determine the Au amount immobilized on the surface of the functional supramolecular fibers. As the most convenient way for AuNP immobilization, the mixing of supramolecular BTA fibers or a BTA fiber dispersion with a PVP@AuNP dispersion was identified. A short mixing time of 5 min is already sufficient to immobilize a high amount of AuNPs depending on the selected BTA. For the different pyridine-containing BTAs **3a**, **9a-b** and **16a-b**, the AuNP adsorption efficiency decreases with decreasing number of pyridine substituents. Surprisingly, replacing one pyridine moiety with one non-functional *tert*-butyl or ethylhexyl group in the BTAs deteriorates the AuNP adsorption efficiency larger than expected. This finding may be attributed to the influence of the aliphatic group on the two pyridine moieties regarding the orientation and interaction between the different substituents. On the fibers' surface of the reference BTA with aliphatic side groups **25** and **26**, only minimal amounts of AuNPs were found after a washing step with water, demonstrating the beneficial role of the functional pyridine moieties.

Especially, it was found that the terpyridine-substituted BTA **24a** is an ideal candidate for the immobilization of a large amount of Citrate@AuNPs or PVP@AuNPs via simple mixing with a fiber dispersion as well as via filtration of a AuNP dispersion through a supramolecular fiber network of **24a** since in both cases the AuNPs are very homogenously distributed on the fiber surface without any AuNP agglomeration. The different stabilization ligands of the AuNPs did not significantly alter the adsorption efficiencies, although deposition of PVP@AuNPs proceeds in a slightly improved manner than those of the Citrate@AuNPs. The maximum Au uptake capacity of **24a** fibers after mixing them for 5 min with a PVP@AuNP dispersion is 140 µg Au per mg **24a** fiber, whereas after mixing for 24 h, a very high maximum Au uptake capacity of 4.5 mg Au per mg **24a** fiber was determined. However, in this case, AuNPs completely cover the individual BTA fibers, and AuNP agglomerates can be found in some locations, which can be attributed to the additional deposition of AuNP agglomerates over the course of 24 h. Nevertheless, these values show the high potential of **24a** as an efficient AuNP carrier. After basic investigations using only the supramolecular **24a** fibers, composite nonwoven sheets **c7**-**c9** composed of PAN short fibers and supramolecular **24a** fibers were loaded with AuNPs by immersing the composite in a AuNP dispersion or by filtering a AuNP dispersion through the composite. Both methods are highly suitable for AuNP immobilization. In the case of the filtration method, a concentration gradient was observed for composite nonwoven sheets **c8** and **c9**, i.e., a higher number of AuNPs was found on the top than on the bottom side of the composite. An advantage of the filtration method compared to the immersion method is that AuNPs can be immobilized within a very short time. In contrast, AuNPs are very homogeneously distributed within all composite nonwoven sheets **c7**-**c9** using the immersion method. The maximum Au uptake capacity in the composite after eightfold filtration of a PVP@AuNP trough composite nonwoven sheet **c8** is 300 µg per mg **24a** fiber,

which is even higher than for the pure **24a** fibers but can be attributed to the different experimental conditions. In all cases, no agglomeration and leaching of AuNPs were determined. Only when the supramolecular **24a** fibers are almost completely occupied by AuNPs, AuNP agglomeration was detected at some places due to the deposition of additional AuNPs on top of the already immobilized AuNPs.

Finally, AuNPs were formed *in situ* on the supramolecular **24a** fibers. This method is characterized, among other things, by the fact that no additional stabilization ligands are required. Very small AuNPs with an average diameter of $\sim$ 2.5 nm were formed on individual supramolecular **24a** fibers and within composite nonwoven sheets within a few minutes by reducing the Au ions using $NaBH_4$. By varying different parameters, it was found that extensive immersion of the composite nonwoven sheets into an aqueous $HAuCl_4$ solution may lead to a disintegration of the supramolecular fibers. To avoid AuNP agglomeration in the composite nonwoven sheet, it is also essential that the composite is rinsed with water after immersion in the $HAuCl_4$ and before placing it in an aqueous $NaBH_4$ solution. This protocol prevents AuNP formation and agglomerates in solution due to a lack of stabilization ligands, which may subsequently settle as agglomerates in the composite. Taking these findings into account, AuNPs are very homogeneously distributed within the composite nonwoven sheets, making them a very promising system for further use in catalysis.

6 Functional composite nonwoven sheets for catalytic applications

To demonstrate the functionality of the Au-loaded composite nonwoven sheets composed of PAN short fibers and functional supramolecular fibers of **24a**, they were used in the catalytic reduction of 4-nitrophenol (4-NP) to 4-aminophenol (4-AP) in the presence of NaBH$_4$. The 4-NP reduction was chosen as a model reaction since it is a well-investigated reaction and a high number of kinetic data can be found in literature. An advantage of this system is that the progress of the catalytic reaction can be followed by *in situ* UV/Vis measurements since the absorption maxima of the formed 4-nitrophenolate at 400 nm decrease over time in the presence of a catalyst and the absorption maxima of 4-aminophenolate are at 300 nm and readily separated from the other one. Visually, the successful reduction of 4-NP can be seen by the decolorization of the yellowish reaction solution. [91,92]

Since a large excess of NaBH$_4$ is used in the catalytic reaction, the reduction of 4-NP follows pseudo-first-order kinetics. To compare the performance of the different catalytic reactions, the apparent kinetic reaction rate constant k_{app} can be determined directly from the plot $-ln(A_t/A_0)$ against the reaction time t according to **equation 8**, since the slope of this plot corresponds to k_{app}.

$$r = \ ln\left(\frac{A_t}{A_0}\right) = -k_{app}t \qquad\qquad \textbf{8}$$

Where r is the rate of reduction, A_t is the absorption of 4-NP at the time t and A_0 is the initial absorption at t=0. More detailed information about the derivation of the equation is described in **chapter 1.5**.

The catalytic studies were performed in a discontinuous manner (**chapter 6.1**) and a continuous manner (**chapter 6.2**). Au-loaded composite nonwoven sheets **c8** and **c9** were selected as catalytically active materials since they feature sufficient mechanical stability, as demonstrated in **chapter 4.2**. In particular, it should be investigated to what extent the different composition of composite nonwoven sheets **c8** and **c9** affects the catalytic performance. Additionally, the difference in catalytic performance depending on the type of immobilized AuNPs (PVP@AuNP or *in situ* formed AuNPs) within the composite nonwoven sheets was examined. The leaching behavior of AuNPs during catalysis and the reusability of the composite nonwoven sheets resemble a sustainable characteristic of such systems and will be addressed in the following.

6.1 Catalysis in a discontinuous system

The general applicability of the Au-loaded composite nonwoven sheets in catalytic reduction of 4-NP was tested in a batch-type manner. In detail, a reaction solution was prepared by filling 1.5 mL of a 0.1 mM aqueous 4-NP solution and 1.5 mL of a 100 mM aqueous $NaBH_4$ solution into a quartz cuvette. Subsequently, a 1.0 cm² piece of the corresponding composite nonwoven sheet **c8** or **c9** was completely immersed and kept in the reaction solution using a tweezer. The reaction was stirred at 25 °C and 600 rpm for 2 h. Every 2 min, a UV/Vis spectrum was recorded in the range of 250-500 nm at a scan speed of 400 nm/min until full conversion of the reaction was monitored. Subsequently, the composite nonwoven sheet was removed from the reaction solution and was washed with water to remove the remaining reactants on the surface. After drying the composite, the procedure was repeated and the composite was reused for catalytic reaction to investigate the reusability. After each cycle, the remaining reaction solution was analyzed by ICP-OES measurements to determine possible Au residues in the solution. The experimental procedure for the catalytic reduction in a batch process is schematically shown in **Figure 126**.
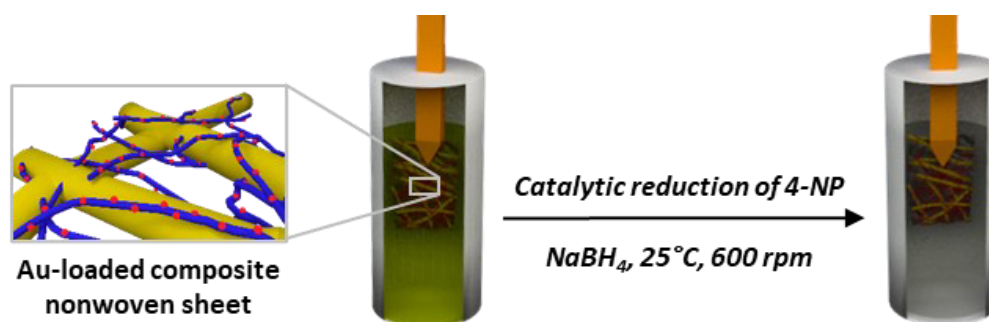
Figure 126: Schematic representation of the process of the catalytic reduction of 4-NP to 4-AP in the presence of $NaBH_4$ using a Au-loaded composite nonwoven sheet. Discoloration of the yellowish reaction solution shows successful reduction of 4-NP to 4-AP.

The reduction of 4-NP only takes place in the presence of a catalyst.[86] To exclude a contribution of the composite nonwoven sheets to the catalytic process, reference experiments with a neat composite nonwoven sheet without AuNPs were carried out. Exemplarily, the UV/Vis spectra of the reaction solution after 0 and 120 min using the neat composite nonwoven sheet **c8** as a reference experiment are shown in **Figure 127A**. The absorption during catalysis did not change in the absence of AuNPs over a period of 120 min. Thus, no reduction of 4-NP took place with a neat composite nonwoven sheet. This observation could be made for all composite materials prepared in this work.

The UV/Vis spectra of the reaction solution measured in steps of 10 min using the Au-loaded composite nonwoven sheet **c8** are shown in **Figure 127B**. For this, AuNPs were immobilized in the composite nonwoven sheet **c8** by immersion into a PVP@AuNP dispersion. A total amount of 52 μg Au was deposited and all AuNPs are homogeneously distributed on the fiber surface of the supramolecular **24a** fibers within composite nonwoven sheet **c8** (see also **chapter 5.2**).
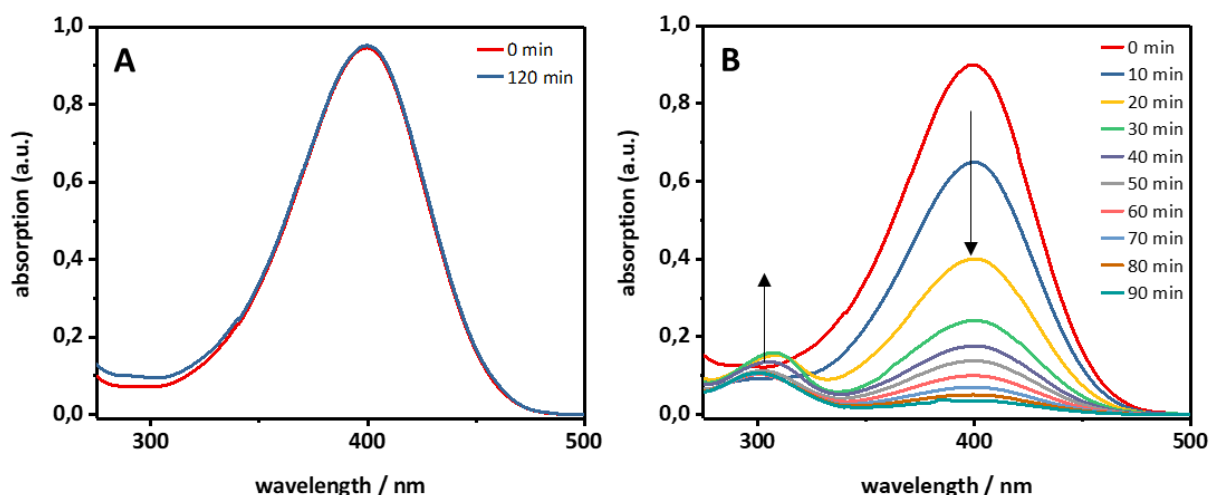
Figure 127: *In situ* recorded UV/Vis spectra of the reaction solution of the 4-NP reduction using the neat (**A**) and Au-loaded composite nonwoven sheet **c8** (**B**). No reduction of 4-NP takes place using the neat composite nonwoven sheet, whereas in the presence of the Au-loaded composite nonwoven sheet, the absorption maximum of 4-nitrophenolate at 400 nm decreases and the absorption of 4-AP at about 300 nm increases over time. Reprinted (adapted) with permission from [138] © 2021 American Chemical Society.

In contrast to the reference experiment, **Figure 127B** shows that with the Au-loaded composite nonwoven sheet **c8**, the absorption maxima of 4-NP at 400 nm decrease, whereas the 4-AP at around 300 nm increases over time. In this case, almost full conversion is determined after about 90 min.

The different compositions of the PAN/BTA composite nonwoven sheets may have an influence on the catalytic activity due to the different morphology of the composite nonwoven sheets and the associated different accessibility of the reactants to the catalytically active AuNP surface. For that reason, catalytic reduction of 4-NP was carried out with Au-loaded composite nonwoven sheets **c8** and **c9**.

The conversion-time diagrams of the catalytic reduction of 4-NP using composite nonwoven sheets **c8** and **c9** are shown in **Figure 128A** and **B**. **Figure 128C** and **D** show the corresponding plots of $-\ln(A_t/A_0)$ against the reaction time. The first and second catalytic cycles for **c8** and **c9** are given in both graphs.

Figure 128: Catalytic reduction of 4-NP to 4-AP using Au-loaded PAN/BTA composite nonwoven sheets **c8** and **c9** in a discontinuous system followed by *in situ* UV/Vis absorption measurements. AuNP immobilization was carried out by immersing the composite nonwoven sheets into PVP@AuNP dispersion. Temporal study of the conversion (**A+B**) and -ln(A_t/A_0) (**C+D**) for composite nonwoven sheets **c8** and **c9** after the first and second cycle.

As can be seen in **Figure 128**, both composite nonwoven sheets **c8** and **c9** show a high catalytic activity, which remains the same with high reproducibility when reused. In detail, the apparent kinetic reaction rate constant k_{app} is in the range of 0.00041-0.00070 s^{-1}. The initial deviation of the fits of **c8** and **c9** may be explained by the formation of hydrogen gas during the catalytic reaction. The hydrogen gas bubbles can cause scattering during UV/Vis measurements, which can lead to deviations in the UV/Vis spectra. Overall, the performance is highly comparable. However, the value of k_{app} strongly depends on the limits chosen for the corresponding fit lines. If the fits are performed over the whole data points, k_{app} is quite similar in the case of **c8** and **c9**. The similar catalytic performance is in agreement with the immobilized Au amount, which is almost identical at 52 µg (**c8**) and 59 µg (**c9**).

ICP-OES measurements showed that leaching of AuNPs in the range < 1 % takes place during catalysis. These values are extremely low and also within the error range of the ICP-OES measurement instrument. **Table 14** summarizes the results from the catalytic experiments using Au-loaded composite nonwoven sheets **c8** and **c9** (PVP@AuNPs were immobilized by immersion), including the immobilized amount of catalyst m_{Au} within the composite and the apparent kinetic reaction rate constant k_{app} after the first and second catalytic cycle.

Table 14: Summary of the results from the catalytic experiments using Au-loaded PAN/BTA composite nonwoven sheets **c8** and **c9** in the reduction of 4-NP to 4-AP. AuNPs were immobilized within the composite nonwoven sheets by immersion into a PVP@AuNP dispersion. The immobilized Au amount within the composite nonwoven sheets and the leaching of AuNPs were determined by ICP-OES measurements.

Sample	AuNP type	Au amount in composite nonwoven [μg/cm²]	Cycle 1		Cycle 2	
			k_{app} [s^{-1}]	Leaching (%)	k_{app} [s^{-1}]	Leaching (%)
c8	PVP@AuNP (16 nm)	59	0.00070	0.6	0.00045	0.4
c9	PVP@AuNP (16 nm)	52	0.00041	0.5	0.00067	0.3

Besides the composition of the composite nonwoven sheets, the AuNP type (PVP@AuNP vs. *in situ* formed AuNPs), which was immobilized via immersion method or via *in situ* formation, can influence the catalytic activity. For that reason, the following experiments were carried out with composite nonwoven sheets **c8** and **c9**, whereby AuNPs were formed *in situ* within the composite before catalysis. **Figure 129A** and **B** show the conversion-time diagrams and **Figure 129C** and **D** show the plot of -ln(A_t/A_0) against the reaction time for the composites **c8** and **c9**. Here, four catalytic cycles were carried out to verify reusability.

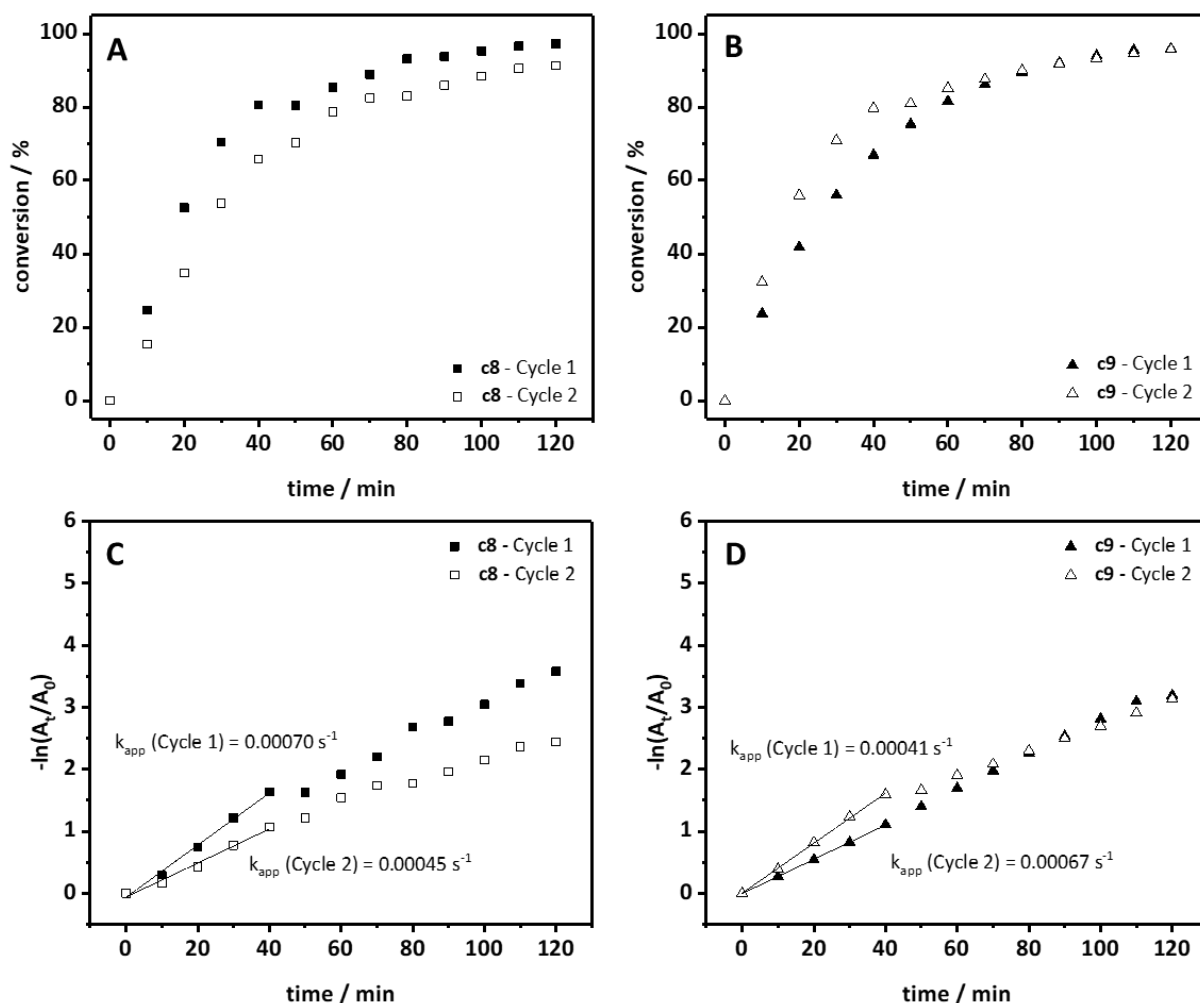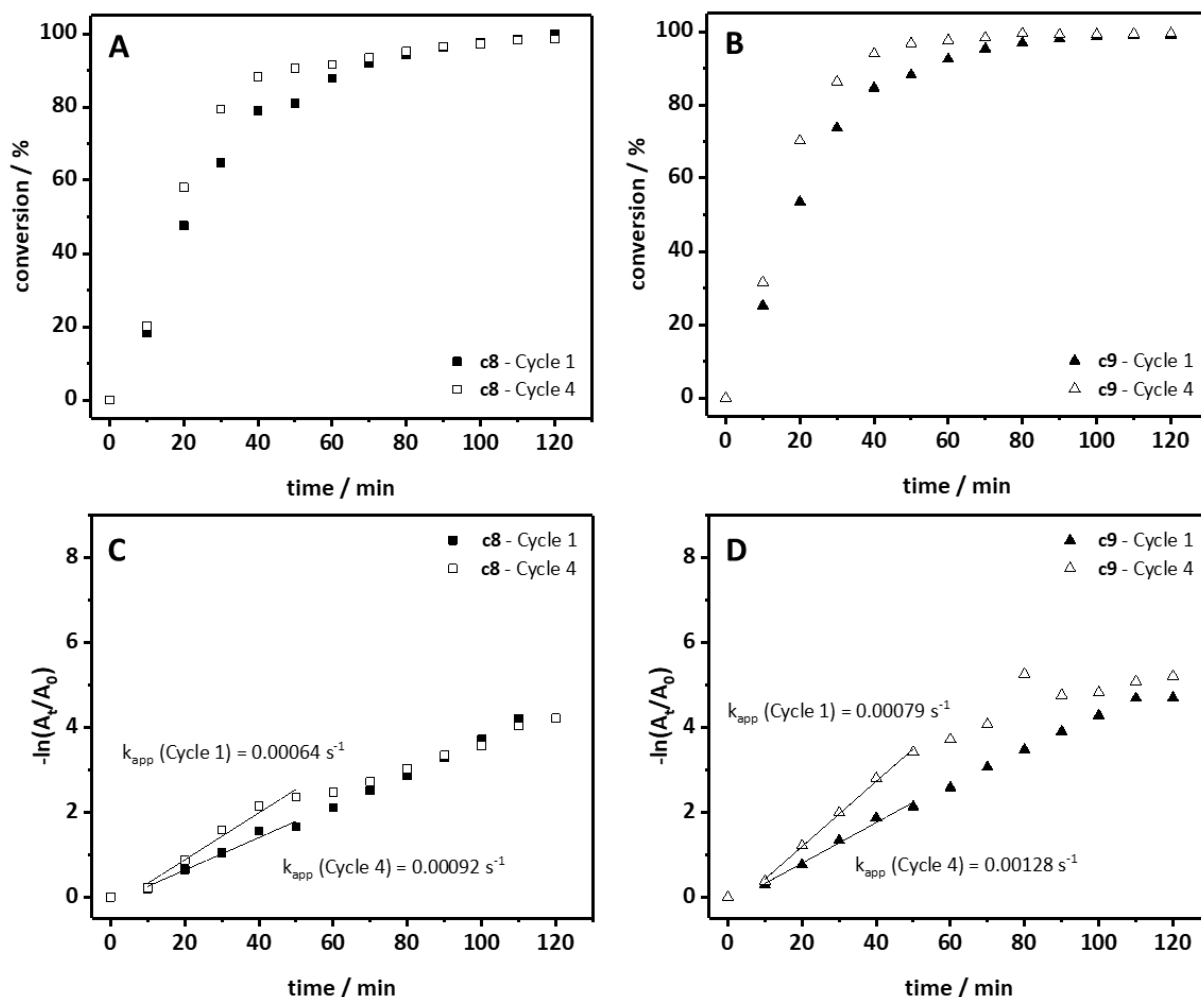**Figure 129:** Catalytic reduction of 4-NP to 4-AP using Au-loaded PAN/BTA composite nonwoven sheets **c8** and **c9** in a discontinuous system followed by *in situ* UV/Vis absorption measurements. AuNP immobilization was carried out by *in situ* formation of AuNPs within the composite nonwoven sheets. Temporal study of the conversion (**A+B**) and -ln(A_t/A_0) (**C+D**) for composites nonwoven sheets **c8** and **c9** after the first and second cycle. Reprinted (adapted) with permission from [138] © 2021 American Chemical Society.

As in the previous catalytic experiments, both composite nonwoven sheets **c8** and **c9** show high catalytic activity. According to **Figure 129A** and **B**, the reaction is almost complete after 2 h (99 % conversion) in both cases. The apparent kinetic reaction rate k_{app} constants are in a range from 0.00079-0.00128 s^{-1}. Compared to **c8**, the apparent kinetic reaction rate constant is slightly higher in the case of **c9** due to the larger amount of AuNPs. Both composite nonwoven sheets **c8** and **c9** could successfully be reused several times. **Figure 129C** and **D** show that k_{app} is maintained or even slightly improved after four cycles of use for composite nonwoven sheets **c8** and **c9**. This effect may possibly be attributed to an increasing wettability of the composite nonwoven sheets with repeating cycles. Consequently, the reactants can diffuse faster into the composite nonwoven sheets. From ICP-OES measurements, it was found that minimal leaching takes place during catalysis. However, these values are extremely low and also within the error range of the ICP-OES measurement instrument. **Table 15** summarizes the results from the catalytic experiments using Au-loaded composite nonwoven

sheets **c8** and **c9** (AuNPs were formed *in situ*), including the immobilized amount of catalyst m_{Au} within the composite and the apparent kinetic reaction rate constant k_{app} after the different catalytic cycles.

Table 15: Summary of the results from the catalytic experiments using Au-loaded PAN/BTA composite nonwoven sheets **c8** and **c9** in the reduction of 4-NP to 4-AP. AuNPs were formed *in situ* within the composite nonwoven sheets. The immobilized Au amount within the composite nonwoven sheets and the leaching of AuNPs were determined by ICP-OES measurements.

Sample	AuNP type	Au amount in composite nonwoven [µg/cm²]	Cycle 1		Cycle 4	
			k_{app} [s⁻¹]	Leaching (%)	k_{app} [s⁻¹]	Leaching (%)
c8	*in situ* AuNP (2.4 nm)	50	0.00064	0.6	0.00092	0.6
c9	*in situ* AuNP (2.4 nm)	58	0.00079	0.7	0.00128	1.2

When comparing the catalytic activity depending on the Au type (PVP@AuNP vs. *in situ* formed AuNPs), it can be seen that composite nonwoven sheets with *in situ* formed AuNPs provide a significantly faster reduction of 4-NP. An influence of the Au amount is ruled out, as it is almost identical for all composites. The improvement in the reduction time is attributed to the significantly smaller diameter of AuNPs (2.4 nm) compared to PVP@AuNPs (16 nm), providing a much larger active surface in the case of the *in situ* formed AuNPs. Another aspect is that composites with AuNPs formed *in situ* do not contain additional ligands that coordinate to the NP surface and can thus hinder the reactants' diffusion to the Au surface.

In order to check the homogeneity of the AuNP distribution and agglomeration of AuNPs within the composite nonwoven sheets before and after catalysis, TEM and small-angle X-ray scattering (SAXS) measurements were performed.

The TEM sample preparation and TEM measurements were performed by Chen Liang (Macromolecular Chemistry II, University of Bayreuth). Since TEM measurements on composite nonwoven sheet **c8** are not possible, the samples of the composite were cut in a blender before and after catalysis so that a fiber dispersion in water was obtained. A droplet of the PAN/BTA fiber dispersion was then applied to a TEM grid and micrographs of the supramolecular **24a** fibers were taken. **Figure 130** shows that no significant change in the morphology and distribution of the Au-loaded supramolecular fibers of **24a** can be observed after the fourth catalytic cycle compared to the initial composite.
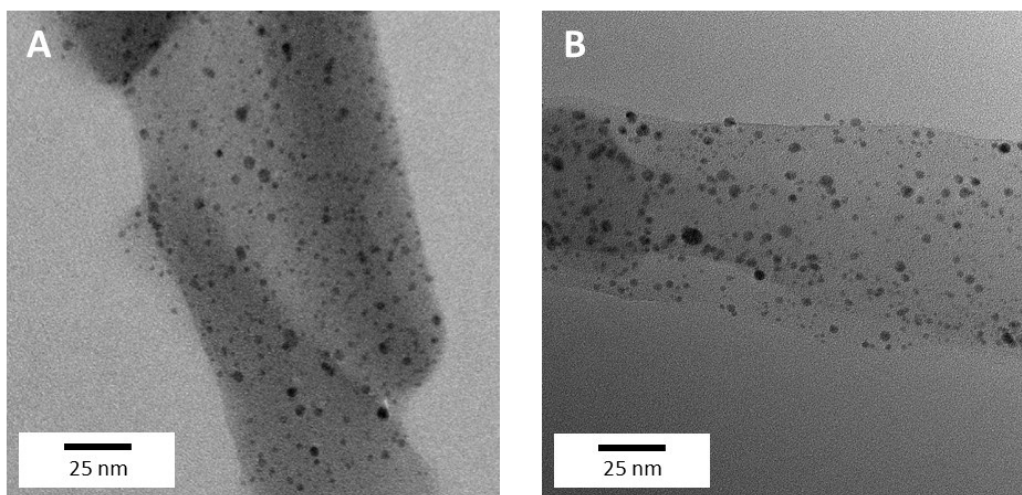
Figure 130: TEM micrographs of supramolecular nanofibers of **24a** with *in situ* formed AuNPs before usage in the catalytic reaction (**A**) and after the fourth catalytic cycle (**B**). Reprinted (adapted) with permission from [138] © 2021 American Chemical Society.

SAXS allows the investigation of the Au-loaded composite nonwoven sheets before and after catalysis with respect to the AuNP distribution and agglomeration without the need to destroy the composite. SAXS experiments and evaluation of the results were carried out by Sabine Rosenfeld (Physical Chemistry I, University of Bayreuth). SAXS measurements were performed on neat composite nonwoven sheet **c8** and composite nonwoven sheet **c8** with *in situ* formed AuNPs before and after catalysis.

After placing the composite nonwoven sheet into the sample holder, SAXS measurements were carried out at ambient conditions using a Double Ganesha AIR system (SAXSLAB). Monochromatic radiation with a wavelength of 1.54 Å was produced by rotating a Cu anode (MicroMax 007 HF, Rigaku Corporation). The data were acquired with a position-sensitive detector (PILATUS 300 K, Dectris), which was placed at different distances from the sample to cover a wide range of scattering vectors q, where q is given as $q = |\vec{q}| = \frac{4\pi}{\lambda} \cdot \sin\left(\frac{\theta}{2}\right)$ with λ representing the wavelength of the incident beam and ϑ the scattering angle. 1D-intensity profiles of $I(q)$ vs. q were obtained by radial averaging. Background correction was carried out by subtracting the signal without a sample in the air.

Figure 131 shows the SAXS intensities of the neat and Au-loaded composite nonwoven sheet **c8** before and after the catalysis, as well as the scattering contribution of neat AuNPs after subtracting the intensity profile of the Au-loaded composite nonwoven sheet **c8.**
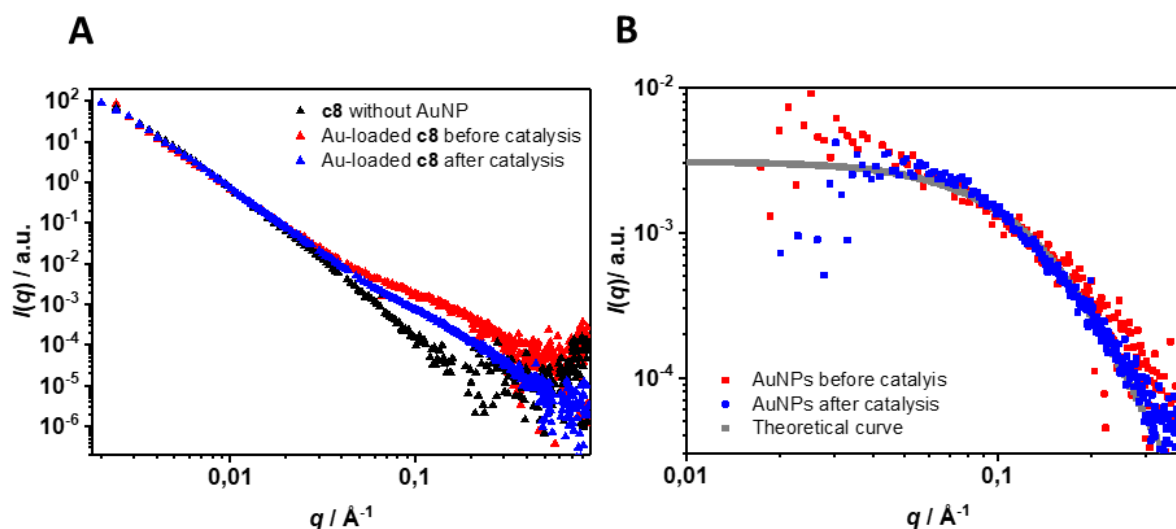
Figure 131: (**A**) SAXS intensities of composite nonwoven sheets **c8** without (black triangles) and with *in situ* formed AuNPs before (red triangles) and after (blue triangles) first catalytic cycle. The SAXS intensities were normalized to the same forward scattering. (**B**) The scattering contribution of AuNPs alone before (red squares) and after (blue squares) the first catalytic cycle was determined by subtraction of the intensity of the corresponding composite nonwoven sheet **c8** without AuNPs. The fluctuation of the data points for q < 0.04 Å^{-1} can be reasoned by an uncertainty in the absolute scale during the composite subtraction step. The experimental data were described with the model of Gaussian-distributed spheres with a homogenous electron density. The theoretical intensity of spheres with a diameter of d$_{SAXS}$ of 2.4 ± 0.8 nm agrees very well. Reprinted (adapted) with permission from [138] © 2021 American Chemical Society.

Before comparing the composite nonwoven sheet **c8** before and after catalysis, the SAXS intensities, which were normalized to the same forward scattering, of the neat composite and the Au-loaded composite nonwoven sheet **c8** are discussed. According to **Figure 131A**, the AuNP-loaded composite nonwoven sheet **c8** exhibits similar features as the neat composite nonwoven sheet **c8** for q < 0.04 Å^{-1} but differs for q > 0.04 Å^{-1}. For q < 0.04 Å^{-1}, a power law of ~q$^{-3.3}$ was determined as expected for mesoscale porous materials, such as non-oriented fibers or nonwovens. For higher q values (q > 0.04 Å^{-1}), an additional scattering is observed for the AuNP-loaded composite nonwoven sheet **c8** due to the presence of the small AuNPs on the **24a** fiber surface. After subtracting the intensity profile of composite nonwoven sheet **c8** from the AuNP-loaded composite nonwoven sheet **c8** and normalizing again to the same forward scattering, more information can be obtained about the AuNPs alone (**Figure 131B**). The scattering intensity of the AuNPs alone is described very well by a model of spheres with a homogenous x-ray contrast. No significant deviation from the theoretical curve, particularly at very small q values, is indicative of non-agglomerated AuNP species. Based on this model, an average diameter of d$_{SAXS}$ of 2.4 ± 0.8 nm of Gaussian-distributed spheres was determined. This value is in very good agreement with the findings of the TEM analysis, as shown in **Figure 130** (see also **chapter 5.3**).

The SAXS intensity profile of the Au-loaded composite nonwoven sheet **c8** after catalysis is quite similar to the composite before catalysis at small q values, whereas some deviation in the larger q regime for

the AuNPs can be found (**Figure 131A**). ICP-OES measurements of the reaction solutions after the respective catalytic cycle showed no significant loss of AuNPs during catalysis. Therefore, the SAXS intensity profiles were normalized to the same Au amount and the same forward scattering (**Figure 131B**). Based on this assumption, the SAXS intensity patterns before and after the catalytic reaction agree very well with the theoretical scattering of the AuNPs alone, indicating that the average size of AuNPs remains the same and no agglomeration of AuNP takes place during the catalytic reaction. For that reason, it was assumed that the deviation of the SAXS intensities before and after the catalytic reaction resulted from a small variation or reorganization of the supramolecular or polymer fibers in the composite nonwoven sheet.

Table 16 shows the experimental parameters and catalytic data of our composite nonwoven sheet **c8** compared to similar catalyst systems found in literature.

Table 16: Comparison of the experimental parameters for the reduction of 4-NP in the presence of NaBH$_4$ at room temperature of our work with reported parameters of other catalyst systems, which can be found in literature.[88,142–146]

Literature	Support	Catalyst	k_{app} (s^{-1})	Conditions				
				d_{AuNP} (nm)	Au amount (µg)	4-NP (vol/conc.)	NaBH$_4$ (vol/conc.)	Mass of composite (mg)
Our work	PAN/BTA composite **c8**	AuNPs	0.0009	2.4 ± 0.8	50	1.5 mL/ 0.1 mM	1.5 mL/ 0.1 M	1.8
[94]	Aminated electrospun PAN membrane	AuNPs	0.0005	7.5	-	50 mL/ 1.73 mM	2 mL/ 0.17 M	10
[146]	PEI/PVA electrospun nanofiber mat	Au/Ag NPs	0.0011[a]	4.9 ± 1.8	146.4[b]	0.6 mL/ 10 mM	0.6 mL/ 10 M	18
[147]	PCL/PEO electrospun composite	AuNPs	0.0060	5-10	-	10 mL/ 5 mM	20 mL/ 0.1 M	10
[148]	Cellulose film	AuNPs	0.0006	10-20	-	5 mL/ 3 mM	5 mL/ 0.3 M	10 mg of cellulose film
[149]	FeSO$_4$@SiO$_2$-NH$_2$	AuNPs	0.0078	6.7 ± 1.6	-	0.1 mL/ 5 mM	1 mL/ 0.2 M	3 mg of FeSO$_4$@SiO$_2$-NH$_2$-Au
[150]	Polymeric monolith	AuNPs	0.019	3.5	-	10 mL/ 0.5 mM	1 mL/ 1 M	1 mg of monolith

[a] not specified, approximately determined from the graph; [b] bimetallic NPs, 96.06 µg Au and 50.37 µg Ag.

A direct comparison of the catalytic activity with other catalytic systems is difficult since not all test parameters are always given or differ significantly from our system. Altogether the apparent kinetic reaction rate constant of the composite nonwoven sheets **c8** and **c9** are in a similar range compared to other Au-loaded nonwoven support systems from literature (**Table 16** [94,146-147]).

196

6.2 Catalysis in a continuous system

Various continuous flow reactors are established for catalytic reactions and are of great significance from a technical point of view compared to a discontinuous system. In particular, the high throughput and conversion render continuous flow highly appealing. Moreover, with the help of continuous flow-through systems, in which the reaction solution is pumped through a catalytically active membrane instead of being immersed, the catalytic activity can be significantly increased due to the higher mass transfer. So far, only a few continuous systems for the reduction of 4-NP can be found in literature. [147-149] Since the composite nonwoven sheets **c8** and **c9** have already proven their applicability in the discontinuous system, these findings should be transferred into a continuous flow system. To demonstrate the proof-of-concept, composite nonwoven sheet **c8** was selected, exemplarily.

For this purpose, a custom-made apparatus, shown in **Figure 132**, was developed and used.
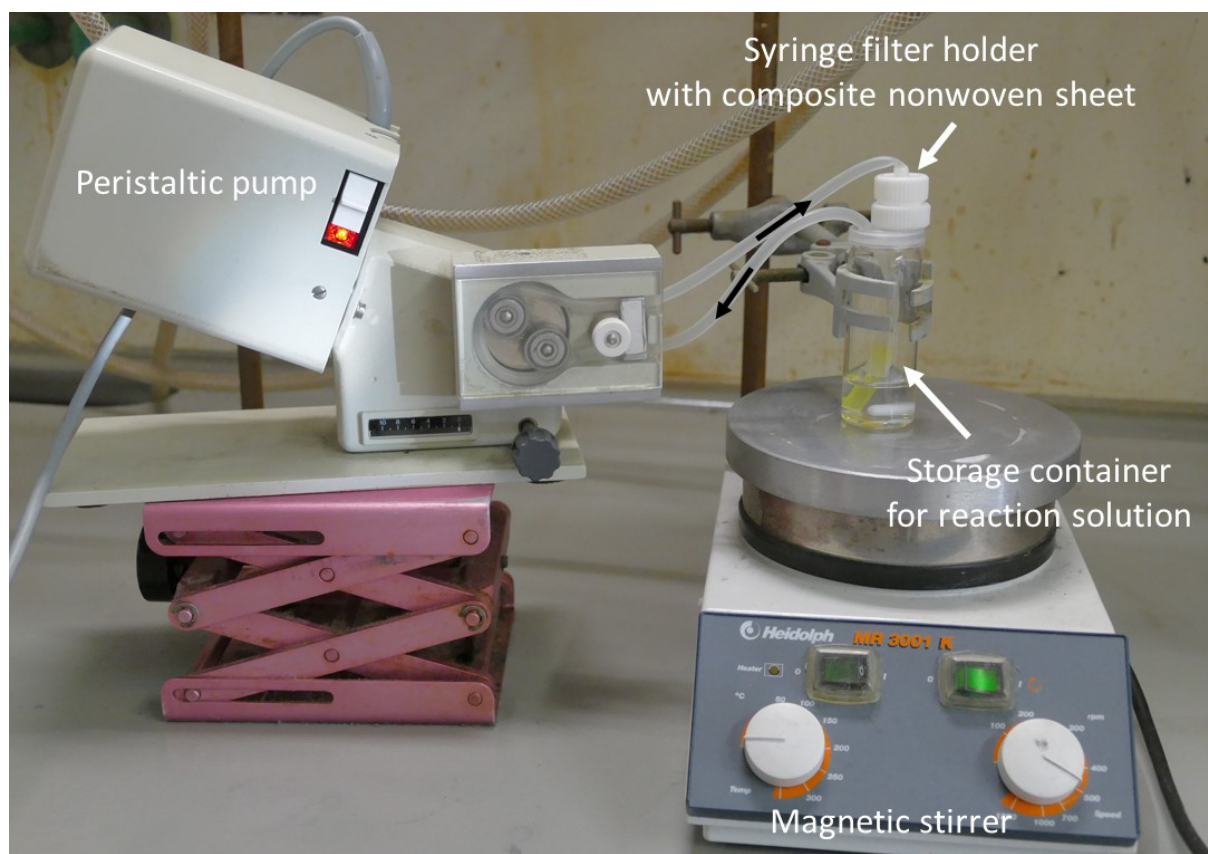
Figure 132: Custom-made apparatus for carrying out the reduction of 4-NP to 4-AP in a continuous flow-type reactor. The reaction solution is stored in a glass container and pumped by means of the peristaltic pump through the syringe filter holder, which is equipped with the Au-loaded composite nonwoven sheet. The flow direction of the reaction solution is indicated by the black arrows.

A round piece of the composite nonwoven sheet **c8** loaded with *in situ* formed AuNPs was cut off and placed in a reusable PTFE syringe filter holder. The sheet was placed on a PTFE-based washer of the PTFE syringe filter holder. The peristaltic pump allows different pump speed levels (0-5). A corresponding flow rate in mL/min was determined by pumping water through the setup for 10 s at each pump speed level, collecting and weighing the liquid and subsequently calculating the flow rate. It was found that the flow rate at level 0 corresponds to $\sim$ 36 mL/min, at level 1 $\sim$ 54 mL/min and at level 2 $\sim$ 68 mL/min. The tests also showed that a flow rate higher than 68 mL/min leads to a too high-pressure build-up resulting in the destruction of the composite nonwoven sheet.

In order to perform catalysis in a continuous flow mode, 3 mL of a 0.1 mM aqueous 4-NP solution and 3 mL of a 100 mM aqueous $NaBH_4$ solution were added to the storage container. The solution in the storage container was stirred continuously at 500 rpm. The peristaltic pump was used to pump the solution through the syringe filter at different flow rates below 68 mL/min for 20 min. To control the progress of the reaction, samples were taken at intervals of 5 min and analyzed by UV/Vis spectroscopy. The Au amount immobilized in composite nonwoven sheet **c8** is similar for all experiments with a Au amount of 55-56 µg. **Figure 133** shows the conversion-time diagrams and the plot of -ln(A_t/A_0) against the reaction time for the composite nonwoven sheet **c8** at three different flow rates.
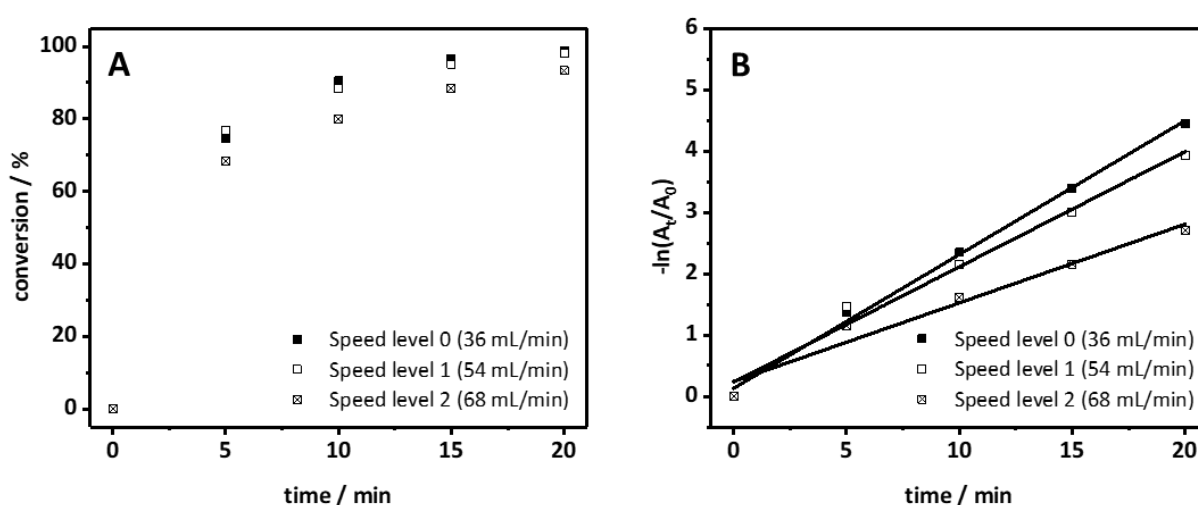
Figure 133: Catalytic reduction of 4-NP to 4-AP using Au-loaded PAN/BTA composite nonwoven sheets **c8** in a continuous flow reaction system followed by UV/Vis absorption measurements. AuNP immobilization (each time 55-56 µg Au) was carried out by *in situ* formation of AuNPs within composite nonwoven sheet **c8**. Temporal study of the conversion (**A**) and -ln(A_t/A_0) (**B**) for composite nonwoven sheet **c8** after the first catalytic cycle in dependence on three different flow rates.

Figure 133A shows that within a very short time of 5 min, a conversion of 60-70 % is already achieved using composite nonwoven sheet **c8** at the three different flow rates. After 20 min, 4-NP was completely reduced to 4-AP at a flow rate of 36 mL/min and 56 mL/min, respectively. The conversion at the highest flow rate of 68 mL/min is slightly lower, with 93 % after 20 min. When comparing the

apparent kinetic reaction rate constants at the different flow rates, it is noticeable that the fastest reduction of 4-NP takes place with the lowest flow rate. The difference of k_{app} at a flow rate of 36 mL/min (k_{app} = 0.00364 s^{-1}) and 56 mL/min (k_{app} = 0.00313 s^{-1}) is only small. In contrast, k_{app} is significantly lower with 0.00214 s^{-1} at the highest flow rate of 68 mL/min. Consequently, these data suggest that the slower the flow rate, the longer the contact time of the reactants with the active AuNP surface resulting in a fast reduction of 4-NP to 4-AP. ICP-OES measurements revealed only minimal initial leaching of AuNPs during catalysis, which might be attributed to the cutting process of the composite nonwoven sheet resulting in a detachment of single supramolecular **24a** fibers. Composite nonwoven sheet **c8** showed very good shape persistence to be used for further catalysis cycles. **Table 17** summarizes the three catalytic reactions with three different flow rates.

Table 17: Summary of the catalytic reduction of 4-NP to 4-AP using the Au-loaded composite nonwoven sheet **c8** in a continuous flow reaction system at three different flow rates. The immobilized Au amount was determined by ICP-OES measurements.

Sample	Flow rate [ml/min]	m_{AuNP} [µg]	k_{app} [s^{-1}]
	36	56	0.00364
c8	54	55	0.00313
	68	55	0.00214

Compared to the discontinuous system, the apparent kinetic reaction rate constant k_{app} is about four times higher with 0.00364 s^{-1} in the continuous system using the same composite nonwoven sheet **c8** with an identical Au amount and AuNPs size at a flow rate of 36 mL/min. Here, it should be noted that even a larger volume of the reaction solution was used in the continuous system than in the discontinuous system, indicating that the performance of the Au-loaded composite nonwoven sheet is even more effective in the continuous system. Full conversion was achieved in the continuous system after only 20 min at a flow rate of 36 mL/min, whereas in the discontinuous system, full conversion took more than 100 min. In a discontinuous process, the diffusion of the reactants is a limiting factor, but not the contact time of the reactants with the active Au surface. However, the latter plays an essential role in the continuous process since a too-fast flow rate significantly reduces the contact time of the reactants with the active Au surface. The diffusion of the reactants in the continuous process is assumed to be notably improved compared to the discontinuous system.

Only a few continuous flow reactor systems for the reduction of 4-NP using AuNPs are described in literature rendering a comprehensive comparison not applicable. Moreover, not all-important data about the catalyst and process conditions are available for appropriate comparison with our system. A noteworthy example, besides a Au-loaded carbon nanotube membrane, is a packed bed reactor composed of macroporous polymer beads to support AuNPs immobilized in an agarose gel. Other

groups reported used cigarette filters with immobilized AuNPs or Au-loaded wood for the 4-NP reduction in continuous flow reaction mode.[148–151] They demonstrated that in most cases, only very low flow rates could be applied or are necessary to achieve full conversion of 4-NP to 4-AP. The significantly lower flow rates increase the contact time of the reactants with the catalytically active Au surface, resulting in a faster reduction of 4-NP than with the Au-loaded composite nonwoven sheets in some systems reported in literature. With this proof-of-concept, it was clearly demonstrated that the Au-loaded composite nonwoven sheet **c8** is very well suited for use in a continuous flow reactor system and enables a significantly faster reduction of 4-NP than in a discontinuous system.

6.3 Conclusion

The functionality of the Au-loaded composite nonwoven sheets was successfully demonstrated in the catalytic reduction of 4-NP to 4-AP in both a discontinuous and continuous system. Both composite nonwoven sheets **c8** and **c9** with PVP@AuNPs and *in situ* formed AuNPs showed high catalytic activity. The different compositions of the composite nonwoven sheets did not significantly affect the catalytic performance and the different apparent kinetic reaction rate constants most likely came from the different Au amounts within the composites. Due to the small size of the *in situ* formed AuNPs and the absence of additional stabilizing ligands, higher apparent kinetic reaction rates were obtained with composite loaded with *in situ* AuNPs than with PVP@AuNPs. Both Au-loaded composite nonwoven sheets **c8** and **c9** were successfully reused several times without loss of catalytic activity. TEM and SAXS measurements showed that the AuNPs are homogenously distributed before and after catalysis and no agglomeration of AuNPs takes place during catalysis. In addition, no or minimal leaching was detected by ICP-OES measurements, which can be attributed to single Au-loaded supramolecular fibers, which disintegrate from the edges of the composite due to the cutting process of the composite nonwoven sheet before.

In addition to the fundamental investigations of the catalytic performance of the composite nonwoven sheets in a discontinuous system, the use of the composites in a custom-made continuous flow reactor system is much more relevant from a technical point of view and was successfully demonstrated in a proof-of-concept. In contrast to the discontinuous system, significantly faster conversion of 4-NP could be achieved, which may be attributed to a better diffusion of reactants to the active Au surface due to the flow of the reaction solution while maintaining a sufficient contact time. It was also shown that faster conversion of 4-NP is achieved with lower flow rates. Thus, a compromise must be found between the highest possible throughput and fast conversion of 4-NP. In conclusion, the Au-loaded composite nonwoven sheets of PAN short fibers and supramolecular **24a** fibers are highly suitable for the reduction of 4-NP. Therefore, it is anticipated that the catalytic performance of these promising composite nonwoven sheets can be further optimized in future studies, especially in a continuous flow reactor approach.

7 Experimental Part

7.1 Materials and methods

The synthesis of the individual intermediates and pyridine-/terpyridine-substituted BTAs outlined in this thesis was performed by myself. In distinct cases, the synthetic procedures were supported by Sandra Ganzleben and Jutta Failner, which are acknowledged individually. Characterization, analysis and evaluation were performed by myself.

All chemicals were commercially available and used without further purification, except for chloroform, dichloromethane and hexane, which were purified by distillation or according to standard procedures. A list of suppliers of all chemicals and solvents is provided below.

Name (abbreviation)	CAS number	supplier, purity
1-Propanol (NPA)	71-23-8	Roth, 99.5 %
1,3,5-Benzenetricarboxylic acid chloride	4422-95-1	TCI, > 98 %
2-butanone (MEK)	78-93-3	Roth, 99.5 %
2-Propanol (IPA)	67-63-0	Roth, 99.5 %
2-Ethyl-1-hexylamin	104-75-6	abcr, 98 %
3-Amino-1-propanol	156-87-6	Aldrich, > 99 %
3,5-Dinitrobenzoyl chloride	99-33-2	abcr, 98 %
4-Aminopyridine	504-24-5	abcr, 98 %
4-(Aminomethyl)pyridine	3731-53-1	Aldrich, 98 %
4-(2-Aminoethyl)pyridine	13258-63-4	abcr, 95 %
4'-Chloro-2,2':6',2''-terpyridine	128143-89-5	TCI, > 98 %
4-Nitrophenol	100-02-7	Aldrich, 98 %
4-Amino-1-butanol	13325-10-5	Aldrich, 98 %
5-Amino-1-pentanol	2508-29-4	Aldrich, 95 %
5-Nitroisophthalic acid	618-88-2	Aldrich, 98 %
6-Amino-1-hexanol	156-87-6	Aldrich, 97 %
Ammonia solution	1336-21-6	VWR, 25 %
Dimethyl sulfoxide (DMSO, anhydrous)	67-68-5	Aldrich, ≥ 99.9 %

Cyclohexylamine	108-91-8	Aldrich, 99.9 %
Dichloromethane (DCM, anhydrous)	75-09-2	Aldrich, $\geq$ 99.8 %
Dichloromethane (DCM)	75-09-2	technical grade
Dimethylformamide (DMF)	68-12-2	technical grade
Dimethylformamide (DMF, extra dry)	68-12-2	Acros, 99.8 %
Ethanol (EtOH)	64-17-5	VWR, $\geq$ 99.8 %
Ethanolamine	141-43-5	Aldrich, > 98 %
Hexane	110-54-3	technical grade
Isonicotinic acid	55-22-1	Acros, 99 %
Methanol (MeOH)	67-56-1	Fisher, $\geq$ 99.9 %
Oxalyl chloride	79-37-8	Acros, 98 %
Palladium on activated carbon (10 %)	-	Aldrich
Potassium hydroxide (KOH, powder)	1310-58-3	Fluka, $\geq$ 85 %
Pyridine (anhydrous)	110-86-1	abcr, 99.5 %
Sodium borohydrate ($NaBH_4$)	16940-66-2	abcr, 98 %
Sodium hydrogen carbonate	144-55-8	abcr, 99 %
Sodium sulfate (Na_2SO_4, anhydrous)	7757-82-6	Bernd Kraft, 99 %
Tert-butylamine	75-64-9	Aldrich, 99,5 %
Tetrahydrofuran (THF, anhydrous)	109-99-9	Aldrich, $\geq$ 99.5 %
Triethylamine	121-44-8	Aldrich, $\geq$ 99.5 %

Milli-Q® water (demineralized and purified with a Millipore-Q Plus purification system; column: QPAK®2; electrical conductivity: 18.2 MΩ·cm)

Methods

^{1}H-NMR Spectroscopy:

^{1}H-NMR spectra were recorded on a Bruker Avance 300 spectrometer (300 MHz) at RT. Deuterated dimethyl sulfoxide (DMSO-d6) or chloroform (CDCl$_3$) were used as solvents. All spectra were evaluated with the software MestReNova (Mestrelab Research S.L, version 14.2.0-26256). All chemical shifts are reported in ppm (δ) and referenced to the chemical shifts of the solvents (DMSO-d$_6$ = 2.50 ppm or CDCl$_3$ = 7.26 ppm). Multiplicities are indicated as s (singlet), d (doublet), t (triplet), q (quartet) and m (multiplet).

Mass Spectrometry

Mass spectrometry was performed on a Finnigan MAT 8500 spectrometer from Thermo Fisher Scientific using electron spray ionization (EI). The mass spectra of all terpyridine-substituted BTAs were recorded using a Varian 1200L from Agilent with triple quadrupole (Q3). In this case, the samples were dissolved in acetonitrile and directly injected into the ionization source.

Fourier-Transform Infrared (FT-IR) Spectroscopy

Fourier transform infrared (FT-IR) spectra were recorded on a PerkinElmer Spectrum 100 FT-IR equipped with a Universal ATR accessory at a resolution of 4 cm^{-1}. For each measurement, four scans were performed in a wavenumber range between 4000 cm^{-1} and 650 cm^{-1}.

Thermogravimetric Analysis (TGA)

Thermogravimetric analysis and simultaneous differential thermal analysis (SDTA) were performed on a Mettler TGA/SDTA851e. The measurements were carried out under a nitrogen atmosphere in a temperature range from 30-700 °C at a scan rate of 10 K min^{-1}.

Differential Scanning Calorimetry (DSC)

DSC measurements were performed on a Mettler DSC/SDTA 821e with a scan rate of 10 K min^{-1}. The investigated upper temperature limit was selected based on the previously performed TGA measurement. In most cases, this upper temperature limit is close to the start weight loss due to decomposition or sublimation. A small amount of the sample was weighed into a high-pressure pan at ambient conditions. Two heating and cooling cycles were performed within each measurement.

UV/Vis Spectroscopy

UV/Vis spectra were recorded using a Jasco Spectrometer V-670. For the measurement of samples containing a dispersion of AuNPs, PS disposable cuvettes (d = 10 mm) were used. Quartz cuvettes (d = 10 mm) were used for the reduction of 4-NP. Baseline correction was performed by measuring a blank sample using Milli-Q® water.

Inductively Coupled Plasma – Optical Emission Spectrometry (ICP-OES)

The ICP-OES measurements were carried out using a Perkin Elmer Avio 200 equipped with an S10 autosampler, Echelle polychromator, Argon humidifier and a DBI-CCD detector. The samples were calibrated against a single Au standard (Perkin Elmer Pure, Gold 1000 mg L^{-1} in 10 % HCl) with concentrations of 0.05 mg L^{-1}, 0.1 mg L^{-1}, 0.5 mg L^{-1}, 1 mg L^{-1} and 10 mg L^{-1}, respectively. Each sample was evaporated completely at 70 °C, dissolved in 0.5 mL aqua regia and diluted with 9.5 mL of Milli-Q® water.

Scanning Electron Microscopy (SEM)

SEM micrographs were recorded using a FEI Quanta FEG 250 at an acceleration voltage of 5 kV in low vacuum mode (40 Pa). Before measurement, all samples were sputter-coated in case of supramolecular nanofibers with 1.3 nm and in case of nonwovens with 2.0 nm thick platinum layer utilizing a Cressington sputter coater (208HR, 40 mA). Samples with AuNPs were used as prepared without sputter-coating. For detection, a low-vacuum secondary electron (LFD) detector was used. The average fiber diameter was determined by measuring at least 100 fibers in SEM micrographs using *ImageJ.* For cross-section imaging of a composite nonwoven, a sample was frozen in water using liquid nitrogen and then cutting it. SEM micrographs were obtained using a Zeiss Leo 1530 with a Schottky field-emission cathode at an acceleration voltage of 3 kV.

Energy-Dispersive X-ray Spectroscopy (EDX)

EDX measurements were performed on a Zeiss Ultra plus with Ultra Dry-EDX detector (30 mm², Thermo Fisher Scientific NS7) at an acceleration voltage of 10 kV. The samples were sputtered with carbon before measurement.

Transmission Electron Microscopy (TEM)

TEM micrographs were recorded on a Jeol JEM-2200FS at an acceleration voltage of 200 kV. Before measurement, one droplet of a Au-loaded supramolecular BTA fiber dispersion or PAN/BTA short fiber dispersion with immobilized AuNPs was placed on a carbon-coated copper grid (Carbon Support Film, 200 mesh, copper). The supernatant solvent was removed by a filter paper. The average AuNP diameter was determined by measuring at least 100 AuNPs in TEM micrographs using *ImageJ.*

Porometry

The pore size of the prepared composite nonwovens and reference nonwovens was determined with a PSM 165/H (Dresden, Germany). A sample holder with a measurement area of 4.15 cm² and Topor as test liquid (density: 1.9 g cm^{-3}; surface tension = 16.0 mN m^{-1}) were used. At least two measurements were carried out for each sample and averaged.

Experimental procedure

Preparation of electrospun PAN short fiber dispersions

First, randomly oriented PAN fibers were obtained via electrospinning of a 19 wt% PAN solution in DMF. The fibers were collected on a rotating collector (diameter: 16 cm, length: 45 cm, rotating speed: 65 rpm) covered with baking paper at a distance of 25 cm from the needle. For homogenous fiber deposition, a voltage of + 20.0 kV was set to the needle and - 0.9 kV to the collector. The flow rate of the PAN solution was 0.5 mL/h. All experiments were conducted at a temperature of 20-22 °C and relative humidity of around 17-22 %. Finally, short polymer fibers were prepared by putting the electrospun PAN fibers into water (c = 0.05 wt%) and cutting them in a mixer (Vital mixer basic, Gastroback, 21.000 rpm) for a short time until a homogeneous dispersion was obtained.

*Fabrication of PAN/BTA **24a** composite nonwoven sheets*

838 mL of the electrospun PAN short fiber dispersion with a concentration of 0.05 wt% in H_2O were mixed with 419 mL of a freshly prepared solution of **24a** in isopropanol/H_2O 9:1 (w/w) at room temperature with a concentration of 0.01 wt%, 0.05 wt% and 0.1 wt% in case of route A or with a fiber dispersion of 0.05 wt% **24a** in isopropanol/H_2O 9:1 (w/w) in case of route B. Subsequently, a solvent mixture of about 2.5 L (1742 mL H_2O and 754 mL isopropanol) was added to the above dispersion mixture resulting in a total volume of about 3.7 L. The composite nonwovens were fabricated using a HAAGE sheet former BB equipped with a sheet forming column and vacuum pump. To keep a slower depositing of the fibers, four layers of cellulose filtration paper with a diameter of 20 cm were placed between the sieve frame and the sheet support sieve. The fibers were collected on a round stainless steel mesh (325 mesh, wire thickness of 36 µm), which was placed on top of the sheet forming sieve frame. The total amount of the 3.7 L fiber dispersion mixture was shaken for a few seconds and then poured into the sheet forming column, additionally homogenized for 10 s with compressed air and filtered off to obtain the composite nonwovens. The prepared composite nonwovens were removed and finally dried at 60 °C for 10 min under vacuum (900 mbar). The thicknesses of the composite nonwovens were determined by a screw micrometer in at least five positions.

7.2 Synthesis and characterization

7.2.1 Benzenetrisamides with three pyridine substituents

The syntheses of the three BTAs with three pyridine substituents **3a-c** were performed by Sandra Ganzleben and Jutta Failner. For the general reaction scheme, see **Scheme 1**.

Synthesis of BTA 3a (N^1,N^3,N^5-Tri(pyridin-4-yl)benzene-1,3,5-tricarboxamide)
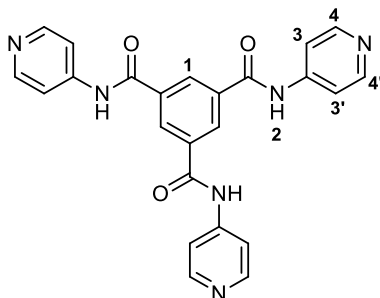
20.0 g (75 mmol) of 1,3,5-benzenetricarboxylic acid chloride were added at 0 °C under argon atmosphere to a mixture of 500 mL of dried THF, 50 mL of triethylamine and 35.5 g (376 mmol) of 4-aminopyridine. The mixture was stirred overnight under reflux. After cooling to RT, the mixture was filtered and the residue was stirred with brine. The precipitate was filtered off, boiled twice in MeOH and recrystallized from DMSO/H_2O. Drying in vacuo yielded 28.2 g (64 mmol, 85 %) of **3a** as a white solid.

^{1}H NMR (DMSO-d_6, δ in ppm): 10.96 (s, 3H, H_2), 8.76 (s, 3H, H_1), 8.54 (m, 6H, $H_{4,4'}$), 7.83 (m, 6H, $H_{3,3'}$)

IR (ṽ in cm^{-1}): 3160, 3075, 1688, 1589, 1509, 1415, 1329

MS (in m/z): 438 [M$^+$]

TGA: 5 % weight loss at 371 °C

Melting temperature: 367 °C (SDTA), - (DSC)

Synthesis of BTA 3b ($N^1,N^3,N^{5'}$-Tris(pyridin-4-ylmethyl)benzene-1,3,5-tricarboxamide)
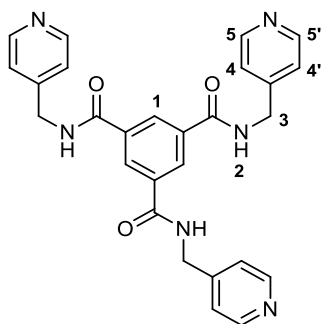
3.00 g (11 mmol) of 1,3,5-benzenetricarboxylic acid chloride were added at 0 °C under argon atmosphere to a mixture of 100 mL of dried THF, 10 mL of triethylamine and 4.0 g (37 mmol) of 4-(aminomethyl)pyridine. The mixture was stirred for two days under reflux. After cooling to RT, the mixture was concentrated and the residue dissolved in 50 mL MeOH. Afterwards, water was added until a yellowish solid precipitated. The crude product was recrystallized twice in MeOH and subsequently boiled in 100 mL of acetone, yielding 3.0 g (6 mmol, 70 %) of **3b** as a white solid.

^{1}H NMR (DMSO-d$_6$, δ in ppm): 9.43 (t, 3H, H$_2$), 8.57 (s, 3H, H$_1$), 8.52 (m, 6H, H$_{5,5'}$), 7.34 (m, 6H, H$_{4,4'}$), 4.54 (d, 6H, H$_3$)

IR (ṽ in cm^{-1}): 3305, 3025, 1645, 1602, 1547, 1516, 1416, 1370

MS (in m/z): 480 [M$^+$]

TGA: 5 % weight loss at 364 °C

Melting temperature: 269 °C (SDTA), 264 °C (DSC)

Synthesis of BTA 3c (*N¹,N³,N⁵*-Tris(2-pyridin-4-yl)ethyl)benzene-1,3,5-tricarboxamide)
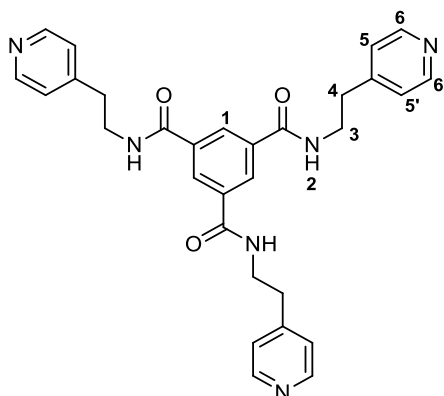
3.2 g (12 mmol) of 1,3,5-benzenetricarboxylic acid chloride were added at 0 °C under argon atmosphere to a mixture of 100 mL of dried THF, 10 mL of triethylamine and 4.8 g (39 mmol) of 4-(2-aminoethyl)pyridine. The mixture was stirred overnight under reflux. After cooling to RT, the solvent was evaporated and the concentrated organic mixture was stirred in water overnight. The organic solvent was decanted and the residue was dried. For further purification, the product was boiled in acetone, recrystallized in DMF and finally boiled in hexane (80 mL), yielding 25.0 g (5 mmol, 40 %) of **3c** as yellow solid.

^{1}H NMR (DMSO-d$_6$, δ in ppm): 8.82 (t, 3H, H$_2$) 8.47 (m, 6H, H$_{6,6'}$), 8.34 (s, 3H, H$_1$), 7.28 (m, 6H, H$_{5,5'}$), 3.56 (q, 6H, H$_3$), 2.89 (m, 6H, H$_4$)

IR (ṽ in cm^{-1}): 3258, 1659, 1587, 1521, 1479, 1418, 1326

MS (in m/z): 522 [M$^+$]

TGA: 5 % weight loss at 297 °C

Melting temperature: 204 °C (SDTA), 193 °C and 200 °C (DSC)

7.2.2 Benzenetrisamides with two pyridine substituents

The syntheses of the three BTAs with two pyridine substituents **9a**, **9b** and **9c** were performed in four steps, respectively. The syntheses were performed by Sandra Ganzleben und Jutta Failner. For the general reaction scheme, see **Scheme 2**.

Synthesis of BTA 9a (*N,N'*-(5-((*Tert*-butyl)carbamoyl)-1,3-phenylene)diisonicotinamide)
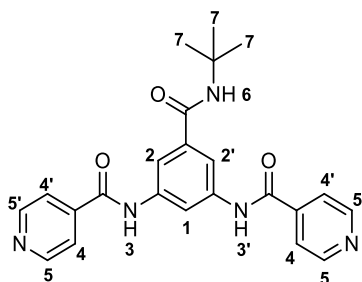
3.5 g (48 mmol) of *tert*-butylamine were added dropwise under argon atmosphere and ice-cooling to a mixture of 10 g (43 mmol) of 3,5-dinitrobenzoyl chloride, 3.7 g (48 mmol) of pyridine and 150 mL of dried THF. The reaction mixture was stirred for 2 h at RT and then precipitated in 1.5 L of ice water. After stirring overnight, the product was filtered off and dried, yielding 7.7 g (29 mmol, 67 %) of *N*-(*tert*-butyl)-3,5-dinitrobenzamide (**6a**).

^{1}H NMR (DMSO-d$_6$, δ in ppm): 9.11 (t, 1H, H$_{NH}$), 9.05 (d, 2H, H$_{aromat}$), 8.94 (t, 1H, H$_{aromat}$), 3.26 (t, 2H, H$_{N-CH2}$), 1.64-1.52 (s, 1H, H$_{CH}$), 1.42-1.20 (m, 8H, H$_{CH2}$), 0.91-0.82 (m, 6H, H$_{CH3}$)

7.7 g (29 mmol) of **6a** were placed inside the hydrogenation reactor together with 300 mL of THF, 30 mL of EtOH and 0.3 g of a suspension of palladium on activated carbon (10 %). The hydrogenation was performed at 35 °C and a pressure of 5 bar overnight under stirring. Palladium on activated carbon was filtered off via AloxN. The product was then concentrated and dried under high vacuum yielding 5.1 g (25 mmol, 85 %) of 3,5-diamino-*N*-(*tert*-butyl)benzamide (**7a**).

^{1}H NMR (DMSO-d$_6$, δ in ppm): 9.11 (t, 1H, H$_{NH}$), 9.05 (d, 2H, H$_{aromat}$), 8.94 (t, 1H, H$_{aromat}$), 3.26 (t, 2H, H$_{N-CH2}$), 1.64-1.52 (s, 1H, H$_{CH}$), 1.42-1.20 (m, 8H, H$_{CH2}$), 0.91-0.82 (m, 6H, H$_{CH3}$)

12.1 g (95 mmol) of oxalyl chloride were slowly added under an argon atmosphere and ice-cooling to a mixture of 7.8 g (64 mmol) of isonicotinic acid and 40 mL of DCM. A few drops of DMF were then added to start the reaction. The mixture was stirred overnight at RT and at the end of the reaction for 2 h under reflux. Excess of oxalyl chloride and DCM were removed using a cold trap and diaphragm pump. The product was dried under high vacuum for 1 h yielding 9.0 g (64 mmol, 100 %) of isonicotinoyl chloride (**8**).

7.6 g (54 mmol) of **8** were added to a solution of 5.1 g (25 mmol) of **7a**, 16.9 mL (123 mmol) of triethylamine and 250 mL of THF under cooling and argon atmosphere. The solution was stirred at RT overnight and then at 50 °C overnight. Afterwards, the reaction mixture was poured into 2.0 L of ice

water. The product was filtered off, dried and boiled in 300 mL of ethyl acetate for further purification. Drying under high vacuum yields 7.3 g (17 mmol, 71 %) of **9a** as a yellowish-brown solid.

^{1}H NMR (DMSO-d$_6$, δ in ppm): 10.70 (s, 2H, H$_{3,3'}$), 8.81 (m, 4H, H$_{5,5'}$), 8.53 (t, 1H, H$_6$), 7.91 (m, 4H, H$_{4,4'}$), 7.85 (m, 3H, H$_{1,2,2'}$) 1.39 (s, 9H, H$_7$)

IR (ṽ in cm^{-1}): 3274, 2973, 1673, 1638, 1604, 1554, 1448, 1427

MS (in m/z): 417 [M$^+$]

TGA: 5 % weight loss at 347 °C

Melting temperature: 270 °C (SDTA), 156 °C and 259 °C (DSC)

Synthesis of BTA 9b (*N,N*′-(5-((2-Ethylhexyl)carbamoyl)-1,3-phenylene)diisonicotinamide)
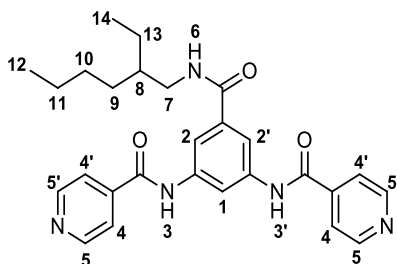
6.2 g (48 mmol) of 2-ethyl-1-hexyl amine were added dropwise under argon atmosphere and ice-cooling to a mixture of 10.0 g (43 mmol) of 3,5-dinitrobenzoyl chloride, 3.7 g (48 mmol) of pyridine and 200 mL of dried THF. The reaction mixture was stirred for 2 h at RT and then precipitated in 2 L of ice water. After stirring for 1 h, the product was filtered off and precipitated in a MeOH/water mixture yielding 11.6 g (36 mmol, 83 %) of *N*-(2-ethylhexyl)-3,5-dinitrobenzamide (**6b**).

^{1}H NMR (DMSO-d_6, δ in ppm): 9.11 (t, 1H, H_{NH}), 9.05 (d, 2H, H_{aromat}), 8.94 (t, 1H, H_{aromat}), 3.26 (t, 2H, H_{N-CH2}), 1.64-1.52 (s, 1H, H_{CH}), 1.42-1.20 (m, 8H, H_{CH2}), 0.91-0.82 (m, 6H, H_{CH3})

11.6 g (36 mmol) of **6b** were placed inside the hydrogenation reactor together with 300 mL of THF, 30 mL of EtOH and 0.4 g of a suspension of palladium on activated carbon (10 %). The hydrogenation was performed at 35 °C and a pressure of 5 bar overnight under stirring. Palladium on activated carbon was filtered off via AloxN. The product was then concentrated and dried under high vacuum yielding 9.3 g (35 mmol, 98 %) of 3,5-diamino-*N*-(2-ethylhexyl)benzamide (**7b**).

^{1}H NMR (DMSO-d_6, δ in ppm): 9.11 (t, 1H, H_{NH}), 9.05 (d, 2H, H_{aromat}), 8.94 (t, 1H, H_{aromat}), 3.26 (t, 2H, H_{N-CH2}), 1.64-1.52 (s, 1H, H_{CH}), 1.42-1.20 (m, 8H, H_{CH2}), 0.91-0.82 (m, 6H, H_{CH3})

15.0 g (119 mmol) of oxalyl chloride were slowly added under an argon atmosphere and ice-cooling to a mixture of 9.7 g (79 mmol) of isonicotinic acid and 50 mL of DCM. A few drops of DMF were then added to start the reaction. The mixture was stirred overnight at RT and at the end of the reaction for 2 h under reflux. Excess of oxalyl chloride and DCM were removed using a cold trap and diaphragm pump. The product was dried under high vacuum for 1 h yielding 11.2 g (79 mmol, 100 %) of isonicotinoyl chloride (**8**).

11.0 g (77 mmol) of **8** were added to a solution of 9.3 g (35 mmol) of **7b**, 24.4 mL (176 mmol) of triethylamine and 200 mL of THF under cooling and argon atmosphere. The solution was stirred at RT overnight. Afterwards, the reaction mixture was poured into 2.0 L of ice water. The product was boiled three times in DCM, was then recrystallized twice in 100 mL of MeOH and dried under vacuum yielding 10.1 g (21 mmol, 60 %) of **9b** as a white solid.

^{1}H NMR (DMSO-d$_6$, δ in ppm): 10.73 (s, 2H, H$_{3,3'}$), 8.81 (m, 4H, H$_{5,5'}$), 8.49 (t, 1H, H$_6$), 8.40 (t, 1H, H$_1$), 7.94 (d, 2H, H$_{2,2'}$), 7.90 (m, 4H, H$_{4,4'}$), 3.19 (t, 2H, H$_7$), 1..57 (s, 1H, H$_8$), 1.40-1.20 (m, 8H, H$_{9-11,13}$), 0.92-0.81 (t, 6H, H$_{12,14}$)

IR (ṽ in cm^{-1}): 3270, 2929, 1673, 1641, 1597, 1549, 1424

MS (in m/z): 473 [M$^+$]

TGA: 5 % weight loss at 375 °C

Melting temperature: 215 °C (SDTA), 210 °C (DSC)

Synthesis of BTA 9c *(N,N'-(Cyclohexylcarbonyl)-1,3-(phenylene)diisonicotinamide)*
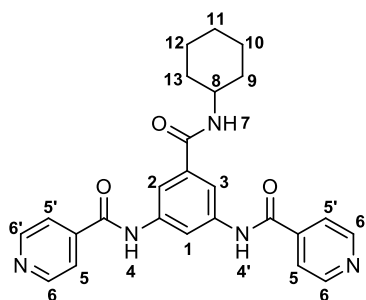
4.7 g (48 mmol) of cyclohexylamine were added dropwise under argon atmosphere and ice-cooling to a mixture of 10.0 g (43 mmol) of 3,5-dinitrobenzoyl chloride, 3.7 g (48 mmol) of pyridine and 200 mL of dried THF. The reaction mixture was stirred for 2 h at RT and then precipitated in 2 L of ice water. After stirring for 1 h, the product was filtered off and boiled in 300 mL of MeOH, yielding 10.3 g (35 mmol, 81 %) of *N*-cyclohexyl-3,5-dinitrobenzamide (**6c**).

^{1}H NMR (DMSO-d$_6$, δ in ppm): 9.06 (d, 2H, H$_{arom}$), 8.97 (d, 1H, H$_{arom}$), 8.94 (t, 1H, H$_{N-H}$), 3.82 (s, 1H, CN-H), 1.94-1.58 (m, 5H, H$_{cyclohexan}$), 1.44-1.08 (m, 5H, H$_{cyclohexan}$)

10.3 g (35 mmol) of **6c** were placed inside the hydrogenation reactor together with 100 mL of THF, 100 mL of DMF, 30 mL of EtOH and 0.4 g of a suspension of palladium on activated carbon (10 %). The hydrogenation was performed at 35 °C and a pressure of 5 bar overnight under stirring. Palladium on activated carbon was filtered off via AloxN and was washed with DMF. The product was then concentrated and dried under high vacuum yielding 8.1 g (35 mmol, 98 %) of 3,5-diamino-*N*-cyclohexylbenzamide (**7c**).

^{1}H NMR (DMSO-d$_6$, δ in ppm): 7.73 (d, 1H, H$_{arom}$), 6.18 (d, 2H, H$_{arom}$), 5.9 (t, 1H, H$_{N-H}$), 4.82 (s, 4H, NH$_2$), 3.64 (s, 1H, CN-H), 1.85-1.50 (m, 5H, H$_{cyclohexan}$), 1.36-0.98 (m, 5H, H$_{cyclohexan}$)

15.4 g (122 mmol) of oxalyl chloride were slowly added under an argon atmosphere and ice-cooling to a mixture of 10.0 g (81 mmol) of isonicotinic acid and 50 mL of DCM. A few drops of DMF were then added to start the reaction and the mixture was stirred overnight at RT and at the end of the reaction for 2 h under reflux. Excess of oxalyl chloride and DCM were removed using a cold trap and diaphragm pump. The product was dried under high vacuum for 1 h yielding 11.5 g (81 mmol, 100 %) of isonicotinoyl chloride (**8**).

10.7 g (76 mmol) of **8** were added to a solution of 8.1 g (35 mmol) of **7c**, 24.0 mL (172 mmol) triethylamine and 400 mL of NMP under cooling and argon atmosphere. The solution was stirred at RT overnight. Afterwards, the reaction mixture was poured into 4.0 L of ice water and stirred for 15 min. After settling the product, H$_2$O was decanted and the sticky solid dissolved in MeOH and concentrated. For further purification, the product was recrystallized twice in MeOH and dried under vacuum at 100 °C yielding 9.4 g (21 mmol, 62 %) of **9c** as a white solid.

^{1}H NMR (DMSO-d$_6$, δ in ppm): 10.72 (s, 2H, H$_{4,4'}$), 8.81 (m, 4H, H$_{6,6'}$), 8.52 (t, 1H, H$_7$), 8.28 (d, 1H, H$_1$), 7.91 (m, 6H, H$_{2,3,4,4'}$), 3.77 (s, 1H, H$_8$), 1.90-1.51 (m, 5H, H$_{9-13}$), 1.40-1.04 (m, 5H, H$_{9-13}$)

IR (ṽ in cm^{-1}): 3341, 3223, 2940, 2849, 1680, 1654, 1638, 1592, 1542, 1439, 1418, 1321

MS (in m/z): 443 [M$^+$]

TGA: 5 % weight loss at 390 °C

Melting temperature: 258 °C (SDTA), 253 °C (DSC)

7.2.3 Benzenetrisamides with one pyridine substituent

The syntheses of the three BTAs with one pyridine substituent **16a**, **16b** and **16c** were performed in five steps, respectively. The syntheses were performed by Sandra Ganzleben and Jutta Failner. For the general reaction scheme, see **Scheme 2**.

Synthesis of BTA 16a *(N^1,N^3-Di-tert*-butyl-5-(isoniotinamido)isophthalamide)
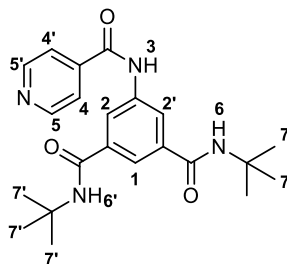
18.0 g (142 mmol) of oxalyl chloride were added at 0 °C under an argon atmosphere to a mixture of 10.0 g (47 mmol) of 5-nitroisophthalic acid and 40 mL of DCM. After the addition of a few droplets of DMF as a catalyst, the reaction mixture was stirred overnight at RT and finally under reflux for 10 min. The excess of oxalyl chloride and DCM was removed with an extra cold trap using a diaphragm pump and the product was dried under high vacuum yielding 11.7 g (47 mmol, 99 %) of 5-nitroisophthaloyl dichloride (**11**).

11.7 g (47 mmol) of **11** in THF were added dropwise under argon atmosphere and ice-cooling to a mixture of 11.1 g (152 mmol) of *tert*-butylamine, 8.4 mL (104 mmol) of pyridine and 200 mL of THF. The reaction mixture was stirred overnight at RT. Afterwards, the reaction mixture was poured into 3.0 L of ice water, stirred for 2 h and filtered off. For further purification, the product was recrystallized in ethyl acetate and dried under vacuum yielding 13.6 g (42 mmol, 89 %) of *N´,N´´*-di-*tert*-butyl-5-nitroisophthalamide as a white solid (**13a**).

^{1}H NMR (DMSO-d$_6$, δ in ppm): 8.68 (t, 2H, H$_{NH}$), 8.59 (d, 1H, H$_{aromat}$), 8.33 (s, 2H, H$_{aromat}$), 1.45-1.35 (m, 18H, H$_{CH3}$)

13.6 g (42 mmol) of **13a** were placed inside the hydrogenation reactor together with 300 mL of THF, 30 mL of MeOH and 0.5 g of a suspension of palladium on activated carbon (10 %). The hydrogenation was performed at 35 °C and a pressure of 5 bar overnight under stirring. Palladium on activated carbon was filtered off via AloxN. The product was then concentrated and dried under high vacuum yielding 12.3 g (42 mmol, 100 %) of 5-amino-*N´,N´´*-di-*tert*-butylisophthalamide (**14a**).

9.2 g (73 mmol) of oxalyl chloride were slowly added under argon atmosphere and ice-cooling to a mixture of 6.0 g (49 mmol) isonicotinic acid and 50 mL of DCM. A few drops of DMF were then added to start the reaction and the mixture was stirred at RT for 1 h and at the end of the reaction for 2 h under reflux. Excess of oxalyl chloride and DCM were removed using a cold trap and diaphragm pump.

The product was dried under high vacuum yielding 6.9 g (49 mmol, 100 %) of isonicotinoyl chloride (**15**).

6.9 g (49 mmol) of **15** were added to a solution of 12.3 g (42 mmol) of **14a**, 3.9 mL (49 mmol) of pyridine and 300 mL of THF under cooling and argon atmosphere. The solution was stirred at RT overnight. Afterwards, the reaction mixture was poured into ice water, stirred overnight and filtered off. For further purification, the product was recrystallized in MeOH, hexane and another two times in MeOH, yielding 6.5 g (16 mmol, 39 %) of **16a** as a white solid.

^{1}H NMR (DMSO-d_6, δ in ppm): 10.72 (s, 1H, H$_3$), 8.82 (dd, 2H, H$_{5,5'}$), 8.25 (d, 2H, H$_{2,2'}$), 7.96-7.90 (m, 4H, H$_{4,4',6,6'}$), 7.85 (t, 1H, H$_1$), 1.40 (s, 18H, H$_7$)

IR ($\tilde{v}$ in cm^{-1}): 3327, 3263, 3071, 2966, 1666, 1636, 1602, 1557, 1479, 1451, 1437

MS (in m/z): 396 [M$^+$]

TGA: 5 % weight loss at 313 °C

Melting temperature: no melting up to 300 °C

Synthesis of BTA 16b (N^1,N^3-Bis(2-ethylhexyl)-5-(isoniotinamido)isophthalamide)
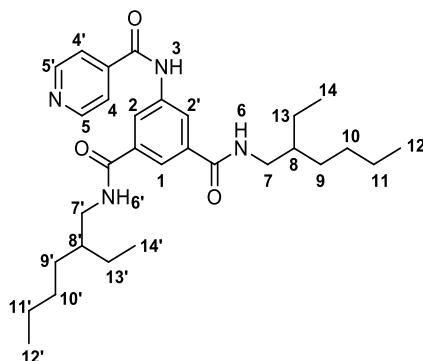
18.0 g (142 mmol) of oxalyl chloride were added at 0 °C under argon atmosphere to a mixture of 10.0 g (47 mmol) of 5-nitroisophthalic acid and 40 mL of DCM. After the addition of a few droplets of DMF as a catalyst, the reaction mixture was stirred overnight at RT and finally under reflux for 10 min. The excess of oxalyl chloride and DCM was removed with an extra cold trap using a diaphragm pump and the product was dried under high vacuum yielding 11.5 g (46 mmol, 98 %) of 5-nitroisophthaloyl dichloride (**11**).

5.5 g (22 mmol) of **11** in THF were added dropwise under argon atmosphere and ice-cooling to a mixture of 6.3 g (49 mmol) of 2-ethyl-1-hexylamine, 3.9 mL (49 mmol) of pyridine and 250 mL of THF. The reaction mixture was stirred overnight at RT. Then, the mixture was concentrated and stirred after the addition of 250 mL of water. The mixture was extracted with DCM, the organic phases were concentrated and the product was boiled in 200 mL of hexane. A white solid was filtered off and dried under high vacuum yielding 8.5 g (20 mmol, 88 %) of N',N''-bis(2-ethylhexyl)-5-nitroisophthal-amide (**13b**).

^{1}H NMR (DMSO-d$_6$, δ in ppm): 8.90 (t, 2H, H$_{NH}$), 8.78 (d, 2H, H$_{aromat}$), 8.73 (t, 1H, H$_{aromat}$), 3.23 (t, 4H, H$_{N-CH2}$), 1.64-1.52 (s, 2H, H$_{CH}$), 1.32-1.27 (m, 16H, H$_{CH2}$), 0.89-0.84 (m, 12H, H$_{CH3}$)

8.5 g (20 mmol) of **13b** were placed inside the hydrogenation reactor together with 300 mL of THF, 30 mL of EtOH and 0.2 g of a suspension of palladium on activated carbon (10 %). The hydrogenation was performed at 35 °C and under a pressure of 5 bar overnight under stirring. Palladium on activated carbon was filtered off via AloxN. The product was then concentrated and dried under high vacuum yielding 7.9 g (35 mmol, 100 %) of 5-amino-N',N''-bis(2-ethylhexyl)isophthalamide (**14b**).

4.6 g (36 mmol) of oxalyl chloride were slowly added under argon atmosphere and ice-cooling to a mixture of 3.0 g (24 mmol) isonicotinic acid and 15 mL of DCM. A few drops of DMF were then added to start the reaction and the mixture was stirred at RT for 1 h and at the end of the reaction for 2 h under reflux. Excess of oxalyl chloride and DCM were removed using a cold trap and diaphragm pump. The product was dried under high vacuum yielding 3.4 g (24 mmol, 100 %) of isonicotinoyl chloride (**15**).

3.4 g (24 mmol) of **15** were added to a solution of 7.9 g (19.6 mmol) of **14b**, 13.6 mL (98.0 mmol) of triethylamine and 300 mL of THF under cooling and argon atmosphere. The solution was stirred at RT overnight. Afterwards, the reaction mixture was poured into 2.5 L of ice water, stirred and filtered off. For further purification, the product was recrystallized in 200 mL of MeOH and dried under vacuum yielding 7.6 g (15 mmol, 76 %) of **16b** as a white solid.

^{1}H NMR (DMSO-d_6, δ in ppm): 10.76 (s, 1H, H_3), 8.81 (m, 2H, $H_{5,5'}$), 8.48 (t, 2H, $H_{6,6'}$), 8.32 (d, 2H, $H_{2,2'}$), 7.99 (t, 1H, H_1), 7.91 (m, 2H, $H_{4,4'}$), 3.21 (t, 4H, $H_{7,7'}$), 1.57 (s, 2H, $H_{8,8'}$), 1.35-1.24 (m, 16H, $H_{9-11,13,9-11',13'}$), 0.89-0.84 (m, 12H, $H_{12,12',14,14'}$)

IR (ṽ in cm^{-1}): 3270, 2926, 1677, 1645, 1602, 1552, 1419

MS (in m/z): 508 [M$^+$]

TGA: 5 % weight loss at 375 °C

Melting temperature: 216 °C (SDTA), 212 °C (DSC)

Synthesis of BTA 16c (*N¹,N³*- Dicyclohexyl-5-(isonicotinamido)isophthalamide)
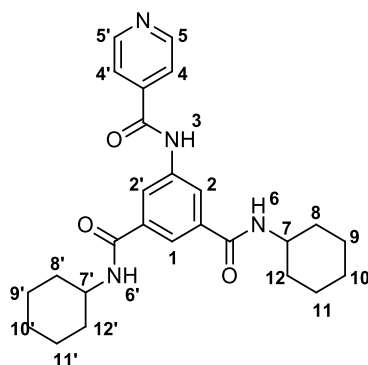
18.0 g (142 mmol) of oxalyl chloride were added at 0 °C under argon atmosphere to a mixture of 10.0 g (47 mmol) of 5-nitroisophthalic acid and 40 mL of DCM. After the addition of a few droplets of DMF as a catalyst, the reaction mixture was stirred overnight at RT and finally under reflux for 10 min. The excess of oxalyl chloride and DCM was removed with an extra cold trap using a diaphragm pump and the product was dried under high vacuum yielding 11.6 g (47 mmol, 99 %) of 5-nitroisophthaloyl dichloride (**11**).

11.6 g (47 mmol) of **11** dissolved in THF were added dropwise at 0 °C under argon atmosphere to a mixture of 9.9 g (103 mmol) of cyclohexylamine, 8.3 mL (103 mmol) of pyridine and 400 mL of THF. After stirring for 2 h at RT, the reaction mixture was precipitated in 4.0 L of ice water, stirred for 1 h, filtered off and dried at 80 °C yielding 16.8 g (45 mmol, 96 %) of $N^{'},N^{''}$-dicyclohexyl-5-nitroisophthalamide (**13c**).

^{1}H NMR (DMSO-d$_6$, δ in ppm): 8.79 (d, 3H, H$_{NH\&aromat}$), 8.75 (s, 1H, H$_{aromat}$), 8.71 (t, 1H, H$_{aromat}$), 3.80 (s, 2H, H$_{N-CH}$), 1.64-1.52 (s, 2H, H$_{CH}$), 1.92-1.55 (m, 10H, H$_{CH2}$), 1.43-1.05 (m, 12H, H$_{CH2}$)

5.0 g (13 mmol) of **13c** were dissolved in 300 mL of DMF and 30 mL of EtOH at 35 °C and then placed inside a hydrogenation reactor together with 0.1 g of a suspension of palladium on activated carbon (10 %). The hydrogenation was performed at 35 °C and a pressure of 5 bar overnight under stirring. Palladium on activated carbon was filtered off via AloxN. The product was then concentrated and dried under high vacuum yielding 4.2 g (12 mmol, 91 %) of 5-amino-$N^{'},N^{''}$-dicyclohexyl-5-nitroisophthalamide (**14c**).

^{1}H NMR (DMSO-d$_6$, δ in ppm): 8.08 (d, 2H, H$_{NH}$), 7.29 (t, 1H, H$_{aromat}$), 7.06 (d, 2H, H$_{aromat}$), 5.38 (s, 2H, H$_{NH}$), 3.71 (s, 2H, H$_{N-CH}$), 1.86-1.66 (m, 8H, H$_{CH-CH2}$), 1.66-1.54 (d, 2H, H$_{CH2}$), 1.38-1.19 (m, 8H, H$_{CH2}$), 1.18-1.04 (m, 2H, H$_{CH2}$)

3.3 g (27 mmol) of oxalyl chloride were slowly added under argon atmosphere and ice-cooling to a mixture of 2.2 g (18 mmol) isonicotinic acid and 15 mL of DCM. One droplet of DMF was then added to start the reaction and the mixture was stirred overnight at RT and at the end of the reaction for 2 h under reflux. Excess of oxalyl chloride and DCM was removed using a cold trap and diaphragm pump.

The product was dried under high vacuum yielding 2.5 g (18 mmol, 100 %) of isonicotinoyl chloride (**15**).

2.5 g (18 mmol) of **15** were added to a solution of 4.2 g (12.2 mmol) of **14c**, 1.4 mL (18 mmol) of pyridine and 200 mL of THF under cooling and argon atmosphere. The solution was stirred at RT overnight. Afterwards, the reaction mixture was poured into 2.5 L of ice water, stirred and filtered off. For further purification, the product was recrystallized in 300 mL of MeOH and dried under vacuum at 80 °C yielding 3.3 g (7 mmol, 60 %) of **16c** as a white solid.

^{1}H NMR (DMSO-d$_6$, δ in ppm): 10.77 (s, 1H, H$_3$), 8.81 (m, 2H, H$_{5,5'}$), 8.37 (d, 2H, H$_{6,6'}$), 8.30 (d, 2H, H$_{2,2'}$), 7.96 (t, 1H, H$_1$), 7.91 (m, 2H, H$_{4,4'}$), 3.77 (s, 2H, H$_{7,7'}$), 1.90-1.66 (m, 8H, H$_{8,8',12,12'}$), 1.66-1.56 (d, 2H, H$_{11}$), 1.42-1.21 (m, 8H, H$_{9,9',11,11'}$), 1.20-1.02 (m, 2H, H$_{11}$)

IR (ṽ in cm^{-1}): 3247, 3068, 2926, 2853, 1675, 1600, 1630, 1544, 1443, 1412

MS (in m/z): 448 [M$^+$]

TGA: 5 % weight loss at 379 °C

Melting temperature: 162 °C & 300 °C (SDTA), 290 °C (DSC),

7.2.4 Benzenetrisamides with terpyridine substituents

The syntheses of BTAs with terpyridine substituents **21a-c** and **24a-e** were performed in two steps, respectively. For the general reaction scheme, see **Scheme 4-7**.

Synthesis of BTA 21a

(N^1,N^3,N^5-Tris(2-([2,2':6',2''-terpyridin]-4'-ylamino)ethyl)benzene-1,3,5-tricarboxamide)
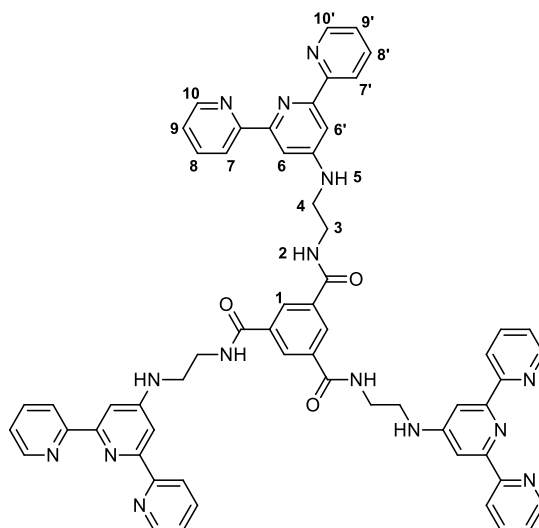
0.5 g (2 mmol) of 4'-chloro-2,2';6',2''-terpyridine were suspended in 3.0 g (45 mmol) of ethylenediamine. After stirring overnight at 110 °C, the reaction mixture was cooled to RT, poured into 200 mL of deionized water and stirred for 4 h. The white precipitate was filtered off, washed with water and dried. The product was further purified by column chromatography (DCM:MeOH/NH$_3$(9:1) = 90:10), dried under vacuum at 40 °C yielding 0.3 g (1.0 mmol, 50 %) of N^1-([2,2':6',2''-terpyridin]-4'-yl)ethane-1,2-diamine (**19a**) as a light yellow solid.

^{1}H NMR (CDCl$_3$, δ in ppm): 8.65 (ddd, 2H, H$_{9,9'}$), 8.60 (dt, 2H, H$_{6,6'}$) 7.85 (td, 2H, H$_{7,7'}$), 7.72 (s, 2H, H$_{5,5'}$),7.30 (ddd, 2H, H$_{8,8'}$), 4.90 (s, 1H, H$_4$), 3.43 (q, 2H, H$_3$), 3.05 (dd, 2H, H$_2$)

0.3 g (1 mmol) of **19a** were added to a solution of 2.0 mL (27 mmol) of 1,3,5-benzenetricarboxylic acid chloride, 2.0 mL (27 mmol) of triethylamine and 30 mL of dry THF under cooling and argon atmosphere. The solution was stirred at RT for 5.5 h. Afterwards, the reaction mixture was concentrated to obtain a yellowish solid. The product was stirred in water overnight and then dried under vacuum. For further purification, the product was boiled in MeOH, subsequently filtered off and dried under vacuum at 70 °C yielding 0.2 g (0.2 mmol, 63 %) of **21a** as a yellowish solid.

^{1}H NMR (DMSO-d$_6$, δ in ppm): 8.92 (t, 3H, H$_2$), 8.63 (ddd, 6H,H$_{10,10'}$), 8.55 (ddd, 6H,H$_{7,7'}$), 8.52 (s, 3H, H$_1$), 7.94 (td, 6H, H$_{8,8'}$), 7.72 (s, 6H, H$_{6,6'}$), 7.42 (ddd, 6H, H$_{9,9'}$), 7.07 (t, 3H, H$_5$), 3.58-3.42 (m, 12H, H$_{3,4}$)

IR (ṽ in cm^{-1}): 3343, 3060, 1648, 1604, 1582, 1564, 1515, 1461, 1442, 1418, 1406

TGA: 5 % weight loss at 387 °C　　　　　　　Melting temperature: - (SDTA), - (DSC)

Synthesis of BTA 21b

N^1,*N*^{3},*N*^{5}-Tris(3-([2,2':6',2''-terpyridin]-4'-ylamino)propyl)benzene-1,3,5-tricarboxamide
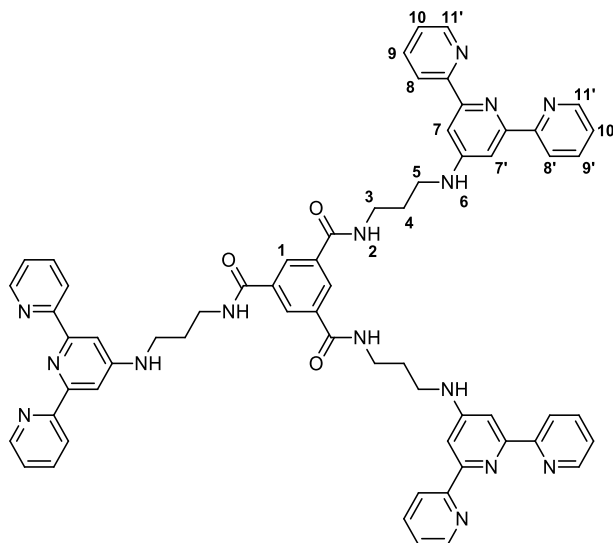
0.5 g (2 mmol) of 4'-chloro-2,2';6',2''-terpyridine were suspended in 3.8 mL (45 mmol) of 1,3-diamino propane. After stirring overnight at 120 °C, the reaction mixture was cooled to RT, poured into 150 mL of deionized water and stirred for 2 h. The white precipitate was filtered off, washed with water and dried under vacuum at 40 °C yielding 0.5 g (1.5 mmol, 75 %) of *N*^{1}-([2,2':6',2''-terpyridin]-4'-yl)propane-1,3-diamine (**19b**) as a white solid.

^{1}H NMR (CDCl$_3$, δ in ppm): 8.68 (ddd, 2H, H$_{10,10'}$), 8.62 (dt, 2H, H$_{7,7'}$) 7.84 (ddd, 2H, H$_{8,8''}$), 7.67 (s, 2H, H$_{6,6'}$), 7.31 (ddd, 2H, H$_{9,9'}$), 5.15 (t, 1H, H$_5$), 3.47 (td, 2H, H$_4$), 2.91 (t, 2H, H$_2$), 1.84 (m, 2H, H$_3$)

0.1 g (0.4 mmol) of 1,3,5-benzenetricarboxylic acid chloride were added to a solution of 0.5 g (1.5 mmol) of **19b**, 3.0 mL (41 mmol) of triethylamine and 30 mL of dry THF under cooling and argon atmosphere. The solution was stirred at RT overnight. Afterwards, the reaction mixture was concentrated to obtain a yellowish solid. The product was stirred in water for 2 h, filtered off and dried. For further purification, the product was boiled in a 3:7 (w/w) EtOH/H$_2$O solvent mixture, subsequently filtered off and dried under vacuum at 40 °C yielding 0.1 g (0.1 mmol, 21 %) of **21b** as a yellowish solid.

^{1}H NMR (CDCl$_3$, δ in ppm): 8.80 (t, 3H, H$_2$), 8.62 (ddd, 6H, H$_{11,11'}$), 8.55 (ddd, 6H, H$_{8,8'}$), 8.43 (s, 3H, H$_1$), 7.93 (td, 6H, H$_{9,9'}$), 7.68 (s, 6H, H$_{7,7'}$), 7.41 (ddd, 6H, H$_{10,10'}$), 6.93 (t, 3H, H$_6$), 4.31 (t, 6H, H$_2$), 3.42-3.21 (m, 12H, H$_{3,5}$), 1.91 (p, 6H, H$_4$)

IR (ṽ in cm^{-1}): 3313, 3056, 2932, 1651, 1604, 1582, 1563, 1516, 1462, 1440, 1418, 1405

TGA: 5 % weight loss at 396 °C   Melting temperature: - (SDTA), - (DSC)

Synthesis of BTA 21c

N^1,N^3,N^5-Tris(4-([2,2':6',2''-terpyridin]-4'-ylamino)butyl)benzene-1,3,5-tricarboxamide

0.5 g (2 mmol) of 4'-chloro-2,2';6',2''-terpyridine were suspended in 4.5 mL (45 mmol) of 1,4-diamino butane. After stirring overnight at 120 °C, the reaction mixture was cooled to RT, poured into 250 mL of deionized water and stirred for 2 h. The white precipitate was filtered off, washed with DCM and dried. The product was further purified by column chromatography (CH$_2$Cl$_2$:CH$_3$OH/NH$_3$(9:1) = 90:10), dried under vacuum at 40 °C yielding 0.3 g (0.9 mmol, 47 %) of N^1-([2,2':6',2''-terpyridin]-4'-yl)butane-1,4-diamine (**19c**) as a white solid.

^{1}H NMR (CDCl$_3$, δ in ppm): 8.69 (ddd, 2H, H$_{11,11'}$), 8.62 (dt, 2H, H$_{8,8'}$), 7.85 (td, 2H, H$_{9,9'}$), 7.67 (s, 2H, H$_{7,7'}$), 7.33 (ddd, 2H, H$_{10,10'}$), 4.65 (s, 1H, H$_6$), 3.41 (s, 2H, H$_5$), 2.80 (t, 2H, H$_2$), 1.77 (dt, 2H, H$_4$), 1.62 (q, 2H, H$_3$)

0.07 g (0.3 mmol) of 1,3,5-benzenetricarboxylic acid chloride were added to a solution of 0.3 g (0.9 mmol) of **19c**, 2.0 mL (27 mmol) of triethylamine and 30 mL of dry THF under cooling and argon atmosphere. The solution was stirred at RT for 4 h. Afterwards, the reaction mixture was concentrated to obtain a yellowish solid. The product was stirred in water for 2 h, filtered off and dried. For further purification, the product was first boiled in MeOH and then purified by column chromatography (CH$_2$Cl$_2$:CH$_3$OH = 4:1), dried under vacuum at 70 °C yielding 0.2 g (0.2 mmol, 69 %) of **21c** as a yellowish solid.

^{1}H NMR (DMSO-d$_6$, δ in ppm): 8.73 (t, 3H, H$_2$), 8.64 (ddd, 6H, H$_{12,12'}$), 8.54 (ddd, 6H, H$_{9,9'}$), 8.39 (s, 3H, H$_1$), 7.94 (ddd, 6H, H$_{10,10'}$), 7.66 (s, 6H, H$_{8,8'}$), 7.42 (ddd, 6H, H$_{11,11'}$), 6.91 (t, 3H, H$_7$), 3.52-3.20 (m, 12H, H$_{3,6}$), 1.68 (m, 12H, H$_{4,5}$)

IR (ṽ in cm^{-1}): 3296, 3059, 2932, 2863, 1651, 1605, 1583, 1564, 1520, 1464, 1441, 1418, 1405

TGA: 5 % weight loss at 408 °C   Melting temperature: - (SDTA), - (DSC)

Synthesis of BTA 24a

N¹,N³,N⁵-Tris(2-([2,2':6',2''-terpyridin]-4'-yloxy)ethyl)benzene-1,3,5-tricarboxamide
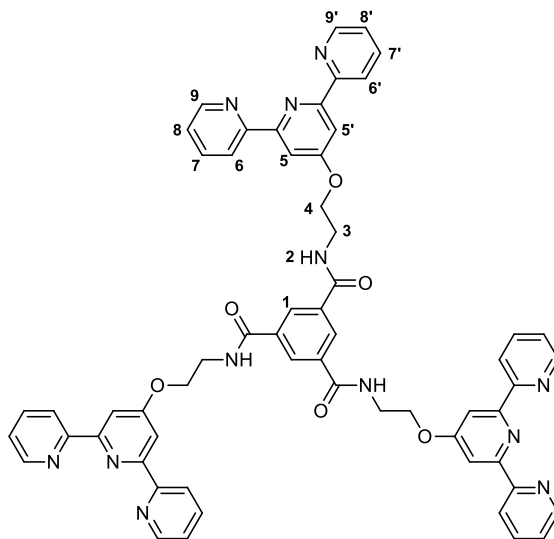
2.6 mL (43 mmol) of ethanolamine were added to a suspension of 5.2 g (93 mmol) of KOH in 95 mL of DMSO at 40 °C. The suspension was stirred for 20 min, followed by the addition of 5.0 g (19 mmol) of 4'-chloro-2,2';6',2''-terpyridine. After stirring for 3 h at 40 °C, the reaction mixture was cooled to RT. Then 300 mL of methylene chloride were added and the reaction mixture was washed with 3 x 200 mL of water. The organic phases were separated, dried over anhydrous Na_2SO_4 and concentrated. The residue was purified by column chromatography (CH_2Cl_2:CH_3OH/NH_3(9:1) = 80:20) and dried under vacuum at 50 °C yielding 3.3 g (11.3 mmol, 60 %) of 2-([2,2':6',2''-terpyridin]-4'-yloxy)-ethanamine (**23a**) as a light yellow solid.

¹H NMR (CDCl₃, δ in ppm): 8.68 (ddd, 2H, $H_{8,8'}$), 8.59 (ddd, 2H, $H_{5,5'}$), 8.01 (s, 2H, $H_{4,4'}$), 7.83 (td, 2H, $H_{6,6'}$), 7.32 (ddd, 2H, $H_{7,7'}$), 4.25 (t, 2H, H_3), 3.17 (t, 2H, H_2)

3.3 g (11 mmol) of **23a** were added to a solution of 1.0 g (4 mmol) of 1,3,5-benzenetricarboxylic acid chloride, 0.8 mL (6 mmol) of triethylamine and 250 mL of dry THF under cooling and argon atmosphere. The solution was stirred at RT overnight. Afterwards, the reaction mixture was poured into 2.5 L of ice water, stirred for another 2 h and filtered off. For purification, the product was boiled in EtOH, subsequently filtered off and dried under vacuum at 80 °C yielding 3.2 g (3 mmol, 85 %) of **24a** as a white solid.

¹H NMR (DMSO-d₆, δ in ppm): 9.00 (t, 3H, H_2), 8.60 (ddd, 6H,$H_{9,9'}$), 8.59 (dt, 6H,$H_{6,6'}$), 8.49 (s, 3H, H_1), 7.99 (td, 6H, $H_{7,7'}$), 7.95 (s, 6H, $H_{5,5'}$), 7.47 (ddd, 6H, $H_{8,8'}$), 4.43 (t, 6H, H_4), 3.77 (d, 6H, H_3)

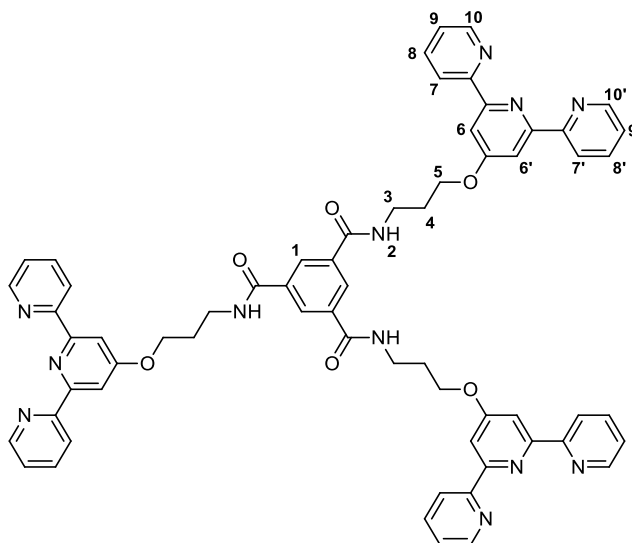IR (ṽ in cm⁻¹): 3246, 3052, 1644, 1581, 1560, 1468, 1442, 1406

LC-MS (in m/z): 1032 $[C_{60}H_{48}N_{12}O_6]^+$ and m/z = 1054 $[C_{60}H_{48}N_{12}O_6 + Na]^+$

TGA: 5 % weight loss at 327 °C   Melting temperature: 177 °C (SDTA), 170 °C (DSC)

226

Synthesis of BTA 24b

N^1,*N*^{3},*N*^{5}-Tris(2-([2,2':6',2''-terpyridin]-4'-yloxy)propyl)benzene-1,3,5-tricarboxamide

0.4 mL (5 mmol) of 3-amino-1-propanol were added to a suspension of 1.1 g (20 mmol) of KOH in 20 mL of DMSO at 60 °C. The suspension was stirred for 30 min, followed by the addition of 1.1 g (4.0 mmol) of 4'-chloro-2,2';6',2''-terpyridine. After stirring for 39 h at 65 °C, the reaction mixture was cooled to RT. 200 mL of deionized water were poured into the reaction and the mixture was stirred for another 2 h. After extraction with 300 mL of methylene chloride, the organic phases were separated, dried over anhydrous Na$_2$SO$_4$ and concentrated. The residue was purified by column chromatography (CH$_2$Cl$_2$:CH$_3$OH/NH$_3$(9:1) = 80:20), dried under vacuum yielding 0.9 g (3 mmol, 71 %) of 3-([2,2':6',2''-terpyridin]-4'-yloxy)-propan-1-amine (**23b**) as a yellow solid.

^{1}H NMR (CDCl$_3$, δ in ppm): 8.69 (ddd, 2H, H$_{9,9'}$), 8.61 (dt, 2H, H$_{6,6'}$), 8.02 (s, 2H, H$_{5,5'}$), 7.85 (ddd, 2H, H$_{7,7'}$), 7.33 (ddd, 2H, H$_{8,8'}$), 4.33 (t, 2H, H$_4$), 2.95 (t, 2H, H$_2$), 2.00 (p, 2H, H$_3$)

0.2 g (0.8 mmol) of 1,3,5-benzenetricarboxylic acid chloride were added to a solution of 0.9 g (3 mmol) of **23b**, 5.5 mL (74 mmol) of triethylamine and 55 mL of dry THF under cooling and argon atmosphere. The solution was stirred at RT for 4.5 h. Afterwards, the reaction mixture was poured into water, stirred for another 1 h and filtered off. The product was dried under vacuum at 50 °C yielding 0.8 g (0.7 mmol, 88 %) of **24b** as a yellow solid.

^{1}H NMR (CDCl$_3$, δ in ppm): 8.86 (t, 3H, H$_2$), 8.67 (ddd, 6H, H$_{10,10'}$), 8.59 (dt, 6H, H$_{7,7'}$), 8.44 (s, 3H, H$_1$), 7.99 (td, 6H, H$_{8,8'}$), 7.96 (s, 6H, H$_{6,6'}$), 7.48 (ddd, 6H, H$_{9,9'}$), 4.31 (t, 6H, H$_5$), 3.49 (m, 6H, H$_3$), 2.06 (m, 6H, H$_4$)

IR (ṽ in cm^{-1}): 3239, 3073, 2957, 2926, 2859, 1636, 1559, 1466, 1442, 1406

LC-MS (in m/z): 1075 [C$_{63}$H$_{54}$N$_{12}$O$_6$]$^+$

TGA: 5 % weight loss at 341 °C   Melting temperature: 225 °C (SDTA), 228 °C (DSC)

Synthesis of BTA 24c

N¹,N³,N⁵-Tris(2-([2,2':6',2''-terpyridin]-4'-yloxy)butyl)benzene-1,3,5-tricarboxamide

0.7 mL (8 mmol) of 4-amino-1-butanol were added to a suspension of 1.1 g (19 mmol) of KOH in 22.5 mL of DMSO at 60 °C. The suspension was stirred for 5 min, followed by the addition of 0.5 g (2 mmol) of 4'-chloro-2,2';6',2''-terpyridine. After stirring for 23 h at 60 °C, the reaction mixture was cooled to RT. The reaction mixture was poured into 200 mL of deionized water and stirred for another 5 h. The orange precipitate was filtered off, washed with water and dried under vacuum yielding 0.3 g (0.8 mmol, 40 %) of 4-([2,2':6',2''-terpyridin]-4'-yloxy)-butane-1-amine (**23c**) as an orange solid.

^{1}H NMR (CDCl$_3$, δ in ppm): 8.69 (ddd, 2H, H$_{10,10'}$), 8.6 (dt, 2H, H$_{7,7'}$), 8.00 (s, 2H, H$_{6,6'}$), 7.85 (ddd, 2H, H$_{8,8'}$), 7.33 (ddd, 2H, H$_{9,9'}$), 4.25 (t, 2H, H$_5$), 2.80 (t, 2H, H$_2$), 1.90 (m, 2H, H$_4$), 1.68 (m, 2H, H$_3$)

0.06 g (0.2 mmol) of 1,3,5-benzenetricarboxylic acid chloride were added to a solution of 0.3 g (0.8 mmol) of **23c**, 1.6 mL (22 mmol) of triethylamine and 16.5 mL of dry THF under cooling and argon atmosphere. The solution was stirred at RT for 3 h. Afterwards, the reaction mixture was poured into water, stirred for several hours and filtered off. For purification, the product was boiled in EtOH, subsequently filtered off and dried under vacuum at 60 °C yielding 0.2 g (0.2 mmol, 66 %) of **24c** as a white solid.

^{1}H NMR (DMSO-d$_6$, δ in ppm): 8.78 (t, 3H, H$_2$), 8.68 (ddd, 6H, H$_{11,11'}$), 8.61 (dt, 6H, H$_{8,8'}$), 8.42 (s, 3H, H$_1$), 7.98 (td, 6H, H$_{9,9'}$), 7.97 (s, 6H, H$_{7,7'}$), 7.48 (ddd, 6H, H$_{10,10'}$), 4.30 (t, 6H, H$_6$), 3.38 (m, 6H, H$_3$), 1.94-1.70 (m, 12H, H$_{4,5}$)

IR (ṽ in cm^{-1}): 3247, 3064, 2947, 2874, 1640, 1581, 1559, 1468, 1443, 1406

LC-MS (in m/z): 1117 [C$_{66}$H$_{60}$N$_{12}$O$_6$]$^+$

TGA: 5 % weight loss at 362 °C   Melting temperature: 237 °C (SDTA), 236 °C (DSC)

228

Synthesis of BTA 24d

N^1,N^3,N^5-Tris(2-([2,2':6',2''-terpyridin]-4'-yloxy)pentyl)benzene-1,3,5-tricarboxamide
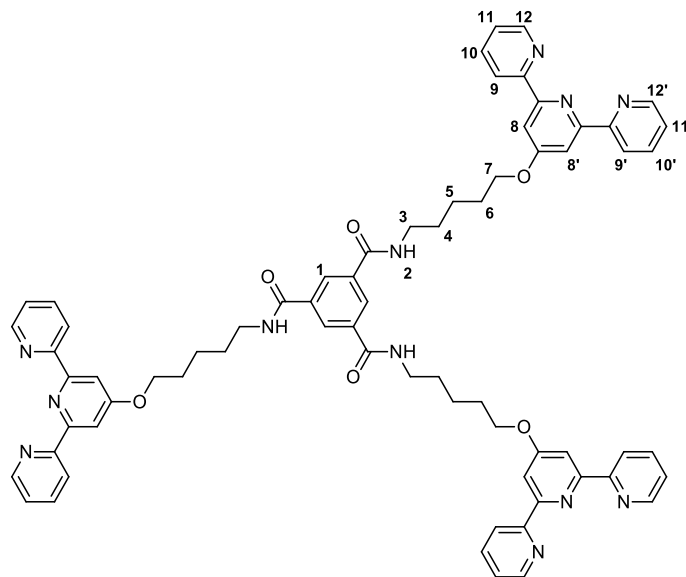
1.8 mL (16 mmol) of 5-amino-1-pentanol were added to a suspension of 0.5 g (9 mmol) of KOH in 45 mL of DMSO at 40 °C. The suspension was stirred for 20 min, followed by the addition of 1.0 g (4 mmol) of 4'-chloro-2,2';6',2''-terpyridine. After stirring for 2.5 h at 40 °C, the reaction mixture was cooled to RT and poured into 400 mL of deionized water. The white precipitate was filtered off, washed with water and dried under vacuum yielding 0.9 g (3 mmol, 72 %) of 5-([2,2':6',2''-terpyridin]-4'-yloxy)-pentane-1-amine (**23d**) as a white solid.

^{1}H NMR (CDCl$_3$, δ in ppm): 8.69 (ddd, 2H, H$_{11,11'}$), 8.61 (dt, 2H, H$_{8,8'}$), 8.00 (s, 2H, H$_{7,7'}$), 7.85 (ddd, 2H, H$_{9,9'}$), 7.33 (ddd, 2H, H$_{10,10'}$), 4.24 (t, 2H, H$_6$,), 2.73 (m, 2H, H$_2$), 1.86 (q, 2H, H$_5$), 1.54 (m, 4H, H$_{3,4}$)

0.1 g (0.5 mmol) of 1,3,5-benzenetricarboxylic acid chloride was added to a solution of 0.6 g (2 mmol) of **23d**, 3.6 mL (25 mmol) of triethylamine and 36 mL of dry THF under cooling and argon atmosphere. The solution was stirred at RT for 3 h. Afterwards, the reaction mixture was poured into water, stirred for 1.5 h and filtered off. For further purification, the product was boiled in EtOH, subsequently filtered off and dried under vacuum at 80 °C yielding 0.5 g (0.4 mmol, 84 %) of **24d** as a white solid.

^{1}H NMR (DMSO-d$_6$, δ in ppm): 8.72 (t, 3H, H$_2$), 8.69 (ddd, 6H, H$_{12,12'}$), 8.59 (d, 6H, H$_{9,9'}$), 8.40 (s, 3H, H$_1$), 7.98 (td, 6H, H$_{10,10'}$), 7.94 (s, 6H, H$_{8,8'}$), 7.48 (ddd, 6H, H$_{11,11'}$), 4.23 (t, 6H, H$_7$), 3.32 (m, 6H, H$_3$), 1.83 (m, 6H, H$_6$), 1.69-1.44 (m, 12 H, H$_{4,5}$)

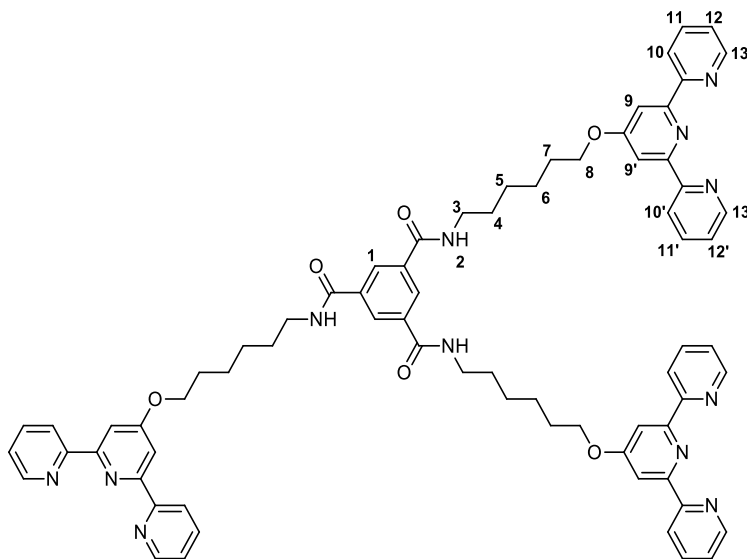IR (ṽ in cm^{-1}): 3250, 3064, 2947, 2866, 1635, 1581, 1563, 1467, 1444, 1406

LC-MS (in m/z): 1159 [C$_{69}$H$_{66}$N$_{12}$O$_6$]$^+$

TGA: 5 % weight loss at 362 °C   Melting temperature: 173 °C (SDTA), 170 °C (DSC)

Synthesis of BTA 24e

N^1,N^3,N^5-Tris(2-([2,2':6',2''-terpyridin]-4'-yloxy)hexyl)benzene-1,3,5-tricarboxamide

1.0 g (8 mmol) of 6-amino-1-hexanol was added to a suspension of 2.1 g (37 mmol) of KOH in 40 mL of DMSO at 65 °C. The suspension was stirred for 30 min, followed by the addition of 2.0 g (8 mmol) of 4'-chloro-2,2';6',2''-terpyridine. After stirring for 24 h at 65 °C, the reaction mixture was cooled to RT. The reaction mixture was poured into 1.5 L of deionized water and stirred for several hours. The white precipitate was filtered off, washed with water and dried under vacuum at 40 °C yielding 2.4 g (7 mmol, 84 %) of 6-([2,2':6',2''-terpyridin]-4'-yloxy)-hexane-1-amine (**23e**) as a white solid.

^{1}H NMR (CDCl$_3$, δ in ppm): 8.68 (ddd, 2H, H$_{12,12'}$), 8.60 (ddd, 2H, H$_{9,9'}$), 8.00 (s, 2H, H$_{8,8'}$), 7.84 (dt, 2H, H$_{10,10'}$), 7.31 (ddd, 2H, H$_{11,11'}$), 4.22 (t, 2H, H$_7$), 2.70 (t, 2H, H$_2$), 1.85 (m, 2H, H$_6$), 1.58-1.33 (m, 6H, H$_{3,4,5}$)

0.5 g (2 mmol) of 1,3,5-benzenetricarboxylic acid chloride were added to a solution of 2.4 g (7 mmol) of **23e**, 12.5 mL (90 mmol) of triethylamine and 125 mL of dry THF under cooling and argon atmosphere. The solution was stirred at RT for 3 h. Afterwards, the reaction mixture was poured into 2.5 L of water, stirred for several hours and filtered off. For purification, the product was boiled in EtOH, subsequently filtered off and dried under vacuum at 50 °C yielding 1.9 g (1.6 mmol, 83 %) of **24e** as a white solid.

^{1}H NMR (DMSO-d$_6$, δ in ppm): 8.69 (ddd, 6H, H$_{13,13'}$), 8.68 (t, 3H, H$_2$), 8.59 (dt, 6H, H$_{10,10'}$), 8.38 (s, 3H, H$_1$), 7.97 (ddd, 6H, H$_{11,11'}$), 7.94 (s, 6H, H$_{9,9'}$), 7.48 (ddd, 6H, H$_{12,12'}$), 4.22 (t, 6H, H$_8$), 3.30 (m, 6H, H$_3$), 1.79 (m, 6H, H$_7$), 1.64-1.34 (m, 18 H, H$_{4,5,6}$)

IR (ṽ in cm^{-1}): 3224, 3063, 2930, 2855, 1635, 1581, 1560, 1470, 1453, 1406

LC-MS (in m/z): 1201 [C$_{72}$H$_{72}$N$_{12}$O$_6$]$^+$ and m/z = 1223 [C$_{72}$H$_{72}$N$_{12}$O$_6$ + Na]$^+$

TGA: 5 % weight loss at 382 °C   Melting temperature: 219 °C (SDTA), 218 °C (DSC)
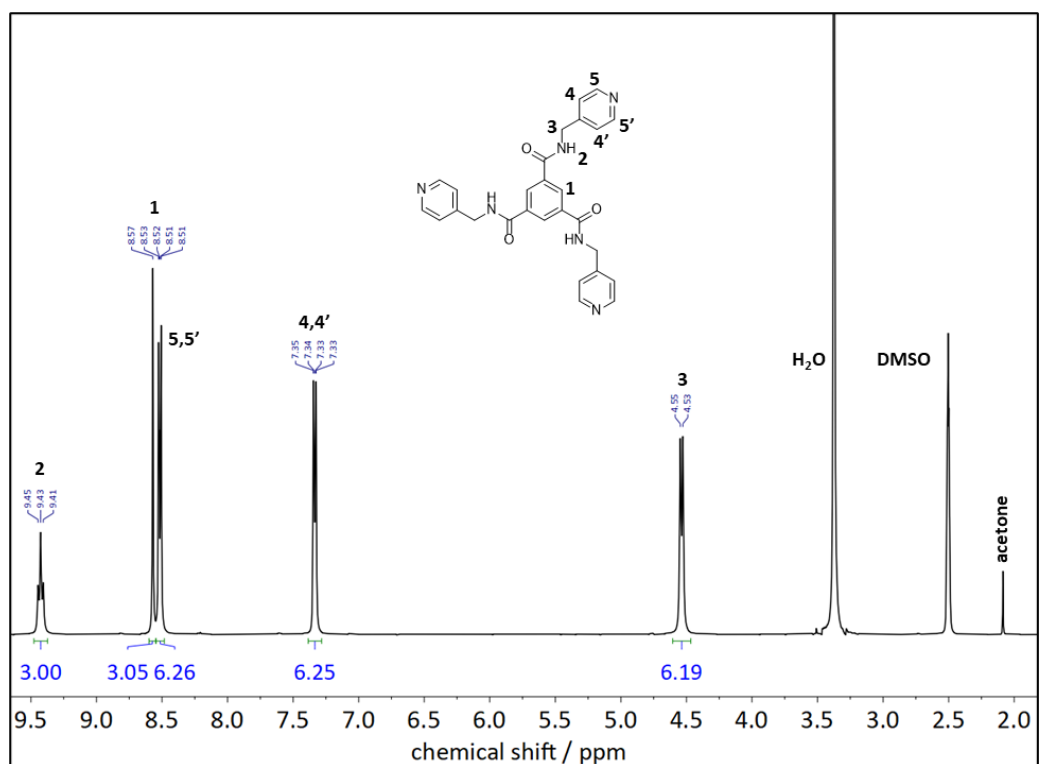
230

8 Appendix
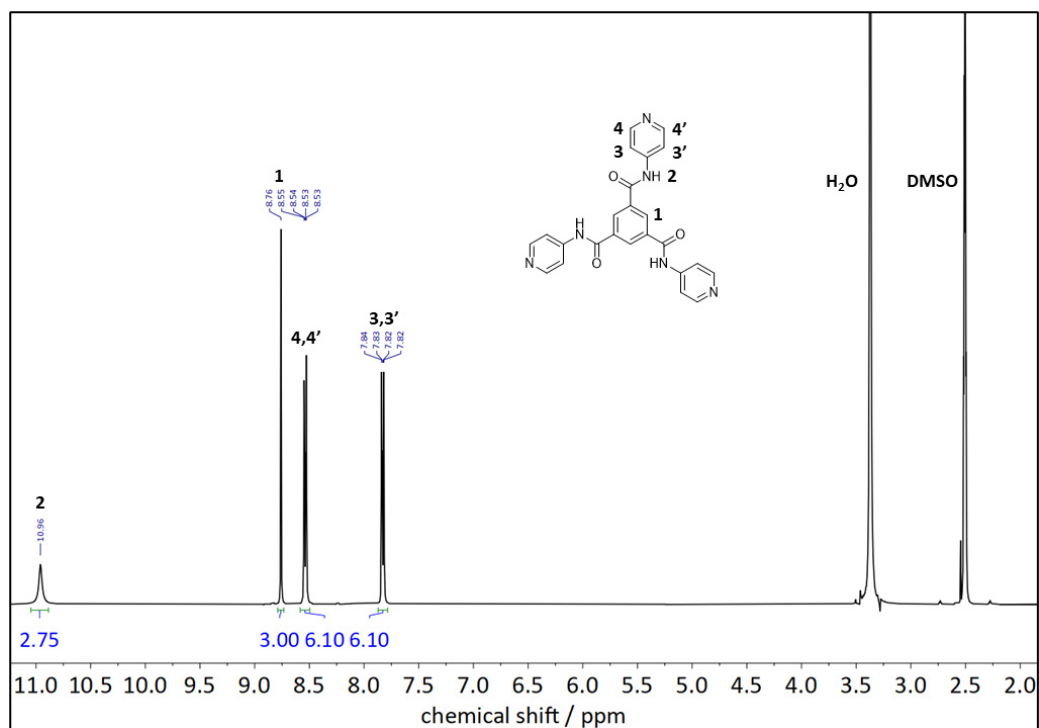
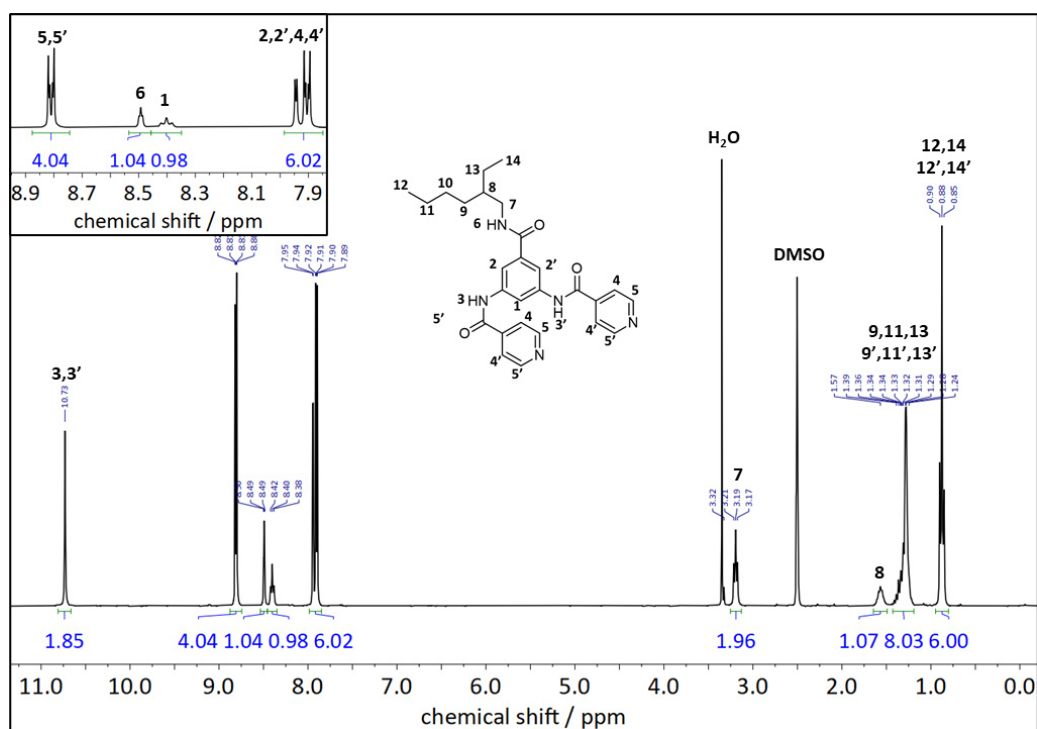**Figure 134:** NMR spectrum of **3a.**

Figure 135: NMR spectrum of **3b.**

Figure 136: NMR spectrum of **9b.**
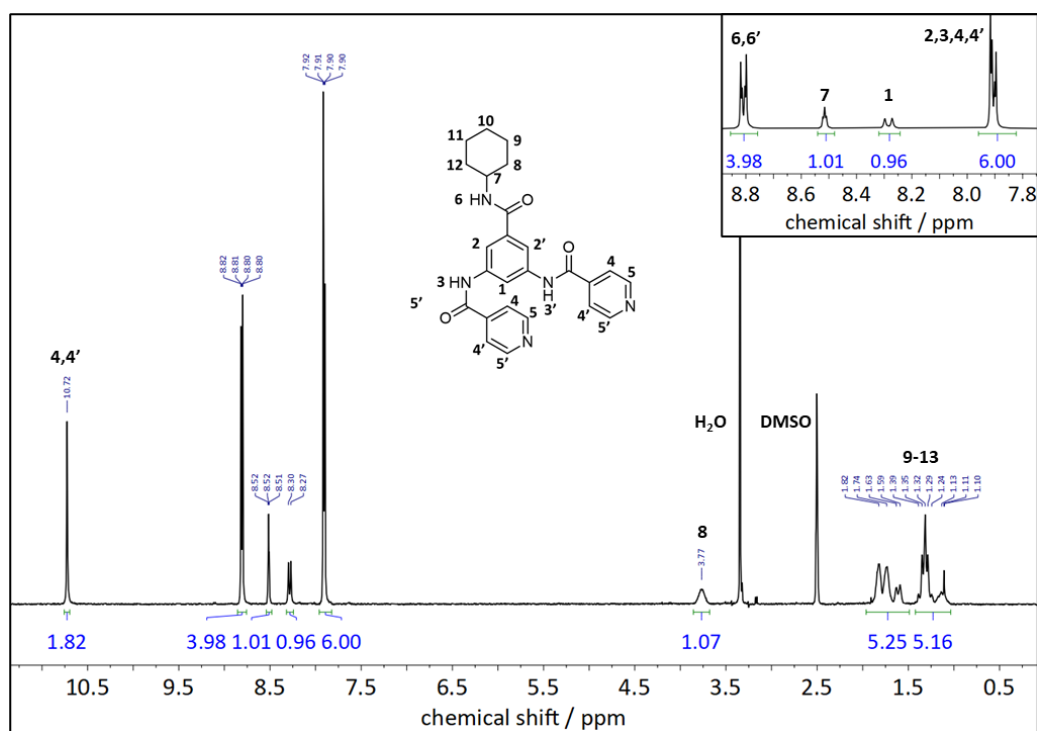
Figure 137: NMR spectrum of **9c.**
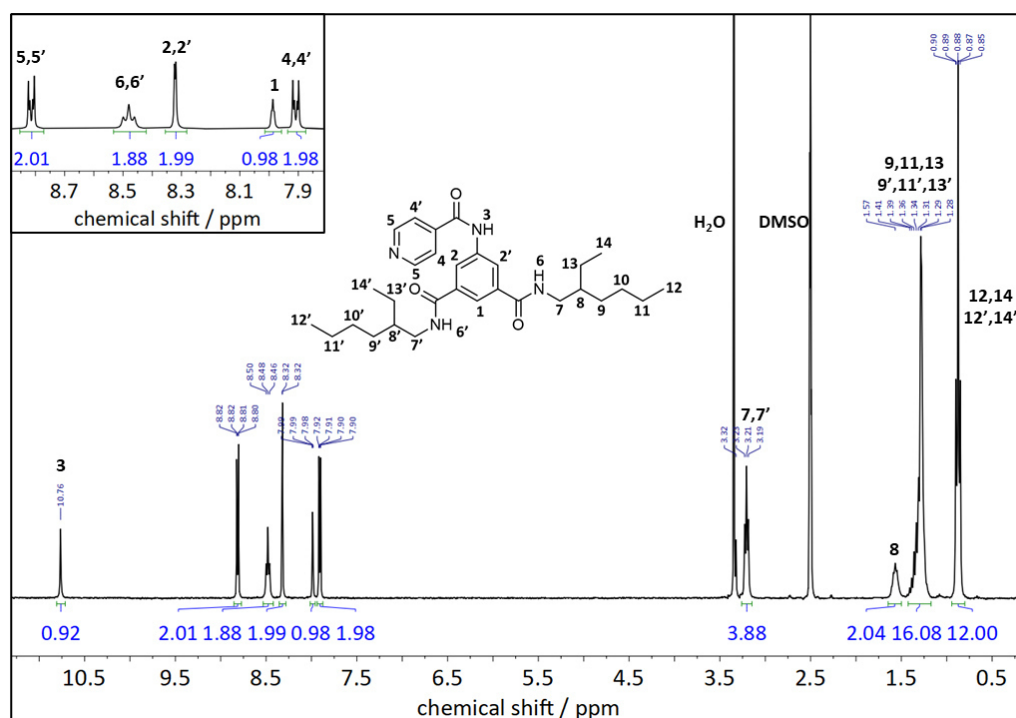
Figure 138: NMR spectrum of **16b.**
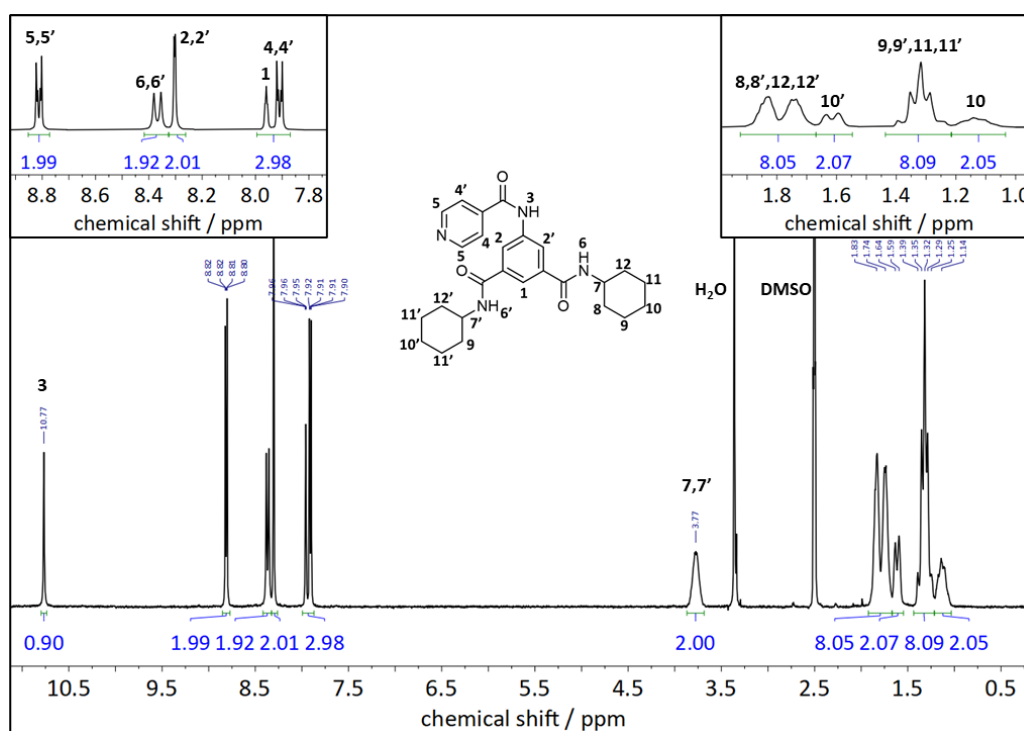
Figure 139: NMR spectrum of **16c.**

233
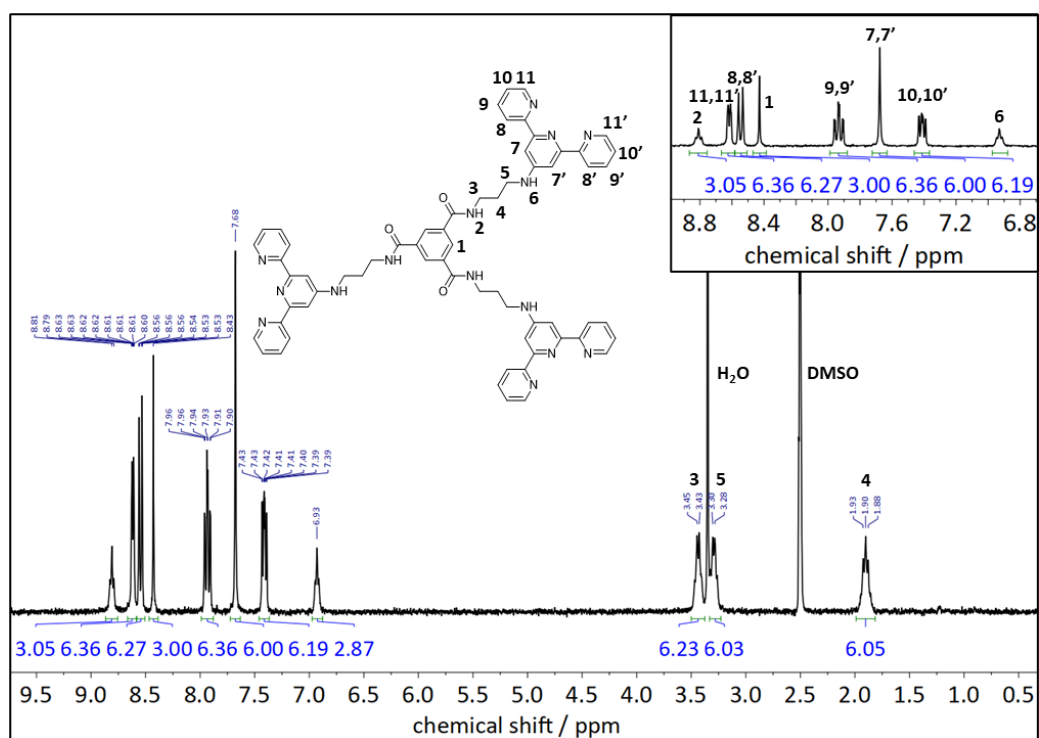
Figure 140: NMR spectrum of **21b.**
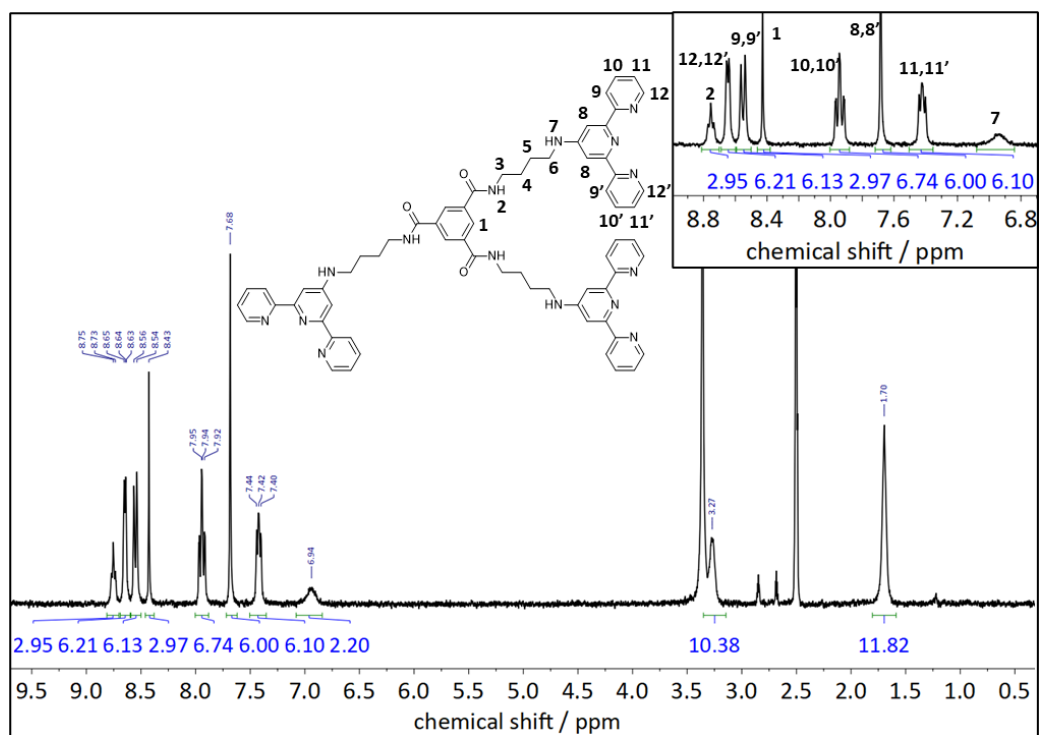
Figure 141: NMR spectrum of **21c.**

Figure 142: NMR spectrum of **24b.**

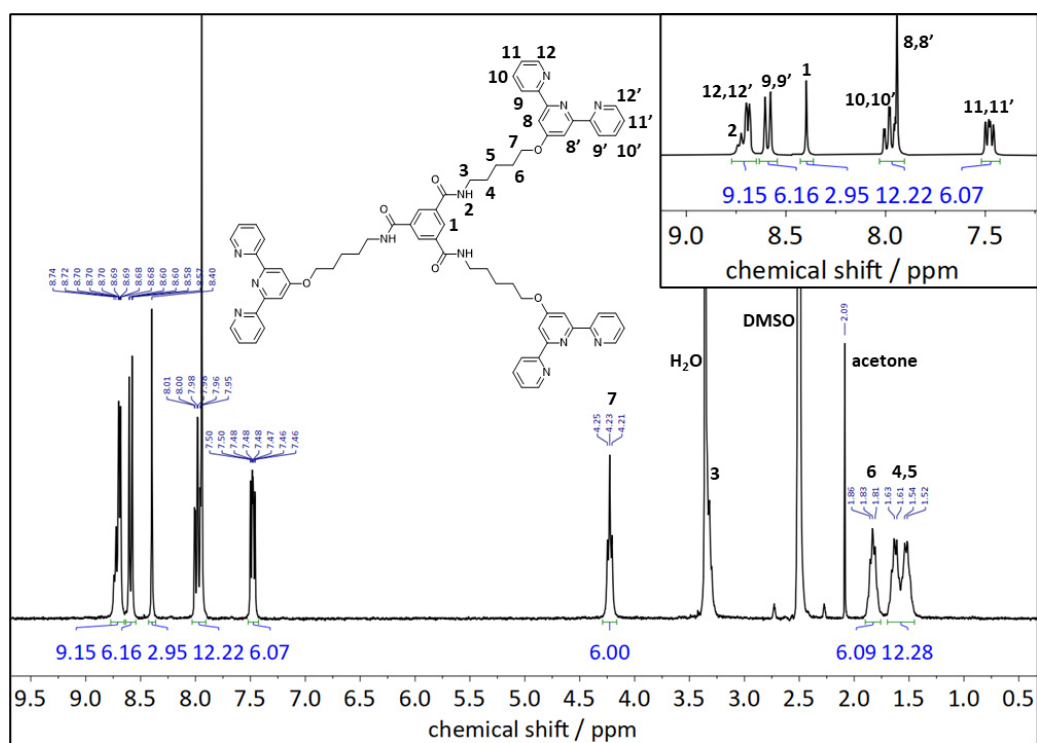**Figure 143:** NMR spectrum of **24c.**

235

Figure 144: NMR spectrum of **24d.**

Figure 145: NMR spectrum of **24e.**
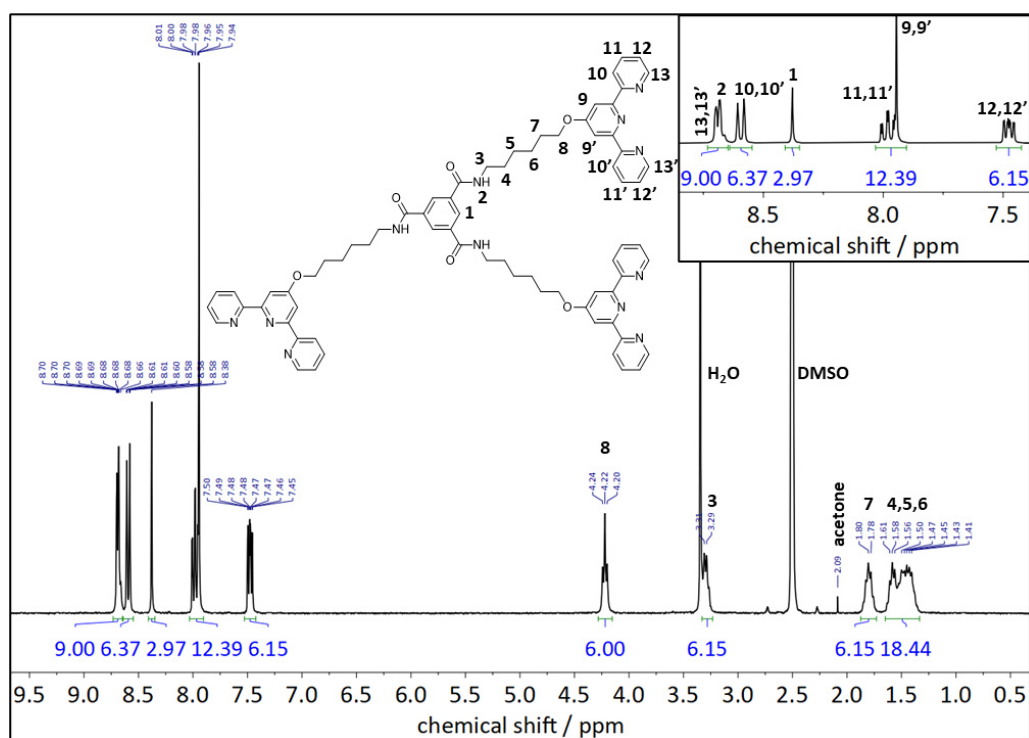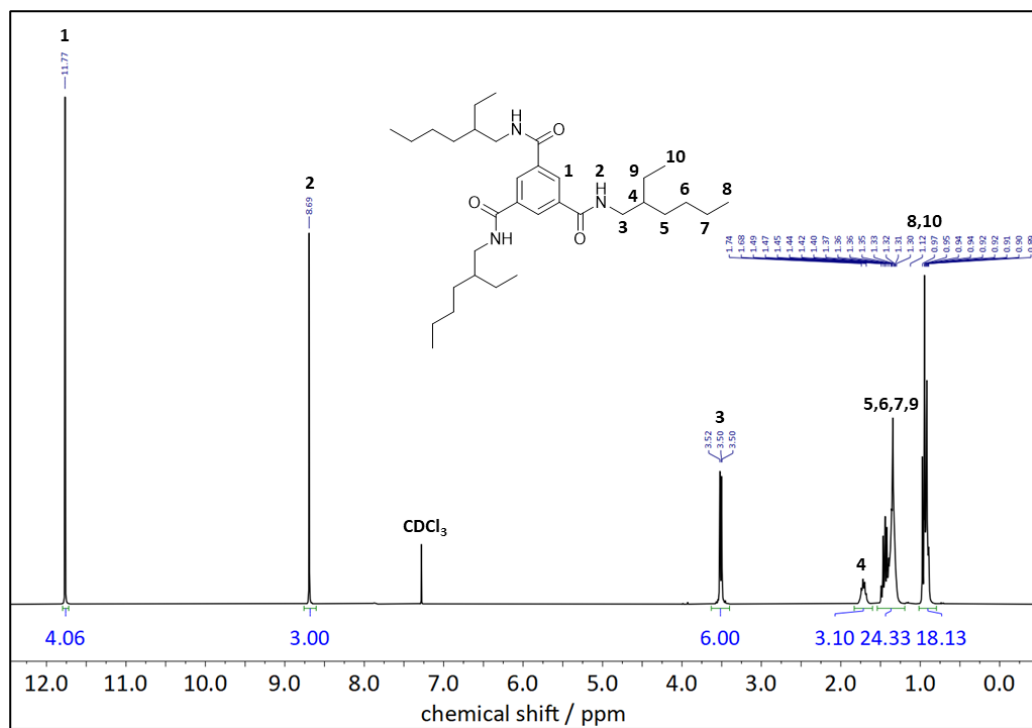
Figure 146: NMR spectrum of **25**.

Figure 147: First and second DSC heating and cooling scans of **21a-c**. The DSC curves were recorded in a temperature range of 50-300 °C with a scanning rate of 10 K/min.

Figure 148: First and second DSC heating and cooling scans of **24a-e**. The DSC curves were recorded in a temperature range of 50-300 °C with a scanning rate of 10 K/min.

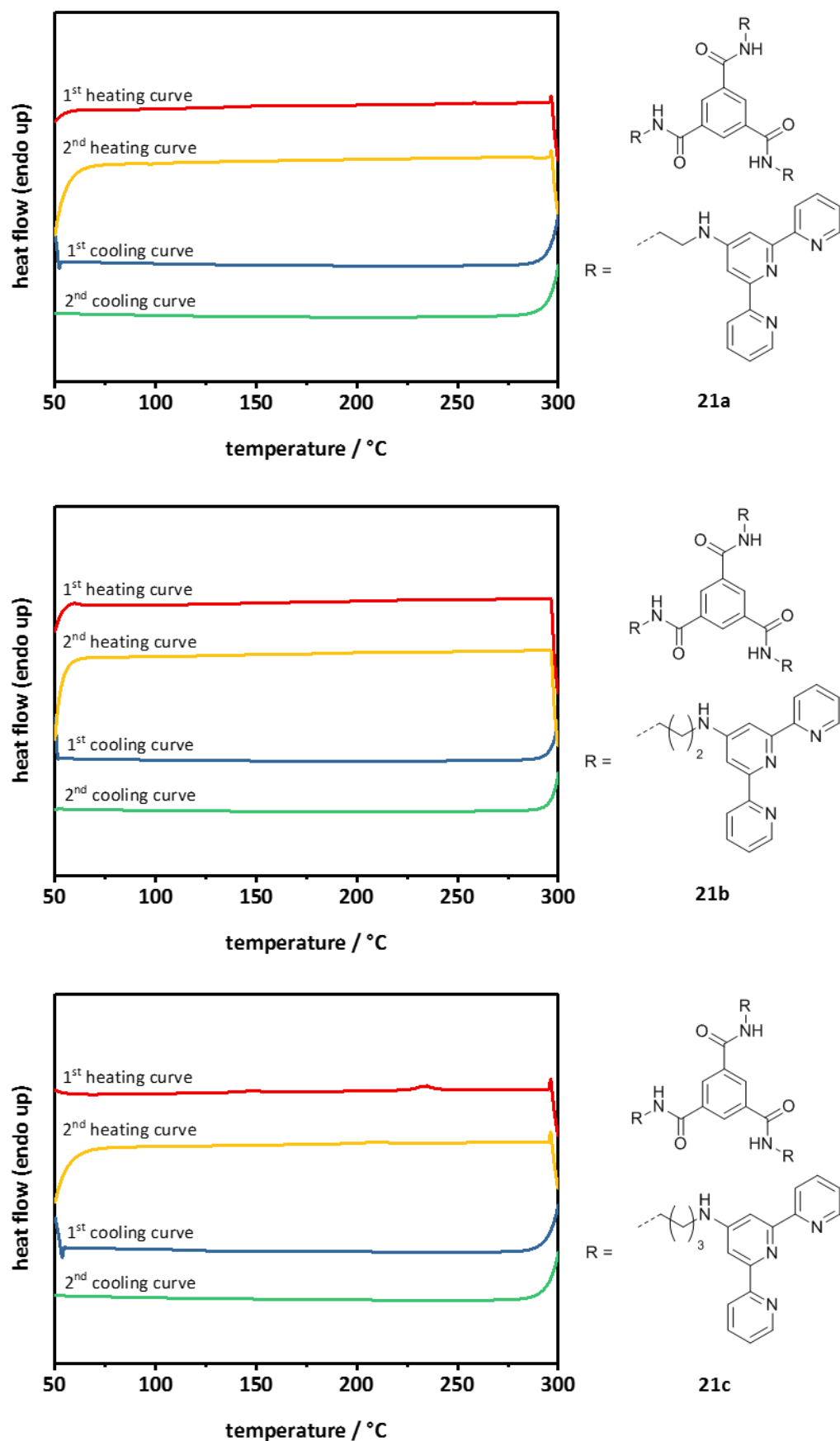**Figure 148 (continued)**: First and second DSC heating and cooling scans of **24a-e**. The DSC curves were recorded in a temperature range of 50-300 °C with a scanning rate of 10 K/min.
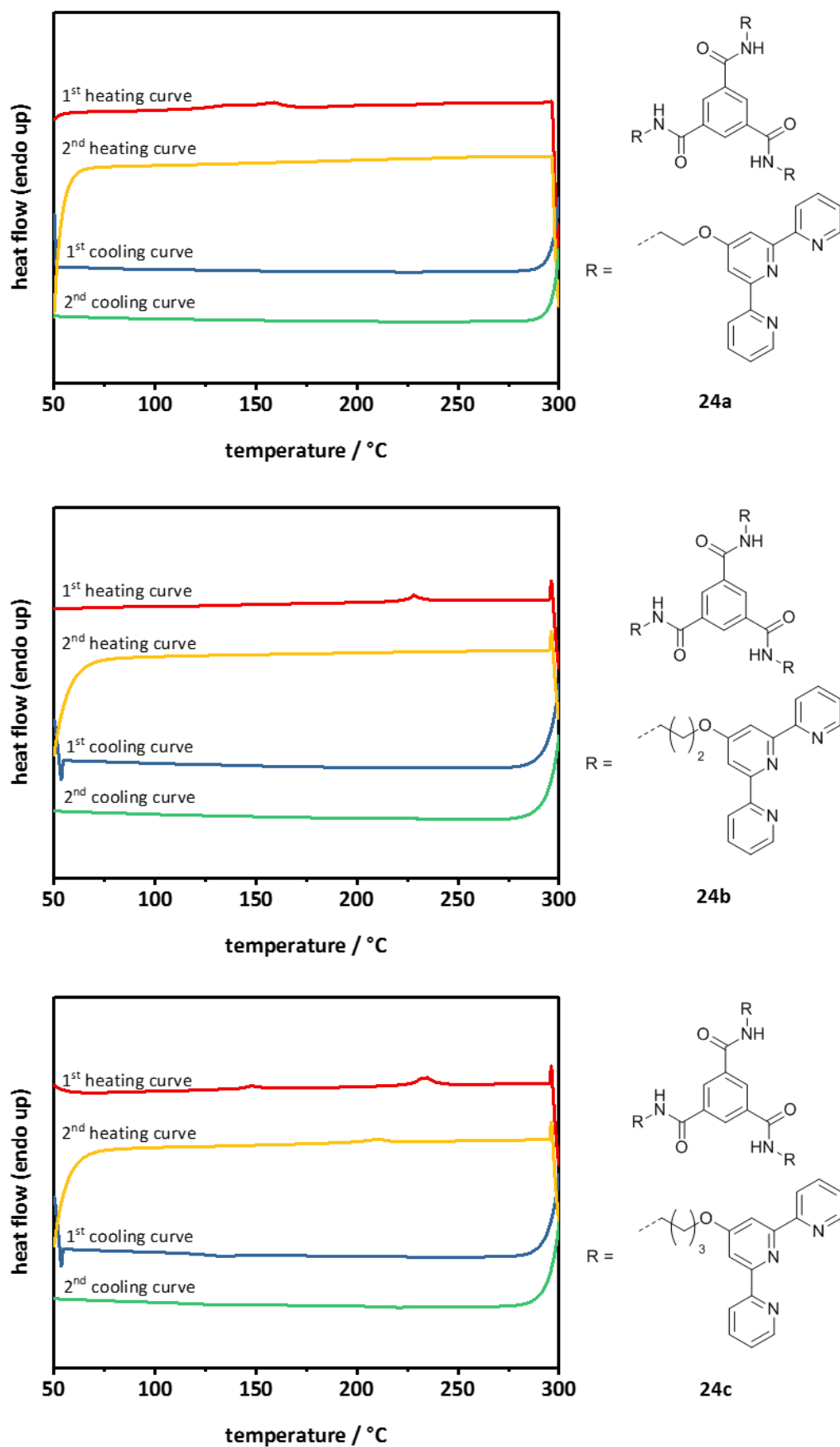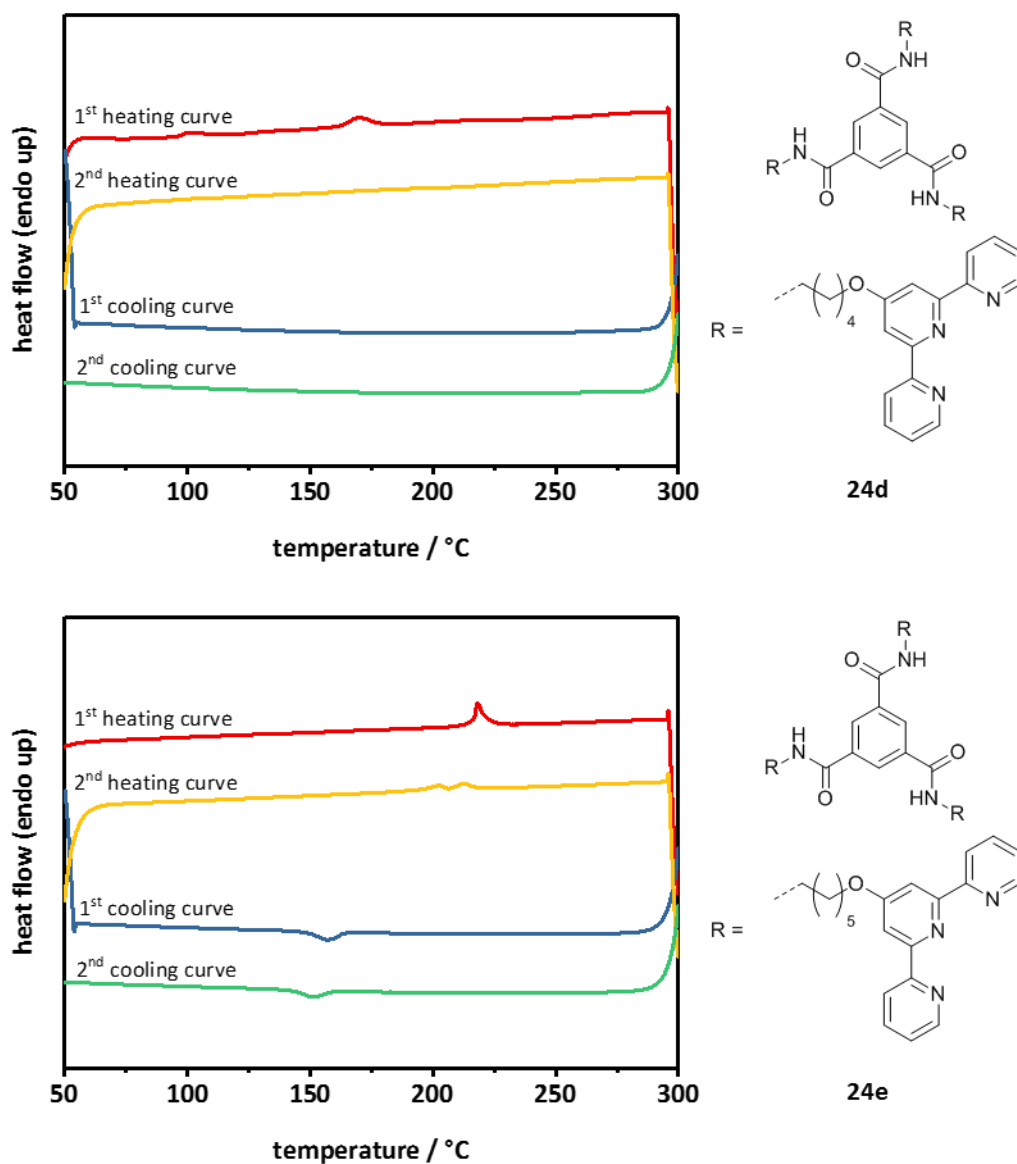
9 Literature

[1]   A. Barhoum, M. Bechelany, A. S. H. Makhlouf, *Handbook of Nanofibers*, Springer International Publishing, Cham **2019**.

[2]   C. J. Luo, S. D. Stoyanov, E. Stride, E. Pelan, M. Edirisinghe, *Chem. Soc. Rev.* **2012**, *41*, 4708.

[3]   D. Das, B. Pourdeyhimi (Eds.), *Composite nonwoven materials: Structure, properties and applications*, Elsevier/Woodhead Publishing, Cambridge, England **2014**.

[4]   G. Kellie (Ed.), *Advances in technical nonwovens*, Woodhead, Duxford, UK **2016**.

[5]   B. Ding, X. Wang, J. Yu (Eds.), *Electrospinning: Nanofabrication and applications*, Elsevier, Amsterdam, Netherlands **2019**.

[6]   T. Lin, *Nanofibers - Production, Properties and Functional Applications*, InTech **2011**.

[7]   Q. Wei, *Functional nanofibres and their applications*, Woodhead, Oxford **2012**.

[8]   D. Han, A. J. Steckl, *ChemPlusChem* **2019**, *84*, 1453.

[9]   J. W. Steed, J. L. Atwood, *Supramolecular chemistry*, Wiley, Chichester **2009**.

[10]   L. S. Pinchuk, V. A. Goldade, A. V. Makarevich, V. N. Kestelman, *Melt Blowing*, Springer, Berlin, Heidelberg **2002**.

[11]   R. Nayak, *Polypropylene nanofibers: Melt electrospinning versus meltblowing*, Springer, Cham **2017**.

[12]   J. L. Daristotle, A. M. Behrens, A. D. Sandler, P. Kofinas, *ACS Appl. Mater. Interfaces* **2016**, *8*, 34951.

[13]   S. Agarwal, *Electrospinning: A practical guide to nanofibers*, De Gruyter, Berlin, Boston **2016**.

[14]   Y. Lu, K. Fu, S. Zhang, Y. Li, C. Chen, J. Zhu, M. Yanilmaz, M. Dirican, X. Zhang, *J. Power Sources* **2015**, *273*, 502.

[15]   M. Afshari (Ed.), *Electrospun nanofibers*, Woodhead Publishing, Duxford **2017**.

[16]   D. H. Reneker, A. L. Yarin, H. Fong, S. Koombhongse, *Int. J. Appl. Phys.* **2000**, *87*, 4531.

[17]   S. L. Shenoy, W. D. Bates, H. L. Frisch, G. E. Wnek, *Polymer* **2005**, *46*, 3372.

[18]   W. K. Son, J. H. Youk, T. S. Lee, W. H. Park, *Polymer* **2004**, *45*, 2959.

[19]   J. Martín, J. Maiz, J. Sacristan, C. Mijangos, *Polymer* **2012**, *53*, 1149.

[20]   S. Grimm, R. Giesa, K. Sklarek, A. Langner, U. Gösele, H.-W. Schmidt, M. Steinhart, *Nano Lett.* **2008**, *8*, 1954.

[21]   P. A. Gale, J. W. Steed, *Supramolecular materials chemistry*, Wiley, Chichester **2012**.

[22]   T. Shimizu, *Self-Assembled Nanomaterials I*, Springer, Berlin, Heidelberg **2008**.

[23]   S. Cantekin, T. F. A. de Greef, A. R. A. Palmans, *Chem. Soc. Rev.* **2012**, *41*, 6125.

[24]   Y. Matsunaga, N. Miyajima, Y. Nakayasu, S. Sakai, M. Yonenaga, *Bull. Chem. Soc. Jpn.* **1988**, *61*, 207.

[25]   A. Timme, R. Kress, R. Q. Albuquerque, H.-W. Schmidt, *Chem. Eur. J.* **2012**, *18*, 8329.

[26]   P. J. M. Stals, J. C. Everts, R. de Bruijn, I. A. W. Filot, M. M. J. Smulders, R. Martín-Rapún, E. A. Pidko, T. F. A. de Greef, A. R. A. Palmans, E. W. Meijer, *Chem. Eur. J.* **2010**, *16*, 810.

[27] P. J. M. Stals, M. M. J. Smulders, R. Martín-Rapún, A. R. A. Palmans, E. W. Meijer, *Chem. Eur. J.* **2009**, *15*, 2071.

[28] D. K. Kumar, D. A. Jose, P. Dastidar, A. Das, *Chem. Mater.* **2004**, *16*, 2332.

[29] M. P. Lightfood, Mair Francis S., R. G. Pritchard, J. E. Warren, *Chem. Commun.* **1999**.

[30] M. Kristiansen, P. Smith, H. Chanzy, C. Baerlocher, V. Gramlich, L. McCusker, T. Weber, P. Pattison, M. Blomenhofer, H.-W. Schmidt, *Cryst. Growth Des.* **2009**, *9*, 2556.

[31] C. A. Jiménez, J. B. Belmar, L. Ortíz, P. Hidalgo, O. Fabelo, J. Pasán, C. Ruiz-Pérez, *Cryst. Growth Des.* **2009**, *9*, 4987.

[32] K. Hanabusa, C. Koto, M. Kimura, H. Shirai, A. Kakehi, *Chem. Lett.* **1997**, *26*, 429.

[33] R. Q. Albuquerque, A. Timme, R. Kress, J. Senker, H.-W. Schmidt, *Chem. Eur. J.* **2013**, *19*, 1647.

[34] D. Weiss, K. Kreger, H.-W. Schmidt, *Macromol. Mater. Eng.* **2017**, *302*, 1600390.

[35] A. Bernet, R. Q. Albuquerque, M. Behr, S. T. Hoffmann, H.-W. Schmidt, *Soft matter* **2012**, *8*, 66.

[36] Z. Shen, T. Wang, M. Liu, *Angew. Chem. Int. Ed.* **2014**, *53*, 13424.

[37] N. Mohmeyer, N. Behrendt, X. Zhang, P. Smith, V. Altstädt, G. M. Sessler, H.-W. Schmidt, *Polymer* **2007**, *48*, 1612.

[38] M. Blomenhofer, S. Ganzleben, D. Hanft, H.-W. Schmidt, M. Kristiansen, P. Smith, K. Stoll, D. Mäder, K. Hoffmann, *Macromolecules* **2005**, *38*, 3688.

[39] F. Abraham, S. Ganzleben, D. Hanft, P. Smith, H.-W. Schmidt, *Macromol. Chem. Phys.* **2010**, *211*, 171.

[40] F. Richter, H.-W. Schmidt, *Macromol. Mater. Eng.* **2013**, *298*, 190.

[41] F. Abraham, H.-W. Schmidt, *Polymer* **2010**, *51*, 913.

[42] M. Aksit, B. Klose, C. Zhao, K. Kreger, H.-W. Schmidt, V. Altstädt, *J. Cell. Plast.* **2019**, *55*, 249.

[43] M. Aksit, C. Zhao, B. Klose, K. Kreger, H.-W. Schmidt, V. Altstädt, *Polymers* **2019**, *11*.

[44] M. Burgard, D. Weiss, K. Kreger, H. Schmalz, S. Agarwal, H.-W. Schmidt, A. Greiner, *Adv. Funct. Mater.* **2019**, *29*, 1903166.

[45] D. Weiss, D. Skrybeck, H. Misslitz, D. Nardini, A. Kern, K. Kreger, H.-W. Schmidt, *ACS Appl. Mater. Interfaces* **2016**, *8*, 14885.

[46] H. Misslitz, K. Kreger, H.-W. Schmidt, *Small* **2013**, *9*, 2053.

[47] N. M. Matsumoto, R. P. M. Lafleur, X. Lou, K.-C. Shih, S. P. W. Wijnands, C. Guibert, J. W. A. M. van Rosendaal, I. K. Voets, A. R. A. Palmans, Y. Lin, E. W. Meijer, *J. Am. Chem. Soc.* **2018**, *140*, 13308.

[48] S. J. Kadolph, S. B. Marcketti, *Textiles*, Pearson, Boston **2017**.

[49] T. Hemamalini, V. R. Giri Dev, *J. Nat. Fibers* **2019**, *13*, 1.

[50] R. Sinclair, *Textiles and fashion: Materials, design and technology*, Elsevier, Amsterdam **2015**.

[51] S. J. Doh, J. Y. Lee, D. Y. Lim, J. N. Im, *Fibers Polym.* **2013**, *14*, 2176.

[52] H. Liu, S. Zhang, L. Liu, J. Yu, B. Ding, *Adv. Funct. Mater.* **2019**, *29*, 1904108.

[53] S. Al Aani, C. J. Wright, M. A. Atieh, N. Hilal, *Desalination* **2017**, *401*, 1.

[54] S. Huang, J. Li, X. Wu, X. Zhang, M. Luo, F. Luo, *Inorg. Chem. Commun.* **2014**, *39*, 1.

[55] M. Faccini, G. Borja, M. Boerrigter, D. Morillo Martín, S. Martìnez Crespiera, S. Vázquez-Campos, L. Aubouy, D. Amantia, *J. Nanomater.* **2015**, *2015*, 1.

[56] M. Langner, A. Greiner, *Macromol. Rapid Commun.* **2016**, *37*, 351.

[57] S. Reich, M. Burgard, M. Langner, S. Jiang, X. Wang, S. Agarwal, B. Ding, J. Yu, A. Greiner, *npj Flex. Electron.* **2018**, *2*, 1417.

[58] E. Krieg, H. Weissman, E. Shirman, E. Shimoni, B. Rybtchinski, *Nat. Nanotechnol.* **2011**, *6*, 141.

[59] C.-C. Cheng, T.-W. Chiu, X.-J. Yang, S.-Y. Huang, W.-L. Fan, J.-Y. Lai, D.-J. Lee, *Polym. Chem.* **2019**, *10*, 827.

[60] S. Anu Mary Ealia, M. P. Saravanakumar, *IOP Conf. Ser.: Mater. Sci. Eng.* **2017**, *263*, 32019.

[61] D. C. Crans, S. Thota (Eds.), *Metal nanoparticles: Synthesis and applications in pharmaceutical sciences*, Wiley-VCH, Weinheim, Germany **2018**.

[62] B. Bhushan, *Springer Handbook of Nanotechnology*, Springer, Berlin, Heidelberg **2017**.

[63] Y.-C. Yeh, B. Creran, V. M. Rotello, *Nanoscale* **2012**, *4*, 1871.

[64] H. Dong, Z. Wu, Y. Gao, A. El-Shafei, B. Jiao, Y. Dai, X. Hou, *Org. Electron.* **2014**, *15*, 1641.

[65] Q.-L. Zhu, Q. Xu, *Chem* **2016**, *1*, 220.

[66] L. M. Rossi, J. L. Fiorio, M. A. S. Garcia, C. P. Ferraz, *Dalton Trans.* **2018**, *47*, 5889.

[67] C.-J. Jia, F. Schüth, *Phys. Chem. Chem. Phys.* **2011**, *13*, 2457.

[68] J. Turkevich, P. C. Stevenson, J. Hillier, *Discuss. Faraday Soc.* **1951**, *11*, 55.

[69] P. Zhao, N. Li, D. Astruc, *Coord. Chem. Rev.* **2013**, *257*, 638.

[70] R. Herizchi, E. Abbasi, M. Milani, A. Akbarzadeh, *Artif. Cells Nanomed. Biotechnol.* **2016**, *44*, 596.

[71] N. G. Bastús, J. Comenge, V. Puntes, *Langmuir* **2011**, *27*, 11098.

[72] J. Piella, N. G. Bastús, V. Puntes, *Chem. Mater.* **2016**, *28*, 1066.

[73] M. Giersig, P. Mulvaney, *Langmuir* **1993**, *9*, 3408.

[74] M. G. Angelo da Silva, M. R. Meneghetti, A. Denicourt-Nowicki, A. Roucoux, *RSC Adv.* **2014**, *4*, 25875.

[75] J. Kronawitt, Z. Fan, M. Schöttle, S. Agarwal, A. Greiner, *ChemNanoMat* **2018**, *114*, 4580.

[76] A. G. da Silva, C. M. Kisukuri, T. S. Rodrigues, E. G. Candido, I. C. de Freitas, A. H. da Silva, J. M. Assaf, D. C. Oliveira, L. H. Andrade, P. H. Camargo, *Appl. Catal. B* **2016**, *184*, 35.

[77] S. Peng, Y. Lee, C. Wang, H. Yin, S. Dai, S. Sun, *Nano Res.* **2008**, *1*, 229.

[78] I. Cano, A. M. Chapman, A. Urakawa, P. W. N. M. van Leeuwen, *J. Am. Chem. Soc.* **2014**, *136*, 2520.

[79] F. Schüth, *Phys. Status Solidi B* **2013**, *250*, 1142.

[80] J. Schöbel, M. Burgard, C. Hils, R. Dersch, M. Dulle, K. Volk, M. Karg, A. Greiner, H. Schmalz, *Angew. Chem. Int. Ed.* **2017**, *56*, 405.

[81] Y. Liu, G. Jiang, L. Li, H. Chen, Q. Huang, T. Jiang, X. Du, *MRS Commun.* **2016**, *6*, 31.

[82] C.-L. Zhang, S.-H. Yu, *Chem. Soc. Rev.* **2014**, *43*, 4423.

[83] S. Thomas, D. Pasquini, S.-Y. Leu, D. A. Gopakumar (Eds.), *Nanoscale materials in water purification*, Elsevier, Amsterdam **2019**.

[84] F. Aubrit, F. Testard, A. Paquirissamy, F. Gobeaux, X. Wang, F. Nallet, P. Fontaine, V. Ponsinet, P. Guenoun, *J. Mater. Chem. C* **2018**, *6*, 8194.

[85] Y. Lu, M. Ballauff, *Prog. Polym. Sci.* **2016**, *59*, 86.

[86] M. I. Din, R. Khalid, Z. Hussain, T. Hussain, A. Mujahid, J. Najeeb, F. Izhar, *Crit. Rev. Anal. Chem.* **2019**.

[87] X. Fang, H. Ma, S. Xiao, M. Shen, R. Guo, X. Cao, X. Shi, *J. Mater. Chem.* **2011**, *21*, 4493.

[88] Y. Liu, G. Jiang, L. Li, H. Chen, Q. Huang, T. Jiang, X. Du, W. Chen, *J. Mater. Sci.* **2015**, *50*, 8120.

[89] S. A. C. Carabineiro, *Front. Chem.* **2019**, *7*, 702.

[90] S. Chakraborty, S. M. Ansar, J. G. Stroud, C. L. Kitchens, *J. Phys. Chem. C* **2018**, *122*, 7749.

[91] P. Zhao, X. Feng, D. Huang, G. Yang, D. Astruc, *Coord. Chem. Rev.* **2015**, *287*, 114.

[92] S. Wunder, Y. Lu, M. Albrecht, M. Ballauff, *ACS Catal.* **2011**, *1*, 908.

[93] S. Wunder, F. Polzer, Y. Lu, Y. Mei, M. Ballauff, *J. Phys. Chem. C* **2010**, *114*, 8814.

[94] S. Panigrahi, S. Basu, S. Praharaj, S. Pande, S. Jana, A. Pal, S. K. Ghosh, T. Pal, *J. Phys. Chem. C* **2007**, *111*, 4596.

[95] W. Liu, X. Yang, L. Xie, *J. Colloid Interface Sci.* **2007**, *313*, 494.

[96] C. Liang, J. Y. Cheong, G. Sitaru, S. Rosenfeldt, A. S. Schenk, S. Gekle, I.-D. Kim, A. Greiner, *Adv. Mater. Interfaces* **2022**, *9*, 2100867.

[97] P. Haider, A. Urakawa, E. Schmidt, A. Baiker, *J Mol Catal A Chem.* **2009**, *305*, 161.

[98] M. Moreno, F. J. Ibañez, J. B. Jasinski, F. P. Zamborini, *J. Am. Chem. Soc.* **2011**, *133*, 4389.

[99] M. Ibrahim, M. A. S. Garcia, L. L. R. Vono, M. Guerrero, P. Lecante, L. M. Rossi, K. Philippot, *Dalton Trans.* **2016**, *45*, 17782.

[100] I. Schrader, J. Warneke, J. Backenköhler, S. Kunz, *J. Am. Chem. Soc.* **2015**, *137*, 905.

[101] Y. Wang, X.-K. Wan, L. Ren, H. Su, G. Li, S. Malola, S. Lin, Z. Tang, H. Häkkinen, B. K. Teo, Q.-M. Wang, N. Zheng, *J. Am. Chem. Soc.* **2016**, *138*, 3278.

[102] P. Munnik, P. E. de Jongh, K. P. de Jong, *Chem. Rev.* **2015**, *115*, 6687.

[103] A. G. M. da Silva, T. S. Rodrigues, L. S. K. Taguchi, H. V. Fajardo, R. Balzer, L. F. D. Probst, P. H. C. Camargo, *J. Mater. Sci.* **2016**, *51*, 603.

[104] R.-Y. Zhong, X.-H. Yan, Z.-K. Gao, R.-J. Zhang, B.-Q. Xu, *Catal. Sci. Technol.* **2013**, *3*, 3013.

[105] T. A. G. Silva, R. Landers, L. M. Rossi, *Catal. Sci. Technol.* **2013**, *3*, 2993.

[106] A. R. A. Palmans, Vekemans, Jef A. J. M., H. Kooijman, A. L. Spek, E. W. Meijer, *Chem. Commun.* **1997**.

[107] S. Hasegawa, S. Horike, R. Matsuda, S. Furukawa, K. Mochizuki, Y. Kinoshita, S. Kitagawa, *J. Am. Chem. Soc.* **2007**, *129*, 2607.

[108] B.-C. Tzeng, T.-H. Chiu, B.-S. Chen, G.-H. Lee, *Chem. Eur. J.* **2008**, *14*, 5237.

[109]   Y.-Q. Fan, J. Liu, Y.-Y. Chen, X.-W. Guan, J. Wang, H. Yao, Y.-M. Zhang, T.-B. Wei, Q. Lin, *J. Mater. Chem. C* **2018**, *6*, 13331.

[110]   H.-L. Yang, X.-W. Sun, Y.-M. Zhang, Z.-H. Wang, W. Zhu, Y.-Q. Fan, T.-B. Wei, H. Yao, Q. Lin, *Soft matter* **2019**, *15*, 9547.

[111]   J. Liu, Y.-Q. Fan, S.-S. Song, G.-F. Gong, J. Wang, X.-W. Guan, H. Yao, Y.-M. Zhang, T.-B. Wei, Q. Lin, *ACS Sustainable Chem. Eng.* **2019**, *7*, 11999.

[112]   L. Rajput, K. Biradha, *J. Mol. Struct.* **2011**, *991*, 97.

[113]   P. D. Beer, N. C. Fletcher, A. Grieve, J. W. Wheeler, C. P. Moore, T. Wear, *J. Chem. Soc., Perkin Trans. 2* **1996**.

[114]   D. Moon, S. Kang, J. Park, K. Lee, R. P. John, H. Won, G. H. Seong, Y. S. Kim, G. H. Kim, H. Rhee, M. S. Lah, *J. Am. Chem. Soc.* **2006**, *128*, 3530.

[115]   J. Park, S. Hong, D. Moon, M. Park, K. Lee, S. Kang, Y. Zou, R. P. John, G. H. Kim, M. S. Lah, *Inorg. Chem.* **2007**, *46*, 10208.

[116]   Y. Wang, T. Okamura, W.-Y. Sun, N. Ueyama, *Cryst. Growth Des.* **2008**, *8*, 802.

[117]   R. Moi, K. Nath, K. Biradha, *Asian J. Chem.* **2019**, *14*, 3742.

[118]   S. Hong, Y. Zou, D. Moon, M. S. Lah, *Chem. Commun.* **2007**.

[119]   X.-Z. Luo, X.-J. Jia, J.-H. Deng, J.-L. Zhong, H.-J. Liu, K.-J. Wang, D.-C. Zhong, *J. Am. Chem. Soc.* **2013**, *135*, 11684.

[120]   Y.-Q. Fan, Q. Huang, Y.-M. Zhang, J. Wang, X.-W. Guan, Y.-Y. Chen, H. Yao, T.-B. Wei, Q. Lin, *Polym. Chem.* **2019**, *10*, 6489.

[121]   H.-L. Yang, Q.-P. Zhang, Y.-M. Zhang, G.-F. Gong, Y.-Y. Chen, Qi-Zhou, H. Yao, T.-B. Wei, Q. Lin, *Dyes Pigm.* **2019**, *171*, 107745.

[122]   O. Kotova, R. Daly, C. M. G. dos Santos, M. Boese, P. E. Kruger, J. J. Boland, T. Gunnlaugsson, *Angew. Chem. Int. Ed.* **2012**, *51*, 7208.

[123]   O. Kotova, R. Daly, C. M. G. dos Santos, P. E. Kruger, J. J. Boland, T. Gunnlaugsson, *Inorg. Chem.* **2015**, *54*, 7735.

[124]   R. Daly, O. Kotova, M. Boese, T. Gunnlaugsson, J. J. Boland, *ACS nano* **2013**, *7*, 4838.

[125]   S. H. Jung, J. Jeon, H. Kim, J. Jaworski, J. H. Jung, *J. Am. Chem. Soc.* **2014**, *136*, 6446.

[126]   S. H. Jung, K.-Y. Kwon, J. H. Jung, *Chem. Commun.* **2015**, *51*, 952.

[127]   H.-Y. Wang, Z.-J. Ding, Z. Li, Y. Zhang, H. Li, *Colloid Polym Sci.* **2018**, *296*, 53.

[128]   Z. Hou, P. Li, H.-Y. Wang, Z. Li, H. Li, *Dyes Pigm.* **2017**, *147*, 429.

[129]   H. Luo, Q. Liu, W. Zhu, K. Wang, X. Luo, *Acta Chim. Sin.* **2015**, *73*, 1031.

[130]   D. Kluge, J. C. Singer, J. W. Neubauer, F. Abraham, H.-W. Schmidt, A. Fery, *Small* **2012**, *8*, 2563.

[131]   P. Sutar, T. K. Maji, *Chem. Commun.* **2016**, *52*, 13136.

[132]   J. Park, J. H. Lee, J. Jaworski, S. Shinkai, J. H. Jung, *Inorg. Chem.* **2014**, *53*, 7181.

[133]   G. Maayan, B. Yoo, K. Kirshenbaum, *Tetrahedron Lett.* **2008**, *49*, 335.

[134]   S. Sarkar, A. Mondal, A. K. Tiwari, R. Shunmugam, *Chem. Commun.* **2012**, *48*, 4223.

[135]   H. Yang, A. Wang, L. Zhang, X. Zhou, G. Yang, Y. Li, Y. Zhang, B. Zhang, J. Song, Y. Feng, *New J. Chem.* **2017**, *41*, 15173.

[136]   O. Inhoff, J. M. Richards, J. W. Brîet, G. Lowe, R. L. Krauth-Siegel, *J. Med. Chem.* **2002**, *45*, 4524.

[137]   P. R. Andres, R. Lunkwitz, G. R. Pabst, K. Böhn, D. Wouters, S. Schmatloch, U. S. Schubert, *Eur. J. Org. Chem.* **2003**, *2003*, 3769.

[138]   M. Drummer, C. Liang, K. Kreger, S. Rosenfeldt, A. Greiner, H.-W. Schmidt, *ACS Appl. Mater. Interfaces* **2021**.

[139]   C. S. Zehe, J. A. Hill, N. P. Funnell, K. Kreger, K. P. van der Zwan, A. L. Goodwin, H.-W. Schmidt, J. Senker, *Angew. Chem. Int. Ed.* **2017**, *56*, 4432.

[140]   C. Lin, K. Tao, D. Hua, Z. Ma, S. Zhou, *Molecules* **2013**, *18*, 12609.

[141]   C. Deraedt, L. Salmon, S. Gatard, R. Ciganda, R. Hernandez, J. Ruiz, D. Astruc, *Chem. Commun.* **2014**, *50*, 14194.

[142]   D. Hu, Y. Xiao, H. Liu, H. Wang, J. Li, B. Zhou, P. Liu, M. Shen, X. Shi, *Colloids Surf. A: Physicochem. Eng. Asp.* **2018**, *552*, 9.

[143]   C. Wang, S. Sun, L. Zhang, J. Yin, T. Jiao, L. Zhang, Y. Xu, J. Zhou, Q. Peng, *Colloids Surf. A: Physicochem. Eng. Asp.* **2019**, *561*, 283.

[144]   C. R. Cabreira, F. F. Camilo, *Cellulose* **2020**, *27*, 3919.

[145]   K. Bhaduri, B. D. Das, R. Kumar, S. Mondal, S. Chatterjee, S. Shah, J. J. Bravo-Suárez, B. Chowdhury, *ACS omega* **2019**, *4*, 4071.

[146]   L. Tan, B. Tan, *Chem. Eng. Sci.* **2020**, *390*, 124485.

[147]   J. Miao, J. Lu, H. Jiang, Y. Liu, W. Xing, X. Ke, R. Chen, *AIChE J* **2019**, *65*.

[148]   R. Szűcs, D. Balogh-Weiser, E. Sánta-Bell, E. Tóth-Szeles, T. Varga, Z. Kónya, L. Poppe, I. Lagzi, *RSC Adv.* **2019**, *9*, 9193.

[149]   H. Wang, Z. Dong, C. Na, *ACS Sustainable Chem. Eng.* **2013**, *1*, 746.

[150]   Z.-T. Xie, T.-A. Asoh, H. Uyama, *J. Hazard. Mater.* **2020**, *400*, 123303.

[151]   Y. Yu, Q. Zhang, M. Chi, H. Jiang, X. Liu, S. Wang, D. Min, *Cellulose* **2021**, *28*, 7283.

Danksagung

An erster Stelle möchte ich mich bei meinem Doktorvater, Herrn Prof. Hans-Werner Schmidt, für das interessante und anwendungsbezogene Thema meiner Doktorarbeit, für die Unterstützung und hilfreichen Ratschläge bei wissenschaftlichen Diskussionen, für die Bereitstellung eines sehr gut ausgestatteten Labor- und Arbeitsplatzes sowie die Freiheit, wissenschaftlichen Fragestellungen nach eigenem Ermessen nachzugehen, bedanken.

Für die finanzielle Unterstützung bedanke ich mich bei der Deutschen Forschungsgemeinschaft (DFG) im Rahmen des Sonderforschungsbereiches 840 „Von partikulären Nanosystemen zur Mesotechnologie" im Teilprojekt B8 „Mesoskopisch strukturierte funktionale Kompositvliese für Anwendung in der Separation und Katalyse".

Mein besonderer Dank gilt Dr. Klaus Kreger und David Nardini, die durch ihre vielseitige Unterstützung, zahlreichen Diskussionen und Hilfestellungen und ihr großes Fachwissen zum Gelingen dieser Arbeit maßgeblich beigetragen haben.

Des Weiteren danke ich Prof. Dr. Andreas Greiner (Makromolekulare Chemie II) für die Koordination des Teilprojektes B8 und die hilfreichen wissenschaftlichen Diskussionen, sowie Julia Kronawitt und Chen Liang für die gemeinsame Bearbeitung des Teilprojektes B8, die zahlreichen Diskussionen und die gegenseitige Hilfe. Außerdem bedanke ich mich bei Christian Hils für jegliche Hilfestellungen und Diskussionen bezüglich dem Elektrospinnen, der Immobilisierung von Nanopartikeln oder der Katalyse und für die Einweisung in die ICP-OES.

Ich bedanke mich auch bei den technischen Angestellten Jutta Failner und Sandra Ganzleben für die zahlreichen Synthesen von Trisamiden und bei Alexander Kern und Jonas Mayer für ihre Hilfe bei jeglichen Fragen technischer Art. Mein Dank gilt Dr. Beate Förster, Dr. Ulrich Mansfeld, Martina Heider (alle REM) und Dr. Markus Drechsler (TEM) für die Einweisung und Beantwortung jeglicher Fragen im Bereich der Elektronenmikroskopie. Dr. Holger Schmalz danke ich für die Raman-Messungen und Dr. Sabine Rosenfeld für die Durchführung der SAXS-Messungen und Hilfe bei der Auswertung und Interpretation der Daten.

Ferner bedanke ich mich bei Martin Schlagbauer, Lukas Dietz, Maximilian Kleiner, Michael Hoffmann, Hendrik Volz und Alexander Berger für die Unterstützung in zahlreichen Experimenten und in der Literaturrecherche im Rahmen von Mitarbeiterpraktika.

Mein großer Dank gilt natürlich auch allen Arbeitskollegen am Lehrstuhl Makromolekulare Chemie I für die angenehme und freundliche Arbeitsatmosphäre, die zahlreichen wissenschaftlichen und privaten Gespräche, die Unterstützung bei Problemen jeglicher Art und die Aktivitäten außerhalb des Universitätslebens. Besonders bedanken möchte ich mich bei meinem Labor 597 (Basti, Daniel, Christoph, Simon, Johannes, Jessy) für die gemeinsame Zeit, in der der Spaß nicht zu kurz kam und jeder ein offenes Ohr für den/die andere(n) hatte. Vielen Dank auch ans „Mensaessen"-Team mit Julia,

Andi S., Felix K., Christoph, Jannik, Christina S., Francesco, Christian B., Nora, Johannes, Lukas für die zahlreichen Gespräche in der Mensa und die privaten Kochabende oder Freizeitaktivitäten.

Für jegliche Unterstützung in verwaltungstechnischen Aufgaben gilt mein großer Dank Petra Weiss und Christina Wunderlich.

All meinen Freunden – egal ob aus meinem Studium, aus der KHG oder vom Gospelchor – danke ich für die schöne und erlebnisreiche Zeit in Bayreuth. Ich werde die vielen Momente immer in guter Erinnerung behalten. Ganz wichtig ist auch, dass ihr es immer wieder geschafft habt, mich zu motivieren und mit Freizeitaktivitäten vom Unialltag abzulenken.

Zu guter Letzt ein ganz großes Dankeschön an meine Familie – besonders an meine Eltern, die mich während des ganzen Studiums und der Doktorarbeit immer unterstützt und an mich geglaubt haben – und an meine Frau Elena, die mich immer wieder motiviert hat und mir stets beiseite stand.

(Eidesstattliche) Versicherungen und Erklärungen

(§ 9 Satz 2 Nr. 3 PromO BayNAT)

Hiermit versichere ich eidesstattlich, dass ich die Arbeit selbstständig verfasst und keine anderen als die von mir angegebenen Quellen und Hilfsmittel benutzt habe (vgl. Art. 64 Abs. 1 Satz 6 BayHSchG).

(§ 9 Satz 2 Nr. 3 PromO BayNAT)

Hiermit erkläre ich, dass ich die Dissertation nicht bereits zur Erlangung eines akademischen Grades eingereicht habe und dass ich nicht bereits diese oder eine gleichartige Doktorprüfung endgültig nicht bestanden habe.

(§ 9 Satz 2 Nr. 4 PromO BayNAT)

Hiermit erkläre ich, dass ich Hilfe von gewerblichen Promotionsberatern bzw. -vermittlern oder ähnlichen Dienstleistern weder bisher in Anspruch genommen habe noch künftig in Anspruch nehmen werde.

(§ 9 Satz 2 Nr. 7 PromO BayNAT)

Hiermit erkläre ich mein Einverständnis, dass die elektronische Fassung meiner Dissertation unter Wahrung meiner Urheberrechte und des Datenschutzes einer gesonderten Überprüfung unterzogen werden kann.

(§ 9 Satz 2 Nr. 8 PromO BayNAT)

Hiermit erkläre ich mein Einverständnis, dass bei Verdacht wissenschaftlichen Fehlverhaltens Ermittlungen durch universitätsinterne Organe der wissenschaftlichen Selbstkontrolle stattfinden können.

…………………………………………………………………………………………..

Ort, Datum   *Unterschrift*